Dicyanomethylene Squaraines: Aggregation and G-Quadruplex Complexation

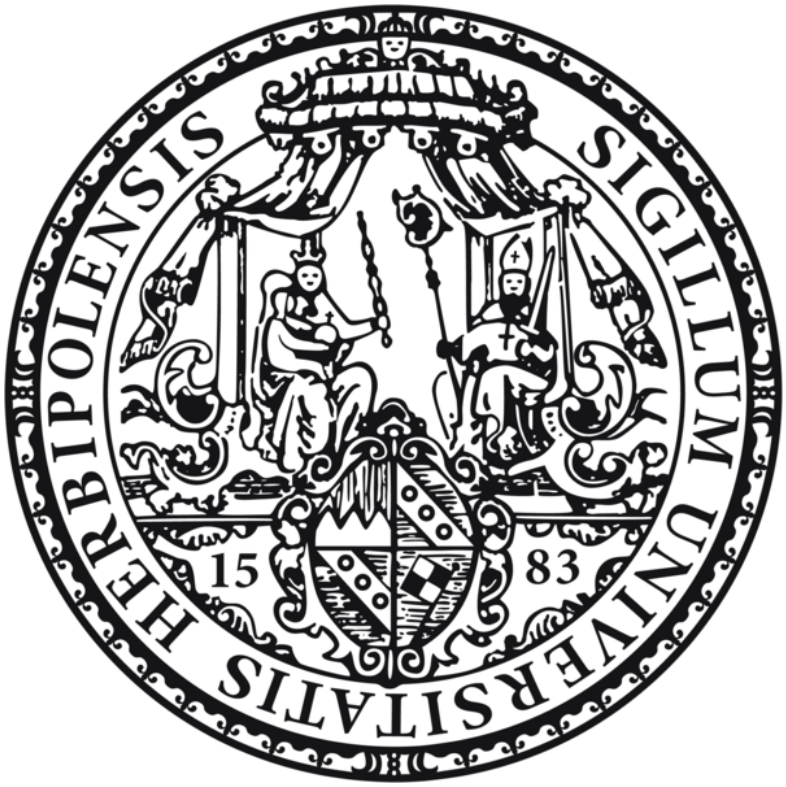

Dissertation zur Erlangung des
naturwissenschaftlichen Doktorgrades der
Julius-Maximilians-Universität Würzburg

Vorgelegt von

Chia-An Shen

aus Taoyuan, Taiwan

Würzburg, 2021

Eingereicht bei der Fakultät für Chemie und Pharmazie am:

_____

Gutachter der schriftlichen Arbeit:

1. Gutachter: Prof. Dr. Frank Würthner

2. Gutachter:

Prüfer des öffentlichen Promotionskolloquiums:

1. Prüfer: Prof. Dr. Frank Würthner

2. Prüfer:

3. Prüfer:

Datum des öffentlichen Promotionskolloquiums:

_____

Doktorurkunde ausgehändigt am:

_____

List of Abbreviations

1D/2D/3D	one-dimensional/ two-dimensional/ three-dimensional
A	acceptor
Abs.	absorption
Ac	acetyl
AFM	atomic force microscopy
AM1	Austin Model 1
ATP	adenosine triphosphate
a.u.	arbitrary unit
B3LYP	Becke-3-parameter-Lee-Yang-Parr (exchange-correlation functional)
β-CD	β-cyclodextrin
BHJ	bulk heterojunction
BSA	bovine serum albumin
BTA	benzene-1,3,5-tricarboxamide
BTW	biological transparency window
CB	circular birefringence
CD	circular dichroism
CMC	critical micelle concentration
COD	1,5-cyclooctadiene
CP	circular polarized
CREKA	Cys-Arg-Glu-Lys-Ala (peptide sequence)
CTAB	cetrimonium (hexadecyltrimethylammonium) bromide
Cys	cysteine
d	doublet
D	donor
DCTB	*trans*-2-[3-(4-*tert*-butylphenyl)-2-methyl-2-propenylidene]malononitrile
decomp.	decomposed
DFT	density functional theory
DMF	*N,N'*-dimethylformamide
DMSO	dimethylsulfoxide
DNA	deoxyribonucleic acid
DOSY	diffusion ordered spectroscopy
ds	double-stranded

DSPE	1,2-distearoyl-sn-glycero-3-phosphoethanol
DSSC	dye-sensitized solar cell
ECD	electronic circular dichroism
EDTA	ethylenediaminetetraacetic acid
e.g.	for example (Latin: *exempli gratia*)
et al.	and others (Latin: *et alia*)
etc.	and so forth (Latin: *et cetera*)
EtOH	ethanol
eq.	equivalents
Eq.	equation
ESI	electrospray ionization
ESM	Essential States Model
FL	fluorescence
FLIM	fluorescence lifetime imaging microscopy
FWHM	full width at half maximum
G4	G-quadruplex
GPC	gel permeation chromatography
h	hour
Hcy	homocysteine
HOPG	highly oriented pyrolytic graphite
HRMS	high-resolution mass spectrometry
HSA	human serum albumin
IC	internal conversion
ICG	indocyanine green
ICT	*inter*molecular charge transfer
i.e.	which means (Latin: *id est*)
i-PrOH	isopropanol
LB	Langmuir-Blodgett
LC	liquid crystal
m	multiplet
MALDI	matrix-assisted laser desorption/ionization
MeOH	methanol
min	minute
Mp.	melting point

n.d.	not determined
neg.	negative
NIR	near-infrared
NMR	nuclear magnetic resonance (spectroscopy)
NOESY	nuclear Overhauser enhancement spectroscopy
norm.	normalized
NP	nanoparticle
o	*ortho*
OD	optical density
OEG	oligoethylene glycol
OFET	organic field-effect transistor
OLED	organic light-emitting diode
OPA	one-photon absorption
OPV	organic photovoltaics
OTFT	organic thin-film transistor
p	*para*
PA	photoacoustic
PAA-Na	poly(acrylic acid) sodium salt
Pc	phthalocyanine
PCBM	phenyl-C_{61}-butyric acid methyl ester
PCM	polarizable continuum model
PEG	polyethylene glycol
Ph	phenyl
PM6	parameterized model 6
pos.	positive
PPG	polypropylene glycol
ppm	parts per million
q	quartet
quint	quintet
QY	quantum yield
ref.	reference
RNA	ribonucleic acid
ROESY	rotating frame nuclear Overhauser effect spectroscopy
rpm	revolutions per minute

rt	room temperature
s	singlet; second
SAXS	small angle X-ray scattering
SDS	sodium dodecyl sulfate
SEM	scanning electron microscopy
SI	supporting information
SiO_x	silica wafer
ss	single-stranded
t	triplet
TBTA	tris(benzyltriazolylmethyl)amine
TCE	1,1,2,2-tetrachloroethane
TCSPC	time-correlated single photon counting
TD	time-dependent
TEG	triethylene glycol
TEM	transmission electron microscopy
THF	tetrahydrofuran
TRIS	tris(hydroxymethyl)aminomethane
TPA	two-photon absorption
TPEF	two-photon excited fluorescence
UAHF	United Atom Topological Model applied on radii optimized for the HF/6-31G(d) level of theory
UV	ultra-violet
Vis	visible
vol.	volume
WAXS	wide angle X-ray scattering

List of Variables and Constants

α	twist angle; dihedral angle
α_{agg}	degree of aggregation
δ	chemical shift
ε	extinction coefficient; solvent permittivity
ε_o	permittivity of vacuum
η_{CT} / η_z	energy of the charge separated state / energy of the zwitterionic state
θ	slip angle
λ	wavelength
λ^2	Huang-Rhys factor
$\tilde{\nu}$	wavenumber
$\hat{\mu}$	dipole moment operator
$\vec{\mu}_{eg}$ / $\vec{\mu}_g$	transition dipole moment / ground state dipole moment
ρ	zwitterionic character; density
σ	cooperativity factor
σ_2	two-photon absorption cross-section
τ_{FL}	fluorescence lifetime
Φ_{FL}	fluorescence quantum yield
Ψ	wave function
ω_{vib}	frequency of harmonic oscillator
ħ	reduced Planck constant
$\|A\rangle$	anionic state
A	absorbance
b	light path length
c	concentration; speed of light
c_0	total concentration
$\|C\rangle$	cationic state
c_T	total concentration
d	density
$\|e\rangle$	excited state
E	energy
f	oscillator strength
$\|g\rangle$	ground state

ΔG	change of Gibbs free energy
h	helical pitch; Planck constant
h.c.	the Hermitian conjugate
$\hat{H}$	Hamiltonian
ΔH	change of enthalpy
ΔH_e / ΔH_{pol}	elongation enthalpy / polymerization enthalpy
J	exciton coupling energy
K	elongation constant
K_{11} / K_{12}	first / second binding constant
K_2	dimerization constant
K_a	dimensionless equilibrium constant for the activation step of the supramolecular polymerization
K_b	binding constant
k_{FL} / k_{nr}	rate constant of radiative pathway / rate constant of non-radiative pathway
m	mass
M	molar mass
n	refractive index
N	number of molecules
$\|N\rangle$	neutral state
N_A	Avogadro constant (6.022×10^{23})
q	point integer charge
r	distance between the centers of the molecules; radius
R	ideal gas constant
ΔS	change of entropy
T	temperature
T_e / T_m	elongation temperature / melting temperature
t_{CT}	*inter*molecular CT coupling strength
t_Z	transfer integral
v	volume
$\hat{V}_{Coul}$	Coulomb operator
V_{mol} / V_{rod}	molecular volume / volume of one pitch of the nanorod
$\|Z\rangle$	zwitterionic state

Table of Contents

Chapter 1 – Introduction and Aim of Thesis 1

Chapter 2 – State of Knowledge 6

2.1 Squaraines Dyes (Structures and Structure−Absorption/Emission Relationships) 6

2.1.1 Core-Substituted Squaraine Dyes 7

2.1.2 Dicyanomethylene Substituted Squaraine Dyes with Donor Variations 10

2.1.3 Squaraine Polymers 12

2.2 Self-Assembled Squaraines and Squaraine Materials 18

2.2.1 Aggregation of Squaraines in Langmuir-Blodgett Films 19

2.2.2 Aggregation of Squaraines in Solutions 20

2.2.3 Aggregation of Squaraines in the Solid State 41

2.3 Theoretical Interpretation of the Optical Properties of Dye Aggregates 48

2.3.1 Exciton Theory 48

2.3.2 Essential States Model (ESM) 51

Chapter 3 – NIR-Emitting Squaraine J-Aggregate Nanosheets 53

3.1 Introduction 54

3.2 Results and Discussion 55

3.2.1 Design and Synthesis 55

3.2.2 Molecular Optical Properties 56

3.2.3 Self-Assembly Studies 58

3.2.4 Structural Investigation 59

3.3 Conclusions 61

Chapter 4 – Polymorphism in Squaraine Dye Aggregates by Self-Assembly Pathway Differentiation: Panchromatic Tubular Dye Nanorods versus J-Aggregate Nanosheets 62

4.1 Introduction 63

4.2 Results and Discussion 65

4.2.1 Synthesis and Molecular Properties 65

4.2.2 Self-Assembly into Supramolecular Polymers 66

4.2.3 Structural Insights and Packing Model 68
4.2.4 Concentration-Dependent UV/Vis/NIR Spectroscopy 71
4.2.5 Theoretical Calculations for Dye-Dye Interactions 74
4.3 Conclusion 78
Chapter 5 – A Double J-Coupling Strategy for Near-Infrared Emitters 80
5.1 Introduction 80
5.2 Results and Discussion 82
5.2.1 Synthesis 82
5.2.2 Molecular Optical Properties 82
5.2.3 Self-Assembly Studies 85
5.2.4 Structural Investigations 87
5.3 Conclusion 90
Chapter 6 – Selective Parallel G-Quadruplex Recognition by a NIR-to-NIR Two-Photon Squaraine 91
6.1 Introduction 92
6.2 Results and Discussion 93
6.2.1 Design and Synthesis 93
6.2.2 Aggregation in Water 94
6.2.3 G4 Binding 96
6.2.4 Two-Photon Absorption 100
6.3 Conclusions 102
Chapter 7 – Summary and Conclusion 104
Chapter 8 – Zusammenfassung und Fazit 110
Chapter 9 – Appendix 117
9.1 Supporting Information for *Chapter 3*: NIR-Emitting Squaraine J-Aggregate Nanosheets 117
9.1.1 Materials and Methods 117
9.1.2 Synthesis and Characterizations 119

9.1.3 UV/Vis Absorption and Fluorescence Spectroscopy 125
9.1.4 Determination of Absolute Fluorescence Quantum Yield 126
9.1.5 Self-Assembly Studies 126
9.1.6 DOSY NMR 130
9.1.7 AFM Studies 132
9.1.8 Proposed Packing Model 133
9.1.9 NMR Spectra 134
9.2 Supporting Information for *Chapter 4*: Polymorphism in Squaraine Dye Aggregates by Self-Assembly Pathway Differentiation: Panchromatic Tubular Dye Nanorods versus J-Aggregate Nanosheets 141
9.2.1 Materials and Methods 141
9.2.2 Synthesis and Characterizations 143
9.2.3 UV/Vis/NIR Absorption and Fluorescence Spectroscopy 144
9.2.4 Determination of Absolute Fluorescence Quantum Yield 145
9.2.5 Self-Assembly Studies 146
9.2.6 Proposed Packing Models 146
9.2.7 Data Evaluation 148
9.2.8 Computational Chemistry 152
9.2.9 Essential States Model 152
9.2.10 NMR Spectra 163
9.3 Supporting information for *Chapter 5*: A Double J-Coupling Strategy for Near Infrared Emitters 164
9.3.1 Materials and Methods 164
9.3.2 Synthesis and Characterizations 165
9.3.3 Molecular Optical Properties 169
9.3.4 Aggregation of **BisSQ3** in Toluene 172
9.3.5 AFM Images of **BisSQ3** Aggregates 173
9.3.6 Packing Model of **BisSQ3** Nanofibers 174

9.3.7 NMR and Mass Spectra 177

9.4 Supporting Information for *Chapter 6*: Selective Parallel G-Quadruplex Recognition by a NIR-to-NIR Two-Photon Squaraine..... 185

9.4.1 Materials and Methods.....185

9.4.2 Synthesis and Characterizations.....189

9.4.3 Optical Studies in Organic Solvents 192

9.4.4 Optical Studies in Aqueous Media.....193

9.4.5 G-Quadruplex Studies.....194

9.4.6 Two-Photon Absorption.....213

9.4.7 ECD Spectra.....214

9.4.8 NMR and HRMS Spectra of **CAS-C1**.....215

List of Publications 217

Individual Contribution..... 218

Acknowledgements..... 221

References..... 224

Chapter 1

–

Introduction and Aim of Thesis

With the thriving development in the field of organic chemistry nowadays, we can rationally design and synthesize a wide range of desired molecules. However, it is still challenging to construct larger molecules, molecular assemblies or even systems beyond the molecular level through traditional chemical bonds.[1,2,3] To fabricate materials beyond the molecular level, i.e., at the nano- or microscale, industry usually makes use of the "top-down" approach to divide objects into smaller sizes in a macroscopic manner.[4] The term "top-down" is defined as the approach that carves nanoscale structures by controlled removal of materials from larger or bulk solids.[5] Techniques such as photolithography,[6] electron-beam lithography,[7] and vapor treatment[8] can be regarded as top-down approaches to engineer nanostructures. However, there are still a number of technical bottlenecks to achieve dimensions smaller than 100 nm.[6,9,10] Richard P. Feynman stated in his famous talk in 1959, "there is plenty of room at the bottom",[11] therefore, new strategies instead of the "top-down" approach have to be applied for further miniaturization to explore more possibilities at the nanoscale for novel functional materials. Accordingly, a promising strategy is to arrange building blocks at the molecular level in a "bottom-up" manner through "self-assembly".[4,10] George Whitesides defined self-assembly as "the autonomous organization of components into patterns or structures without human intervention." Self-assembling processes are common throughout nature and technology, which involve components from the molecular (crystals) to the planetary (weather systems) scale and many different kinds of interactions.[12] Chemists, who dedicate their work to manipulating atoms and molecules, are in the ideal position to develop bottom-up strategies for the construction of nanoscale devices and materials.

The field of supramolecular chemistry, defined as the "chemistry beyond molecules",[13] deals with the organization and interaction of molecules, which are based on a complex interplay of

non-covalent *inter*molecular interactions.[4,14] Nature elegantly makes use of such interactions and created numerous functional supramolecular structures over millions of years. In addition, supramolecular interactions in nature manifest unique optical and electronic properties when dye molecules are involved. The most renowned examples are the efficient light harvesting dye aggregates found in purple[15] and green bacteria.[16] Notably, the assemblies in green bacteria mainly consist of chlorin dyes which self-assemble into extended rod aggregates (chlorosomes) without any assistance of proteins unlike other photosynthetic antenna complexes.[16b] Inspired by nature, a variety of biomimetic aggregates have been designed from synthetic chromophores such as porphyrins,[17] chlorins,[18] naphthalene[19] and perylene bisimides[20] *via* non-covalent interactions. Moreover, dye assemblies commonly exhibit optical and electronic properties that are not given in the individual dye molecules but arise upon aggregation. Therefore, in order to rationally design functional materials, studies on mechanism and spectral changes upon aggregation is required.[20b-c,21]

Squaraine dyes have gained a lot of attention in recent years due to their typical cyanine-like properties, i.e., strong and usually narrow absorption in the red part of the visible light spectrum, along with strong fluorescence.[22] In addition, their molecular structure can be easily functionalized, making them attractive for applications in the fields of bioimaging[23] and host-guest systems.[24] Furthermore, squaraines also show excellent p-type semiconductivity in organic thin-film transistors[25] and solar cells.[26] However, despite of this wide scope of applications, self-assembly of squaraines into dye aggregates remains less explored and the relationship between packing structure and functional properties is often rather serendipitous and unpredictable.

During the last decade, Mayerhöffer and Würthner have developed and investigated a series of squaraine dyes, in which one oxygen of the squaric carbonyl group is replaced with dicyanomethylene groups (Figure 1), which shifts the absorption and emission into the near-infrared (NIR) region.[27] The substitution also leads to a rigid, planar structure with C_{2v} symmetry instead of a centrosymmetric geometry owing to steric effects, giving rise to a ground state dipole moment. Therefore, such squaraines prefer to stack co-facially, leading to H-aggregates (Figure 1) with blue-shifted absorption bands[28] and a quenched fluorescence. Moreover, extended aggregates based on such dicyanomethylene-substituted squaraines are hard to achieve due to dipole-dipole cancellation between two neighboring squaraines. Hence, the construction of extended dye aggregates based on squaraine dyes with absorption approaching the NIR region is a challenging task.

The aim of this thesis (*Chapters 3* and *4*) was the realization of J-type exciton coupling within aggregates consisting of dicyanomethylene-substituted squaraines. Inspired by successful fabrication of extended dye aggregates based on merocyanine dyes[29] which also possess intrinsic permanent dipole moments,[30] similar strategies for the dicyanomethylene-substituted squaraine dyes were adopted. Accordingly, the covalent linkage of two squaraine units was envisioned to form a bis-chromophore structure, where each of the two chromophores can interact with the chromophore of the neighboring molecule in order to form elongated supramolecular structures.[29] In addition, a slip-stacked arrangement between the interacting chromophores is expected due to the steric hindrance caused by the twist angle (α, see Figure 1) within the bis-chromophore. Hence, **BisSQ1** and **BisSQ2**, in which two dicyanomethylene squaraine chromophores are covalently linked with and without a phenyl spacer unit were designed (Figure 1). The aim is to investigate the influence of the concept of bis-chromophore on the aggregation behavior of squaraine dyes in solution by means of spectroscopic and microscopic methods.

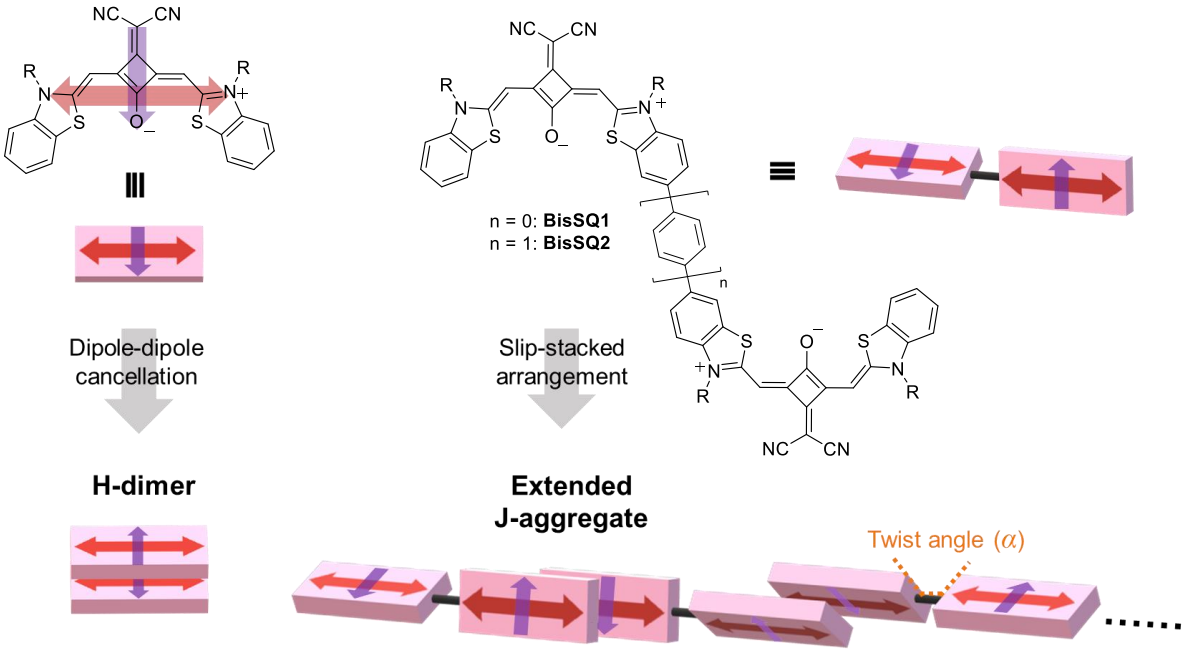

Figure 1. Molecular structure of the dicyanomethylene substituted squaraine scaffold and the concept of bis-chromophore utilized for **BisSQ1** and **BisSQ2** (top), and graphical illustration of the packing arrangements (bottom) expected for squaraine dyes and orientation of the permanent (μ_g, purple arrows) and transition dipole moments (μ_{eg}, red double-headed arrows).

Additionally, it was discovered that a series of squaraine dyes bearing 4-methylquinolinium donor units exhibit pronounced bathochromic shifts compared to squaraine dyes bearing benzothiazolium donor units (Figure 1) in absorption and emission approaching the upper limit

of the NIR-I window (λ = 700–900 nm), among which the longest absorption and emission wavelengths are at 900 and 922 nm, respectively.[31] In combination with the bis-chromophore approach, a novel bis(squaraine) dye **BisSQ3** based on 4-methylquinolinium donors was designed. The envisioned goal (*Chapter 5*) was to further shift the absorption and emission spectrum in the NIR-II window (λ = 1000–1700 nm) by means of a "double J-coupling strategy" which involves both *intra*molecular J-coupling by the head-to-tail connection of two squaraine dyes ("J-dimer") and the self-assembly of these dyes into *inter*molecularly J-coupled dye aggregates.

Because dicyanomethylene-substituted squaraines not only serve as potential building blocks for extended J-type aggregates, but were recently introduced as suitable G-quadruplex (G4) binders owing to their planar core structure,[32,33,34] the last project of this thesis (*Chapter 6*) was to decorate the dicyanomethylene squaraine dye with bulky water-soluble brush-type substituents (**CAS-C1**, Figure 2) and investigate its binding strengths and selectivity towards parallel G4s.

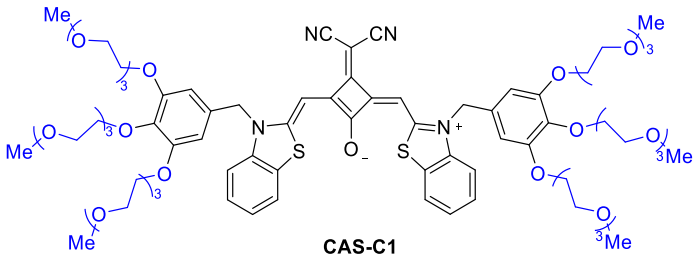

Figure 2. Molecular structure of the dicyanomethylene-substituted squaraine **CAS-C1**.

In the following, the organization of this thesis is presented:

Chapter 2 gives an overview on the state of knowledge in the field of squaraine chemistry. First, the molecular structures of common squaraine dyes and how structure variation influences the molecular optical properties are presented. Furthermore, the development of self-assembled squaraines and squaraine materials is reviewed by demonstrating a number of representative examples in solution and thin films. Last but not least, theoretical methods which can be utilized for the interpretation of squaraine-squaraine interactions in aggregates and materials are introduced.

Chapter 3 demonstrates the "bis-chromophore" strategy that aims for the formation of J-type aggregates. First, the synthesis and self-assembly studies of bis(squaraine) **BisSQ1**, in which two squaraines are covalently connected without spacer moiety, are presented. Temperature-

and concentration-dependent UV/Vis/NIR spectroscopic measurements and atomic force microscopy (AFM) manifest a cooperative self-assembly process into nanosheets and a tentative packing model is proposed and discussed accordingly.

Chapter 4 presents the self-assembly behaviors of bis(squaraine) **BisSQ2**, in which two squaraines are covalently connected *via* a *p*-phenylene spacer. Upon cooling down, **BisSQ2** self-assembles into two different polymorphs depending on the cooling rate. The self-assembly pathways and the two polymorphs are investigated in detail by means of UV/Vis/NIR spectroscopy, atomic force microscopy (AFM), as well as wide-angle X-ray scattering (WAXS). Based on these results, molecular packing models are proposed. In addition, a theoretical analysis based on the Essential States Model (ESM) is presented in order to rationalize the uncommon spectral features and the proposed packing models.

Chapter 5 aims for shifting the absorption and emission of squaraine dye aggregates into the NIR-II region while retaining the quantum yield. Therefore, bis(squaraine) dye **BisSQ3** was designed and synthesized to realize the double J-type coupling strategy, where both *intra*- and *inter*molecular exciton coupling are involved. The optical properties of molecular and aggregated **BisSQ3** in solution are presented and a packing motif for aggregated **BisSQ3** is proposed based on the morphological information revealed by AFM.

Chapter 6 deals with the synthesis and the binding properties of the water-soluble squaraine dye **CAS-C1** towards parallel G-quadruplexes (G4s). Titration experiments with G4s yield the binding constants and the binding mode between the squaraine and the G4 is derived by docking analyses. Moreover, the two-photon absorption (TPA) properties of the complexes of **CAS-C1** with parallel G4s are characterized and presented.

Chapter 7 and *Chapter 8* conclude this work with summaries both in English and in German.

In *Chapter 9*, a documentation of the materials and methods used in this thesis as well as the experimental details are provided.

Chapter 2

—

State of Knowledge

2.1 Squaraines Dyes (Structures and Structure−Absorption/Emission Relationships)

Squaraines were first discovered by Treibs and Jacob in 1965.[35] They are a class of organic dyes that have a resonance stabilized zwitterionic structure with an electron deficient central four-membered ring. A representative example is shown in Scheme 1.[22]

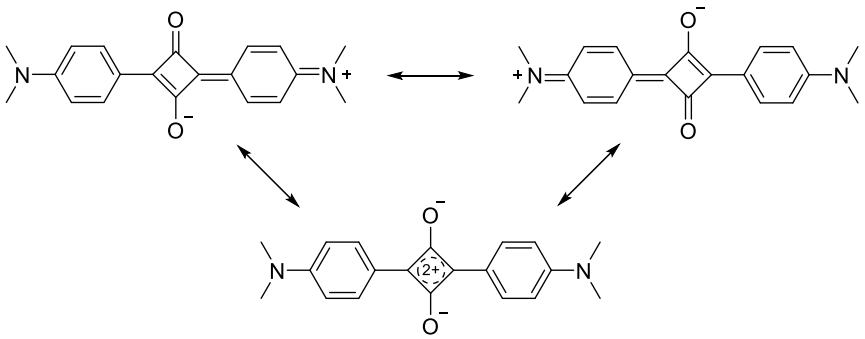

Scheme 1. Exemplary resonance zwitterionic structure of a squaraine dye.

Squaraines are derived from the highly electron deficient aromatic squaric acid core and the opposite sides of the four-membered ring are usually substituted by electron-donating aromatic rings. Because of their planar structure and zwitterionic properties, squaraines typically exhibit strong absorption and emission in the visible and near-infrared (NIR) region. Common structures of squaraine chromophores that are widely reported in literature are summarized in Figure 3. These squaraine dyes are prepared by condensation reactions with Ar_1 and Ar_2 generally being electron-rich anilines or heterocyclic methylene bases derived from trimethylindolenine, benzothiazoles, or benzoselenazoles.[23b] Not only are there a number of aromatic and heterocyclic systems with varying donor strengths available, but also the squaric

acid core can be modified *via* nucleophilic substitution with various functional groups such as amino or dicyanomethylene moieties.[27,36] Thus, variation of the squaric core and the donor units enables the design of a variety of squaraine dyes with tunable optical properties in the visible to NIR range, which possess great potential for applications in electronic and photonic devices.

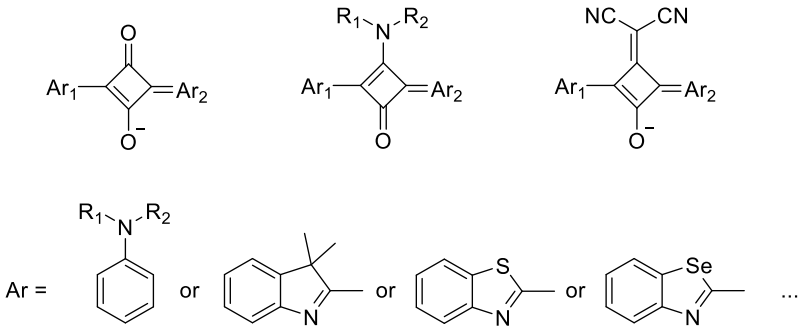

Figure 3. Common structures of squaraines.

2.1.1 Core-Substituted Squaraine Dyes

A series of core-substituted squaraine dyes was first developed by Tatarets and co-workers, who discovered that trimethylindolenine-derived semisquarates could be easily functionalized with electron acceptors on the squaric acid core. These substituted semisquaraines can then subsequently react with a second equivalent of the trimethylindolenine base to give a number of core-substituted squaraines **1** – **5**, as illustrated in Scheme 2.[37] The C_{2h} symmetrical squaraine dye **6a** (Figure 4a) serves as the non-substituted reference. The molecular optical properties were measured in chloroform and are given in Table 1. In contrast to squaraine **6a**, **1** – **5** exhibit red-shifted absorption and emission maxima due to the substitution of acceptor at the squaraine ring oxygen. Moreover, dyes **1** – **5** show additional absorption bands in the 380 – 460 nm region with extinction coefficients of about 1.6 – 4.0 × 10^4 M^{-1} cm^{-1}. Similar phenomena were also found in squaraine **6b** and the diethylbarbiturate derivative **7** (Figure 4a), where **6b** shows the typical strong and sharp absorption band (Figure 4b, λ_{max} = 638 nm, CH_3CN) arising from the cyanine-like transition associated with the delocalization of the nitrogen lone pairs all over the main conjugation axis of the molecule, while for **7**, an additional higher energy transition is present.[38] The presence of this high energy absorption band can be exploited in the preparation of photovoltaic devices with improved light-harvesting capabilities.[23a]

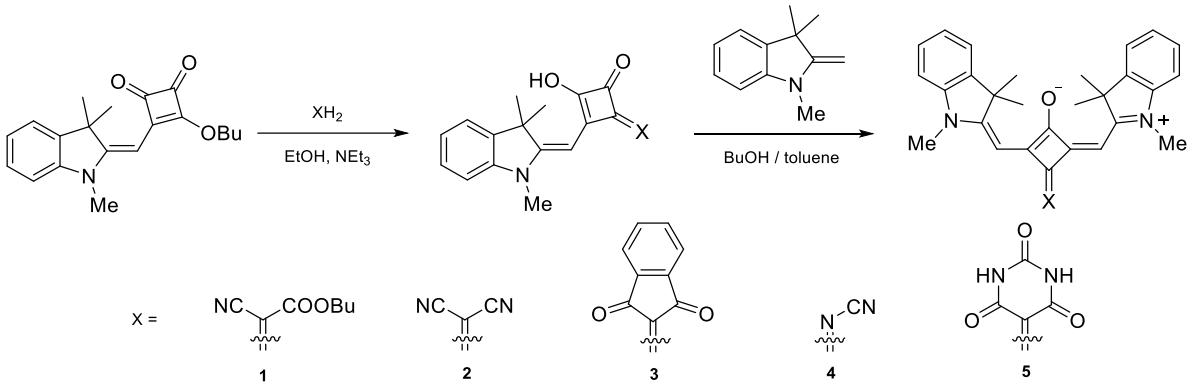

Scheme 2. Synthesis of some core-substituted squaraine derivatives **1** – **5**.

Table 1. Optical properties of squaraines **1**–**5**, **6a** in chloroform.[37]

Compound	λ_{max} (nm)	ε (M^{-1} cm^{-1})	λ_{em} (nm)
1	691 / 393	134000 / 32000	708
2	684 / 380	196000 / 38000	700
3	675 / 460	128000 / 42000	699
4	655	n.d.[a]	665
5	644 / 430	103000 / 27000	665
6a	635	219000	643

[a] Compound unstable.

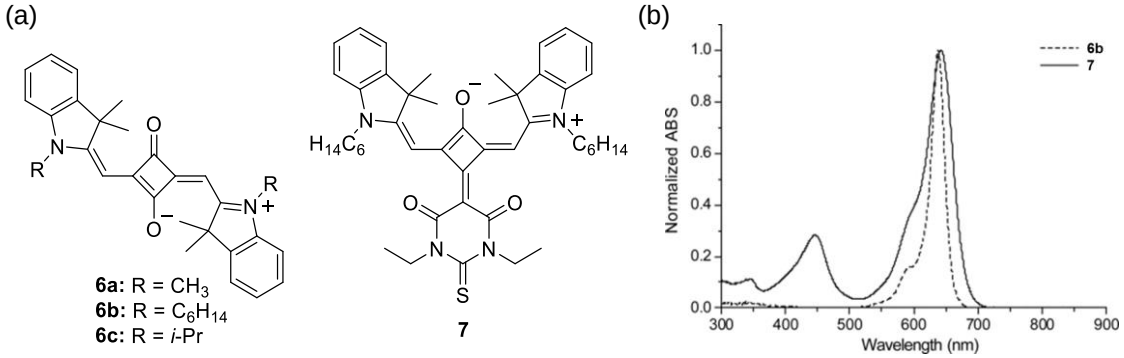

Figure 4. (a) Molecular structures of squaraines **6a–c** and **7**. (b) UV/Vis absorption spectra of squaraine **6b** (dashed line) and core-substituted squaraine **7** (solid line) in CH_3CN.[38] Adapted with permission from Ref. 38. Copyright 2009 WILEY-VCH Verlag GmbH & Co. KGaA.

Systematic studies on core-substituted squaraine dyes were performed and illustrated by Mayerhöffer *et al*.[27] Squaraine dyes **8** – **10** (Figure 5a) could be synthesized by similar strategy with decent yields (50 – 54%). Unlike non-substituted C_{2h} symmetric squaraines such as **6a**–**c**, which exhibit a quadrupole moment, the core-substituted squaraines studied here possess a permanent dipole moment due to their C_{2v} molecular symmetry as a result of the steric

hindrance caused by the core substituents. This intrinsic difference also reflects on the spectral properties shown in Figure 5b and Table 2. Again, **6c** exhibits the characteristic cyanine-like sharp and intense absorption band in the red part of the visible light region. For the core-substituted squaraines **8** – **10**, two main differences can be seen. One is the additional hypsochromic absorption located between 350 and 500 nm, mentioned in the previous section, which can be attributed to the transition to higher excited states due to their C_{2v} geometry.[39] The other is the bathochromic shift of the main absorption band along with a decrease of the molar absorption coefficient.

Aside from the changes observed in the absorption properties, the core-substitution also alters the fluorescence properties of these squaraine dyes. As summarized in Table 2, a significant loss in fluorescence quantum yield is visible by going from the dicyanomethylene-substituted squaraine **8** with Φ_{FL} = 0.21 to the indandione derivative **10** with Φ_{FL} = 0.07. In the same order, the Stokes shift increases from 315 cm^{-1} for **8** to 955 cm^{-1} for **10**, indicating a pronounced change of the molecular structure in the excited state, which is in line with the increasing steric demand of the acceptor group. The bulkier substituents distort the π system out of planarity, therefore, additional vibrational states are coupled to the electronic transition, which promotes non-radiative deactivation processes of the excited state, giving rise to the observed decrease in the fluorescence quantum yields.[27]

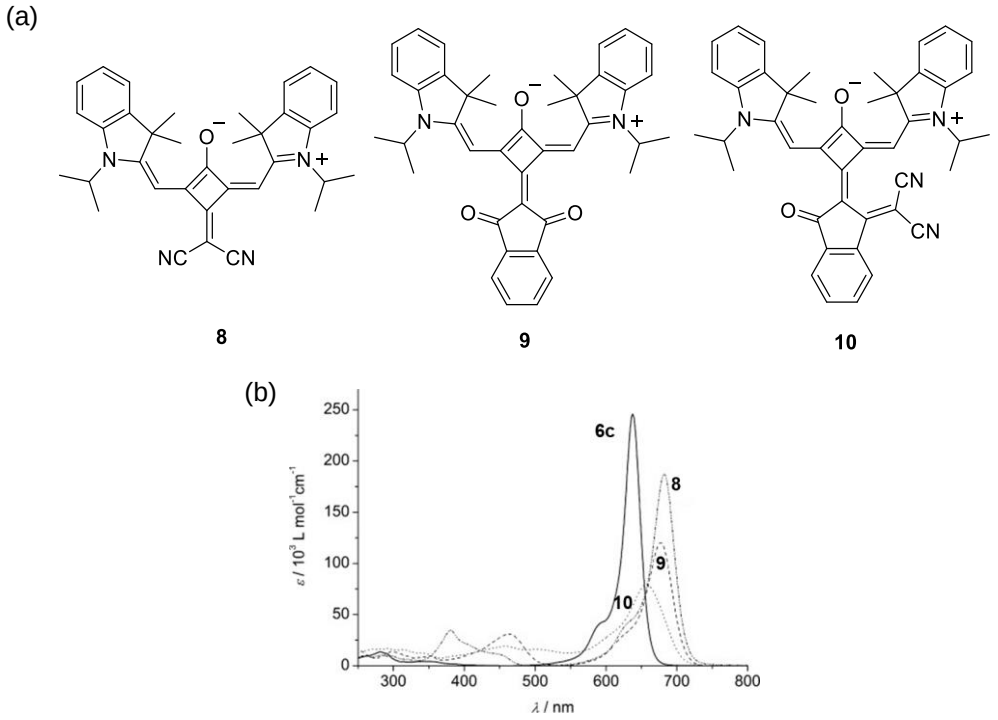

Figure 5. (a) Molecular structures of squaraines **8**−**10**. (b) UV/Vis absorption spectra of squaraines **6c** (solid line), **8** (dashed–dotted line), **9** (dashed line), and **10** (dotted line) in CH_2Cl_2 (c = 10^{-6} M; T = 293 K).[27] Adapted with permission from Ref. 27. Copyright 2012 WILEY-VCH Verlag GmbH & Co. KGaA.

Table 2. Optical properties of squaraines **6c**, **8 – 10** in CH_2Cl_2 at 293 K.[27]

Compound	λ_{max} (nm)	ε (M^{-1} cm^{-1})	λ_{em} (nm)	$\Delta\tilde{\nu}_{Stokes}$ (cm^{-1})	Φ_{FL}[a] (%)
6c	637	250000	646	220	24
8	683	185000	698	315	21
9	678	113000	705	365	7
10	657	80000	701	955	1

[a] Fluorescence quantum yield standard: rhodamine 800 in ethanol; Φ_{FL} = 0.21.[40]

2.1.2 Dicyanomethylene Substituted Squaraine Dyes with Donor Variations

Hence, the most versatile core substituent is the dicyanomethylene group, which not only exhibits the most attractive optical features, but also shows the most favorable reactivity towards different donors. Mayerhöffer *et al.* performed structural variations of squaraine dyes based on this acceptor unit and investigated the influence of different donor groups on the dye properties.[27] They reported a more direct synthetic pathway for symmetric dicyanomethylene squaraines (Scheme 3), in which the squaric acid diethylester is first condensed with malononitrile to give the acceptor-functionalized squaric acid derivative **11**. Owing to the electron-withdrawing character of the dicyanomethylene group, this squaric acid derivative is more electron deficient and thus exhibits a higher reactivity towards nucleophiles. This facilitates the introduction of a wide scope of donor moieties including benzoxazole, indolenine, benzothiazole, and quinolines, leading to a series of squaraines **15** – **17**.

The optical properties of this series of squaraine dyes are summarized in Table 3. The absorption of the dyes manifests a broad spectral coverage from 626 nm (**15a**) up to 900 nm (**17d**). Upon increasing the donor strength from benzoxazole (**15a**, λ_{max} = 626 nm), *via* indolenine (**15b**, λ_{max} = 683 nm), benzothiazole (**15c**, λ_{max} = 701 nm) up to benzoselenazole (**15d**, λ_{max} = 719 nm), a bathochromic shift of the absorption maximum takes place. In addition, the utilization of pyrylium donors allows a further red shift to 759 nm (**16**). A most significant bathochromic shift of the absorption maximum of more than 100 nm is achieved by changing the donor moieties to 4-methylquinolinium derivatives (**17a**–**d**), where **17a** shows an absorption maximum at 870 nm and **17d** at 900 nm. This pronounced spectral shift can be ascribed to the greater conjugation length contributed by the quinoline donors.[31] Accordingly, it is shown that the variation of donor moieties enables the fine tuning of absorption wavelengths.[27]

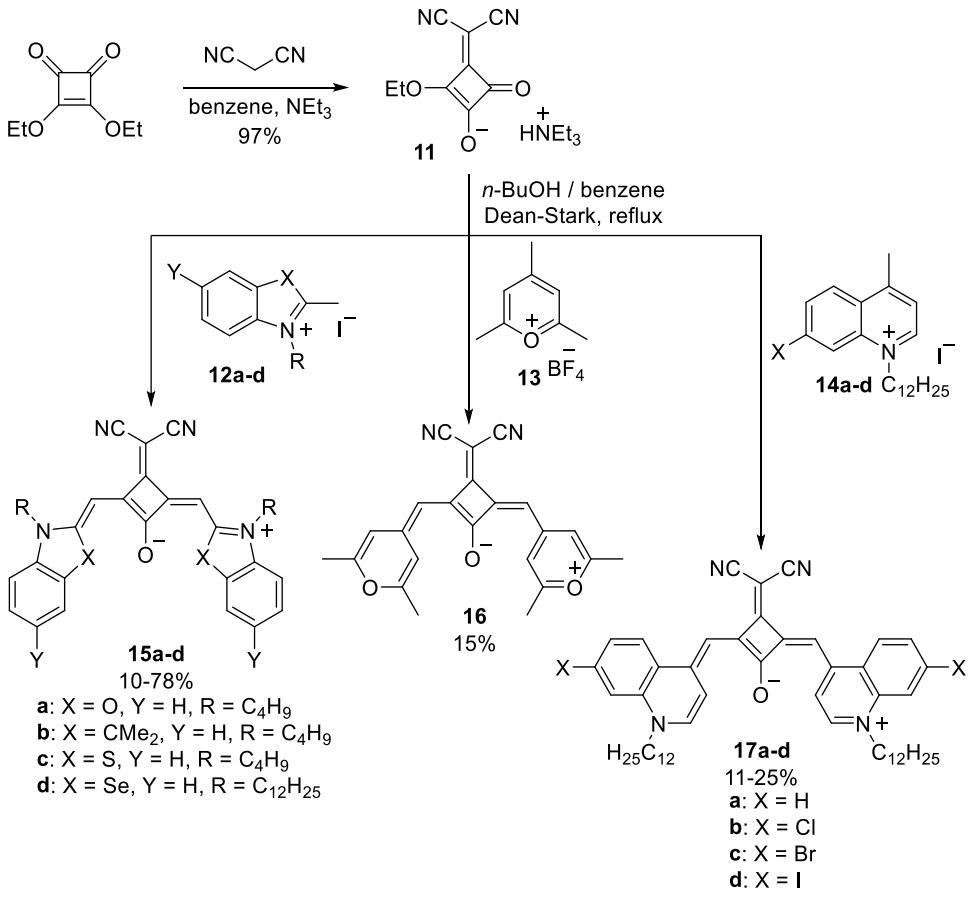

Scheme 3. Synthetic route towards dicyanomethylene-substituted squaraines **15a−d**, **16**, **17a−d** with different donor moieties *via* the functionalized squaric acid derivative **11**.[27]

Table 3. Optical properties of squaraines **15a−d**, **16**, and **17a−d** in CH_2Cl_2 at 293 K.[27]

Compound	λ_{max} (nm)	ε (M^{-1} cm^{-1})	λ_{em} (nm)	Φ_{FL}[a] (%)
15a	626	150000	646	91
15b	683	195000	698	37
15c	701	168000	720	79
15d	719	164000	737	93
16	759	180000	781	13
17a	870	205000	890	10
17b	885	258000	913	11
17c	891	251000	916	12
17d	900	274000	920	17

[a] Fluorescence quantum yield standard for **15a−d** and **16**: rhodamine 800 in ethanol; Φ_{FL} = 0.21.[40] For **17a−d**: ICG in DMSO; Φ_{FL} = 0.13.[41]

The further bathochromic shift observed for the series **17a**–**d** is due to an unexpected halogen effect, accompanied by an increase of the molar absorption coefficient and an increase of the fluorescence quantum yield in the series of substituents H (**17a**) < Cl (**17b**) < Br (**17c**) < I (**17d**). Supported by DFT calculations, the observed halogen effect is attributed to a transfer of electron density from the halogen substituents to the chromophore core which is more pronounced with increasing polarizability of the halogen substituents. Contrary to the common perception about heavy atom quenching effects, this unexpected halogen effect leads to superior fluorescence properties such as an increase of the optical brightness.[31]

More recently, Wang and co-workers reported a NIR-fluorescent dicyanomethylene-substituted squaraine dye **18** with ethyl-grafted 1,8-naphtholactam as donor units. Squaraine **18** shows an intense absorption band at around 930 nm with an emission maximum at 970 nm in THF. It can be encapsulated as a nanoprobe through facile nanoprecipitation and targeting peptide decoration, where the nanoprobe manifests an increase of quantum yield to 1.7% compared with the molecular state of **18** (0.13%). The nanoprobe further demonstrates NIR-II and photoacoustic bimodal imaging capabilities and favorable photothermal effects.[42]

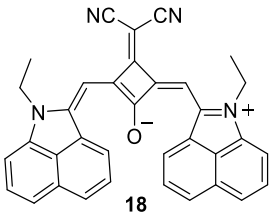

18

Figure 6. Molecular structure of squaraine **18**.

Accordingly, the spectral window for squaraine-based fluorophores can be extended above 900 nm, which provides new opportunities for a wider scope of NIR applications such as bioimaging and sensing.

2.1.3 Squaraine Polymers

A totally different approach to shift the spectra of squaraine dyes is to synthesize oligomers or polymers that exhibit band shifts and broadenings due to the exciton coupling[43] (for detailed illustration of exciton coupling theory, see *Chapter 2.3*) of localized squaraine states. The research group of Lambert has pioneered in this field by investigating the optical properties of a series of squaraine-based polymers.[44,45,46,47]

They first prepared a squaraine homopolymer **19** (Figure 7a) based on indolenine squaraines *via* a Ni-promoted Yamamoto coupling.[44] The absorption spectrum of **19** indeed exhibits a bathochromic shift of the absorption maximum with respect to the monomeric spectrum, but also a weaker band at higher energy. This observation can be explained by a mixture of zigzag and linear alignment of chromophores (Figure 7b), which then demonstrate hypsochromic (H-coupling) and bathochromic (J-coupling) shifts, respectively.

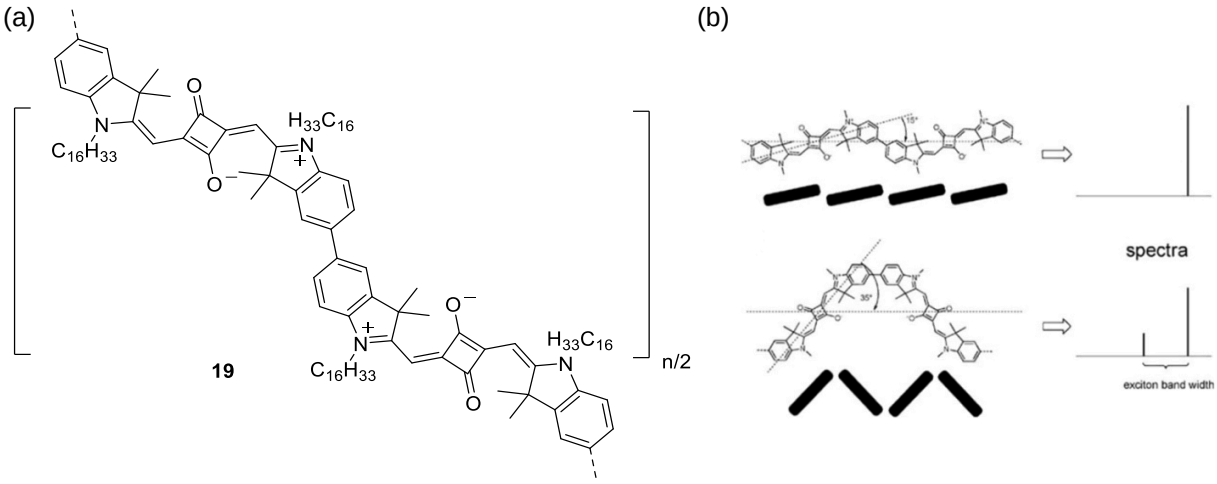

Figure 7. (a) Polysquarine **19**. (b) Idealized polymer sections with elongated herringbone structure (top) and zigzag structure (bottom) and expected absorption spectra.[44] Adapted with permission from Ref. 44. Copyright 2010 WILEY-VCH Verlag GmbH & Co. KGaA.

Later on, they focused on a *cis*-indolenine squaraine where the central squaric ring is functionalized by a dicyanomethylene group.[45] As mentioned in the previous section, this acceptor substitution results in a bathochromic shift of the absorption and a *cis*-conformation of the monomeric indolenine squaraine. Their goal was to achieve a pronounced zigzag or even helical structure of the polymer based on this bent squaraine unit *via* Yamamoto polycondensation reaction (Scheme 4), which is expected to demonstrate distinct optical features compared to the more elongated structure of *trans*-indolenine squaraine polymer **19**. In order to modify solubility, they prepared two different squaraine monomers **20a** and **20b**, which are decorated with hexadecyl chains and 3,7-dimethyloctyl chains, respectively. By performing preparative recycling gel permeation chromatography (GPC), two fractions of different molecular weight could be isolated for each polymer, denoted as **21a-1**, **21a-2**, **21b-1**, and **21b-2**, respectively. Apart from the desired squaraine polymers, they were able to isolate conjugated cyclic trimers **22a,b** from GPC.

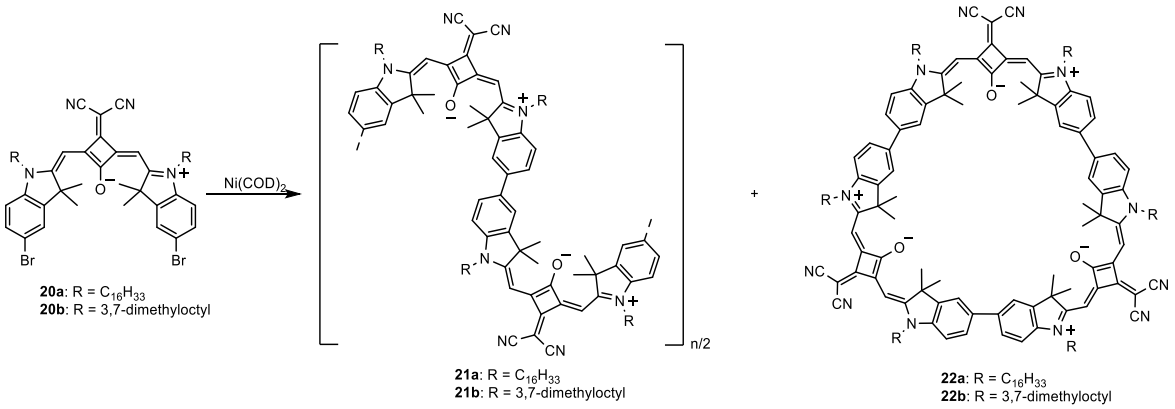

Scheme 4. Yamamoto polycondensation of *cis*-dibromoindolenine squaraine **20a,b** to give polysquaraines **21a,b** and cyclic trimers **22a,b**.

The polymers show a broad absorption in the red-to-NIR region with distinct maxima but a narrow fluorescence (Figure 8a), whereas the trimer exhibits a sharp absorption band and multiple fluorescence bands with an unusually large Stokes shift compared to conventional squaraine dyes (Figure 10a), which will be explained later in more detail.

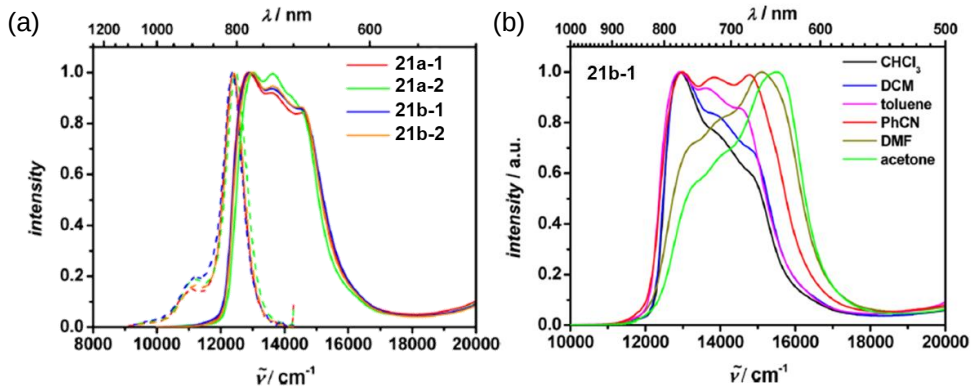

Figure 8. (a) Absorption (solid lines) and fluorescence (dotted lines) spectra of the squaraine polymers in toluene. Excitation is at 680 nm. (b) Normalized absorption spectra of **21b-1** in various solvents of different polarity.[45] Adapted with permission from Ref. 45. Copyright 2012 American Chemical Society.

Due to the bent structure of the *cisoid* dicyanomethylene squaraine units and their conformationally flexible biaryl axis, there are several different macromolecular superstructures possible for the polymers including an open loop, a helix, an elongated structure with zigzag pattern and a mixed structure which contains both helical and zigzag features (Figure 9). The resulting arrangements of transition dipole moments are also shown in Figure 9 (orange arrows), which lead to different spectral features according to exciton coupling theory.[43] For example, the helical structure resembles an H-type aggregate, whereas

the zigzag structure can be conceived as a typical J-type aggregate. Therefore, the authors assume that the polymers display all these superstructures in solution, which gives rise to absorption spectra that show a superposition of the spectral features that are associated with these superstructures. The proportions to which these structures are formed depend on the solvent, resulting in a solvatochromic behavior in the absorption spectra of the polysquaraines. (Figure 8b). And for the cyclic trimer, the optimized geometry based on AM1 calculations proves that it is asymmetric because of some strain in the ring (Figure 9).[45]

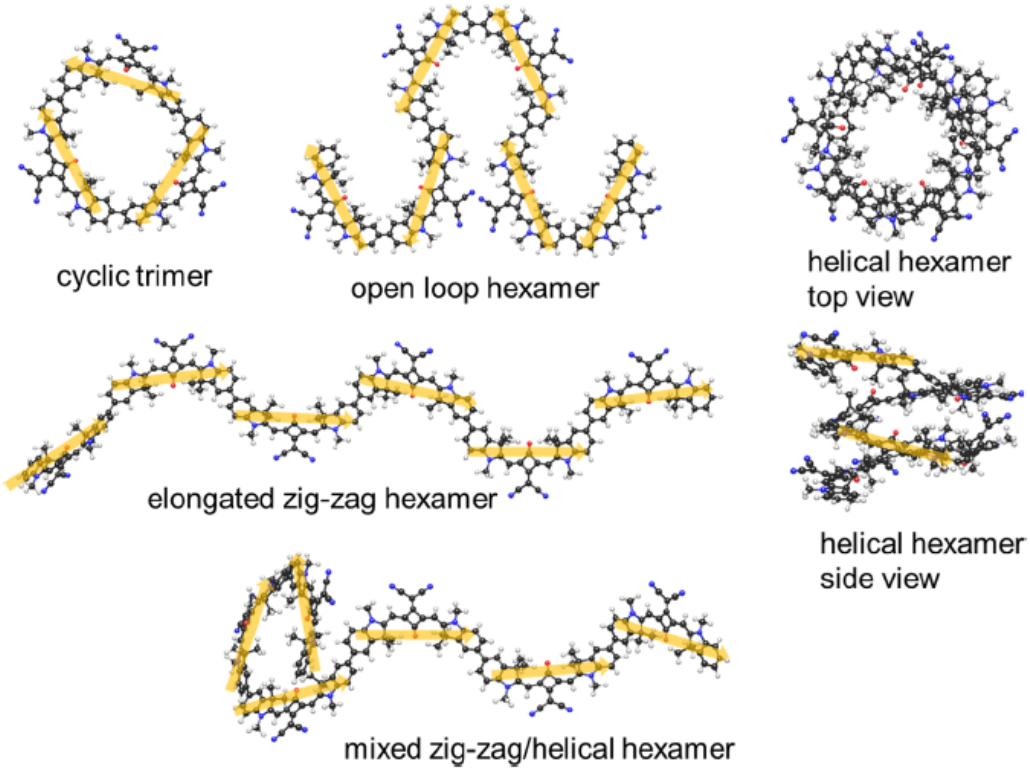

Figure 9. AM1-optimized structures (for simplicity, the long alkyl chains are replaced by methyl groups) of the cyclic trimer, open loop hexamer, helical hexamer (top view and side view), elongated zigzag hexamer, and mixed zigzag/helical hexamer. The orientation of localized transition moments of the lowest energy squaraine transition is indicated by orange arrows.[45] Adapted with permission from Ref. 45. Copyright 2012 American Chemical Society.

They further investigated the optical properties of cyclic trimer **22a** by means of theoretical calculations. As presented in Figure 10a, a large Stokes shift and a vibronic structure of the emission can be observed. Their analysis predicts that these shifts are caused by deviations of the excited state geometry from the strictly symmetric configuration. Breaking the symmetry allows the fluorescence from lower excited states (Figure 10b). The vibronic features can be

identified by using a Frenkel vibronic-coupling model and are determined by properties of the ground state vibrational wave functions.[46]

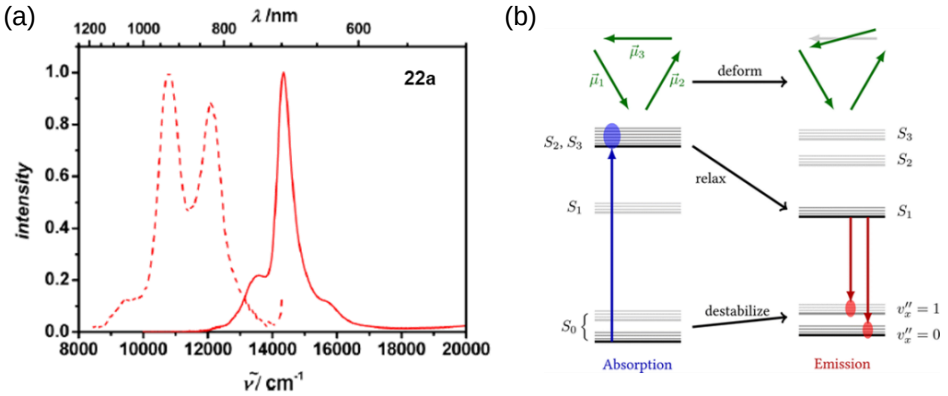

Figure 10. (a) Absorption (solid lines) and fluorescence (dotted lines, λ_{ex} = 700 nm) spectra of the cyclic trimer in toluene.[45] Adapted with permission from Ref. 45. Copyright 2012 American Chemical Society. (b) Radiative and nonradiative processes in the trimer. The geometric arrangement of the individual transition dipole moments (top) and the relevant transitions for the absorption and emission process (bottom) are shown schematically. The manifold of vibrational states is indicated as thin lines.[46] Adapted with permission from Ref. 46. Copyright 2015 American Chemical Society.

The aforementioned squaraine homopolymers **19** and **21** indeed display both a red shift and a significant broadening of the absorption which can be interpreted by exciton coupling theory.[44,45] Hence, the coupling of transition dipole moments appears to be an effective approach to design and fine-tune the absorption properties of conjugated polymers. In 2014, the same research group intended to further broaden the exciton bandwidth by combining two different squaraine monomers to form a [**SQA-SQB**]$_n$ copolymer **23** *via* Suzuki coupling (Scheme 5). The exciton theory predicts allowed transitions for alternating copolymers with elongated zigzag structure (Figure 11) into the bottom and top bands of the exciton manifold, which is in line with the observed absorption band shape (Figure 12). The absorption spectra show a strong transition on the low-energy side and a weaker transition on the high-energy side. However, there is no real gap between these transitions, which is most likely due to disorder and deviation from a fully ideal zigzag structure. Moreover, in toluene solutions, the lowest energy transition is much narrower than in $CHCl_3$ (Figure 12), indicating the delocalization of excitation over several **[SQA-SQB]** monomers as a result of a more ordered structure in toluene. This narrowing emphasizes the essential J-aggregate-like behavior of this polymer, which makes the copolymer **[SQA-SQB]$_n$** a unique model system which combines the excitonic features of J-aggregates with the chemical robustness of a polymer.[47]

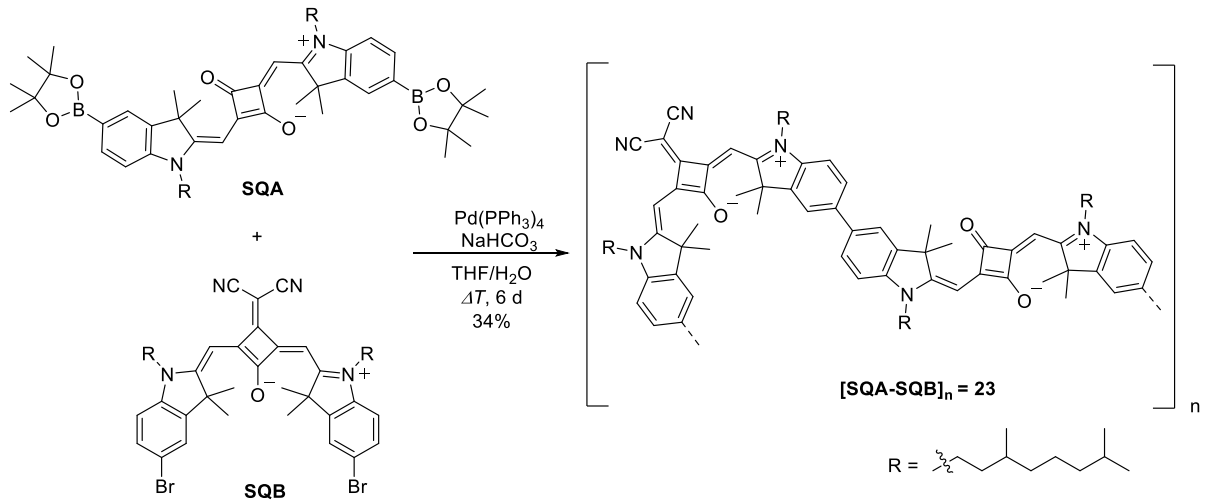

Scheme 5. Synthesis of copolymer **[SQA-SQB]$_n$ 23**.

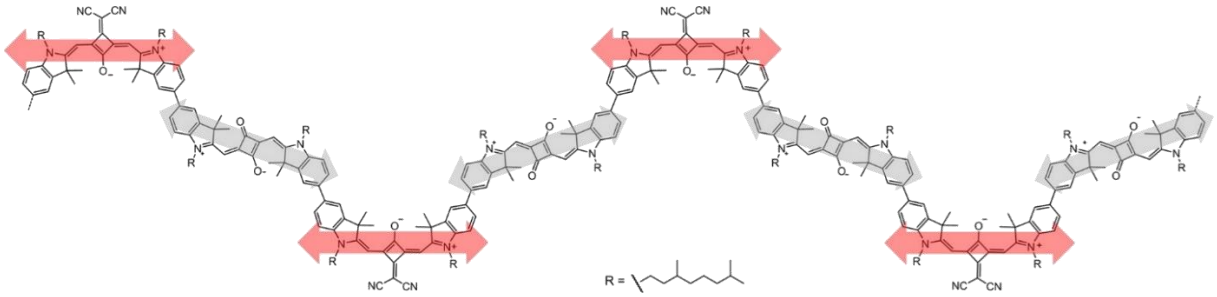

Figure 11. Elongated **[SQA-SQB]$_n$** polymer structure with localized transition moments indicated by gray (**SQA**) and red (**SQB**) arrows.[47] Adapted with permission from Ref. 47. Copyright 2014 American Chemical Society.

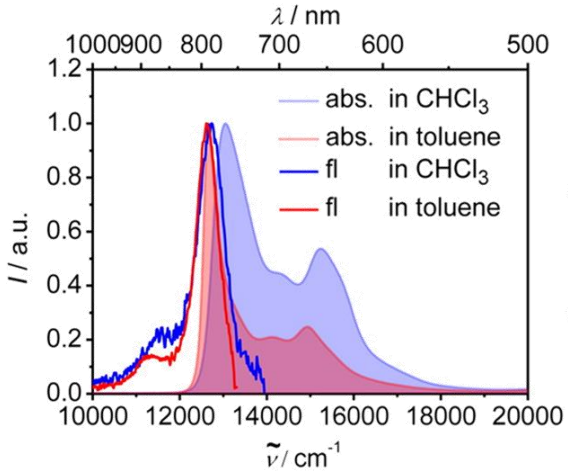

Figure 12. Normalized absorption and fluorescence spectra of **[SQA-SQB]$_n$** in toluene and $CHCl_3$ solution.[47] Adapted with permission from Ref. 47. Copyright 2014 American Chemical Society.

2.2 Self-Assembled Squaraines and Squaraine Materials

Extensive π-systems and the presence of donor and acceptor building blocks, which cause a different distribution of charge densities over the π-system, are characteristic of dye molecules. The supramolecular interactions that occur during aggregation of such π-systems are often classified as the so-called π-π stacking interactions.[4, 48] A number of effects participate in the π-π stacking interactions, including electrostatic and van der Waals interactions, attractive and repulsive orbital interactions, and solvophobic effects.[49] Such diverse contributions show the complexity of these *inter*molecular interactions, hence to what extent these components contribute to the outcome of the π-stacks is still a matter of debate. Moreover, many factors such as the size, structure and electronic nature of the π-core of the molecule, or the number and position of different peripheral substituents are of great importance for the π-π stacking geometry and the magnitude of the binding energy. Furthermore, the solvent plays a crucial role which generally strongly reduces the Gibbs free energy for π-π aggregates compared to the gas phase.[50] Out of all the interactions, the least directional dispersion force dominates, making it more challenging to describe the aggregation behavior theoretically and systematically. Since π-π interactions are of central importance for applications of functional dyes, further fundamental work is required in this field in order to systematically design and construct novel materials with defined morphologies and functions.

Squaraine dyes have gained a lot of attention in recent years because of their outstanding optical properties. They are typically composed of an electron deficient central four membered ring and two electron-donating groups in a donor–acceptor–donor (D–A–D) form.[22] Here, the D–A–D sequence implemented in the squaraine π-scaffold can direct slip-stacked packing arrangements where donor and acceptor units of neighboring dyes are in close π-π-contact. On the other hand, the substituents and media can pose great impact on dispersion forces, which competes with the above mentioned electrostatic and charge transfer interactions that direct the slip-stacked arrangement.[51,52,53] In solutions, dispersions forces are normally stronger, giving rise to blue-shifted absorption bands due to the H-type coupling associated with cofacial stacking arrangements.[28,54,55,56] In the solid state, many of these squaraines exhibit a broad absorption band with significant quenching of the emission due to the aggregation of the dye, which needs to be adjusted in order to improve device efficiency. The following sections will focus on the development and current state of self-assembly of squaraine dyes in solution and solid states.

2.2.1 Aggregation of Squaraines in Langmuir-Blodgett Films

A great number of early research deals with the aggregation behavior of squaraine dyes in Langmuir-Blodgett (LB) films.[51,52,53,57,58] For example, Law and Chen prepared a series of surfactant squaraines **24a-c** (Figure 13a) and investigated their aggregation in LB films. **24a** was found to form blue-shifted, namely H-type aggregates in LB films, whereas **24b** exhibits red-shifted J-type aggregates controlled by *inter*molecular charge-transfer interactions between the electron-donor and -acceptor groups of squaraines.[51]

Whitten and co-workers observed hypsochromically shifted as well as bathochromically shifted absorption bands for the monolayers of squaraines **24a**,**b** and **24d,e** compared to the spectra in solution, which indicate the formation of H- or J-aggregates on surfaces.[52,53] Interestingly, through various heating steps, the H-aggregate formed by **24a** in the film successively transformed into a J-aggregate. Upon steam treatment, the process could be reversed, namely the initial H-aggregate could be reproduced (Figure 13b). The authors attributed this multiple aggregation behavior to the interplay of hydrophobic effects and charge transfer interactions.[52]

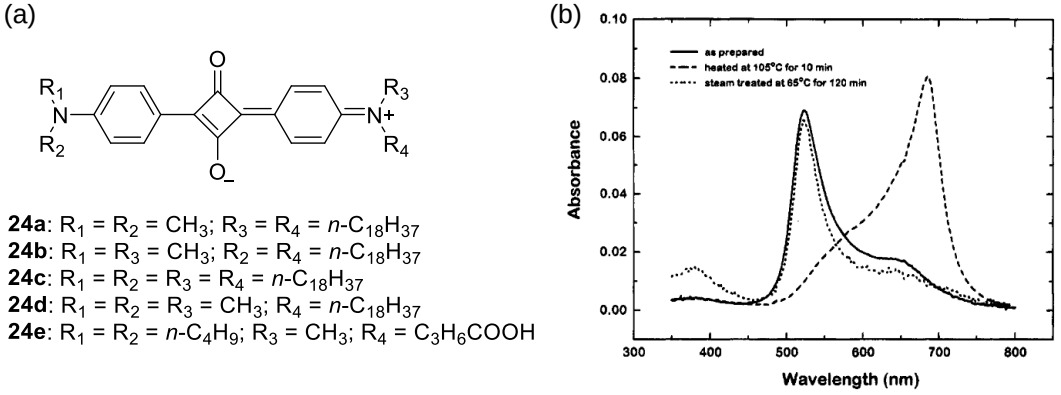

Figure 13. (a) Molecular structures of squaraines **24a**−**e**. (b) Absorption spectra of the LB film of **24a** on glass as a function of heating and the subsequent steam treatment.[52] Adapted with permission from Ref. 52. Copyright 1994 American Chemical Society.

Jiang *et al.* studied the effect of hydroxyl substituents at the benzene ring of the squaraine dye chromophore and different alkyl substituents at the N atom (Figure 14) on the aggregation state of dyes in LB films. The absorption spectra of the LB films indicated that the hydroxyl substituents at the benzene rings gave rise to *inter*molecular hydrogen bonding, which further led to formation of H-aggregates, whereas long alkyl chains hindered the squaraine dyes to form J-aggregates.[57]

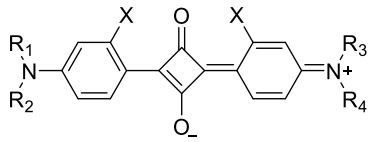

25a: $R_1 = R_2 = R_3 = R_4 = n\text{-}C_3H_7$; X = H
25b: $R_1 = R_2 = R_3 = R_4 = n\text{-}C_2H_5$; X = OH
25c: $R_1 = R_3 = C_2H_5$; $R_2 = R_4 = n\text{-}C_{18}H_{37}$; X = OH

Figure 14. Molecular structures of squaraines **25a**−**c**.

A squaraine-cholesterol dyad **26**, which has been discovered as a good gelator,[59] has been investigated in supported LB films.[58] Both experimental and simulated results suggest a folded structure where attractive non-covalent interactions between the squaraine chromophore and the steroid take place. The absorption spectrum of the LB film is red shifted compared to the monomer in chloroform. Upon heating the film while immersed in pure water from 25 to 50 °C, the red-shifted aggregate gradually and irreversibly converted into a blue-shifted aggregate. On the contrary, heating the dry film in air did not cause the same conversion, indicating that water is necessary to promote the observed conversion.[58]

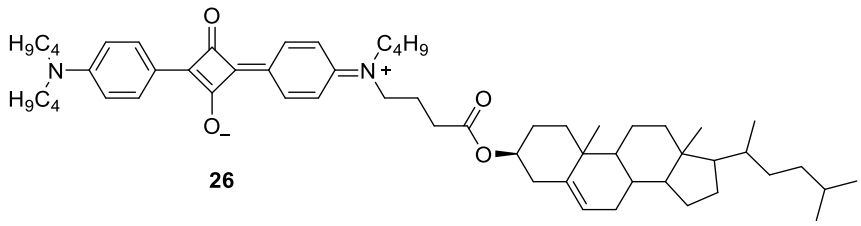

26

Figure 15. Molecular structure of the cholesterol substituted squaraine **26**.

2.2.2 Aggregation of Squaraines in Solutions

2.2.2.1 Aqueous Media

Besides LB films, the self-assembly of squaraines has also been investigated in solutions. An overwhelming amount of these investigations are performed in water or aqueous media. A common method to trigger aggregation of squaraines in aqueous solutions is to prepare stock solutions in organic solvents and then inject them into water or DMSO/water mixtures.[52,54,60] The earliest pieces of work describe only the changes of the UV/Vis absorption bands upon introducing the squaraines into aqueous media without giving information about the structure or elucidating the mechanism of the aggregation processes.[52,54,60] As an example, the group of Buncel has reported solely the observation of a kinetically controlled J-aggregation which transforms into a thermodynamically stable H-aggregate in water-rich environment.[54,60]

Whitten and co-workers performed systematic studies regarding the thermodynamic aspects of the aggregation processes of squaraines **27a-d** shown in Figure 16. For these amphiphilic squaraines, the individual molecules assemble into vesicles with the formation of a hypsochromically shifted absorption band. Aggregation constants for each dye were determined to be in the range from 1×10^{17} M^{-1} to 2×10^{21} M^{-1}. These extremely high values indicate the high driving force caused by the hydrophobic effect due to the aqueous environment.[61]

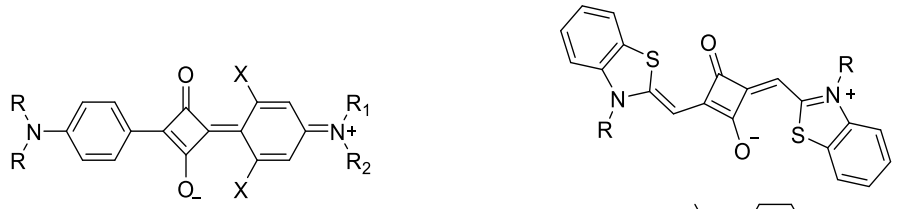

27a: R = C_4H_9; R_1 = CH_3; R_2 = $(CH_2)_3CO_2H$; X = H
27b: R = C_4H_9; R_1 = CH_3; R_2 = $(CH_2)_3CO_2H$; X = OH
27c: R = C_8H_{17}; R_1 = CH_3; R_2 = $(CH_2)_3CO_2H$; X = OH
27d: R = C_4H_9; R_1 = CH_3; R_2 = $(CH_2)_8N(CH_3)_3Br$; X = OH

28a: R = CO_2H
28b: R = CH_2CO_2H

Figure 16. Molecular structures of squaraines **27a–d** and **28a**,**b**.[61,62]

Another detailed investigation of the aggregation of squaraine dyes in water was performed by Das *et al. via* concentration-dependent UV/Vis measurements. They discovered that squaraines **28a** and **28b** form dimer aggregates in water that exhibit blue-shifted (H-type) absorption band compared to the monomeric state. The equilibrium constant for dimerization of **28b** is nearly an order of magnitude less than that of **28a**.[62]

Another study by Hecht and co-workers depicts the aggregation behavior of a chiral squaraine **29** in aqueous solution and on graphite surfaces. As shown in Figure 17, the gradual addition of water to a squaraine solution in acetonitrile leads to a decrease in the absorption of the monomer and the formation of a strongly broadened absorption band with both hypsochromically as well as bathochromically shifted parts which presumably originates from one single aggregated species. The corresponding circular dichroism (CD) spectra exhibit a strong negative Cotton effect that coincides with the position of the bathochromically shifted absorption band of the aggregate. By spin coating a trichlorobenzene solution of squaraine **29** on highly oriented pyrolytic graphite substrates (HOPG), two different aggregation patterns can be observed on the surface: a honeycomb structure and a moiré structure. The driving force for the dye aggregation in aqueous solution is dominated by the hydrophobic effect, which is similar to the above mentioned studies. The aggregation on the graphite surface, on the other

hand, is based on the interaction of the alkyl chains with the graphite surface as well as on dispersive interactions of the squaraine chromophores.[63]

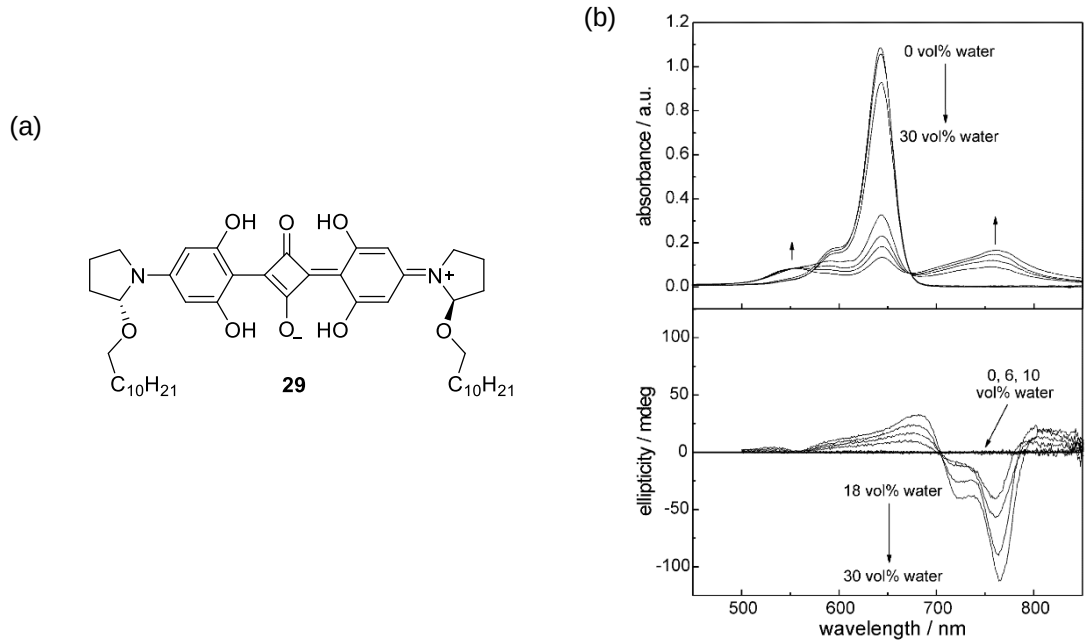

Figure 17. (a) Molecular structure of the chiral squaraine **29** and (b) its UV/Vis absorption (top) and CD spectra (bottom) in acetonitrile (c = 3.8 × 10^{-6} M) containing increasing water content (0, 6, 10, 18, 22, 26, and 30 *vol*.%) at 25 °C.[63] Adapted with permission from Ref. 63. Copyright 2006 WILEY-VCH Verlag GmbH & Co. KGaA.

Pang and co-workers have introduced a series of squaraines **30a-e** with different substituents appended on the central four-membered ring and investigated their aggregation behavior as well as applications in aqueous media.[64,65,66] Addition of an anionic surfactant sodium dodecyl sulfate (SDS) to the aqueous solutions of **30a-c** leads to significant changes in the UV/Vis absorption band shapes, revealing that the surfactant can enhance aggregation. Accordingly, **30c** forms defined J-type aggregates and **30a** forms H-type aggregates, whereas **30b** shows the features of both H- and J-type aggregates (Figure 19b). Such variation indicates the clear impact of the bulkiness of the R group on the dye's packing arrangement in the aggregate. Supported by the crystal structures, the bulky substituents in **30c** are responsible for the slip-stacked arrangement of the chromophores, giving rise to the red-shifted absorption band. As for **30a**, the smaller substituent leads to the formation of H-aggregates, where a maximum π-π interaction can be achieved. Accordingly, **30b**, bearing the substituent with moderate steric bulkiness, presents both H- and J-type characteristics.[64] The group of Pang further utilized the aggregation behavior of **30a** with the assistance of surfactants to detect adenosine triphosphates (ATPs) under physiological conditions. It is hypothesized that the surfactants form a spherical micelle, whose positive charges on the surface of the micelle attract the ATPs to form an

organized nanostructure through electrostatic interactions. The squaraine dyes tend to form H-aggregates with the absence of ATPs. Interestingly, upon interacting with ATPs, the squaraine H-aggregates are found to convert into J-like aggregates as a result of electrostatic interactions between the squaraine and the phosphate groups of ATPs.[65]

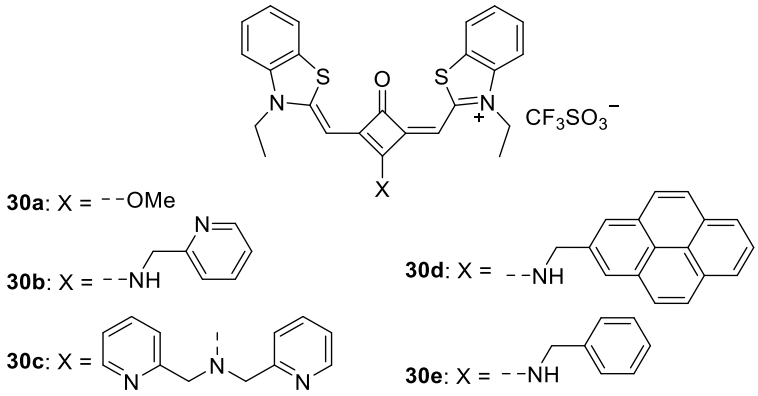

Figure 18. Molecular structures of squaraines **30a–e**.

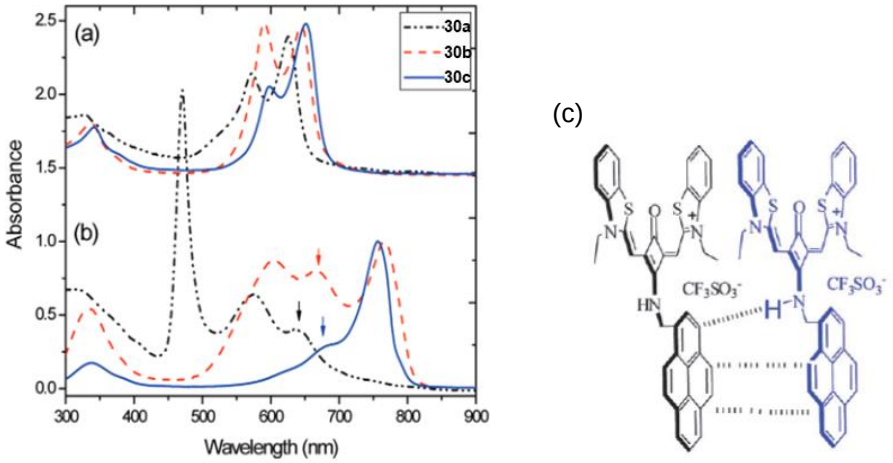

Figure 19. UV/Vis absorption spectra of **30a-c** in water ($c = 5 \times 10^{-6}$ M) in the absence (a) and presence (b) of 0.05% SDS.[64] Adapted with permission from Ref. 64. Copyright 2010 American Chemical Society. (c) The possible self-assembly of **30d** through multiple *inter*molecular interactions.[66] Adapted with permission from Ref. 66. Copyright 2015 Royal Society of Chemistry (Great Britain).

It is presumed that the π-π interaction between squaraine cores alone is not strong enough to stabilize the aggregates of squaraines in aqueous media, therefore additional non-covalent forces or assistance from surfactants[64,65] are required. Recently, Fan *et al*. illustrated the self-assembly of **30d** into nanoparticles *via* multiple interactions and its application for the detection of proteins. Herein, a pyrene group was attached to the squaraine chromophore to introduce additional *inter*molecular π-π interactions through the pyrene segments (Figure 19c),

resulting in higher tendency of aggregation in aqueous solution compared with the reference squaraine **30e**.[66]

Another example of introducing additional *inter*molecular interactions to enhance the aggregation of squaraines is depicted by Liu and co-workers with molecules **31a−c**, utilizing *inter*molecular hydrogen bonds. It is evident from the scanning electron microscopy (SEM) measurements that the morphology of **31a** aggregate is irregular nanoparticle-like (Figure 20b). In contrast, ordered, well-defined morphologies are observed for both **31b** and **31c**, in which H-bond recognition groups are introduced. Upon increase of the H-bond recognition abilities, the morphology changes from one-dimensional nanowires (**31b**) to two dimensional nanoribbons (**31c**), indicating that the supramolecular self-assembly can be effectively controlled by tailoring the H-bond recognition abilities.[67]

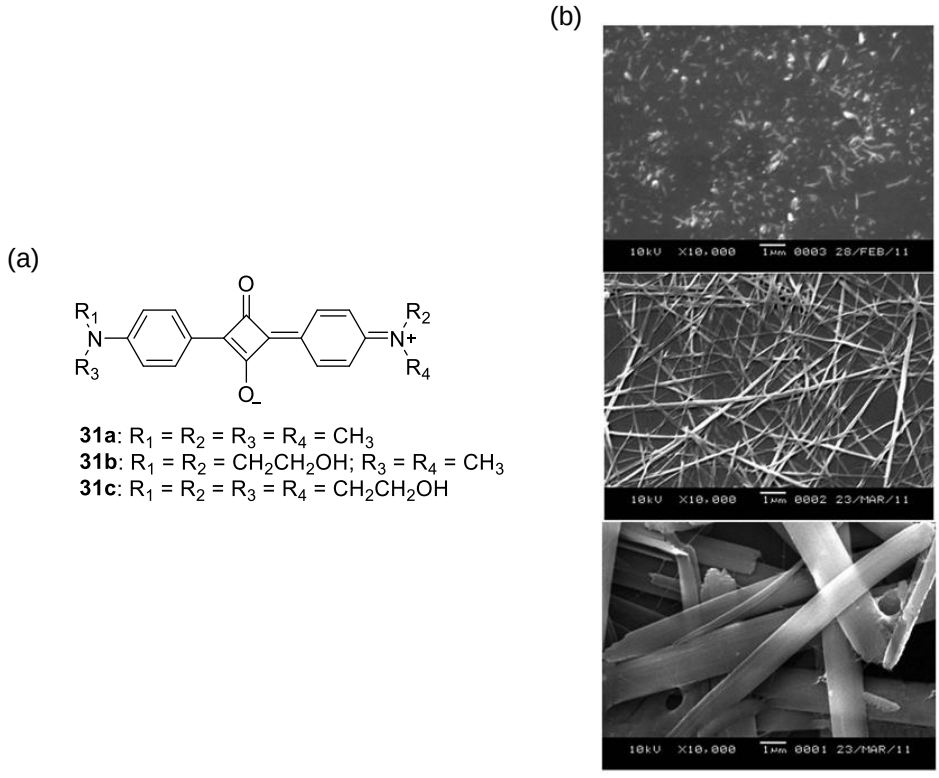

Figure 20. (a) Molecular structure of squaraines **31a−c** and (b) SEM images of aggregates formed from **31a−c** (from top to bottom).[67] Adapted with permission from Ref. 67. Copyright 2013 Royal Society of Chemistry (Great Britain).

As most squaraines tend to form H-type aggregates in aqueous media without the presence of bulky substituents,[61,62,64] very few examples of defined J-type squaraine aggregates have been reported. Yefimova *et al*. demonstrated that the addition of anionic SDS surfactants at

concentrations above the critical micelle concentration (CMC) into a DMF/H_2O (95%) solution is found to promote ordered J-aggregation (Figure 21).[68]

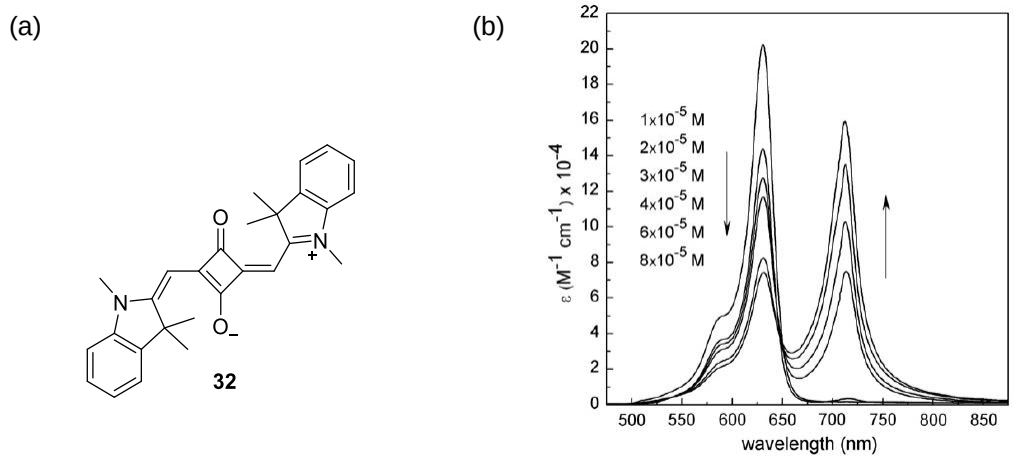

Figure 21. (a) Molecular structure of squaraine **32**. (b) Absorption spectra of squaraine **32** in a DMF/H_2O (95%) binary solution with SDS at different dye concentration. [SDS] = 1×10^{-2} M.[68] Adapted with permission from Ref. 68. Copyright 2012 Elsevier B.V.

Belfield and co-workers reported an interesting example of controlled J-aggregation for a water-soluble cationic squaraine **33** using a polyelectrolyte template. As illustrated in Figure 22, squaraine **33** dimerizes in an H-type fashion in pure water as a result of hydrophobic effect and electrostatic repulsion between the positively charged pendants. In the presence of poly(acrylic acid) sodium salt (PAA-Na), the ionic repulsions among the squaraine molecules can be partly neutralized, thus leading to extended aggregate formation driven by hydrophobic forces. Notably, H-type aggregates were initially formed, followed by a gradual conversion into thermodynamically more stable J-aggregates, exhibiting a sharp and intense red-shifted absorption band. According to the authors, this can be attributed to the flexibility of the polyelectrolyte backbone, which can slide or rotate, causing the transformation of H-aggregates to J-aggregates. Remarkably, removal of the PAA-Na template by the stronger binding calcium ions leads to dissociation of the J-aggregates. This process is proven to be reversible with 60% reversibility of the second cycle.[69]

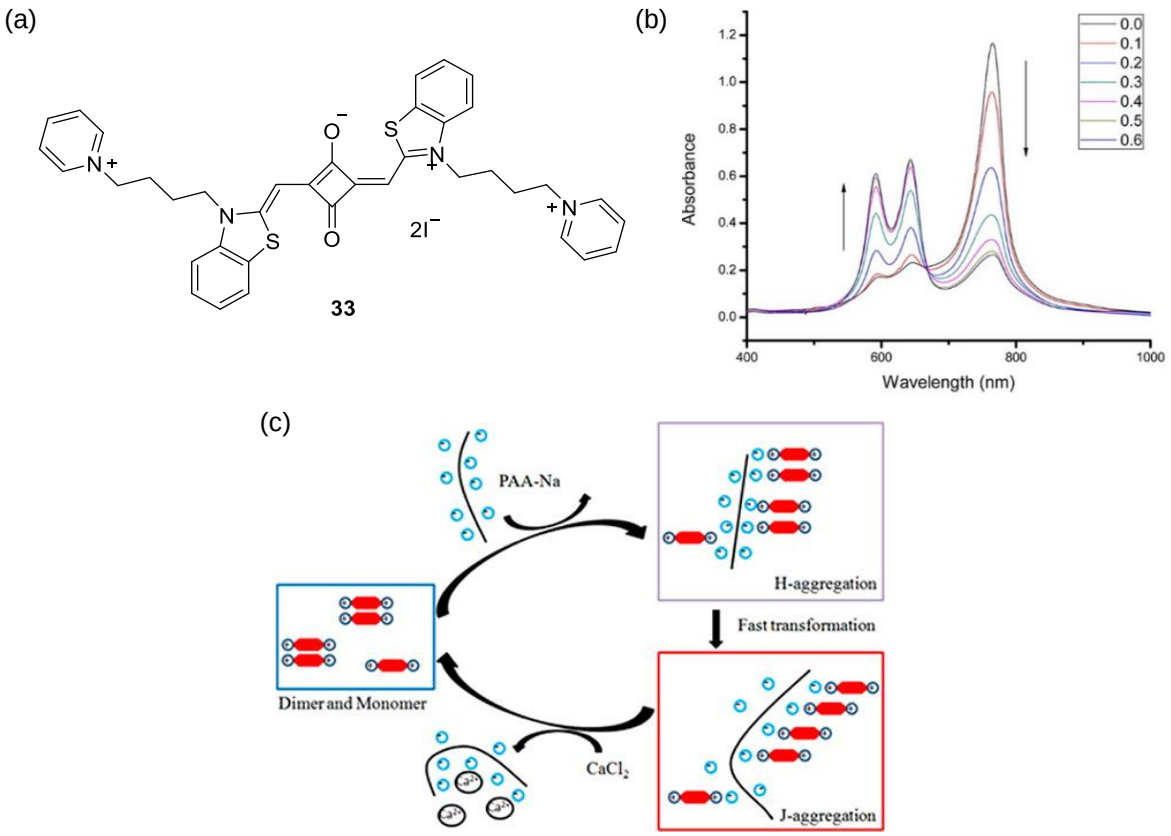

Figure 22. (a) Molecular structure of squaraine **33**. (b) Visible absorption spectra of a solution initially containing 1.0×10^{-5} M squaraine **33** and 0.01 M PAA-Na (black line) after increasing addition of $CaCl_2$. $[Ca^{2+}]/[COONa]$ increased from 0 to 0.6. (c) Illustration of its J-aggregate formation in the presence of a PAA-Na template; the calcium ions disrupted squaraine **33** aggregation by chelating with the PAA-Na template.[69] Adapted with permission from Ref. 69. Copyright 2013 American Chemical Society.

More recently, the group of Belfield examined a squaraine dye **34a** containing adamantyl as terminal groups and triethylene glycol monomethyl ether (TEG) as solubilizing side chains, which also displays a tendency for J-aggregation in aqueous media (Figure 23b). The reference squaraine **34b**, on the other hand, undergoes H-aggregation under the same conditions. The aggregation behavior of **34a** is presumably influenced by the presence of TEG groups close to the squaraine core, which serves as a steric hindrance upon π-π stacking, leading to the slip-stacked arrangement.[70]

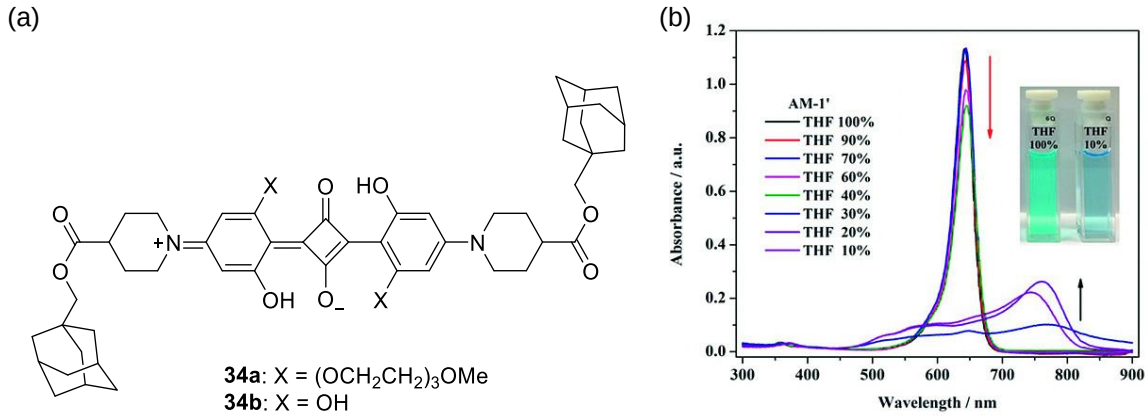

Figure 23. (a) Molecular structure of squaraines **34a-b**. (b) Absorption changes of **34a** in THF/H_2O mixtures. Inset shows the color of **34a** in pure THF and 10 % THF solution.[70] Adapted with permission from Ref. 70. Copyright 2018 WILEY-VCH Verlag GmbH & Co. KGaA.

2.2.2.2 Applications in Aqueous Media

Owing to their outstanding optical properties and the aggregation behavior in aqueous media, which is sensitive to the environment, squaraine dyes are found to be promising candidates for a variety of fields including ion sensors and biological probes. In the following section, an overview of several representative examples will be presented.

(a) Ion Sensors

The group of Ajayaghosh has contributed greatly to the development of cation sensors based on squaraine dyes in combination with aggregation control in aqueous solutions.[71,72,73,74] In 2004, they reported a squaraine tethered bichromophoric podand **35** which showed high selectivity toward alkaline earth metal cations, particularly to Mg^{2+} and Ca^{2+}, whereas they exhibited no binding activity toward alkali metal ions. Interestingly, in the presence of Ca^{2+}, the two molecules come into close proximity and formed a 2:1 sandwich dimer binding Ca^{2+}. In the contrary, when it comes to smaller cations, such as Mg^{2+}, the squaraine podand **35** is able to wrap around the cation to form a 1:1 folded complex, which is confirmed by Job's plot analysis (Figure 24). Both binding events can be monitored and analyzed by the blue shifted absorption band resulting from the face-to-face arrangement of the chromophores.[71]

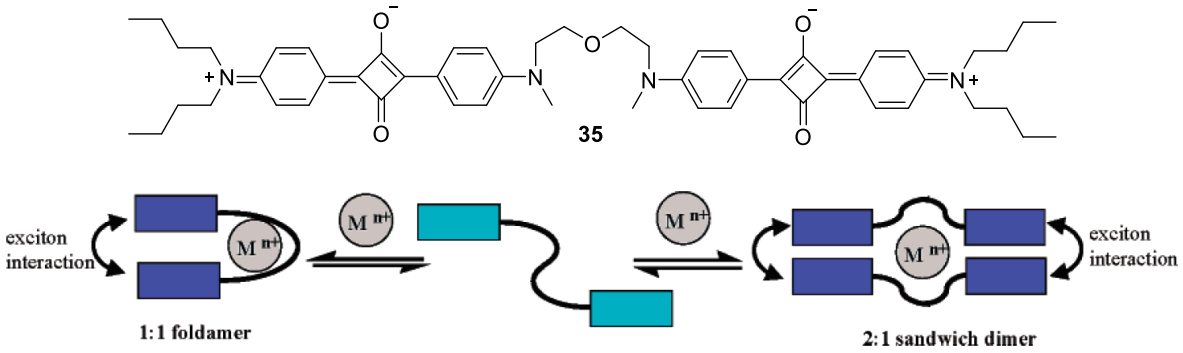

Figure 24. Molecular structure of squaraine podand **35** (top) and schematic representation of a chemosensor based on a cation-driven, exciton interaction in a squaraine-linked podand.[71] Adapted with permission from Ref. 71. Copyright 2004 American Chemical Society.

Meanwhile, the same research group illustrated another elegant example of the formation of extended aggregates of linked bis or tris(squaraines) assisted by Ca^{2+} ions as well.[73,74] The aggregation of the tris(squaraines) **36a-c** can be initiated either by adding water to the acetonitrile solution of the dyes or by adding Ca^{2+} ions. The resulting hypsochromic absorption bands are explained by the folding of the chromophore units, giving rise to a close interaction between the neighboring chromophores. Upon increasing the concentration of a pure acetonitrile solution and subsequent removal of the solvent showed the formation of vesicles, confirmed by AFM and TEM examinations. In the case of Ca^{2+} ion-induced aggregation, however, helical morphologies were observed in AFM studies, which led to a clear CD signal when a chiral moiety was introduced into the dye structure, as shown in **36c**. The formation of the helical aggregates assisted by Ca^{2+} ions could be reversed by adding a stronger ligand such as EDTA. While the Ca^{2+} ions are removed from the aggregates, the squaraines dissociate back into monomers (Figure 25).[73] A similar behavior was discovered for related bis(squaraines) upon the addition of Ca^{2+} ions, which initially form micelles in a kinetically controlled aggregation process, and then subsequently rearrange themselves into extended fibers in a slow thermodynamically controlled transformation accompanied with a strong increase in the absorption intensity.[74]

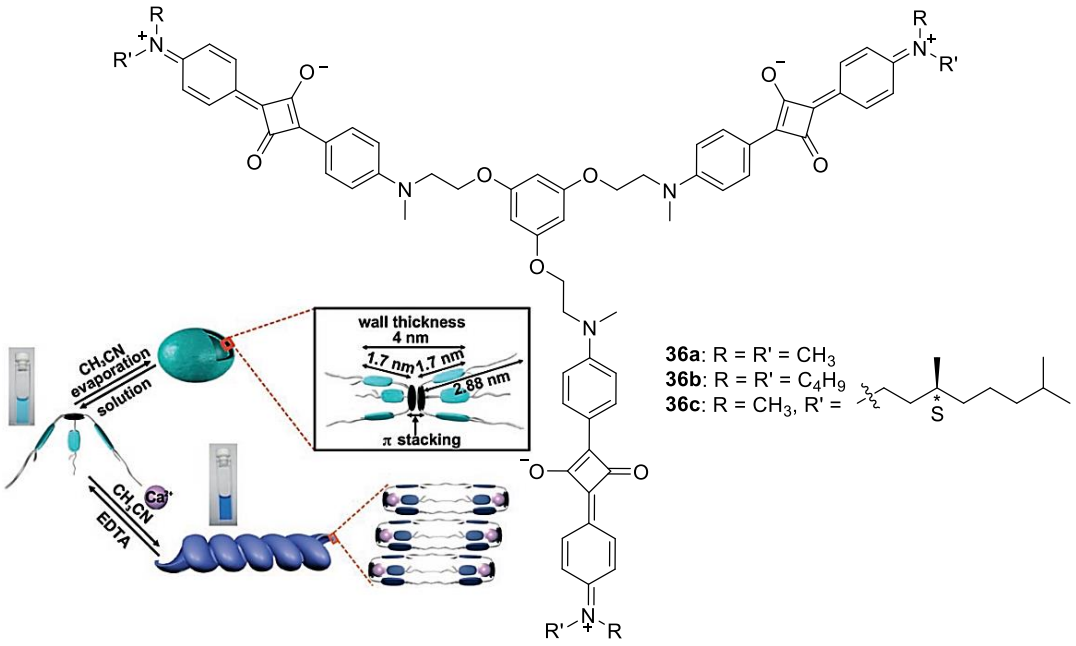

Figure 25. Molecular structure of tris(squaraines) **36a-c**, cartoon representation of the self-assembly processes and morphology changes of **36c**. The solutions in the cuvettes show the actual colors of the tripodal dye before (light blue) and after (dark blue) the addition of Ca^{2+}.[73] Adapted with permission from Ref. 73. Copyright 2006 WILEY-VCH Verlag GmbH & Co. KGaA.

(b) Biological Applications

One of the important advantages of squaraine dyes is their typical cyanine-like strong and usually narrow absorption in the red part of the visible light spectrum or even the near-infrared (NIR) region, along with strong fluorescence.[22,27] In addition, the NIR spectral region is often referred to as the optical window in biological tissues due to low scattering, diminished autoabsorption and autofluorescence, and deep penetration[75], which leads to a wide scope of biological applications.

(1) Co-Assembly of Squaraines with Water-Soluble/Bio-Compatible Materials

Despite their outstanding photophysical properties, the intrinsic chemical instability and self-aggregation tendency of squaraines in aqueous environment hampered their applications under physiological conditions. In particular, self-aggregation of squaraines is contradicting their fluorescent characteristics which serve as a great advantage in biological imaging. Therefore, a number of researches are focusing on isolating the squaraine dyes in biocompatible carriers in order to retain their fluorescent monomeric state and to equip them with biocompatibility at the same time.[76,77] For instance, Wang, Würthner and co-workers demonstrated highly stable and biocompatible supramolecular adducts of a squaraine **37** and

the natural carrier protein, bovine serum albumin (BSA) (**37** ⊂ BSA), where the squaraine **37** is selectively bound to BSA's hydrophobic domain *via* hydrophobic and hydrogen bonding interactions. The **37** ⊂ BSA adduct exhibited up to 80-fold enhanced fluorescence intensity, serving as an effective tumor targeted imaging dye in the NIR region.[76] Using a similar approach, Zhao and co-workers reported a micelle encapsulation of a NIR-absorbing squaraine dye **38** for *in vivo* fluorescence and photoacoustic (PA) bimodal imaging. The encapsulation retains both the photophysical features, i.e., intense absorption and emission from 800 to 900 nm, and the chemical stability of **38** and in the meantime exhibits high photostability and low cytotoxicity in physiological conditions.[77] Moreover, as mentioned in the previous section, with adequate molecular design, the absorption and emission of squaraine dyes can be shifted further into the second window of NIR (NIR-II, 1000–1700 nm). Squaraine **18**, which possesses ethyl-grafted 1,8-naphtholactam as the donor unit, was first co-precipitated with biocompatible DSPE-PEG_{2000} and further functionalized with the breast cancer cell targeting peptide CREKA to obtain the squaraine **18** nanoprobe. This nanoprobe exhibited absorption maximum at 940 nm and a fluorescence peak at 980 nm, extending into the NIR-II region. The nanoprobe showed outstanding tumor imaging performances and deep penetration depth, as well as excellent photothermal conversion, which is an advantage for photothermal therapy of solid tumors.[42]

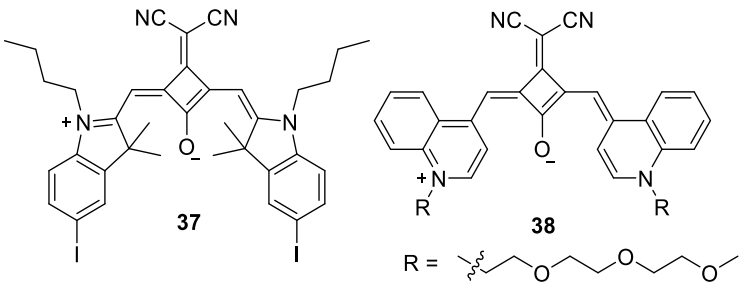

Figure 26. Molecular structure of squaraines **37** and **38**.

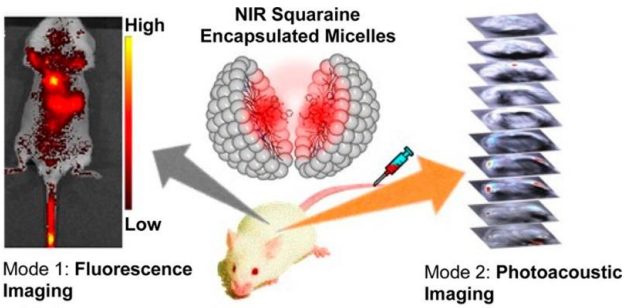

Figure 27. Schematic illustration showing intravenous injection of squraine **38**-micelle for fluorescence and photoacoustic bimodal imaging in a mouse (bottom).[77] Adapted with permission from Ref. 77. Copyright 2015 American Chemical Society.

As mentioned earlier, Belfield and co-workers investigated squaraine **34a** which tends to form J-aggregates in aqueous solutions. Despite its J-type feature, the fluorescence of **34a** aggregate is too weak for optimized cell imaging. They further introduced ß-cyclodextrins (ß-CD) to trigger host-guest interactions, where the adamantyl groups reside in the cavity of ß-CD. This host-guest interaction increases the hydrophobicity of the microenvironment, which resulted in dissociation of the squaraine aggregates, thereby enhancing the fluorescence intensity. In addition to increased local hydrophobicity, the bulkiness of ß-CD also poses a large steric effect, leading to the reduced tendency for aggregation.[70]

Temperature can be an additional factor to enhance dissociation of squaraine dye assemblies. In a recent report from Lee and co-workers, squaraine dye **39** was incorporated into the self-assembled nanovesicle lipid bilayer membrane. The phase transition of the lipid bilayer membrane leads to aggregation and dissociation of the squaraine dye, which then induces the reversible fluorescence switching in a highly cooperative manner (Figure 28).[78]

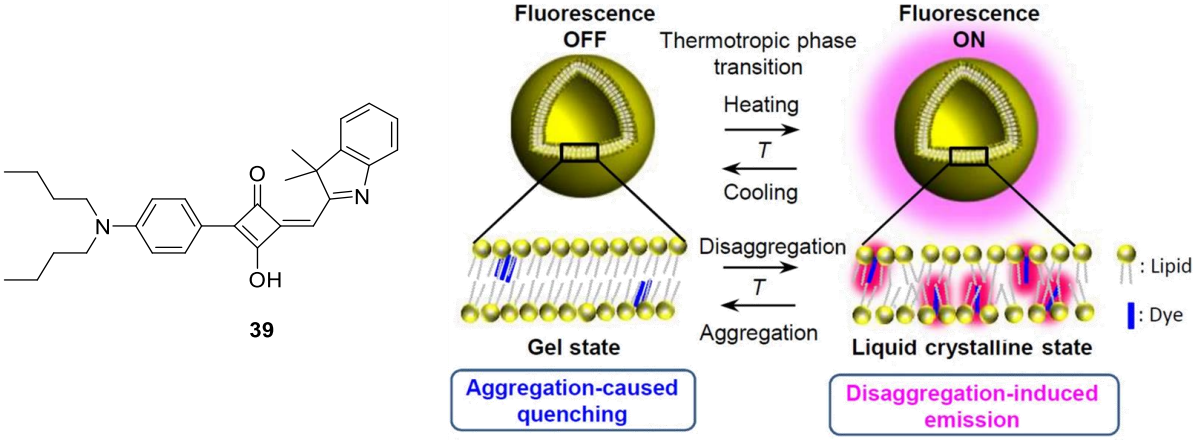

Figure 28. Proposed mechanism for squaraine **39** fluorescence switching in the lipid bilayer membrane as a response to phase transition. The fluorescence off/on switching is a result of the reversible aggregation-caused quenching/disaggregation-induced emission of **39** in the gel to liquid crystalline phase transition temperature (*T*) of the lipid bilayer membrane.[78] Adapted with permission from Ref. 78. Copyright 2019 Springer Nature.

To sum up shortly, squaraine dyes are prone to aggregate in aqueous media, thereby showing decreased fluorescence intensity caused by aggregation-induced quenching. Therefore, the examples illustrated above deal with the dissociation of squaraine dye assemblies in aqueous media in order to achieve high fluorescence intensity. However, many scientists took advantage of this aggregation feature and achieved multi-modal fluorescence or photoacoustic (PA) imaging by manipulating the aggregation process of squaraines under biological conditions.[79,80,81]

In recent years, PA tomography has emerged as a new non-invasive imaging tool due to its higher spatial resolution and greater penetration depth than other optical imaging techniques.[82] Zhang and co-workers have fabricated a biocompatible nanocomplex in aqueous media, which consists of squaraine dye **40** and bovine serum albumin. Upon aggregation, the absorption spectrum of **40** expanded from the visible light region to the NIR region (Figure 29 c) which facilitates PA signal generation in the tissue-transparent NIR optical window (700 – 900 nm).[79]

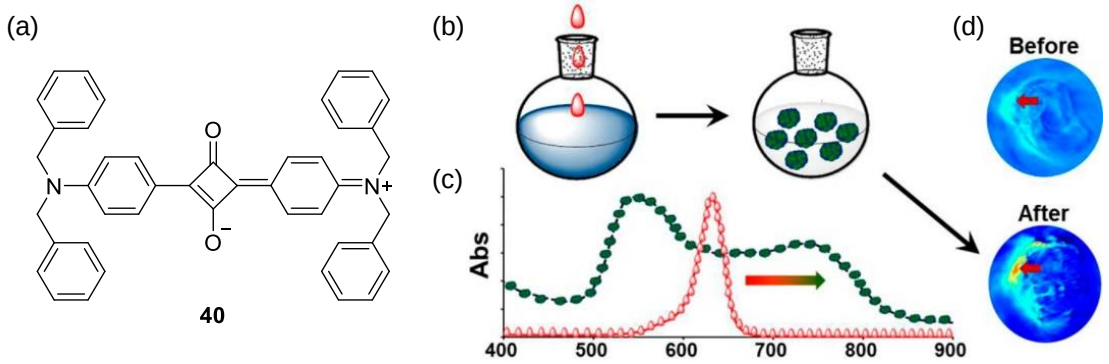

Figure 29. (a) Molecular structure of squaraine **40**. (b) Diagram of **40** nanocomplex preparation. (c) Normalized absorption spectra of **40** in THF (red), **40** nanocomplexes in PBS buffer (green). (d) *In vivo* PA images of tumor (top) without and (bottom) with **40**–albumin-nanocomplex injection. (The red arrows indicate tumors; excitation wavelength = 740 nm.)[79] Adapted with permission from Ref. 79. Copyright 2014 American Chemical Society.

In contrast to fluorescent probes, PA contrast agents require a high light-to-heat conversion efficiency which relates to a low fluorescence quantum yield. For the combined imaging technology, proper adjustment of the self-assembly equilibrium of the fluorescent squaraine monomer and PA squaraine aggregates has been demonstrated by the groups of Wang and Würthner. They reported a squaraine-based self-assembly in nanoconfined hydrophobic phospholipid bilayers of liposomes and the application of such functional liposomes for NIR and PA dual-modular imaging *in vivo* by altering the mixing ratio of squaraine **37** and phospholipid.[80] It is known that the fluorescence quenching upon formation of aggregates leads to the thermal release after laser irradiation.[83] The generation of PA signals is directly related to the thermal expansion which is closely related to the thermal conversion efficiency. Therefore, the higher mixing ratio of squaraine **37** in liposome formed H-type aggregates, exhibiting higher thermal conversion efficiency, further resulting in much stronger PA signal.[80]

While most dye aggregation processes cause fluorescence quenching, the well-known J-aggregation normally results in strong, red-shifted absorption and enhanced fluorescence.[84] Combined with their outstanding photophysical performances, fabricating squaraine dye

J-aggregates becomes a potential approach to develop NIR-I or even NIR-II biological probes. In 2018, the group of Huang introduced a novel system of J-aggregate squaraine nanoparticles (NPs) with bright NIR-II fluorescence. Through co-precipitation of squaraine **41** and the amphiphilic copolymer (PEG-*b*-PPG-*b*-PEG, F-127) following different procedures, water-soluble H- and J-aggregate squaraine NPs are produced. The J-aggregate NPs exhibit an absorption maximum at 901 nm in aqueous solution and a broad emission spectrum extending up to 1400 nm. Remarkably, the J-aggregate NPs showed outstanding brightness both *in vitro* and *in vivo*, at up to 8 mm of penetration depth.[81]

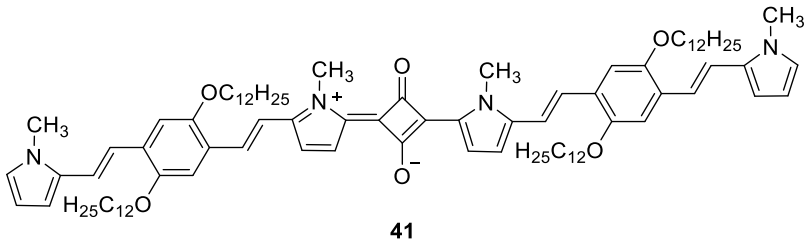

41

Figure 30. Molecular structure of squaraine **41**.

(2) Squaraines as Probes for Biomolecules

As mentioned previously, squaraines are prone to aggregate in aqueous media, resulting in quenched fluorescence. Apart from incorporating them into biocompatible materials in the first place to keep them in the monomeric state in order to retain their strong fluorescence for imaging purposes, the aggregation state of squaraines in aqueous media can serve as a turn-on probe for biomolecules. The squaraine aggregates remain non-fluorescent in the absence of target biomolecules. When the target biomolecules are present and interact with squaraine dyes, the squaraine dyes are released from the aggregated state into monomeric forms, thus leading to an increase, i.e., turn-on in fluorescence. This concept is commonly employed in the sensing of proteins,[64,66,85,86] amino acids[87] and G-quadruplexes.[32,33,88]

In the early 2000s, Yagi and co-workers synthesized a series of bis(squaraine) dyes with red emissions that are found to bind to human serum albumin (HSA) and bovine serum albumin (BSA). UV/Vis absorption measurements indicated that squaraines **42a**–**b** and **43a**–**b** form H-type aggregates in buffer solutions. Upon addition of HSA or BSA, a red-shift in the absorption maximum was observed along with an enhanced fluorescence, suggesting the binding of protein to the bis(squaraine) molecules in a 1:1 ratio.[85]

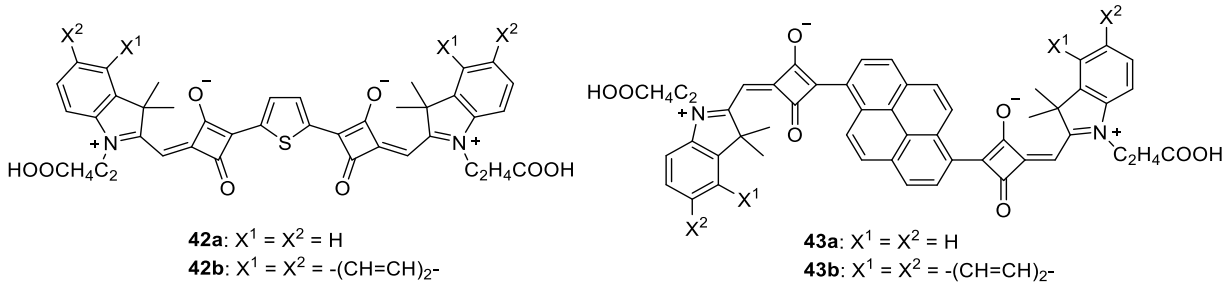

Figure 31. Molecular structures of squaraines **42a**–**b** and **43a**–**b**.

Using a similar approach, Yarmoluk and co-workers reported a series of symmetrical and asymmetrical squaraine dyes **44**–**47** and their application as fluorescent probes for several different albumin proteins. All squaraines studied in this report exhibited considerable increases in emission (24–190 folds) in the presence of BSA. Moreover, the squaraines showed significant selectivity toward BSA compared with other albumins (HSA and ovalbumin).[86]

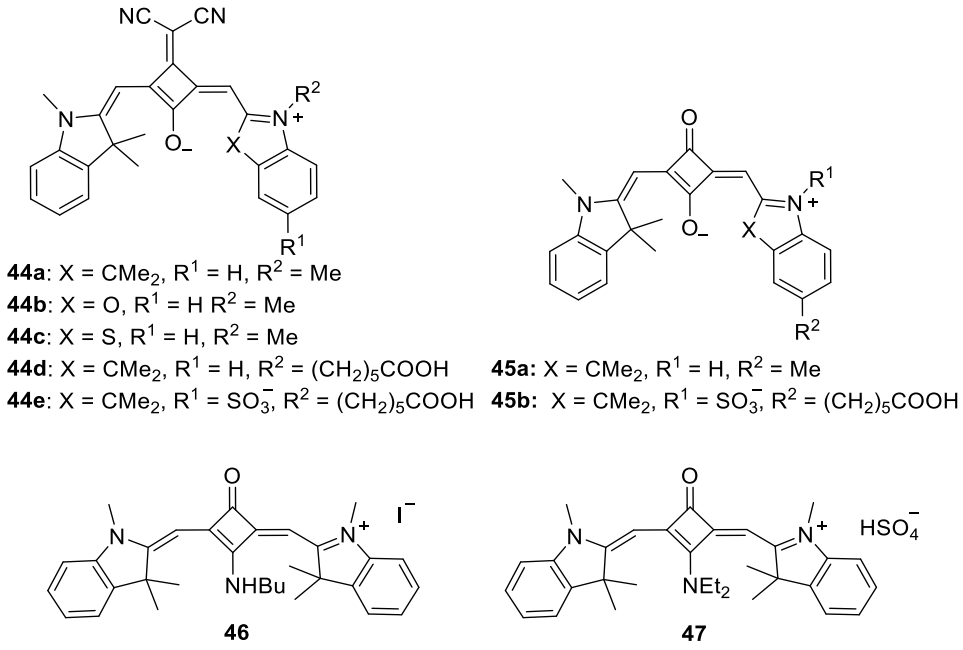

Figure 32. Molecular structures of squaraines **44** – **47**.

However, the reports described above did not investigate the squaraine dye aggregation or the binding mechanisms between squaraine dyes and the proteins in more detail. Until 2010, the group of Pang utilized squaraines **30a**–**c** (Figure 18) as BSA probes and observed a large fluorescence increase (up to 200 folds) compared with the non-binding state. With the assistance of surfactants, squaraines **30a-c** form H-, H- and J-, and J-type aggregates, respectively, in aqueous solutions (Figure 19b). Upon addition of BSA to the solution, the

aggregation bands of squaraines decreased, while their monomeric bands emerged, indicating that BSA interacts with squaraines dyes in the monomeric form, therefore leading to a turn-on in fluorescence. Meanwhile, the absorbance at ca. 270 nm increased, which corresponds to the tryptophan chromophore in BSA, suggesting that the binding event happened at site I of BSA. Moreover, the authors hypothesized that upon complexation with the protein, the environment around the squaraine dyes became more rigid, which in turns caused significant enhancement of the fluorescence intensity.[64]

More recently, Xu *et al.* demonstrated nanoparticles of a new squaraine **30d** for the selective detection of HSA in solution and human blood serum. The detection mechanism of HSA is similar to the above cases, namely the binding of proteins releases the squaraine dyes from the aggregated state into monomeric state, giving rise to the fluorescence turn-on. Moreover, the authors were able to determine that the binding takes place at site II of HSA,[66] where the photodynamic therapies can be the most efficient.[89]

A unique example of amino acid detection was introduced by Pang *et al.* in 2013. They demonstrated a self-assembly platform consisting of squaraine (**30a**)-embedded CTAB (cationic surfactant hexadecyl trimethyl ammonium bromide) micelles that can distinguish cysteine (Cys) and homocysteine (Hcy). While embedded in the micelle, squaraine dyes **30a** tend to aggregate without the presence of analytes. Based on absorption and fluorescence measurements, the authors suggest that upon addition of Cys or Hcy, the environment of the squaraine compartment becomes more hydrophobic, therefore the squaraine dyes are converted to the monomeric state and their molecular rigidity is increased. Due to the structural difference between Cys and Hcy, the extent of hydrophobicity differs as well, leading to different extent of disaggregation of squaraines, which results in an effective colorimetric detection (Figure 33a). Meanwhile, this difference in hydrophobicity also affects the morphology of the micelles (Figure 33b). Interestingly, addition of Cys caused the micelle to transform from sphere to rod.[87]

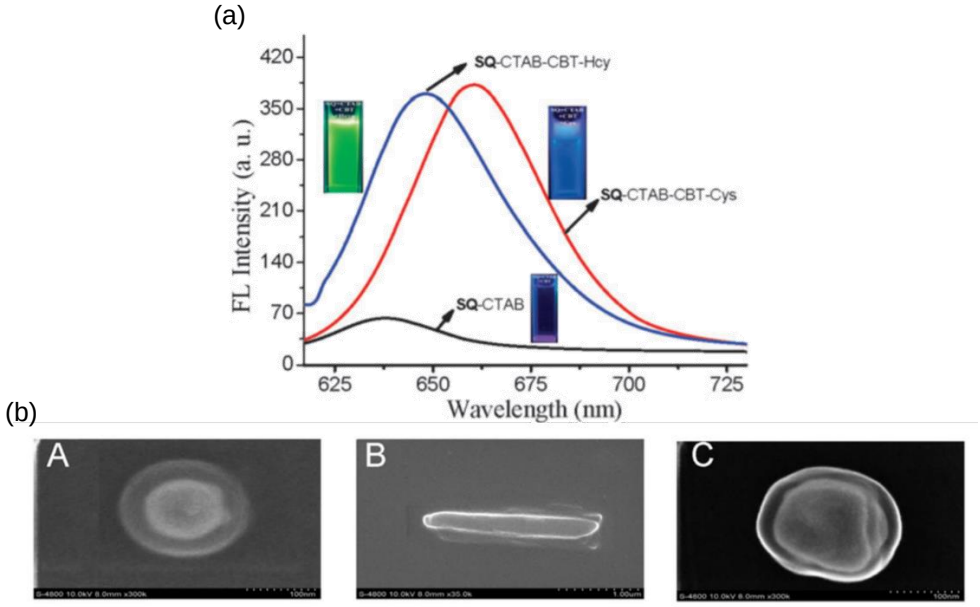

Figure 33. (a) Fluorescence spectra of **30a** (5.0×10^{-6} M) in aqueous solution in the presence of CBT, CTAB (0.05 wt%) upon addition of Cys and Hcy, where [CBT] = [Cys] = [Hcy] = 1.5×10^{-4} M and λ_{ex} = 600 nm. (b) SEM images of **30a**-embedded CTAB micelles in the presence of CBT, where (A) without addition of amino acids, (B) after addition of Cys, (C) after addition of Hcy.[87] Adapted with permission from Ref. 87. Copyright 2013 Royal Society of Chemistry (Great Britain).

Nucleic acids with repetitive guanine-rich sequences can fold into four-stranded G-quadruplex (G4s) structures, which are composed of multilayered stacks of planar G-quartets *via* eight Hoogsteen hydrogen bonds (Figure 34).[34] Such sequences are found in telomeres and promoters of many important genes such as oncogenes. Therefore, G4s are becoming attractive targets for anti-cancer drug discovery.

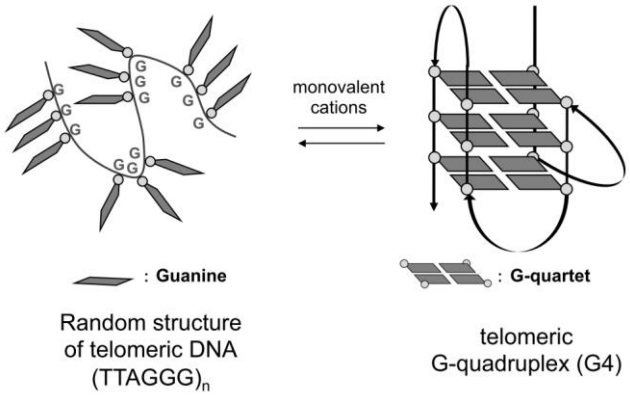

Figure 34. Induction of G-quadruplex formation on telomeric DNA by monovalent cations.[90] Adapted with permission from Ref. 90. Copyright 2013 MDPI (Basel, Switzerland).

The crucial feature of an ideal G-quadruplex-binding molecule is a large flat aromatic core prone to π-stacking with a G-quartet platform, while retaining reasonable water solubility. Due to the highly planar *cisoid*-conformation and functionalizable scaffold plus outstanding photophysical properties, i.e., long-wavelength absorption and emission, dicyanomethylene-substituted squaraines are therefore promising to be developed as G-quadruplex-binders.

In 2014, the Shangguan group reported the first G4-binding squaraine dye **48a** with anionic sulfonic groups as water-soluble moieties. Squaraine **48a** is found to bind selectively to parallel G4s, due to the rigid planar scaffold caused by the dicyanomethylene substituent. The binding results in the transformation of the squaraines from H-aggregates into monomers, which is reflected in the change of absorption spectra and the fluorescence enhancement of **48a** (Figure 35).[32]

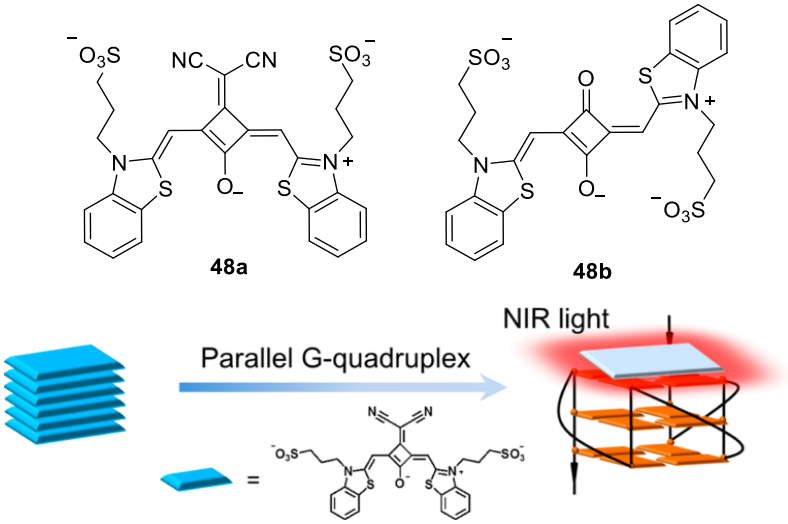

Figure 35. Molecular structures of **48a**–**b**. **48a** transforms from H-aggregates into monomers while binding with parallel G4.[32] Adapted with permission from Ref. 32. Copyright 2013 American Chemical Society.

However, further cell analysis of G4 binding with **48a** was not possible due to poor cellular uptake. This is presumably due to the negative charges on the side chains that hinder the cell membrane penetration. Moreover, the anionic character of squaraine **48a** also lowers its affinity to the negatively charged G4s. Therefore, the same group developed a facile approach using click chemistry to readily produce a library of squaraine analogues **50a**–**e** with different side chains in order to screen potential probes for G4 bindings and *in vivo* applications (Scheme 6). Among this series of squaraines, several exhibit indeed much higher affinity and cellular uptake than **48a**.[88]

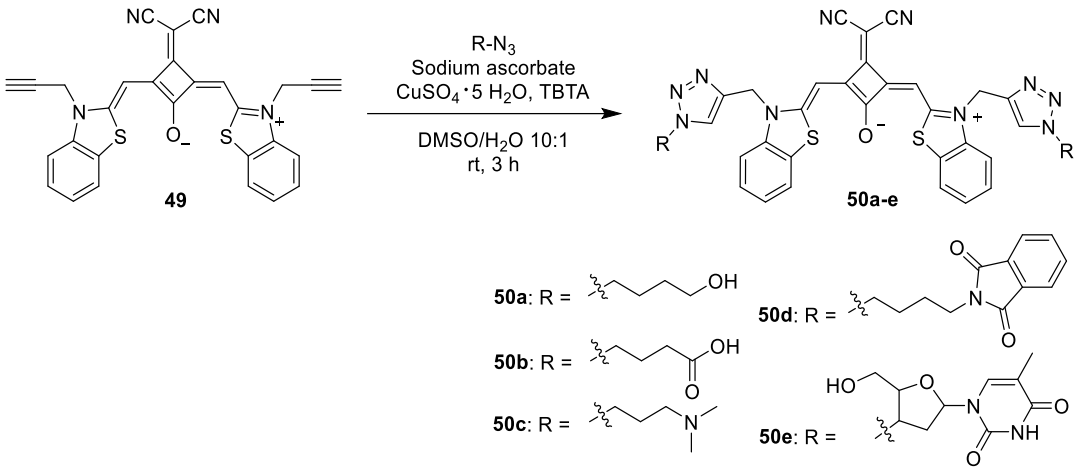

Scheme 6. Synthetic route of squaraines **50a**–**e**.

Meanwhile, Würthner and co-workers also reported an amphiphilic squaraine G4 probe **51** bearing neutral ethylene glycols as solubilizing side chains. The aggregation behavior and G4 binding ability were explored by measuring absorption spectra in different ratios of THF/water (*v*/*v*). When the amount of water increases, the absorption peak of monomer decreases while a broad band showing one red-shifted maximum and a blue-shifted maximum emerges, which indicates the appearance of a newly formed aggregate (Figure 36a). Upon titrating with parallel G4s, the squaraines are released from the non-fluorescent aggregate and form an unconventional sandwich π-complex with two G4s, leading to a strongly fluorescent (Φ_{FL} = 0.61) supramolecular architecture (Figure 36b).[33]

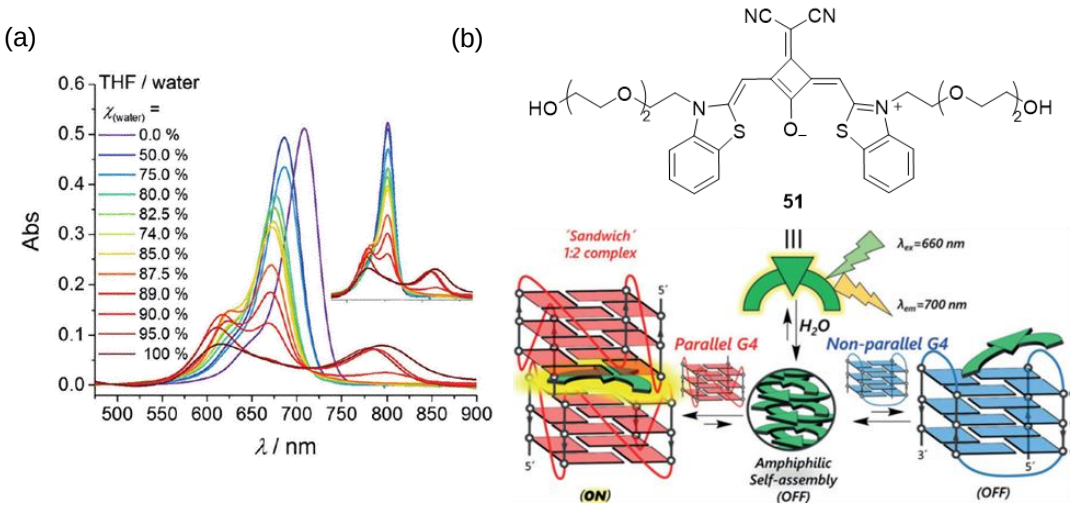

Figure 36. (a) Vis/NIR spectra of **51** (3.7 μM) at 25 °C in THF/water solutions with increasing water volume fractions, $\chi_{(water)}$; inset: spectra corrected for the solvatochromic shift. (b) Molecular structure of squaraine **51** and the mechanism for the selective detection of parallel G4s.[33] Adapted with permission from Ref.33. Copyright 2017 WILEY-VCH Verlag GmbH & Co. KGaA.

2.2.2.3 Organic Media

In contrast to aqueous media, examples of squaraine aggregates in anhydrous media are rare. An early example described the aggregation of squaraines **52a** and **b**, and the concentration-dependent absorption spectra of **52a** in anhydrous acetonitrile is shown in Figure 37b.[91]

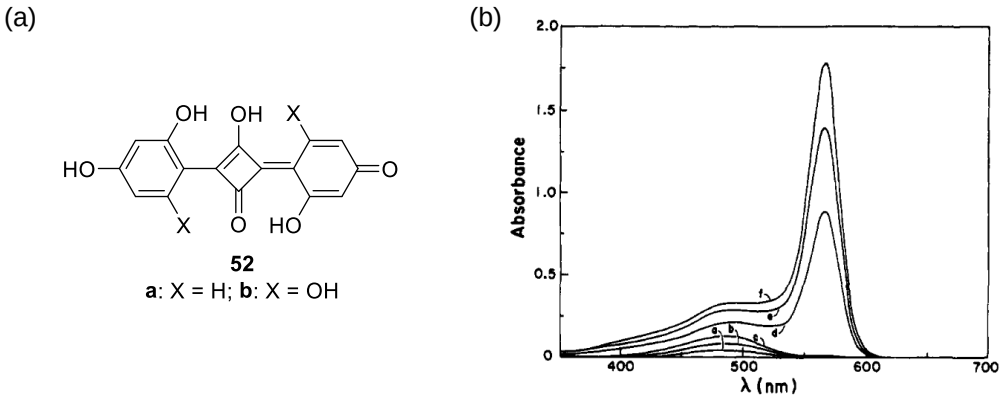

Figure 37. (a) Molecular structure of squaraine **52**. (b) The concentration-dependent UV/Vis absorption spectra of **52a** in anhydrous acetonitrile (a: c = 0.5 μM; b: c = 1.1 μM; c: c = 1.6 μM; d: c = 8.1 μM, e: c = 9.6 μM; f: c = 16.1 μM).[91] Adapted with permission from Ref. 91. Copyright 1993 American Chemical Society.

Both squaraines exhibit similar aggregation behavior. According to the concentration-dependent absorption spectra, with increasing concentration a new strongly bathochromically shifted absorption band (J-type) occurs with respect to the monomer band. The determined aggregation constants are (3.1 ± 0.3) × 10^5 M^{-1} for **52a** and (2.2 ± 0.1) × 10^5 M^{-1} for **52b**. These relatively high values suggest that, as implied by the authors, aside from dispersive and quadrupole interactions, hydrogen bonds play an important role in the aggregation process.[91] Deeper investigations of this dye were carried out in aprotic solvents and it was found that the aggregate formation was disrupted by the addition of protic solvents. This further supported that the aggregate formation was facilitated by *inter*molecular hydrogen bonding.[92]

Another early example of squaraine aggregation in organic solvents is given by the helical chiral squaraine presented by Ramaiah and co-workers.[55] With increasing proportion of acetonitrile in the chloroform / acetonitrile mixture, aggregation of **53a** into helices was observed (Figure 38b). They show a hyosochromic shift in the absorption band and in addition, a strong signal in CD spectra. According to the authors, the chirality can be influenced by three factors: the ratio between “good” and “bad” solvent, the squaraine concentration and finally the temperature.

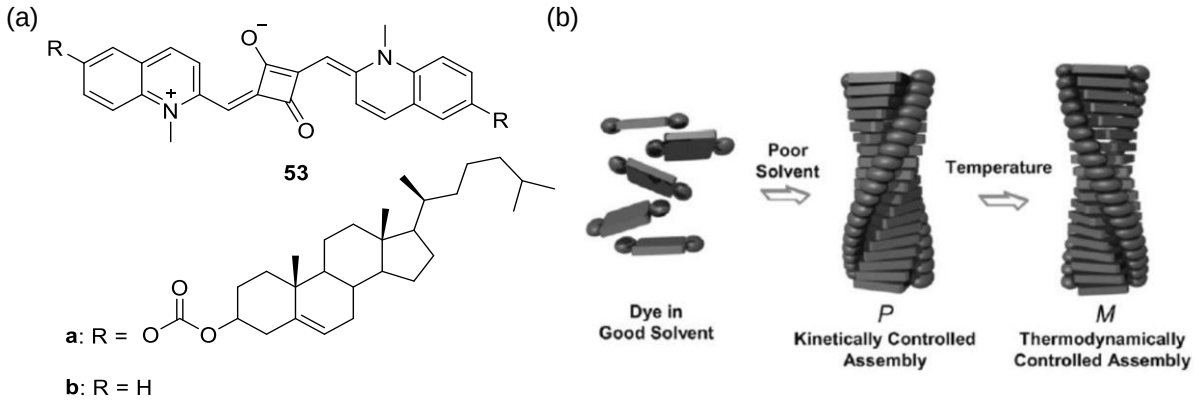

Figure 38. (a) Molecular structures of the squaraines **53a** and **b**. (b) The schematic description of the aggregation model of the kinetically and thermodynamically controlled self-organizations of **53a**.[55] Adapted with permission from Ref. 55. Copyright 2007 WILEY-VCH Verlag GmbH & Co. KGaA.

Hence, a change in the CD signal from a negative Cotton effect (*P*-handed helices) to a positive Cotton effect (*M*-handed helices) was observed upon subsequent heating and cooling, indicating the formation of a thermodynamically stable species. The preferred formation of *P*- or *M*-handed helices were confirmed by AFM measurements.

In 2012, Mayerhöffer *et al.* reported a detailed study of squaraine **54** that self-assembles into extended fiber-like aggregates in organic solvents like toluene and methyl cyclohexane (Figure 39).[56] The aggregates were formed by face-to-face self-assembly of the squaraine dyes and stabilized by dispersive interactions and hydrogen bonds. The thermodynamics of the self-assembly process were well investigated and can be interpreted in terms of the K_2/K model,[93] revealing a cooperative mechanism.

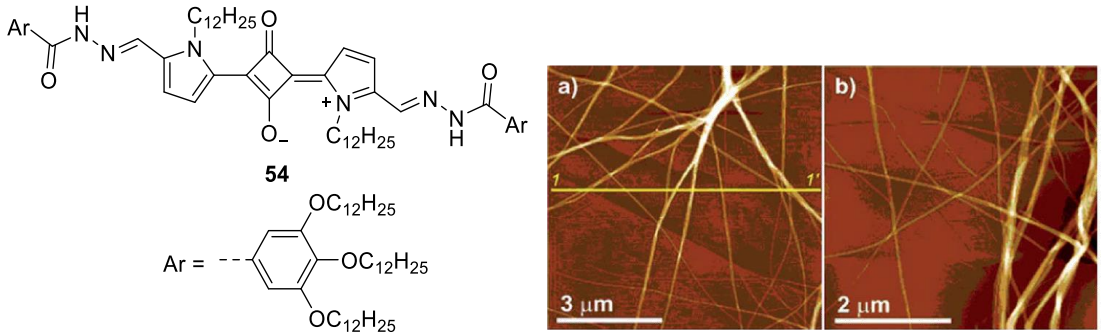

Figure 39. Molecular structure of squaraine **54** and height AFM images of samples spin-coated from a methyl-cyclohexane solution of **54** ($c = 5 \times 10^{-4}$ M, 5000 rpm) on HOPG.[56] Adapted with permission from Ref. 56. Copyright 2012 Royal Society of Chemistry (Great Britain).

In another report from Mayerhöffer *et al.*, a series of halogenated 4-methylquinolinium-based dicyanomethylene squaraine dyes and their self-assembly in toluene were described.[28] For

non-halogenated squaraine **17a** (see Scheme 3), no differences in absorption band shapes were observed upon concentration or temperature variation in toluene, indicating the absence of aggregation. On the contrary, the halogenated squaraines **17b-d** (see Scheme 3) show an additional hypsochromically shifted band upon increasing the concentration in toluene. Therefore, the authors claimed that the aggregation is driven by not only π-π stacking and dipole-dipole interactions, but also dispersive halogen interactions. The aggregation process was properly fitted with the isodesmic model. Furthermore, 2D-NMR measurements confirmed the sandwich-like face to face arrangement of the chromophores (Figure 40), which is in accordance with the blue-shifted absorption band, namely an H-type aggregate.

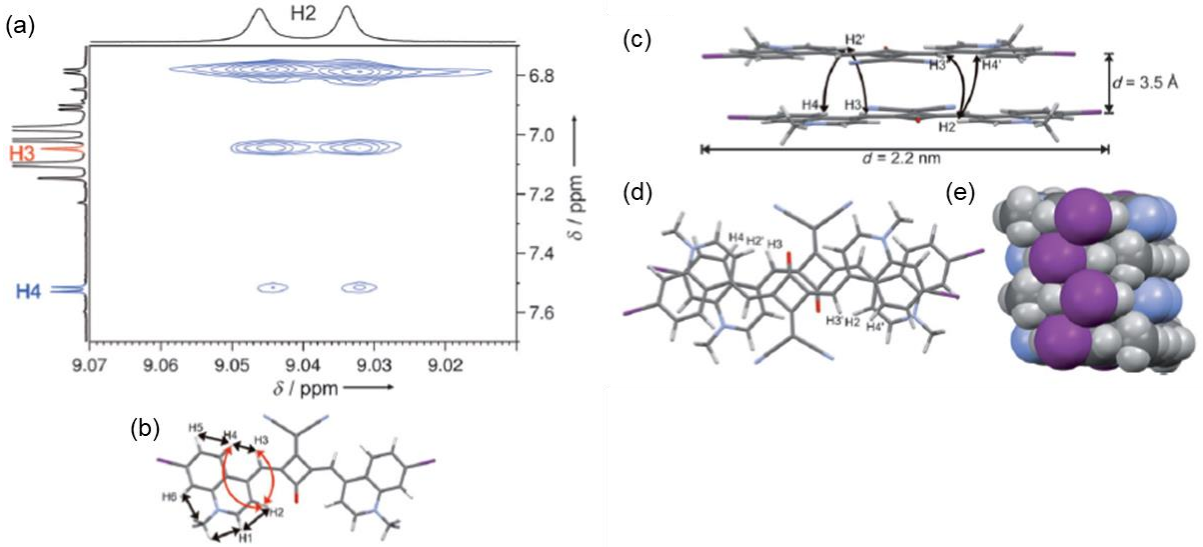

Figure 40. (a) ROESY spectrum of **17d** showing the significant NOE cross-peaks (c = 3 × 10^{-3} M; toluene-d_8; 600 MHz). (b) Calculated molecular structure of **17d** by MM^+ and AM1 methods. The crosspeaks, resulting from *intra*molecular contacts, as observed in the ROESY experiments and which are also observed for monomeric dyes in $CDCl_3$ are indicated by black arrows. Those cross-peaks derived from *inter*molecular contacts, observed only for aggregated dyes in toluene-d_8, are marked with red arrows. (c) Side view of the modeled dimer aggregate of **17d**. The arrows indicate the observed *inter*molecular ROESY and NOESY cross-peaks. (d) Top view of a modeled dimer aggregate of **17d**. (e) Illustration of the proposed π-stacked H-aggregate structure of **17d**. All geometry optimizations were performed at the MM^+ and AM1 levels using HyperChem v8.0.[28] Adapted with permission from Ref. 28. Copyright 2012 WILEY-VCH Verlag GmbH & Co. KGaA.

2.2.3 Aggregation of Squaraines in the Solid State

Organic semiconductor materials have recently attracted great interest for numerous applications since they enable the production of flexible and inexpensive functional building blocks. The main focus is on organic field effect transistors (OFET) and organic solar cells.

Owing to their strong light absorbing properties and the ability to extend the absorption spectrum to the NIR range, squaraine dyes have been widely applied in solar cells. Meanwhile, squaraines are also known to possess semiconductivity in thin films as well as a remarkable photostability under ambient conditions,[22] which is a suitable prerequisite for OFET devices. Since the devices for those applications are fabricated in solid state, aggregation of the squaraine dyes can play a major role in the performances of such devices. For example, aggregation of dye molecules is usually harmful to the photovoltaic conversion process in dye-sensitized solar cells (DSSCs), however, such aggregation behavior can be advantageous for squaraine-based organic photovoltaic (OPV) cells.[94]

In the following section, we summarize several researches that illustrate the relationships between molecular structure, packing motif in the solid state, thin film morphology and the performance of respective devices of the selected squaraine dyes. In addition, we list out some intriguing studies regarding circular dichroism in squaraine thin films.

2.2.3.1 Thin Film Morphology of Squaraines

In 2008, Marks and co-workers have reported the first example of bulk heterojunction (BHJ) solar cells based on squaraine derivatives (**55a**–**b**) as molecular donors and phenyl-C_{61}-butyric acid methyl ester (PCBM) as the acceptor.[95] The absorption of the squaraine films is observed to be broad and cover the 550−900 nm region, where the solar photon flux is at the maximum (Figure 41). Such panchromaticity is beneficial for efficient light harvesting and will be discussed in more details in the next section.

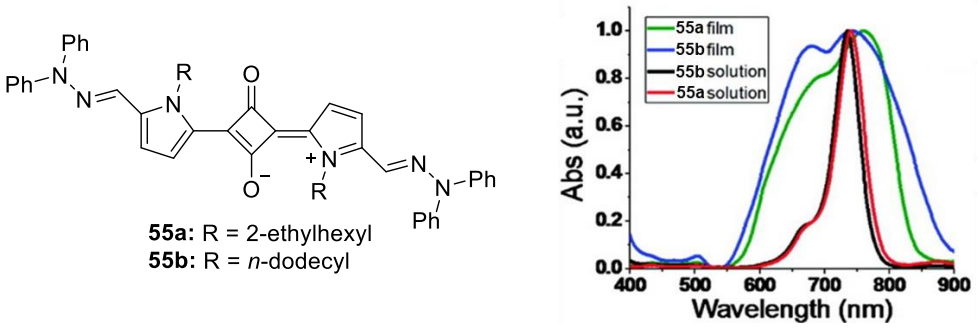

Figure 41. Molecular structure of squaraines **55a**, **55b** and the normalized optical absorption spectra: **55a** (red line) and **55b** (black line) in $CHCl_3$ solutions; **55a** (green line) and **55b** (blue line) as films from $CHCl_3$.[95] Adapted with permission from Ref.95. Copyright 2008 American Chemical Society.

Later on, more in-depth investigations on thin films based on different squaraine-scaffolds have been carried out. A great number of these studies feature anilino-squaraine derivatives[96,97] and

the influences of side chains and hydroxyl groups of these squaraine dyes on material properties.[26e, 98, 99] The results show that despite very small structural differences of the squaraine dyes, they can differ significantly in the molecular packing, which is evident from distinct spectral features of thin films. In addition, processing solvents play a crucial role in the aggregation behaviors.[26e,96] For example, Kido and co-workers systematically examined a series of squaraine dyes **56**–**59** which differ in side chain lengths and number of hydroxyl groups (Figure 42a), thus different absorption spectra of their thin films were observed (Figure 42b). Interestingly, however, all of these show J-aggregation in a $PC_{71}BM$ blended active layer (Figure 42c).[98] They also discovered that the aggregation behavior of squaraine **59** can be controlled *via* processing solvents. Accordingly, low-boiling point solvents led to the J-aggregate state, while the high-boiling point solvents led to H-aggregation. They referred the J-aggregate to the kinetically meta-stable state since it can be trapped and realized in a fast evaporation process.[26e]

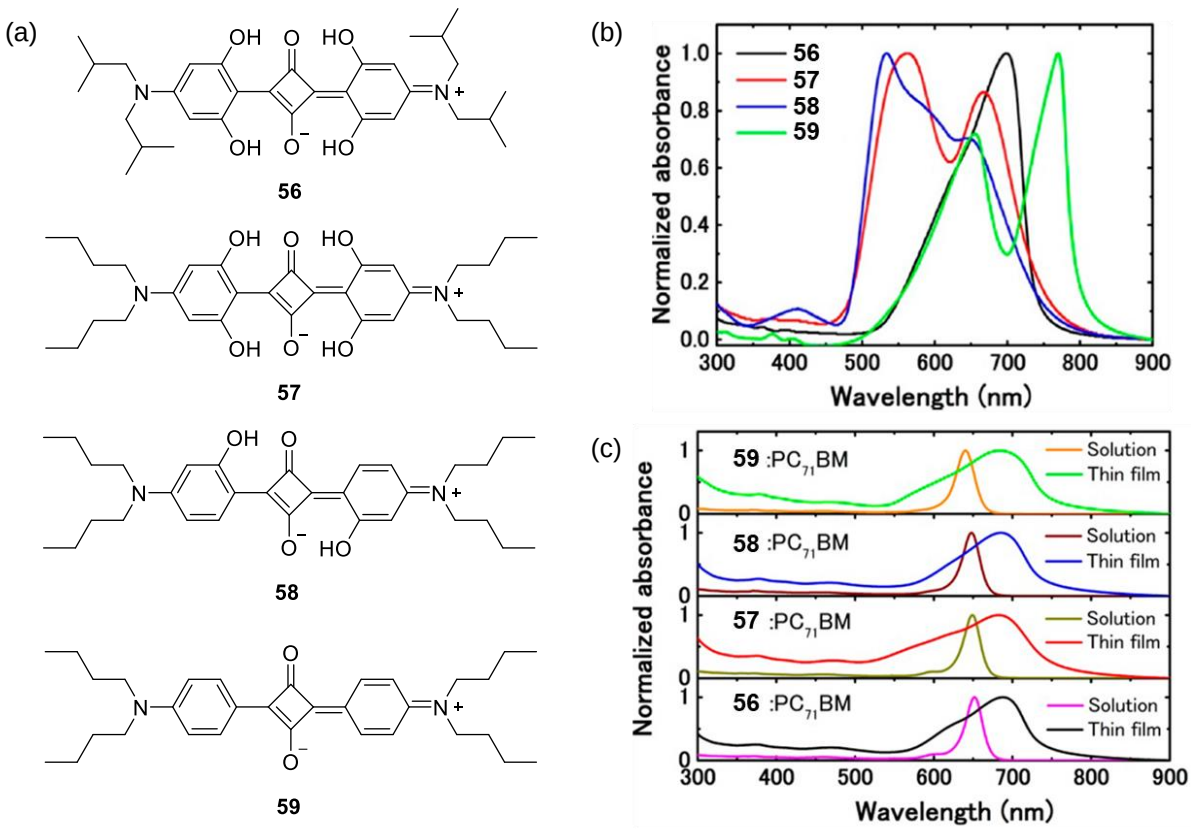

Figure 42. (a) Molecular structures of squaraines **56**–**59**. (b) UV/Vis absorption spectra of **56**–**59** as thin films on quartz substrates. (c) UV/Vis absorption spectra of the squaraine:$PC_{71}BM$ (1:1.5) blends in solution ($c = 1 \times 10^{-5}$ M) and as solid state films.[98] Adapted with permission from Ref. 98. Copyright 2014 American Chemical Society.

Douhal and co-workers have investigated the photophysics of spin-coated thin films of several indole-based *transoid*-squaraines **60**–**65** (Figure 43a). In the absorption spectra of these squaraines, broader bands and red-shifted absorption maxima with respect to the corresponding solution state could be observed along with a blue shifted shoulder (Figure 43b). Notably, the H-type feature (blue shifted shoulder) is more prominent for squaraine **62** and less intense for **60**. The authors concluded that the long alkyl chains in **60** introduce a larger steric hindrance, therefore the formation of face-to-face H-aggregate is less favored.[100]

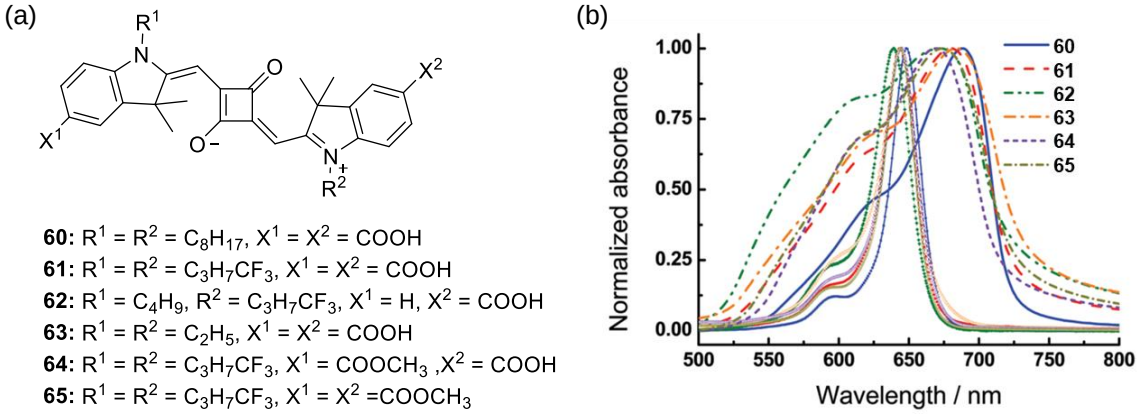

Figure 43. (a) Molecular structures of squaraines **60**-**65**. (b) Normalized UV/Vis steady-state absorption spectra of **60** (solid blue line), **61** (long-dashed red line), **62** (dashed double-dotted green line), **63** (long-dashed dotted line), **64** (short-dashed purple line), and **65** (short-dashed dotted olive line) deposited as thin films on a quartz plate. For comparison, the spectra in MeCN are shown.[100] Adapted with permission from Ref. 100. Copyright 2012 American Chemical Society.

Meerholz, Würthner and co-workers pioneered in the investigation of BHJ solar cells based on dicyanomethylene-substituted squaraines **8** and **15c** (Figure 44a).[26a,b] As mentioned in *Section 2.1.1*, the introduction of dicyanomethylene group leads to a *cisoid*-conformation and a bathochromic shift in the absorption spectra. Despite this mutuality, the molecular structures of squaraines **8** and **15c** exhibit significant differences. Revealed by X-ray analysis of single crystals, the π-backbone of squaraine **8** is bent (Figure 44c), while squaraine **15c**, in contrast, exhibits an almost planar π-skeleton (Figure 44e).[26a] This planarity allows squaraine **15c** to stack in a densely packed "brickwork" arrangement with a closest *inter*planar distance of 3.4 Å (Figure 44f), resulting in pronounced excitonic coupling of the chromophores. Hence, red-shifted and band-broadening is observed in the solid state absorption spectra (dotted and dashed lines in Figure 44g). Remarkably, thermal annealing leads to significantly more red-shifted absorption maxima (dashed line in Figure 44g), indicating more ordered chromophore arrangements.[26a,b] The band broadening and the absorption that expand far into

the NIR region are highly desirable because they enhance the absorption cross section for solar radiation.

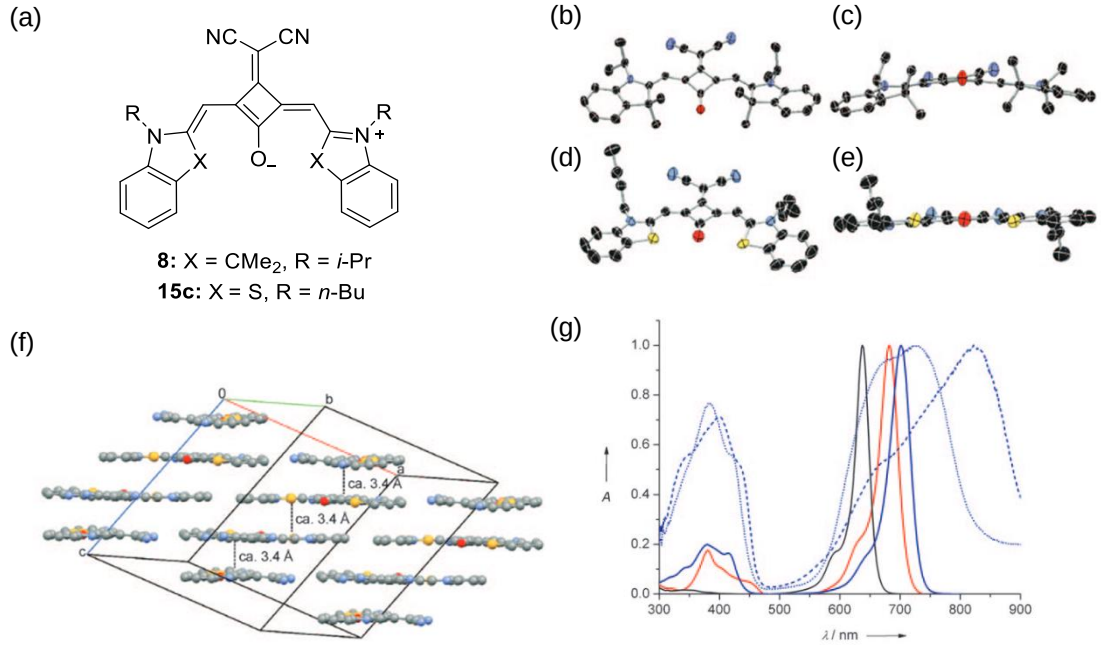

Figure 44. (a) Molecular structures of squaraines **8**, **15c**. (b) Molecular structure and (c) front view of the squaraine plane of **8**. (d) Molecular structure and (e) front view of the squaraine plane of **15c**. Hydrogen atoms, the disorder of one alkyl chain in **15c**, and solvent molecules are omitted for clarity. C: black, N: blue, O: red, S: yellow. (f) Spatial arrangement of **15c** in the crystal lattice (for clarity, only the squaraine π system is shown). (g) UV/Vis absorption spectra of squaraines **6c** (black solid line), **8** (red solid line), and **15c** (blue solid line) in CH_2Cl_2 ($c = 10^{-5}$ M) and of **15c** in films (blue dotted line: as cast; blue dashed line: after annealing at 110 °C for 15 min). Adapted with permission from Ref. 26a. Copyright 2009 WILEY-VCH Verlag GmbH & Co. KGaA.

Subsequently, Würthner and co-workers fabricated organic thin-film transistors (OTFT) by spin coating and solution shearing based on a series of dicyanomethylene-substituted squaraines **15d** and **66**–**68** (Figure 45a). Among them, solution-sheared OTFTs of **15d** perform best with remarkably high hole mobility (0.45 $cm^2\ V^{-1}\ s^{-1}$). The absorption spectra of spin-coated and subsequently annealed thin films of **15d** on quartz substrates exhibit significant red shifts for the lowest-energy transition as compared to those of monomers in solutions (Figure 45b), showing an unambiguous signature of J-type exciton coupling. Next, they investigated the absorption properties of solution-sheared thin films of **15d** since the OTFT performance for solution-sheared devices shows spatial anisotropy. Similar to spin-coated films, a bathochromic shift of the absorption maximum with respect to solution state accompanied by band broadening was observed. As depicted in Figure 45c, rotation of the polarization axis of the incident light from parallel to perpendicular orientation with respect to the shearing direction caused a dramatic drop of the intensity of the long-wavelength band. This was

attributed to the almost parallel alignment of the transition dipole moment and accordingly the long molecular axis of the molecules to the direction of shearing, resulting in the outstanding anisotropic charge-transport behavior in solution-sheared OTFT devices which is absent in spin-coated devices.[25]

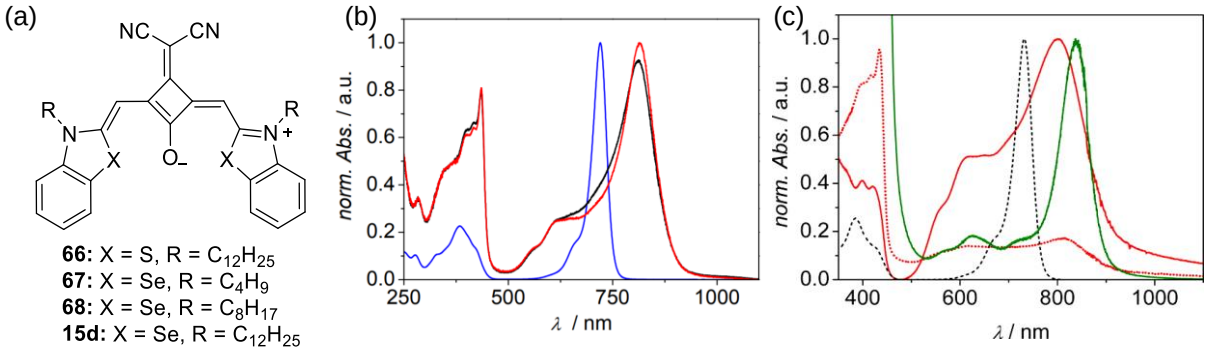

Figure 45. (a) Molecular structures of squaraines **66**–**68**, **15d**. (b) UV/Vis/NIR absorption spectra of thin films on quartz substrates prepared by spin coating from a 10^{-3} M solution of **15d** in chloroform. The spectra of the respective 10^{-5} M solutions in chloroform are shown in blue, the spectra of the as cast films in black, and those recorded after annealing of the spin-coated films (at 130 °C for 10 min under argon) in red. (c) Normalized UV/Vis/NIR absorption spectra of **15d** in *o*-dichlorobenzene solution (black, dashed) and of its solution sheared thin film (red). The thin-film absorbance was measured with linearly polarized light oriented parallel (red solid) and perpendicularly (red dotted) with respect to the shearing direction. For comparison, the normalized UV/Vis/NIR absorption spectrum (green) of a vapor-deposited thin film of **67** on a Si/Al/AlOx/TPA substrate is also shown.[25] Adapted with permission from Ref. 25. Copyright 2014 American Chemical Society.

To sum up, these studies showed that there are three methods to control the aggregation states of squaraine dyes in solid films: (1) molecular structure modification; (2) thermal annealing treatment; (3) variation of the processing solvent.[94] The examples regarding OPVs indicate that J-aggregates are beneficial to OPV applications because the bathochromically shifted, broadened absorption band matches better with the solar spectrum in the red and infrared range. Moreover, due to strong *inter*molecular coupling, J-aggregation provides a potential opportunity to tune the energy levels and charge carrier mobilities of organic thin films.[26b,96,98] Thus, controlling the aggregation behavior of squaraine molecules in solid films plays a crucial role in the advancement of material science.

2.2.3.2 Circular Dichroism in Squaraine Thin Films

Circular birefringence (CB) and circular dichroism (CD) are inherent optical properties of chiral systems from molecular to supramolecular levels. From the perspective of material

science, CD manifests in the differential absorption of left- and right-handed circular polarized (CP) light.[101] This effect can be utilized for light harvesting or emitting devices with direct detectivity[102] or emissivity[103] of CP light, respectively, showing great potential for chiroptical applications. Despite the outstanding photophysical properties of squaraine dyes, researches dealing with their chiral analogues are still limited.[55,63,73,99,101,104,105,106]

In 2017, Schiek and co-workers studied a homochiral L-proline squaraine derivative obtained *via* a facile chiral pool synthesis and accordingly developed a condensed, aggregated material showing H- and J-type spectral features with strong excitonic circular dichroism. They demonstrated the feasibility of inserting the highly circular dichroic active layers into a conventional BHJ photodiode, thus realizing the transfer of molecular chirality to a sizable supramolecular level suitable for thin film device application.[105] The same research team continued with the investigation of such intrinsically circular dichroic materials consist of proline-derived squaraine dyes by synthesizing both enantiopure **(*S*,*S*)-69** and **(*R*,*R*)-69** (Figure 46). Thermal annealing of the spin-casted thin films leads to a giant and sharp excitonic CD signal within the deep-red spectral range located at around 780 nm, which was observed by means of Mueller matrix spectroscopy. Thereby, they claimed a new small molecular benchmark material for the development of organic, technologically applicable thin film based chiroptics.[101]

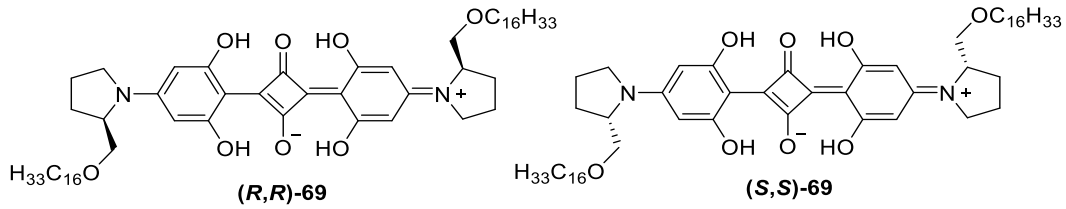

Figure 46. Molecular structures of squaraines **(R,R)-** and **(S,S)-69**.

Inspired by the above reports, Meijer and co-workers designed and synthesized a novel chiral squaraine dye (***S*-70**) and its achiral counterpart (**a-70**). According to the detailed chiroptical studies, the thin films formed by co-assembling the chiral dye with its achiral counterpart exhibit unexpected photophysical properties. The highest CD was not measured for a thin film that contained only enantiopure squaraines, but a co-assembled thin film with only 25% of the chiral dye present in the mixture (Figure 48). This observation indicated that the chiral dye is used solely as a director rather than a structural component. Therefore, the herein presented result emphasizes the impact of supramolecular rather than molecular chirality on material properties.[106]

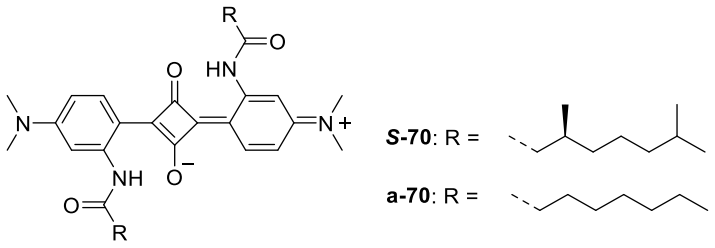

Figure 47. Molecular structures of the chiral ***S*-70** and achiral **a-70**.

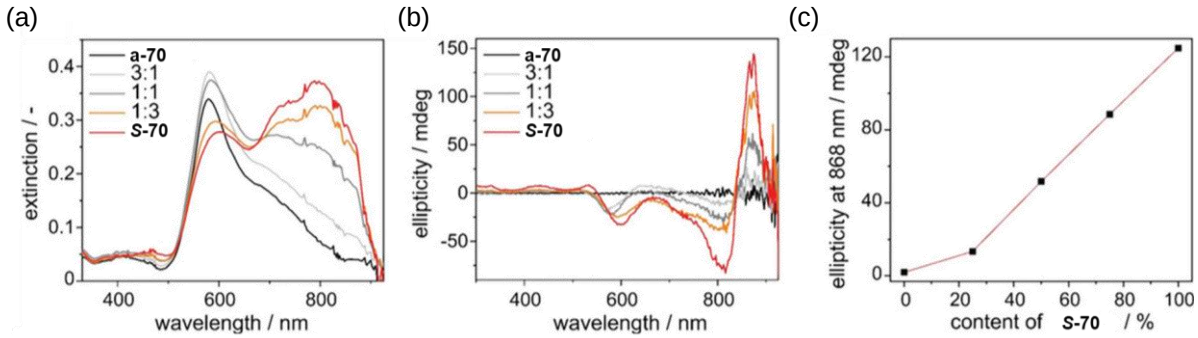

Figure 48. Photophysical properties of thin films prepared from ***S*-70** and **a-70** and mixtures thereof. (a) UV/Vis spectra; (b) CD spectra; (c) variation of the ellipticity with increasing content of ***S*-70** determined at 790 nm. All thin films have a thickness of approximately 40 nm.[106] Adapted with permission from Ref. 106. Copyright 2021 WILEY-VCH Verlag GmbH & Co. KGaA.

2.3 Theoretical Interpretation of the Optical Properties of Dye Aggregates

2.3.1 Exciton Theory

There are numerous methods that can be applied to monitor the self-assembly process of molecules, which enables a quantitative and mechanistic analysis. Among these methods, UV/Vis spectroscopy is a powerful technique especially for functional dyes, as depicted in numerous examples in the previous section. The electronic interaction between the conjugated π-systems often leads to significant changes in absorption spectra.

The observed spectral changes can be explained by the molecular exciton theory introduced by Kasha and McRae in the 1960s.[43] This model describes the electronic interaction between two molecules A and B by a Coulomb coupling of the transition dipole moments. According to the point-dipole approximation, the exciton coupling energy J_{Coul} can be calculated by equation (1)

$$J_{\mathrm{Coul}} = \frac{|\vec{\mu}_{\mathrm{eg}}|^2}{4\pi\varepsilon_0 r_{\mathrm{AB}}^3}(\cos\alpha - 3\cos^2\theta), \qquad (1)$$

where $\vec{\mu}_{eg}$ stands for the transition dipole moment of the monomer, ε_0 is the permittivity of vacuum, and r_{AB} is the distance between the centers of the molecules A and B in the dimer. The angles α and θ are the angle of rotation and the slip angle (Figure 49) through which the rotational or translational offset of the centers of the interacting molecules is described, respectively.

The energy state diagram for the monomer and two Coulombically coupled chromophores are illustrated in Figure 49. ΔE_{vdW} is the contribution of the van-der-Waals interaction to the energy of the ground state and the excited state of the dimer aggregate compared to the monomer. The possible dipole phase relationships for the two arrangements are also shown, where *f* is the oscillator strength which is directly proportional to the square of the transition dipole moment, $|\vec{\mu}_{eg}|^2$. The larger the value of *f*, the more likely is the transition to this energy level, whereas for $f = 0$, the transition is forbidden.

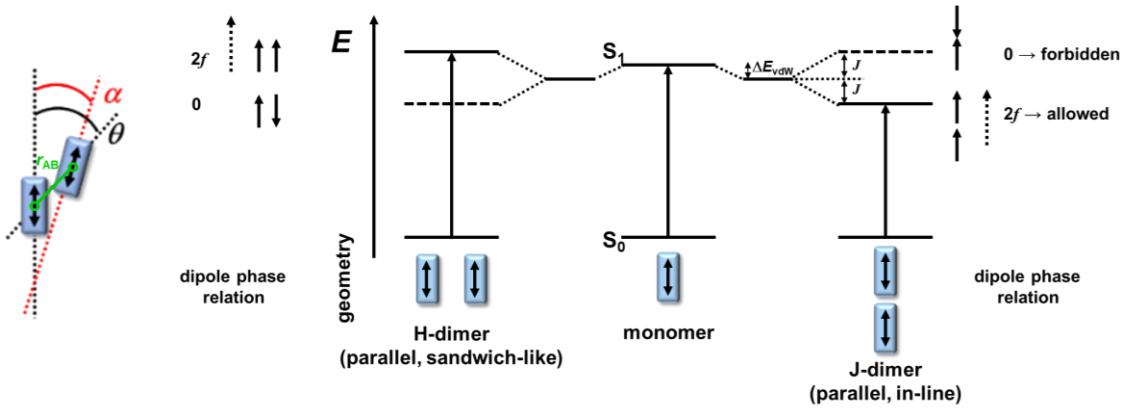

Figure 49. Simplified energy diagram for monomer and dimers with H- and J-type coupling. The geometry and angles α and θ, as well as the dipole phase relations are illustrated.[43b]

For a parallel, sandwich-like arrangement of the transition dipole moments with $\theta = 90°$, the lower exciton state shows an out-of-phase coupling and thus, the transition is forbidden. In contrast, the higher exciton state is characterized by an in-phase coupling, leading to an allowed transition (Figure 49). Accordingly, sandwich-type aggregates with parallel transition dipole moments show a hypsochromic shift of the absorption band with respect to the absorption band of the monomeric chromophores and are referred to as H-aggregates (H denotes hypsochromic). On the other hand, for a parallel, head-to-tail arrangement of the transition dipole moments with $\theta = 0°$, the higher exciton state shows an out-of-phase coupling of the transition dipole moments, resulting in a forbidden transition, whereas the lower exciton state exhibits an in-phase coupling (Figure 49). Thus, the transition to the lower exciton state is strongly allowed.

In consequence, the absorption spectrum shows a bathochromic shift with respect to the absorption band of the monomeric chromophores. These types of aggregates are called Scheibe- or J-aggregates (J denotes Jelley) named after their discoverers Scheibe [107] and Jelley.[108]

In Figure 49, only the two extreme examples of perfectly parallel aligned (α = 0°) chromophores are shown for θ = 90° (H-dimer) and θ = 0° (J-dimer). However, if the slip angle changes continuously from 0° < θ < 90°, at the so-called magic angle (θ = 54.7°), no exciton splitting can be observed regardless of the spatial proximity of the molecules, therefore, no spectral changes are expected (Figure 50a). According to Figure 50a, the maximum exciton coupling energy is higher for J-aggregates and thus should result in a larger spectral shift compared to H-aggregates, which is only true under the assumption of the same center-to-center distance r_{AB} for both types of aggregates. However, the *inter*chromophoric distance is in general smaller for sandwich-type arrangements (i.e., H-aggregates) compared to head-to-tail arranged dyes (i.e., J-aggregates), so that the spectral shift is smaller for J-aggregates. For the case of rotational twist ($\alpha \neq 0°$), as depicted in Figure 50b, the transition to both energy levels is allowed, resulting in a splitting of the absorption band (so-called Davydov splitting).[43]

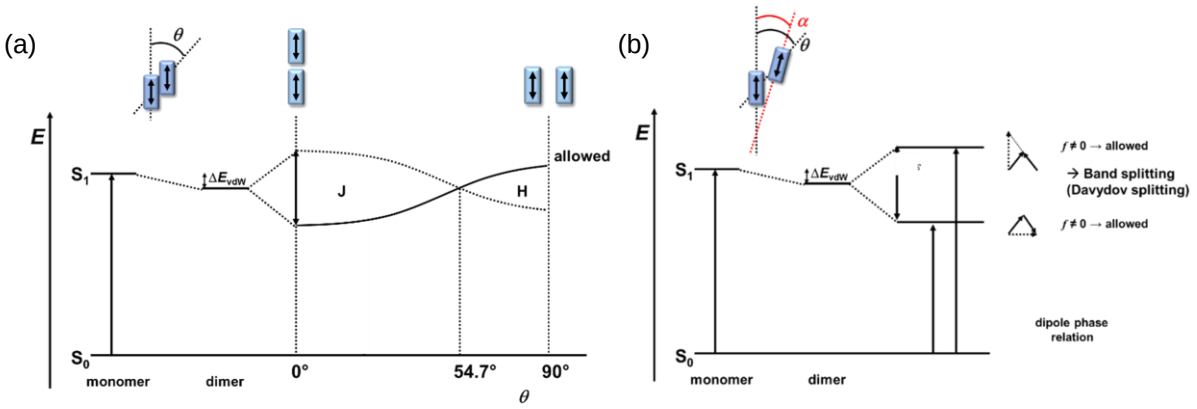

Figure 50. Energy diagram for two Coulombically coupled chromophores (a) with coplanar inclined transition dipole moments under varying slip angle θ, and (b) with oblique ($\alpha \neq 0$) arranged transition dipole moments.[43b]

The above introduced exciton theory provides an efficient and relatively easy approach to explain the optical properties of dye aggregates qualitatively. However, since it is based on several approximations, it often fails to describe the interaction of the dyes properly.[69,109,110] For example, the assumption of point dipoles is in general not justified. Here, the so-called extended dipole model[111] and the concept of transition charges has been introduced for a more

precise calculation of the Coulombic coupling for small interaction distances.[112] Furthermore, the conventional exciton model neglects the wave-function overlap[43b] between the chromophores, which can lead to short-range couplings,[113] which will be discussed in the next section.

2.3.2 Essential States Model (ESM)

In particular for squaraine dyes, however, there is a more severe problem with the exciton model. Thus, several examples of squaraine dye aggregates show broad-band or even panchromatic solid state absorption spectra, where the typical assignments[26b,97,98,99,100] such as "red shift is characteristic of J-aggregates" or "blue shift corresponds to H-aggregates" is not correct, because the spectral shifts result from sources other than excitonic coupling.[113,114]

In contrast to Kasha's exciton theory, the Essential States Model (ESM) pioneered by Painelli and co-workers[115] also accounts for polarizability effects, being crucial for the description of the optical properties of dye aggregates consisting of chromophores composed of alternating donor and acceptor subunits.[110,116] An aforementioned example reported by Belfield and co-workers shows that upon addition of a polyelectrolyte to the solution of the (cationic) squaraine, a strong red-shifted absorption and a complete suppression of fluorescence takes place.[69] This phenomenon can be ascribed to the formation of a "non-fluorescent J-aggregate", which undoubtedly cannot be explained in the scope of the conventional exciton theory. Sissa and co-workers have proven that ESMs support non-fluorescent J-aggregates due to the large polarizability of squaraine molecules.[114c] Moreover, ESM also allows to interpret another unusual type of aggregate, i.e., the red-shifted H-aggregate, which is possible due to a large quadrupole-quadrupole interaction.[110] Therefore, Spano and co-workers have drawn the conclusion that in aggregates of highly polarizable molecules, not only the exciton theory is hardly applicable but that the definition of J- and H-aggregates can be misleading.

Indeed the molecular exciton theory also neglects the possibility of important *inter*molecular charge transfer (ICT) interactions for chromophores at short distances, i.e., π-π stacked geometries, and often considers the dominant Coulombic interactions alone. In 2015, Spano, Collison and co-workers expanded the ESM to include ICT-mediated coupling in order to accurately assign the absorption spectral peaks of squaraine dyes **57** and **71** in the solid state. The good agreement between the simulated and the experimental spectra (Figure 51b) for two symmetric squaraine derivatives confirms that ICT has a major influence on the optical and

electronic properties of squaraine aggregates (Figure 51c), which further accounts for the origin of the strong panchromaticity of these systems.[113] This is also in line with the crystal structure of both dyes, in which the donor moiety of one squaraine is in close proximity to the acceptor moiety of a neighboring squaraine.[117] However, one must notice that not all squaraines exhibit features of ICT. For instance, the monoclinic phase of squaraine **72** crystals exhibits a herringbone packing structure featuring spatially separate donor and acceptor moieties on neighboring molecules, presenting clear evidence of Davydov splitting instead of ICT.[117]

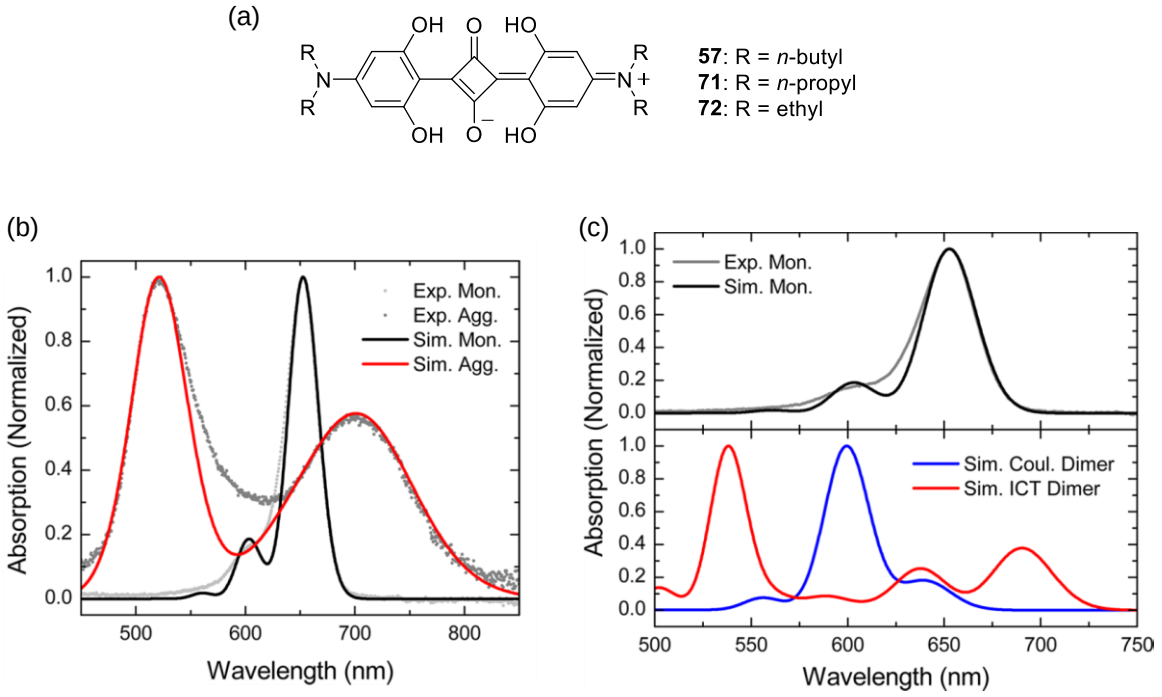

Figure 51. (a) Molecular structure of squaraines **57**, **71**, **72**. (b) Simulated and experimental spectra of **71** aggregates in 50:50 DMSO/H_2O solvent mixtures using the Essential States dimer model including ICT. (c) Simulated monomer (top panel) and dimer aggregate (bottom panel) spectra of **71**. The top panel compares the experimental and simulated monomer spectra in solution.[113] Adapted with permission from Ref.113. Copyright 2015 American Chemical Society.

In conclusion, in the case of squaraine dyes, effects beyond conventional exciton coupling, i.e., polarizability and ICT-mediated coupling in case of pronounced donor-acceptor overlap, have to be considered in order to rationalize the absorption features of the respective aggregates. In this regard, the Essential States Model (ESM) serves as a powerful tool for the investigation of the interaction of the squaraine dyes in the aggregated state. In *Chapter 4*, the application of ESM is presented in assistance of explaining the spectral properties and elucidating the packing models of the aggregate of a novel bis(squaraine) dye in organic solution.

Chapter 3

–

NIR-Emitting Squaraine J-Aggregate Nanosheets

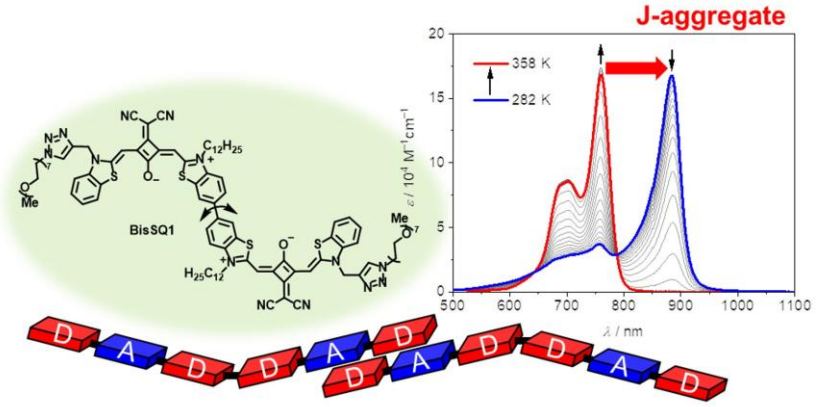

This chapter was published in: C.-A. Shen, F. Würthner,
Chem. Commun. **2020**, *56*, 9878−9881.
Reprinted with permission from reference 118.
Copyright 2020 Royal Society of Chemistry (Great Britain).

Abstract: Click chemistry and Yamamoto coupling afforded an S-shaped π-scaffold composed of two directly connected dicyanomethylene-substituted squaraine dyes. This bis(squaraine) self-assembles into nanosheets in a cooperative self-assembly process, affording an absorption maximum at 886 nm and a fluorescence at 904 nm due to strong J-type exciton coupling.

3.1 Introduction

More than 80 years after their discovery,[107,108] J-aggregates enjoy an ever-increasing popularity. The reason might be that J-aggregates provide the most obvious example for an emergent functionality upon molecular assembly.[20b,119] Thus, depending on the respective dyes, e.g. cyanines,[120] chlorins,[121] bodipys,[122] rylene bisimides,[19,123] squaraines,[81] bathochromic shifts into the NIR spectral range, fluorescence enhancement, light harvesting, and exciton migration are commonly observed and utilized for numerous fundamental studies and applications. Nevertheless, for the supramolecular chemists the required slip-stack arrangement to realize J-type exciton coupling[43b, 124] imposes a challenge because most dyes prefer to stack cofacially,[50] leading to H-aggregates with blue-shifted absorption bands and a quenched fluorescence.[125] Indeed, supramolecular design of J-aggregates remains scarce and presumably the majority of J-aggregates were discovered by serendipity.

With regard to applications and supramolecular design, squaraine dyes[22,24] are particularly promising and indeed for this class of dyes a significant number of functional solid state materials for electronic,[25] photovoltaic[26] photonic[105] and imaging[69] applications take advantage of J-coupled squaraine chromophores. Here, the donor-acceptor-donor sequence implemented in the squaraine π-scaffold directs slip-stacked packing arrangements where donor and acceptor subunits of adjacent dyes are in close π-π-contact (Figure 52, right). Unfortunately, the combined structure-directing impact of electrostatic and charge transfer interactions is obviously too weak compared to dispersion forces to direct the slip-stacked arrangement also for aggregates in solution, that almost exclusively show blue-shifted absorption bands due to the H-type coupling associated with co-facial stacking arrangements (Figure 52, left).[28,55,61] This motivated us to consider more elongated molecules composed of two squaraine dyes. As we will show in the following, self-assembly of bis(squaraine) dye **BisSQ1** indeed affords the highly desired squaraine J-aggregates in solution.

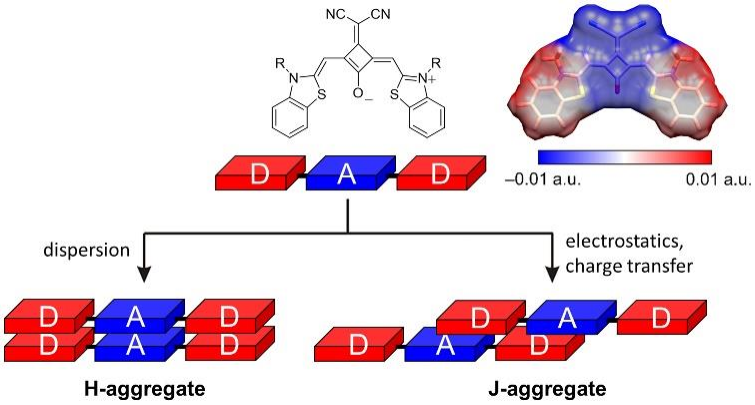

Figure 52. Molecular structure and electrostatic potential energy surface of the squaraine scaffold utilized in this work (top) and packing arrangements (bottom) expected for squaraine dyes from the competition between dispersion (left) and electrostatic plus charge transfer (right) forces, leading to either H- (left) or J-aggregates (right).

3.2 Results and Discussion

3.2.1 Design and Synthesis

The synthesis of bis(squaraine) dye **BisSQ1** is shown in Scheme 7. As a first step, semisquaraine **3** was generated *via* condensation reaction of 1,2-diethoxycyclobutenedione with literature known 2-methyl-3-propargylbenzothiazolium bromide.[88] Compound **3** was further reacted with malononitrile to incorporate the dicyanomethylene moiety, followed by condensation reaction with benzothiazolium salt **5a** to afford the asymmetric squaraine **6a**. Subsequent copper-catalysed click reaction with azide **7** containing a hydrophilic oligoethyleneglycol (OEG) side chain provided amphiphilic squaraine **8a**. Finally, Ni-catalysed Yamamoto coupling afforded the target bis(squaraine) **BisSQ1**. The crude product was purified by recycling gel permeation chromatography (GPC) to give pure **BisSQ1** in a yield of 42%. For details on the synthetic procedures and characterizations of all new compounds, including the monomeric reference dye **SQ1**, see the *Appendix* (*Chapter 9.1*).

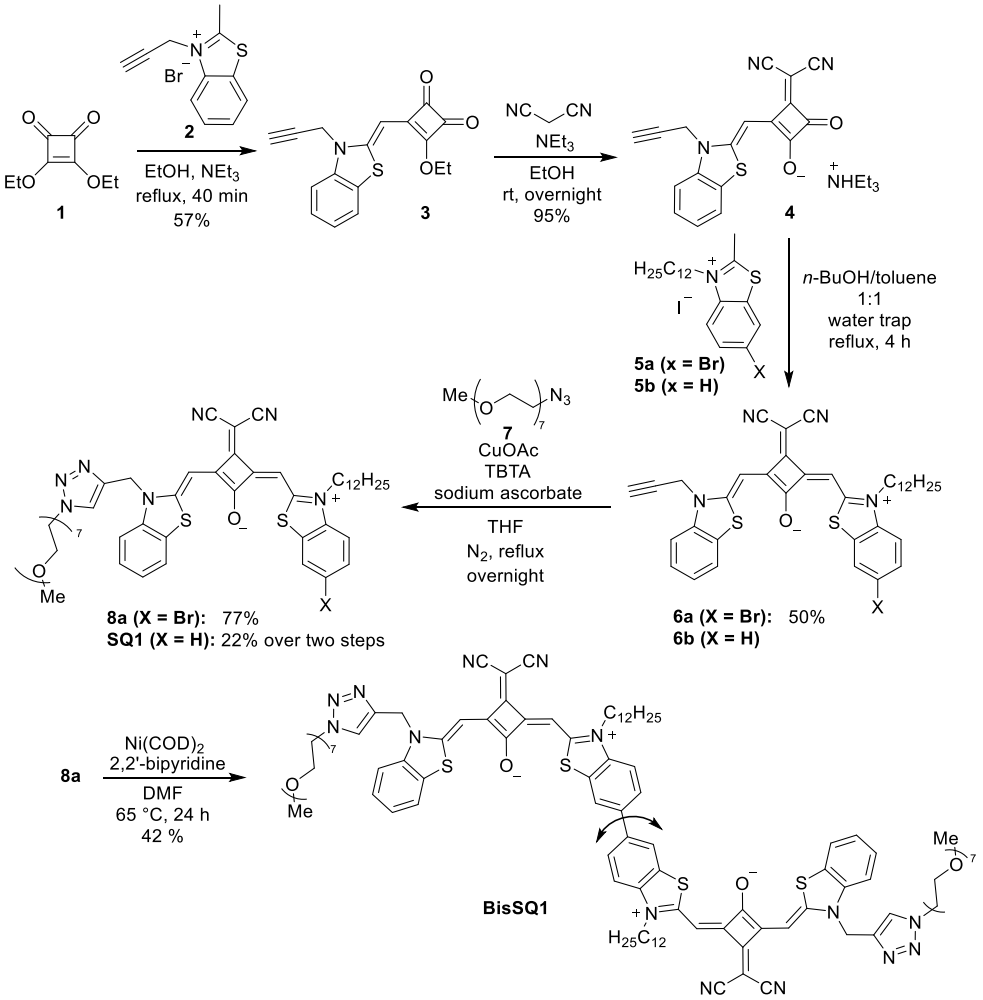

Scheme 7. Syntheses of squaraine **SQ1** and bis(squaraine) **BisSQ1**. TBTA = tris(benzyltriazolylmethyl)amine; THF = tetrahydrofuran; COD = 1,5-cyclooctadiene.

3.2.2 Molecular Optical Properties

The absorption property of **BisSQ1** was first studied under dilute condition ($c_0 = 1 \times 10^{-5}$ M) in $CHCl_3$ to avoid *inter*molecular aggregation. Similar to typical squaraine dyes such as reference dye **SQ1** with C_{2v} symmetry,[27] **BisSQ1** exhibits a characteristic cyanine-like sharp and intense absorption band at long wavelengths and additional absorption bands in the UV region (300 – 450 nm) due to transitions to higher excited states (Figure 53, black line). However, in contrast to the monomeric reference dye **SQ1** with its single sharp absorption peak at $\lambda_{max} = 703$ nm (Figure 53, black dashed line), **BisSQ1** shows two peaks in the long wavelength regime, i.e., a sharp one at $\lambda_{max} = 745$ nm (800 cm^{-1} red-shifted compared to **SQ1**) and a broad one at $\lambda \sim 688$ nm (310 cm^{-1} blue-shifted compared to **SQ1**).

According to earlier reports for related dyes, this spectral feature arises from an equilibrium between *cisoid* folded and *transoid* S-shaped (as depicted in Scheme 7) conformations for such

bis(squaraine) dyes in solution, leading to H-type (blue shift) or J-type (red shift) exciton coupling, respectively.[39,126,127]

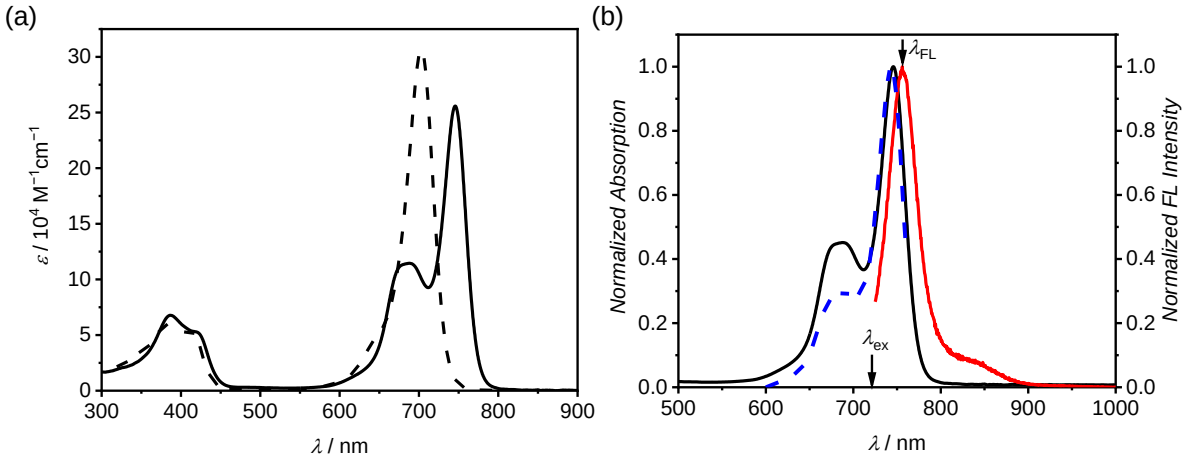

Figure 53. (a) UV/Vis absorption spectra of **SQ1** (dashed black line) and **BisSQ1** (solid black line) in $CHCl_3$ at $c_0 = 1 \times 10^{-5}$ M, 25 °C. The extinction coefficient ε for **SQ1** was doubled for better comparison. (b) Normalized UV/Vis absorption (solid black line), fluorescence (solid red line, $\lambda_{ex} = 720$ nm) and excitation (dashed blue line, $\lambda_{em} = 756$ nm) spectra of **BisSQ1** in $CHCl_3$ at $c_0 = 2 \times 10^{-6}$ M, 25 °C.

The fluorescence spectrum of **BisSQ1** (Figure 53b, red line) exhibits a small Stokes shift (180 cm^{-1}), which is common for dicyanomethylene-substituted squaraines.[27] However, a drastic decrease of the fluorescence quantum yield to 15% can be observed for **BisSQ1** compared to the monomeric squaraine **SQ1** (Table 4). This is in line with the low fluorescence lifetime of 1.06 ns, suggesting a more effective non-radiative decay as obvious from the calculated rate constant k_{nr} (Table 4).

Table 4. Summarized optical data of **SQ1** and **BisSQ1** in $CHCl_3$.

	λ_{max} (nm)	ε_{max} ($M^{-1}cm^{-1}$)	λ_{em} (nm)	$\Delta\tilde{\nu}_{Stokes}$ (cm^{-1})	Φ_{FL}[a] (%)	τ_{FL}[b] (ns)	k_{FL}[c] (10^8 s^{-1})	k_{nr}[c] (10^8 s^{-1})
SQ1	703	150000	724	410	79 ± 0.36	4.78 ± 0.01	1.65 ± 0.01	0.44 ± 0.02
					(81 ± 0.17)		(1.69 ± 0.01)	(0.40 ± 0.01)
BisSQ1	745	255000	756	180	14 ± 0.18	1.06 ± 0.01	1.32 ± 0.03	8.11 ± 0.12
					(19 ± 1.5)		(1.79 ± 0.16)	(7.64 ± 0.25)

[a] Fluorescence quantum yield was determined by a calibrated integrating sphere system. The value corrected from re-absorption are given in brackets (see *Appendix, Chapter 9.1*).

[b] τ_{FL} was determined by tail fit analysis of the data obtained from time-correlated single photon counting measurements with ps laser diode at 670 nm using a magic angle setup.

[c] Determined according to $k_{FL} = \Phi_{FL}/\tau_{FL}$ and $k_{nr} = 1/\tau_{FL} - k_{FL}$. The value calculated from corrected QY is given in brackets.

3.2.3 Self-Assembly Studies

In order to trigger *inter*molecular aggregation, solvents with low polarity are favored.[30] Accordingly, temperature-dependent UV/Vis measurement was carried out in the solvent mixture of toluene/1,1,2,2-tetrachloroethane (TCE) = 98:2 (*v*/*v*). A solution of **BisSQ1** with the concentration of 5 × 10^{-6} M was heated from 282 K to 358 K.‡ At high temperature (*T* = 358 K), the absorption spectrum (red line in Figure 54a) exhibits an absorption maximum at 760 nm and a band shape similar to those observed in the better solubilizing solvent chloroform at room temperature (Figure 53a, black line). In contrast, at low temperature (*T* = 282 K), a largely red-shifted band at λ_{max} = 886 nm is observed (blue line in Figure 54a), indicating a pronounced J-type exciton coupling due to *inter*molecular aggregation. This red-shift of 1870 cm^{-1} compared to the dissociated state for **BisSQ1** in the same solvent at 358 K is indeed among the largest shifts observed for J-aggregates. Compared to the monomeric reference dye **SQ1** the shift is even larger (2680 cm^{-1}). Notably, a defined isosbestic point is present at 788 nm, revealing an equilibrium between only two species.

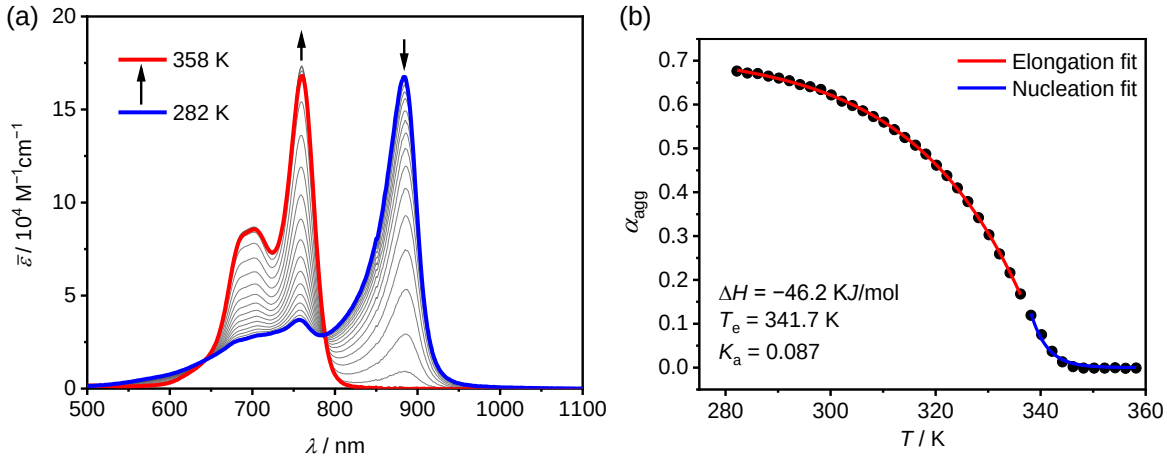

Figure 54. (a) Temperature-dependent UV/Vis spectra of **BisSQ1** in toluene/TCE 98:2 (*v*/*v*) at c_0 = 5.0 × 10^{-6} M, 282 – 358 K. The arrows indicate the spectral changes with increasing temperature. (b) Plot of fractions of aggregate at 886 nm against temperature and fitting with the nucleation-elongation model.[128]

The degree of aggregation was calculated from the experimental data at 886 nm and plotted against the temperature (for details, see *Appendix*, *Chapter 9.1*). To analyse the self-assembly process, we have made use of the nucleation-elongation model of Meijer, Schenning and Van der Schoot.[128] For temperatures below the elongation temperature, we could accurately fit the experimental data to the elongation regime (Figure 54b) with R^2 = 0.9998. At the given concentration of 5 × 10^{-6} M, the enthalpy release during the elongation process (ΔH_e) and the elongation temperature (T_e) were calculated to be −46 KJ/mol and 342 K, respectively. For

temperatures above the elongation temperature, the dimensionless equilibrium constant K_a of the activation step at the elongation temperature was estimated to be 0.087. The low value of this constant is suggestive of a high degree of cooperativity for this self-assembly process.[129] The same spectral changes could also be observed in concentration-dependent experiments, where dilution from $c_0 = 1 \times 10^{-4}$ to 2×10^{-7} M at 298 K led to a transition from aggregated to monomeric species (Figure S6). The experimental data could be properly fitted with the cooperative K_2/K model,[93] where the results are in good agreement with the temperature-dependent measurements (for detailed analysis, see *Appendix*, *Chapter 9.1*).

Since the UV/Vis measurements imply the formation of aggregates with strong J-type coupling which are expected to exhibit a non-forbidden, i.e., fluorescent, lowest excited state, we investigated the emission properties of the **BisSQ1** aggregate. As shown in Figure S8, indeed a weak emission was detected at 904 nm (λ_{ex} = 820 nm, $\Delta\tilde{\nu}_{Stokes}$ = 225 cm^{-1}). It is important to point out that the monomeric state does not absorb at 820 nm; therefore, only the aggregated state was excited. To further confirm the origin of the emission, an excitation spectrum was recorded (Figure S8, dashed blue line, λ_{FL} = 1000 nm) where no contribution from the monomeric state exists. Despite the distortion of the band shape due to some inevitable re-absorption in order to realize a fully aggregated state, the maximum of the excitation curve agrees well with the absorption curve. Namely, by exciting only the aggregated state, an emission takes place, confirming the J-aggregate excitonic characteristic.[130]

3.2.4 Structural Investigation

To gain further insight into the aggregate structure, we performed diffusion ordered spectroscopy (DOSY) NMR measurements in solution. However, a clear interpretation of the data was not possible due to an aggregate size distribution (for details, see *Appendix*, *Chapter 9.1*). Therefore, atomic force microscopy (AFM) measurements were carried out. Toward this goal, a solution of **BisSQ1** in toluene/TCE (98:2, *v*/*v*) with a concentration of 2×10^{-5} M was spin-coated onto highly ordered pyrolytic graphite (HOPG) substrate, leading to sheet-like aggregates (Figure 55a, b) with a height of 2.2 ± 0.1 nm (Figure 55c). This is in good agreement with the dimension of the molecules considering the flexibility of the side-chains (Figure S13). The width of the thin sheets varies between 10−40 nm, while the length reaches up to 200 nm. Notably, similar morphology could be observed on silica wafer and hydrophilic mica surfaces (Figure S11), indicating that the structure is not influenced by

the substrates. Based on the experimental data obtained from UV/Vis and AFM measurements, we propose the packing model for the **BisSQ1** nanosheets shown in Figure 55d.

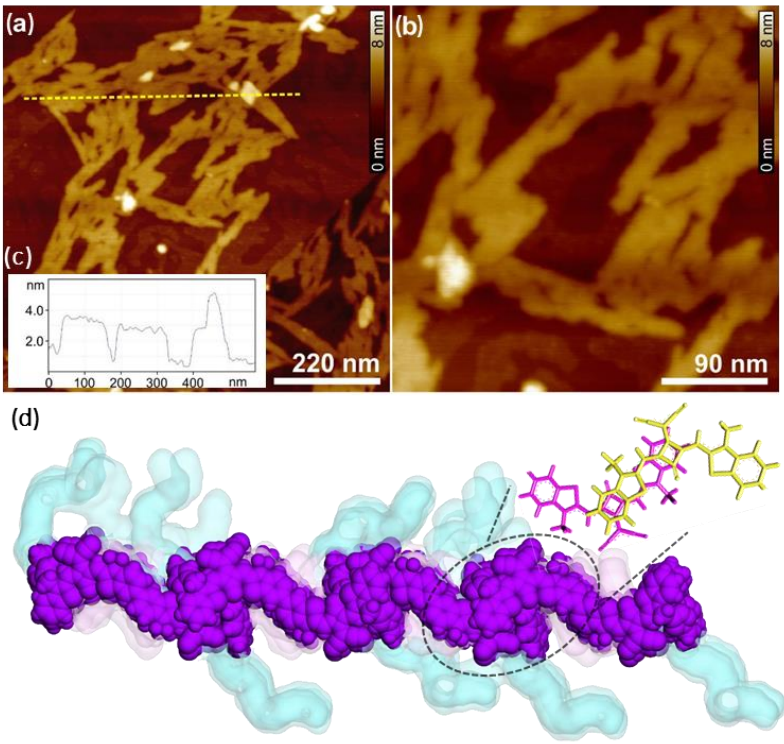

Figure 55. Height (a,b) AFM images of sample **BisSQ1** prepared by spin-coating of toluene/TCE 98:2 (*v*/*v*) solution on HOPG. *Z* scale is 8 nm. Image (c) shows the cross-section analysis from yellow dashed line in image (a) and (d) a tentative packing model with hydrophobic squaraines in violet and hydrophilic oligoethyleneglycol chains in cyan.

Although our packing model is only tentative, it fairly well explains the strong red-shift of the absorption band due to the slip-stacked packing arrangement of **BisSQ1** molecules (Figure 55d) and the formation of lamellar sheets consisting of the hydrophobic S-shaped **BisSQ1** molecules and hydrophobic alkyl chains and the stabilization of this nanosheet against precipitation in the given solvent by solubilizing oligoethyleneglycol chains protruding above and below the sheet into the solvent phase.

Indeed, this two-dimensional sheet structure formation may be considered as a major outcome of our study. Thus, whilst one-dimensional aggregation of squaraines is typically governed by dispersion forces, thereby affording co-facially stacked dyes with H-type coupling, two-dimensional aggregation as directed with our concept of extended bis-chromophores provides J-aggregates. This is most likely induced by the structural distortion between the chromophores with a similar brickwork type organization as observed in many thin film

squaraine aggregates.[25,26,105] We also like to emphasize that the aggregation process in our study was accomplished in an organic solvent and not in water, where hydrophobic effects play an important role and for which indeed some larger colloidal squaraine aggregates showed J-type features.[63,68,70,81] In a particular nice but rather special case Belfield and co-workers could direct such J-aggregation by the interaction of appended cationic pyridinium units by templating with polyanionic poly(acryclic acid).[69]

3.3 Conclusions

In conclusion, we have introduced a very simple but efficient approach to direct squaraine dye aggregation in solution from the very common cofacial stacking leading to H-type exciton coupling to the more desired slip-stacked packing leading to J-type exciton coupling by simply connecting two dyes in a head-to-tail bis-chromophore structure. It will be interesting to see if this simple concept can be applied also to other squaraines or even to entirely different chromophores.

‡Aggregation of reference dye **SQ1** is too weak to be observed in our comparative concentration-dependent experiments (see Figure S4 in the *Appendix*, *Chapter 9.1*).

Chapter 4

–

Polymorphism in Squaraine Dye Aggregates by Self-Assembly Pathway Differentiation: Panchromatic Tubular Dye Nanorods versus J-Aggregate Nanosheets

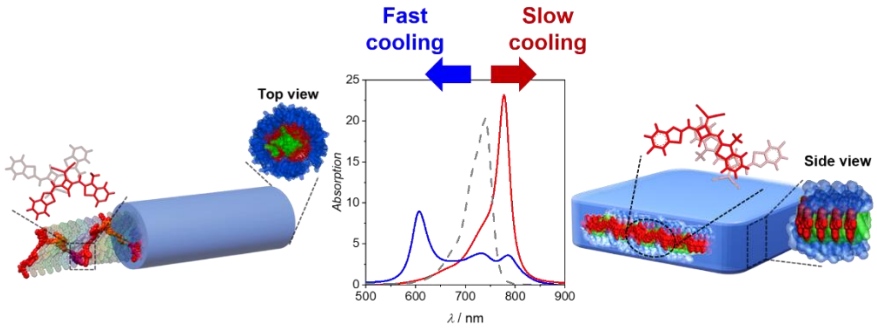

This chapter was published in: C.-A. Shen, D. Bialas, M. Hecht, V. Stepanenko, K. Sugiyasu, F. Würthner, *Angew. Chem. Int. Ed.* **2021**, DOI: 10.1002/anie.202102183.

Reprinted with permission from reference 131.
Copyright 2021 WILEY-VCH Verlag GmbH.

Abstract: A bis(squaraine) dye equipped with alkyl and oligoethyleneglycol chains was synthesized by connecting two dicyanomethylene substituted squaraine dyes with a phenylene spacer unit. The aggregation behavior of this bis(squaraine) was investigated in non-polar toluene/tetrachloroethane (98:2) solvent mixture, which revealed competing cooperative self-assembly pathways into two supramolecular polymorphs with entirely different packing structures and UV/Vis/NIR absorption properties. The self-assembly pathway can be

controlled by the cooling rate from a heated solution of the monomers. For both polymorphs, quasi-equilibrium conditions between monomers and the respective aggregates can be established to derive thermodynamic parameters and insights into the self-assembly mechanisms. AFM measurements revealed a nanosheet structure with a height of 2 nm for the thermodynamically more stable polymorph and a tubular nanorod structure with a helical pitch of 13 nm and a diameter of 5 nm for the kinetically favored polymorph. Together with wide angle X-ray scattering measurements, packing models were derived: the thermodynamic polymorph consists of brick-work type nanosheets that exhibit red-shifted absorption bands as typical for J-aggregates, while the nanorod polymorph consists of eight supramolecular polymer strands of the bis(squaraine) intertwined to form a chimney-type tubular structure. The absorption of this aggregate covers a large spectral range from 550 to 875 nm, which cannot be rationalized by the conventional exciton theory. By applying the Essential States Model and considering *inter*molecular charge transfer, the aggregate spectrum was adequately reproduced, revealing that the broad absorption spectrum is due to pronounced donor-acceptor overlap within the bis(squaraine) nanorods. The latter is also responsible for the pronounced bathochromic shift observed for the nanosheet structure as a result of the slip-stacked arranged squaraine chromophores.

4.1 Introduction

Dye aggregates and color pigments provide the most striking examples for the emergence of new properties originating from *inter*molecular electronic couplings between molecular building blocks as a function of their supramolecular organization.[20b,132] This interrelation is most evident for polymorphic states of a particular molecule, i.e., aggregates or solid state materials assembled by the same molecule in different packing arrangements. Whilst polymorphism in dye aggregates is still a rather new and accordingly less explored phenomenon, there is a long history of polymorphism in color pigments. Indeed, many of the commercially important colorants utilized as color pigments exist in different polymorphic forms with sometimes striking differences in color, shade, lightfastness, weather-fastness, dispersability, etc.[133] This is impressively highlighted by the most important industrial color pigment copper phthalocyanine (CuPc) for which meanwhile ten polymorphs have been identified. The most useful ones are the greenish blue β-form, which provide a perfect cyan shade for color printing applications, the reddish blue α-form used primarily in paints and the most reddish ε-form used in paints and blue color filters in LC displays.[134] Unsurprisingly, the

performance of thin film transistors based on CuPc are also highly dependent on the packing arrangement accomplished by the respective processing conditions and the choice of the substrate. [135] Accordingly, CuPc pigments provide a perfect example how packing arrangements determine functional properties.

Compared to the mature field of color pigments, studies on polymorphism in dye aggregates are at the infant stage. Firstly, because the number of examples for polymorphic dye aggregates is still rather limited.[17c,136,137] Secondly, because the packing arrangements in dye aggregates cannot be determined unambiguously like for their crystalline counterparts by single crystal X-ray crystallography and therefore correlations between structural and functional properties remain often rather speculative. Presumably the most profound studies in this regard exist for the class of perylene bisimide dye aggregates for which the impact of long-range Coulomb and short-range charge transfer coupling has been elaborated in depth and with this knowledge, packing arrangements could be deduced based on UV/Vis absorption spectra.[138]

This situation is, however, entirely different for squaraine dyes that constitute a most interesting class of dyes with regard to applications as they can provide cyanine-like intense and narrow absorption in the red part of the visible light spectrum along with strong fluorescence.[22] Furthermore, they show applicability as histological probes and in bioimaging,[23a] excellent p-type semiconductivity in organic thin-film transistors[25] or solar cells,[26] giant circular dichroism in thin films,[101,105] as well as a plethora of sensing applications in supramolecular host-guest systems.[24] However, despite of this broad variety of applications, self-assembly of squaraines into dye aggregates remains less explored[28,55,56,63,69,139] and the relationship between packing structure and functional properties is often rather promiscuous for squaraine aggregates. Indeed, only most recently Spano and co-workers could unveil the origin of quite unusual absorption spectra of these dyes in thin films that strongly deviated from the expectations based on the common J- and H-aggregate molecular exciton model.[114c]

Motivated by previous success in the non-covalent synthesis of structurally defined rod- and fiber-like dye aggregates by the self-assembly of suitably tethered bis-chromophores,[29a,140] we recently initiated a research program to explore the supramolecular polymerization of bis(squaraine) dyes **BisSQ1** and **BisSQ2**, in which two dicyanomethylene squaraine chromophores are covalently linked either directly or *via* a phenylene spacer unit, respectively (Chart 1). Aliphatic and hydrophilic side chains were attached to enhance microphase segregation. Interestingly, whilst **BisSQ1** self-assembly afforded only one type of dye aggregate that consists of a nanosheet structure with slip-stacked packing arrangement of the

dyes and concomitant J-type exciton coupling,[118] our in-depth UV/Vis/NIR spectroscopic analysis of **BisSQ2** reveals the formation of two dye aggregate polymorphs with entirely different morphologies, i.e., nanorod and nanosheet, as well as optical properties, i.e., panchromatic and red-shifted absorption bands, respectively. Based on a combined effort by experimental work (microscopy and X-ray scattering) and theoretical calculations, we were able to derive reliable packing models for both polymorphs and to establish structure-function relationships. Most importantly, whilst the coloristic properties of the red-shifted nanosheet aggregate polymorph can be explained by the conventional molecular exciton model,[43b] the panchromatic absorption spectrum for the tubular polymorph requires a more sophisticated treatment by the Essential States Model[115] taking into account *inter*molecular charge transfer interactions arising from the donor-acceptor overlap between the chromophores in the aggregated state.

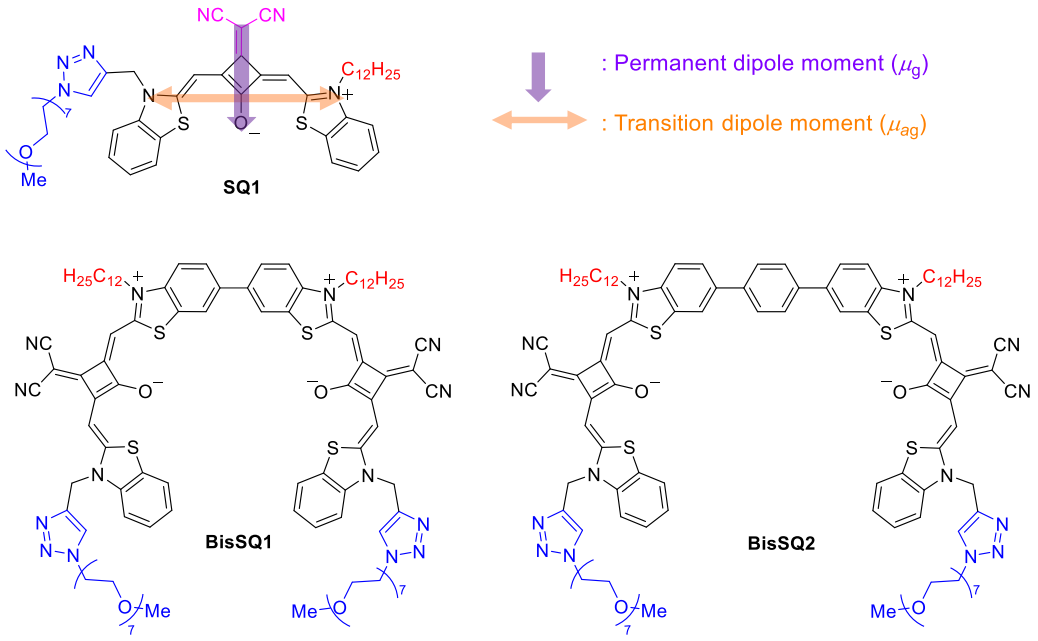

Chart 1. Chemical structure of reference squaraine **SQ1** and bis(squaraine) dyes **BisSQ1**[118] and **BisSQ2** with graphical illustration of the orientation of the permanent and transition dipole moments, indicated by purple and orange arrow, respectively.

4.2 Results and Discussion

4.2.1 Synthesis and Molecular Properties

BisSQ2 was synthesized following the route shown in Scheme 8. Suzuki coupling reaction of compound **8a**[118] with 1,4-benzenediboronic acid bis(pinacol) ester (**11**) afforded the target bis(squaraine) **BisSQ2**. The crude product was purified by recycling gel permeation

chromatography (GPC) to give the pure **BisSQ2** in a yield of 23%. For details on the synthetic procedures and characterizations of all new compounds, see *Appendix* (*Chapter 9.2*).

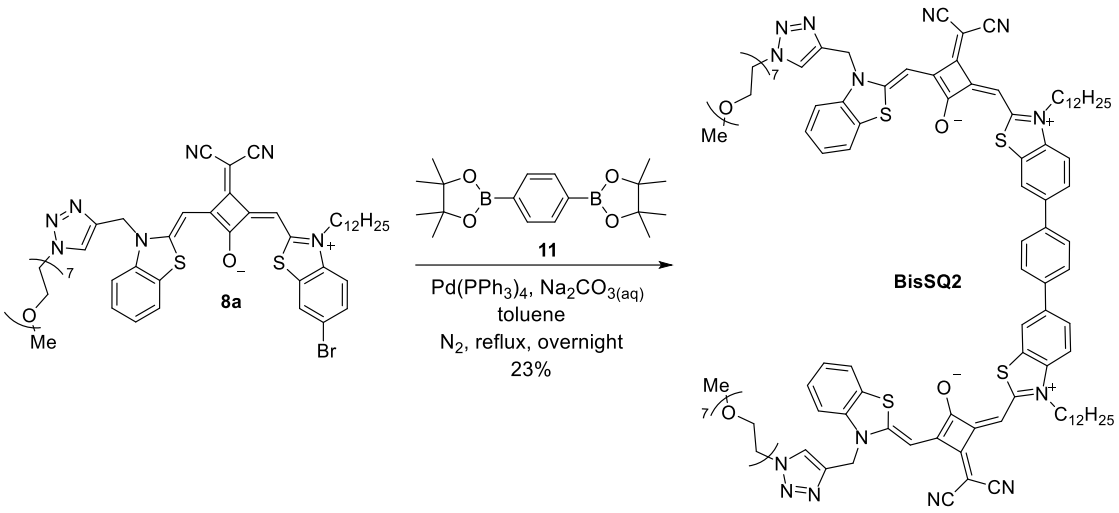

Scheme 8. Synthesis of bis(squaraine) **BisSQ2**.

The absorption band of monomeric **BisSQ2** is broader and slightly red shifted (λ_{max} = 726 nm in $CHCl_3$, Figure S28c, green line) in comparison with the one of **SQ1** (λ_{max} = 703 nm), which is attributable to the conformational flexibility due to the rotation around the phenyl-phenyl bonds in the spacer unit. Hence, various mutual arrangements of the chromophores exist in solution, which in turns leads to different electronic interactions, and thus a broadening of the absorption band.[39,127] Like that of **SQ1**, fluorescence spectrum of **BisSQ2** exhibits a small Stokes shift (260 cm^{-1}) and a mirror image behavior with its absorption spectrum (Figure S29b). However, a significant decrease in the fluorescence quantum yield to 42% and a reduced fluorescence lifetime of 3.01 ns in comparison to **SQ1** (79% and 4.78 ns, respectively) are observed. Our analysis of radiative (k_{FL}) and non-radiative (k_{nr}) decay constants suggests a more effective non-radiative decay originating from the conformational flexibility in **BisSQ2** (Table S2). It is noteworthy that the excitation spectrum of **BisSQ2** resembles the absorption spectrum (Figure S29b), which indicates that the various emissive states resulting from the different conformations are close in energy.

4.2.2 Self-Assembly into Supramolecular Polymers

In order to trigger *inter*molecular aggregation driven by dispersion and dipolar interactions, solvents with low polarity are required.[30,141] Therefore, we have performed aggregation studies for **BisSQ2** in a solvent mixture of toluene/1,1,2,2-tetrachloroethane (TCE) = 98:2 (*v*/*v*). TCE

was used as an additive to increase the solubility of **BisSQ2** in order to cover a broad concentration range. The sample solution was prepared by dissolving **BisSQ2** in TCE first and then diluting with toluene. After heating the as-prepared solution (toluene/TCE 98:2, $c_0 = 2.5 \times 10^{-5}$ M) to 85 °C for 20 minutes to achieve a fully monomeric state (Figure 56, gray dashed curve) and cooling it down to 25 °C, different spectral features are observed depending on the cooling rate. Rapid cooling, i.e., transferring the hot solution immediately into a pre-cooled chamber at 25 °C, leads to the formation of a broad band feature with absorption maxima at 605, 737, and 783 nm (Figure 56, blue curve); hereafter, this aggregate is denoted as **BisSQ2-AggI**. In contrast, slow cooling (cooling rate = 2 °C/min) apparently resulted in a different outcome as suggested by the formation of precipitates. To disperse the precipitates, we applied sonication and measured its absorption spectrum: a bathochromically shifted sharp absorption band (λ_{max} = 780 nm, *FWHM* = 420 cm^{-1}) with respect to the monomeric state (λ_{max} = 739 nm) was observed (Figure 56, red curve). This result indicates the formation of J-type aggregates, which we refer to as **BisSQ2-AggII**. We note that a similar spectrum was observed for a solution before the sonication, although absorbance was smaller because of the precipitation (Figure S32b, blue curve). Thus, we infer that the applied sonication does not lead to dissociation or a new aggregate species.[17c,136c,142] The distinct absorption spectra briefly indicates that a supramolecular polymorphism occurs depending on the cooling rate.

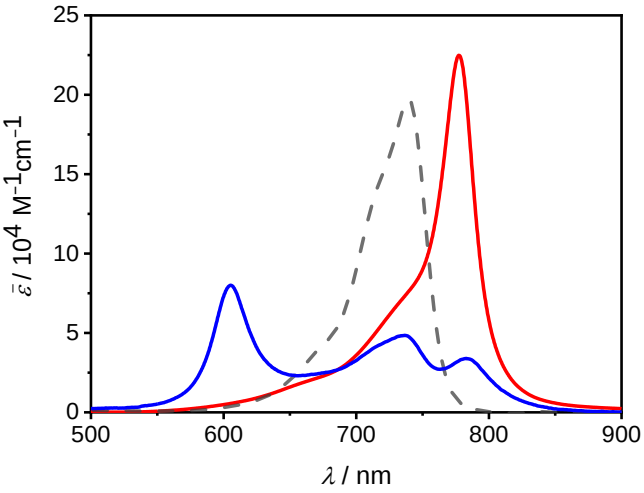

Figure 56. UV/Vis/NIR spectra of a solution of **BisSQ2** ($c_0 = 2.5 \times 10^{-5}$ M, toluene/TCE 98:2) at 85 °C (gray) and those at 25 °C obtained upon rapid cooling (blue: **AggI**) and slow cooling (red: **AggII**). Because precipitation happened during the sample preparation by slow cooling, ultra-sonication was applied for 20 minutes to the solution to disperse the precipitate prior to the measurement.

4.2.3 Structural Insights and Packing Model

To gain deeper insight into the structural features of the **BisSQ2** aggregates, atomic force microscopy (AFM) measurements were performed. A solution of **BisSQ2-AggI** in toluene/TCE (98:2, *v*/*v*) with a concentration of 2.5×10^{-5} M was spin-coated onto a silica wafer (SiO_x); we observed stiff helical rod-like aggregates with lengths up to 1.5 µm, a well-defined diameter of 5.0 ± 0.2 nm, and both left- (*M*) as well as right- (*P*) handedness (Figure 57a-c). The helical pitch was measured to be 13 ± 1 nm (Figure 57d). These results suggest the presence of a complex internal structure consisting of multiple **BisSQ2** units to form the nanorods.[143]

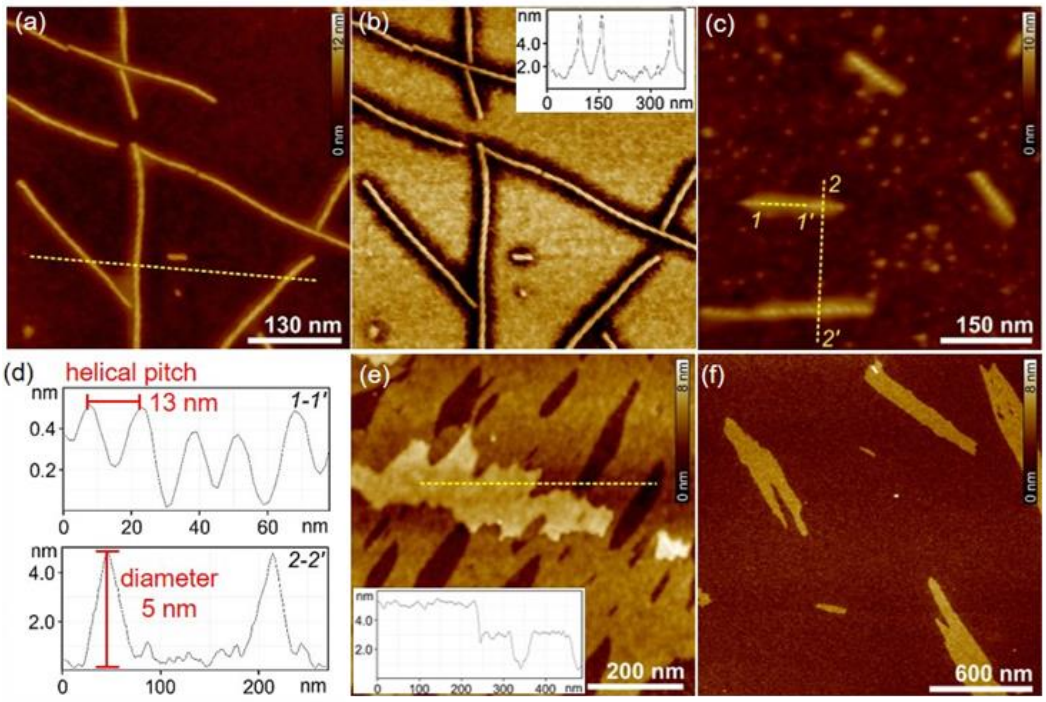

Figure 57. (a) Height (*Z* scale = 12 nm) and (b) phase AFM images of **BisSQ2-AggI**; inset: the cross-section analysis from yellow dashed line in image (a). (c) Height (*Z* scale = 10 nm) AFM image of **BisSQ2-AggI**. (d) Cross-section analyses from the yellow dashed lines 1-1' and 2-2' in image (c). (e) Height AFM image of **BisSQ2-AggII**; inset: the cross-section analysis from yellow dashed line in image (e). (f) Height AFM image of **BisSQ2-AggII** (solution sonicated for 30 sec). *Z* scale is 8 nm for both (e) and (f). All samples for AFM measurements were prepared by spin-coating of toluene/TCE 98:2 solutions of **BisSQ2** ($c_0 = 2.5 \times 10^{-5}$ M) on SiO_x with 2000 rpm.

Interestingly, **BisSQ2-AggII** showed a significantly different morphology. Multi-layers of two-dimensional sheet-like structures with height of 2.1 ± 0.2 nm and widths up to 1 µm are observed (Figure 57e). Such large-sized aggregates are in line with the observation of the precipitation. We have also performed AFM studies on the **BisSQ2-AggII** solution that was

treated by ultra-sonication for 30 seconds. Similar sheet-like structures are visible on the substrate (Figure 57f), corroborating that sonication can fragment the precipitates into small pieces and disperse them in solution but does not change the aggregation mode of **BisSQ2**.

To gain further information about the aggregate structure, X-ray scattering techniques were applied. A thick film was prepared on aluminum foil by slow evaporation of a concentrated solution of **BisSQ2-AggI** (5 g L^{-1} in toluene/TCE = 98:2). Figure 58a depicts the wide and small angle X-ray scattering (WAXS and SAXS) diagram of the film. The diffuse halo in the wide-angle region corresponds to the liquid-like disordered structure of the surrounding alkyl chains. The observed peaks indicate a hexagonal columnar arrangement of rods in the solid state with an *inter*columnar distance of 6.22 nm, which is in good agreement with the rod diameter of 5 nm as determined by AFM measurements (Figure 57d). In contrast, for a thick film drop-casted from a concentrated solution of **BisSQ2-AggII** onto an aluminum foil, the X-ray scattering diagram shows a completely different pattern. Equidistant signals can be observed (labelled as 001 – 004 in Figure 58b). This hints toward a lamellar arrangement with a layer distance of 2.32 nm, in accordance with the layer thickness of 2.1 nm obtained from AFM (Figure 57e).

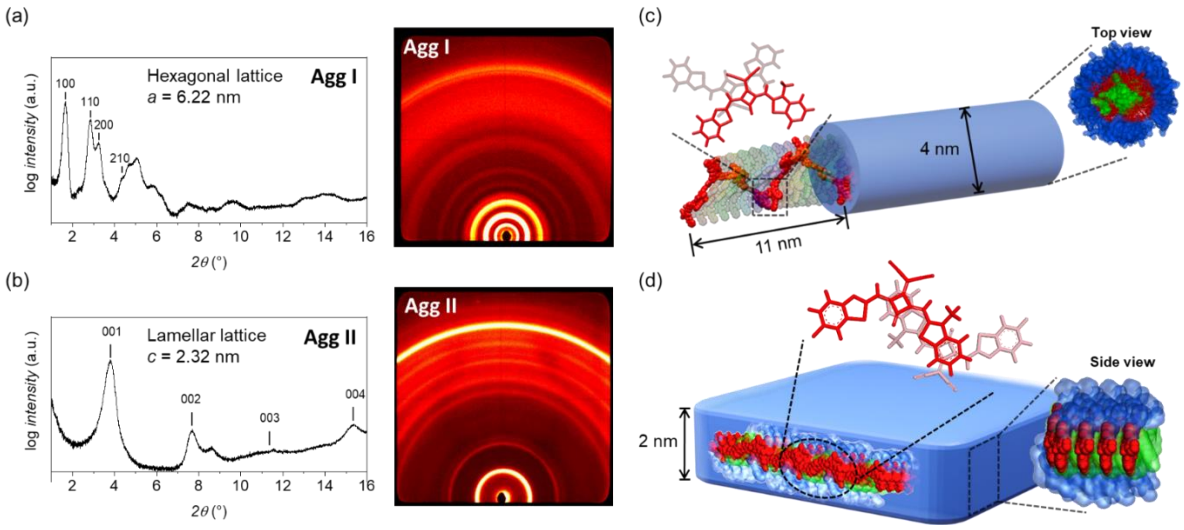

Figure 58. WAXS measurements of (a) **BisSQ2-AggI** and (b) **BisSQ2-AggII** prepared on aluminum foils by multistep evaporation of the respective solutions (toluene/TCE 98:2, c_0 = 5.0 g L^{-1}) and proposed packing model of (c) the tubular nanorod of self-assembled **BisSQ2-AggI**; left: each strand individually colored (side chains omitted), showing a cut-out of a helix comprising two chromophores, which shows a close spatial proximity between donor and the acceptor of the adjacent chromophore; right: top view with hydrophilic side chains (blue) and aliphatic chains (green); (d) the nanosheet of self-assembled **BisSQ2-AggII** with the chromophores colored in red, hydrophilic side chains in blue and the aliphatic chains in green, respectively. Both models were simulated and visualized with the program suite *BIOVIA Materials Studio 2017R2*.

The experimental data obtained from AFM and WAXS measurements enable us to derive packing models for the two different types of aggregates. For **BisSQ2-AggI**, we propose a nanorod structure as displayed in Figure 58c, in which nine **BisSQ2** molecules form one turn of a helical supramolecular polymer chain (pitch of 11 nm, highlighted in red) with a diameter of 4 nm (Figure 58c and Figure S33). Assuming a reasonable density of 1 g/cm^3 for soft organic materials,[144] the number of molecules per repeating unit amounts to 72 molecules (see *Appendix, Chapter 9.2*). This corresponds to eight helically wound strands that intertwine to form the tubular rod-shaped supramolecular polymer structure presented in Figure 58c, where each strand is colored individually. According to this model, the aliphatic chains are closely packed inside the nanorods (Figure 58c top view, green part), while the hydrophilic OEGs point to the outside of the nanorods (blue part), exhibiting an ideal phase segregation. An opposite orientation of the side-chains, i.e., the OEGs point to the inside and the aliphatic side chains to the outside of the nanorod, does not result in a reasonable structure that is consistent with the experimental data. Similar structural arrangements, where OEGs are found on the outer surface, were described for self-assembled nanotubes composed of hexabenzocoronene amphiphiles in toluene.[145] Considering the side chains, the dimensional parameters are in good accordance with the experimental results. A closer look at the chromophores reveals a sandwich-type arrangement with antiparallel orientation of the ground state dipole moments (Figure 58c, cut-out comprising two chromophores colored in red). Remarkably, the chromophores are arranged in a slipped fashion, where the donor parts are in close proximity to the acceptors of the neighboring molecules.

The morphology of **BisSQ2-AggII** revealed by our AFM studies resembles the nanosheet structure observed for bis(squaraine) dye **BisSQ1** (Chart 1) in our earlier work,[118] for which a slip-stacked arrangement between neighboring chromophores was proposed. This is further supported by the observed red-shifted absorption spectrum (Figure 56, red line), indicating a head-to-tail arrangement of the chromophores with J-type coupling[43b] (Figure 58d and Figure S34). The alkyl side chains (Figure 58d, green) accommodate themselves in the hydrophobic cavities between the chromophores, while the polar OEG chains (Figure 58d, blue) extend above and below the sheet into the solvent. The observed height of 2.1 nm by AFM is in good agreement with the dimension of the chromophore considering the flexibility of the side chains (Figure S35a), suggesting the formation of a monolayer on the substrate.

4.2.4 Concentration-Dependent UV/Vis/NIR Spectroscopy

To gain more insight into the aggregation mechanism of **BisSQ2**, concentration-dependent UV/Vis/NIR studies were carried out. A stock solution (toluene/TCE 98:2, $c_0 = 1.8 \times 10^{-4}$ M) of **BisSQ2-AggI** was prepared by the fast-cooling method as mentioned above. For detailed methods for sample preparation, see *Appendix* (*Chapter 9.2*). This **BisSQ2-AggI** stock solution was then diluted into a series of samples with a concentration range of $1.8 \times 10^{-4} – 6.0 \times 10^{-7}$ M and all sample solutions were equilibrated at room temperature for 24 hours prior to the measurements. At high concentration ($c_0 = 1.8 \times 10^{-4}$ M), a broad absorption band characteristic of **BisSQ2-AggI** was observed (Figure 59a, blue line). Upon decreasing the concentration, pronounced spectral changes are visible, revealing dissociation of the aggregates. At low concentration (Figure 59a, red line), the absorption spectrum exhibits a rather sharp band at λ_{max} = 739 nm, which resembles the monomer absorption spectrum observed at high temperatures (see Figure 56). Notably, isosbestic points are observed at 656 and 766 nm, indicating an equilibrium between only two species. The abrupt change of the apparent absorption at 739 nm (Figure S37a) at a critical concentration of $c_T \sim 4 \times 10^{-6}$ M indicates a cooperative aggregation process.[128] Hence, we made use of the cooperative K_2/K model, where two states of the aggregation process are differentiated: the nucleation regime, described by the equilibrium constant K_2 for the dimerization, and the elongation regime, described by the equilibrium constant K.[93] The data could be properly fitted (Figure 59a, inset) to give a cooperativity factor $\sigma = 0.016$ with $K = 2.18 \times 10^5$ M^{-1} for the elongation regime, resulting in an equilibration constant for the dimerization of $K_2 = 3.56 \times 10^3$ M^{-1}. It is noteworthy that the isodesmic (equal-K) model ($\sigma = 1.0$) and monomer-dimer model both failed to describe the aggregation process (Figure S37a). The high cooperativity suggests that only a small number of nuclei are involved in the equilibrium and mainly monomers and extended aggregates are present in the solution over the whole concentration range, which is in agreement with the appearance of the isosbestic points in the concentration-dependent spectral changes (Figure 59a). By applying a global fit analysis[146] (for further details, see *Appendix, Chapter 9.2*), the ideal monomer and aggregate spectra were obtained, which match perfectly with the spectra obtained for the most diluted and most concentrated solutions, respectively (Figure 59a, red and blue solid lines). The aggregate spectrum exhibits a remarkable broad absorption covering the whole range of 550 – 850 nm, edging in the NIR region. The absorption features do not allow us to gain insight into the chromophore arrangement in terms of a simple classification of H- (sandwich type arrangement) and J-aggregates (head-to-tail arrangement),[43b] which will be discussed later.

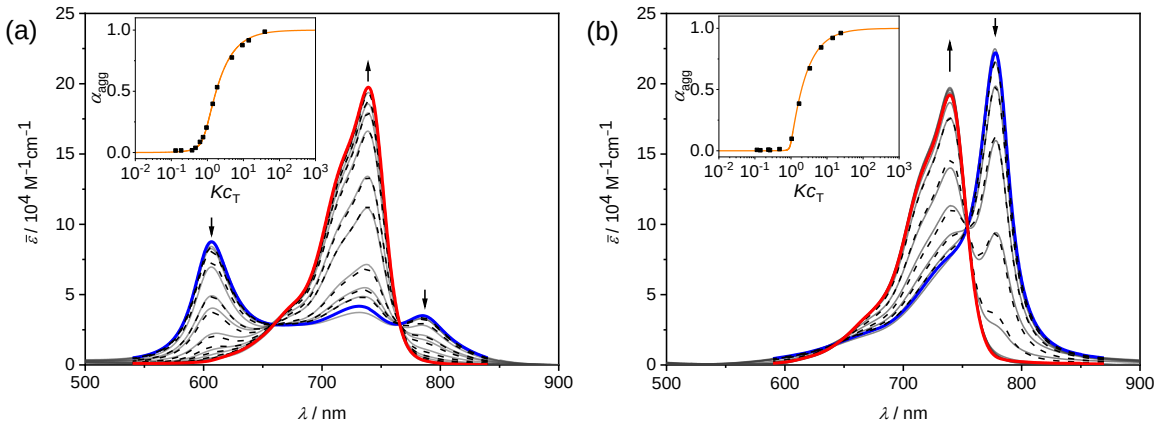

Figure 59. Concentration-dependent UV/Vis/NIR spectra of **BisSQ2** (a) **AggI** (c_0 = 1.8 × 10^{-4} – 6.0 × 10^{-7} M) and (b) **AggII** (c_0 = 3.8 × 10^{-5} – 1.8 × 10^{-7} M) in toluene/TCE 98:2 at 25 °C (grey solid lines) and the global fit analysis according to the cooperative K_2/K model[93] (black dashed lines) and the ideal monomer (red solid line) as well as aggregate spectra (blue solid line) obtained by global fit analysis. The arrows indicate the spectral changes with decreasing concentration. Inset: plot of fractions of aggregate against Kc_T and fit with the cooperative K_2/K model[93] (c_T is the total concentration of **BisSQ2** molecules in solution).

For **BisSQ2-AggII**, since precipitation took place after the cooling process, we prepared a fresh **BisSQ2-AggII** solution (toluene/TCE 98:2, c_0 = 3.8 × 10^{-5} M) and applied ultra-sonication at 25 °C for 20 minutes to disperse the aggregates. The solution was further diluted stepwise to obtain a series of samples with different concentrations. The sample solutions were stored overnight prior to the measurements. Upon dilution, the aggregate band decreases accompanied by the growth of the monomer band peaked at 739 nm with a *FWHM* of 540 cm^{-1} (Figure 59b). As in the case of **BisSQ2-AggI**, a defined isosbestic point can be observed at 754 nm, suggesting an equilibrium between only two species.

The results again infer a cooperative aggregation process (Figure S37b), therefore, we applied the cooperative K_2/K model[93] (Figure 59b, inset) that delivered a cooperativity factor σ = 0.00038 with K = 6.37 × 10^5 M^{-1} for the elongation regime, resulting in an equilibrium constant for the dimerization of K_2 = 2.42 × 10^2 M^{-1}. Again, the isodesmic (equal-K) model (σ = 1.0) and monomer-dimer model failed to describe the aggregation process (Figure S37b). This result reveals a higher cooperativity as well as a larger elongation constant for the aggregation process of **BisSQ2-AggII** compared with **BisSQ2-AggI** (σ = 0.016, K = 2.18 × 10^5 M^{-1}), suggesting that **BisSQ2-AggII** is the thermodynamically favored species. The resulting ideal aggregate spectrum (Figure 59b, blue solid line) obtained by global fit analysis[146] (for further details, see *Appendix*, *Chapter 9.2*) shows a significant red-shift and

sharpening compared to the monomer spectrum (Figure 59b, red solid line). In addition, the aggregate spectrum also shows weak side-bands at higher energies, i.e., shorter wavelengths.

We also performed temperature-dependent UV/Vis/NIR experiments for **BisSQ2-AggII** solution (toluene/TCE 98:2, $c_0 = 2.5 \times 10^{-5}$ M). Even though quantitative analysis of the spectra is not possible due to precipitation, the results suggest that heating leads to the dissociation of **BisSQ2-AggII** directly into monomers without showing absorption features of **BisSQ2-AggI** (Figure S38). Combining this observation with our concentration-dependent kinetic analyses (Figure S40), we infer that **BisSQ2-AggI** is an off-pathway species and **BisSQ2-AggII** the thermodynamically more stable aggregate.[147] Based on these results, we deduce the energy landscape shown in Figure 60 that depicts the two competing self-assembly pathways qualitatively. At high temperature (85 °C), **BisSQ2** molecules remain dissociated. Upon rapid cooling, the aggregation follows the pathway with the lowest energy barrier (solid arrow in Figure 60) and ends up in a kinetically trapped state: i.e., **BisSQ2-AggI**. According to the proposed model shown in Figure 58c, the arrangement of the side chains reveals a phase segregation that may contribute to the low energy barrier of the self-assembly process.[148] In contrast, during the slow cooling process, the system has a time long enough to traverse the energy landscape and find a more stable and well-organized aggregation mode (dotted arrows in Figure 60): as a consequence, **BisSQ2-AggII** is formed.

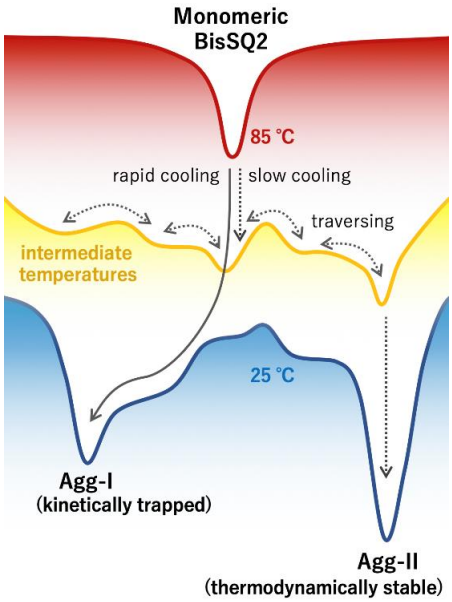

Figure 60. Schematic energy landscape of the two competing pathways for the formation of kinetically favored off-pathway **BisSQ2-AggI** and the thermodynamically more stable **BisSQ2-AggII** in toluene/TCE 98:2. Upon rapid cooling, **BisSQ2-AggI** is formed and kinetically trapped. Note that **BisSQ2-AggI** has less organized structure (Figure 58), thus is kinetically more favored. In contrast, during the slow cooling process, **BisSQ2** has a time long enough to traverse the energy landscape and find a more stable and well-organized aggregation mode.

Polymorphisms in supramolecular polymerization have been observed for monomers bearing multiple non-covalent interaction sites. Prominent examples are benzene-1,3,5-tricarboxamide molecules (BTAs) whose regular self-assembly into 1D fibers[149] was transformed into 2D and 3D morphologies by additional H-bonding interactions by shielding carboxyl groups in a hydrophobic environment[136a] or by alteration of the alkyl chain length for porphyrin molecules, likewise transforming the self-assembly into 1D fibers[17c] by increasing the lateral van der Waals forces to afford a 2D sheet-like morphology. In this context, it is intriguing that we observed polymorphism for **BisSQ2**, but not for **BisSQ1** despite of the absence of specific measures as described above for the BTAs and alkyl porphyrins.[118] Both molecules consist of two squaraine dyes connected in the same angle. It appears that the additional spacer between the squaraine dyes in **BisSQ2** allowed another form of folding and packing (i.e., **BisSQ2-AggI**), which demonstrates a new strategy to realize supramolecular polymorphism. Remarkably, as discussed below, a hitherto unknown panchromatic absorption spectrum, i.e., modulation of the functional properties, was achieved by this simple strategy.

4.2.5 Theoretical Calculations for Dye-Dye Interactions

Since the discovery of J-aggregates by Jelley[108] and Scheibe,[107] scientists were interested to understand how supramolecular arrangements govern dye-dye interactions and how these interactions manifest in absorption spectra and determine functional properties. This is perfectly demonstrated by Kasha's molecular exciton theory that had a great impact on research on dye aggregates and functional molecular materials for more than 50 years.[43b] In this regard, it is most interesting that the absorption features of the **BisSQ2-AggI** cannot be explained for the chromophore arrangement deduced from X-ray analysis in terms of a simple classification of H- (sandwich type arrangement) and J-aggregates (head-to-tail arrangement) by the molecular exciton theory. Based on this model, we would expect a hypsochromic shift (H-aggregate) of the main absorption peak with respect to the monomer according to the packing model shown in Figure 58c, rather than a panchromatic absorption as observed for **BisSQ2-AggI**.[43b] Transitions to both the highest and lowest excited states can be allowed in case of a rotational displacement of the chromophores resulting in the appearance of a weaker J-band in the absorption spectrum (Davydov splitting).[150] However, this would require a large rotational angle in our case since both bands show significant intensity (Figure 59a, blue solid line).[39] For such a situation, however, only small shifts are expected which is obviously not the case for the **BisSQ2-AggI** nanorods (Figure 58c).

Hence, in order to understand the broad panchromatic absorption spectrum of **BisSQ2-AggI** nanorods and also rationalize the bathochromic shift observed for **BisSQ2-AggII** nanosheets, we applied the Essential States Model (ESM).[115] In contrast to conventional molecular exciton theory, this model also accounts for polarizability effects, being crucial for the description of the optical properties of dye aggregates comprising chromophores composed of alternating donor and acceptor subunits.[114e,116] Squaraines exhibit a significant charge transfer character arising from *intra*molecular transfer of electron density from the donor to the acceptor moiety within the donor-acceptor-donor chromophore. Thus, the squaraine chromophore is described by three essential states: two zwitterionic states $|Z_1>$ and $|Z_2>$ bearing a positive charge at one of the donor units and a negative charge at the acceptor moiety, respectively, which are both coupled to the neutral state ($|N>$) by the transfer integral t_Z (Figure 61a).[110] The respective electronic Hamiltonian can be written as[110]

$$\widehat{H}_{el}^{mon} = \eta_Z \sum_{i=1,2} |Z_i><Z_i| + t_Z \sum_{i=1,2}(|N><Z_i| + h.c.), \qquad (2)$$

with η_Z being the energy of the zwitterionic states (note that the energy of the neutral state is set to zero) and *h.c.* the Hermitian conjugate. In order to account for vibronic coupling, as evident from the vibronic progression observed in the UV/Vis/NIR spectrum of **SQ1**, we employed a Holstein-type Hamiltonian (for details see *Appendix*, *Chapter 9.2*). Thereby, each essential state is described by two harmonic oscillators, i.e., one for each donor-acceptor side arm. In doing so, the UV/Vis/NIR spectrum of reference dye **SQ1** is well reproduced by our simulation (Figure S42, blue solid line) using the parameters shown in Table S3, which are in line with previous studies on squaraine dyes.[39] The zwitterionic character ρ in the ground state is given by[110]

$$\rho = \frac{1}{2}\left(1 - \frac{\eta_Z}{\sqrt{\eta_Z^2 + 8t_Z^2}}\right). \qquad (3)$$

In this way, we obtain a value of $\rho = 0.46$ revealing an almost equal contribution of the neutral and zwitterionic states (note that a fully zwitterionic character results in $\rho = 1$, whereas a completely neutral state is characterized by $\rho = 0$). This explains the observation of a sharp cyanine-like absorption band with a weak vibronic side-band (Figure S42, blue solid line and Figure S28c, black line).

Having set the parameters for the monomeric chromophore, we simulated the absorption spectrum for a cut-out of **BisSQ2-AggI** nanorod comprising the two chromophores shown in Figure 58c to reduce computational effort. Even though this is a simplification, it allows us to investigate the origin of the broad absorption spectrum of **BisSQ2-AggI**. Toward this approach, we first evaluated the influence of the Coulomb coupling between the chromophores (for a detailed description, see *Appendix*, *Chapter 9.2*). Using the same parameters as for the monomer (Table S3), the resulting absorption spectrum due to Coulomb coupling shows a main absorption band (Figure 61c, red solid line) with a hypsochromic shift compared to the monomer absorption band (green dash-dotted line). This is in agreement with a sandwich-type cofacial arrangement of the chromophores resulting in H-type exciton coupling.[43b] Hence, it is obvious that the broad absorption spectrum of **BisSQ2-AggI** (Figure 61c, black dotted line) and in particular the pronounced absorption in the NIR-region cannot be rationalized by considering only Coulomb coupling between the chromophores because the shift is too small and no second J-band due to Davydov splitting is present.

However, our modelling studies reveal close spatial proximity of the donor and acceptor groups (Figure 58c), which suggests the importance of *inter*molecular charge transfer (ICT, Figure 61b) to describe the spectral features of **BisSQ2-AggI**.[114c,117] With the additional ICT states, the experimental absorption spectrum can be adequately reproduced (Figure 61c, blue solid line) with the parameters in line with previous studies for thin films of squaraine dyes[114c] (Table S3). We are aware that the chosen dimer unit does not account for all *inter*chromophoric interactions within the aggregate, thus the calculated spectrum had to be shifted by 200 cm^{-1} to higher energies to match the experimental spectrum. Therefore, the coupling strengths should be regarded as effective parameters to describe the absorption features of the tubular **BisSQ2-AggI** nanorod. However, the band shape is well reproduced by our simulations.

Further analysis reveals that mainly two transitions are present when vibronic coupling is neglected, causing the high and low energy absorption band at ~620 and ~780 nm, respectively (Figure S46, orange solid line). Hence, we can attribute the additionally observed absorption band at ~730 nm to a vibronic band, which is caused by structural changes of the chromophores in the *intra*- and *inter*molecular charge transfer states with respect to the neutral state. In order to elucidate the influence of the *inter*molecular CT coupling strength t_{CT} on the absorption properties, which reflects the strength of the donor-acceptor interaction between the two chromophores, we have also calculated the spectra for different coupling strengths. For weak coupling (t_{CT} = 1000 cm^{-1}), which equals a small donor-acceptor overlap between the

chromophores, the spectrum is characterized by one main absorption band (Figure S47, red dotted line). However, upon increasing the coupling strength up to 3000 cm^{-1} (note that we have used a value of t_{CT} = 2550 cm^{-1} to obtain best agreement with the experimental spectrum of **BisSQ2-AggI**), a two-band structure evolves with increasing energetic separation between the two absorption maxima (Figure S47, green and black solid line). These results clearly show that the pronounced donor-acceptor overlap within **BisSQ2-AggI** nanorods is responsible for the panchromatic absorption band observed in the UV/Vis/NIR spectrum, which significantly differs from the predictions based on conventional molecular exciton theory.

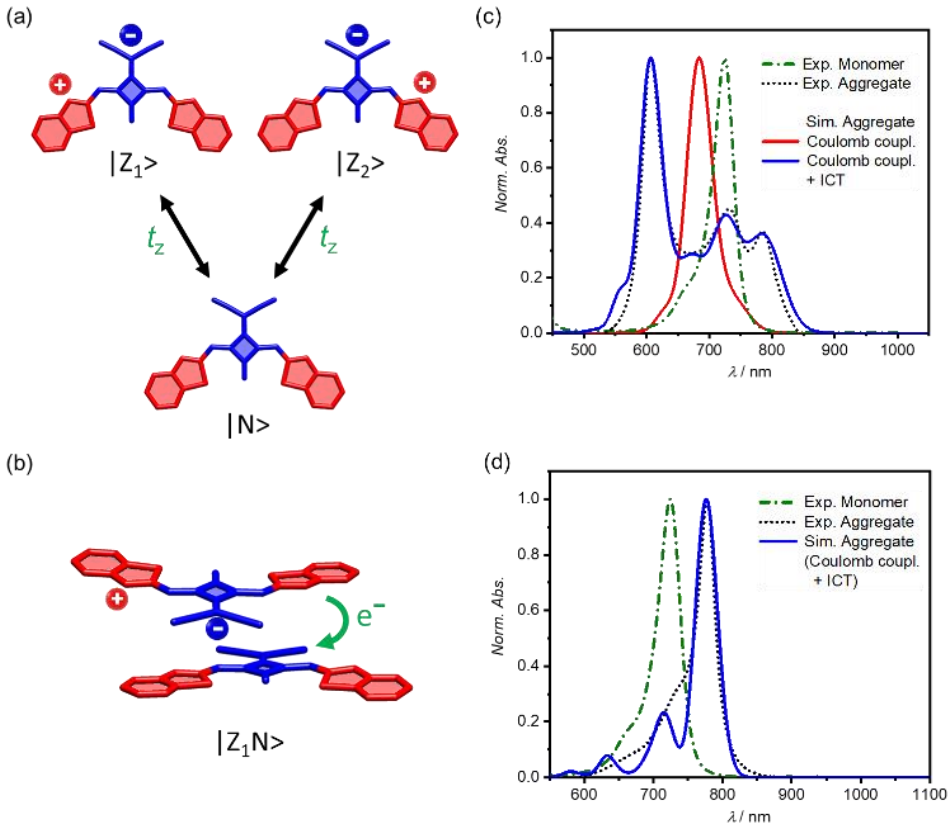

Figure 61. (a) Three diabatic states used for the simulation of the absorption spectrum of **SQ1** monomer and **BisSQ2** aggregates. The zwitterionic states $|Z_1\rangle$ and $|Z_2\rangle$ are characterized by a positive and negative charge at the donor and acceptor moiety highlighted in red and blue, respectively. Both states are coupled to the neutral state $|N\rangle$ by the transfer integral t_Z describing the *intra*molecular electron transfer from the donor to the acceptor unit. (b) Schematic representation of the *inter*molecular electron transfer in the double squaraine stack of **BisSQ2-AggI** in state $|Z_1N\rangle$. Simulated absorption spectrum of the double chromophore stack of (c) **BisSQ2-AggI** and (d) **BisSQ2-AggII** taking Coulomb coupling and *inter*molecular charge transfer states (ICT) into account (blue solid lines). In addition, the simulated spectra of **BisSQ2-AggI** considering only Coulomb coupling (red solid line) is shown in panel (c). The experimental spectra of the aggregates (black dotted lines, toluene/TCE 98:2) and the monomer (green dash-dotted lines) are also shown for comparison. For the simulations, the parameters listed in Table S3 were employed. The calculated spectra (blue lines) were shifted by 200 cm^{-1} (**BisSQ2-AggI**) and –500cm^{-1} (**BisSQ2-AggII**).

In addition, we have also simulated the absorption spectrum of **BisSQ2-AggII**, which also shows a significant donor-acceptor overlap but now with a head-to-tail arrangement of the chromophores (Figure 58d). Indeed, the simulated spectrum (Figure 61d, blue solid line) shows a red-shift of the main absorption band as expected for chromophores showing J-type coupling.[138] Note that the simulated spectrum was additionally shifted by 500 cm^{-1} to lower energies in order to adjust the position of the main absorption peak with the experimental spectrum. We attribute the required correction of the absorption maximum to the chosen system size (dimer), so that only the interaction with one chromophore is considered and next-neighbor couplings are neglected, which should cause a stronger bathochromic shift. In addition, our simulations do not account for the J-type coupling between the two chromophores within the same **BisSQ2** molecule that causes an additional bathochromic shift (Figure S28c). Notably, when only Coulomb coupling is considered, the absorption shows a weaker bathochromic shift (Figure S48, red solid line) compared to the spectrum when also ICT states are considered (blue solid line). This indicates that the pronounced bathochromic shift for **BisSQ2-AggII** is caused by an interplay of Coulomb coupling and donor-acceptor interaction. Thus, whereas the donor-acceptor interaction in a sandwich-type arrangement of the squaraine chromophores induces the panchromatic absorption as observed for **BisSQ2-AggI** (Figure 61c, blue line), it leads to an increase of the bathochromic shift in the case of slip-stacked arranged chromophores like for **BisSQ2-AggII** (Figure 61d, blue solid line).

4.3 Conclusion

In this work, we studied the self-assembly of a new bis(squaraine) dye, in which two chromophores are covalently linked by a para-phenylene spacer moiety. In the low polarity solvent mixture toluene/TCE (98:2, *v*/*v*), **BisSQ2** self-assembles cooperatively into two different supramolecular polymorphs with very distinct structures and absorption spectra depending on the cooling rate. Rapid cooling results in structurally defined rigid helical nanorods with a diameter of ~5 nm and a helical pitch of ~13 nm (**BisSQ2-AggI**) while slow cooling gives rise to a nanosheet structure with a height of ~2 nm (**BisSQ2-AggII**). The self-assembly processes can be well interpreted in terms of the cooperative K_2/K model, revealing a cooperativity factor of σ = 0.016 and binding constants for the nucleation of $K_2 = 3.56 \times 10^3\ M^{-1}$ and for the elongation of $K = 2.18 \times 10^5\ M^{-1}$ for **BisSQ2-AggI**, and $\sigma = 0.00038$, $K_2 = 2.42 \times 10^2\ M^{-1}$ and $K = 6.37 \times 10^5\ M^{-1}$ in the case of **BisSQ2-AggII**. With this information, we were able to derive a qualitative energy landscape (Figure 60) that

illustrates the kinetically favored formation of **BisSQ2-AggI** and the thermodynamically favored formation of **BisSQ2-AggII**. A second important aspect of this work arises from the crystal-like well-defined packing of **BisSQ2** dyes in the two polymorphic aggregates **BisSQ2-AggI** and **BisSQ2-AggII**. Thus, packing arrangements could be derived from microscopic observations and X-ray scattering for both the thermodynamically stable **BisSQ2-AggII** nanosheets and the tubular **BisSQ2-AggI** nanorods. These structural models could be utilized in a subsequent step to elucidate the impact of packing on the UV/Vis/NIR absorption spectra of these dye aggregates. Whilst the conventional molecular exciton model failed to explain the absorption properties of **BisSQ2-AggI** for the given packing arrangement, more profound theoretical investigations based on the Essential States Model reveal the importance of *inter*molecular charge transfer to adequately describe the panchromatic broad absorption in the **BisSQ2-AggI** absorption spectrum. Moreover, the pronounced red-shift observed in the **BisSQ2-AggII** absorption spectrum can be assigned to the interplay of Coulomb coupling and *inter*molecular charge transfer.

In summary, we herein presented a supramolecular polymorphism for the self-assembly of a bis(squaraine) dye leading to unique highly defined nanosheets and tubular dye nanorods whose very different absorption spectra could be related to differences in the donor-acceptor overlap. Beyond the importance of our results for research on supramolecular polymers and dye aggregates, we consider our insights on short-range charge transfer coupling for squaraine dyes with their donor-acceptor-donor structure to be of high relevance for all materials based on alternating donor-acceptor π-systems. This includes in particular acceptor-donor-acceptor (ADA) dyes that are currently the favored class of materials for bulk heterojunction solar cells.[151]

Chapter 5

A Double J-Coupling Strategy for Near-Infrared Emitters

Abstract: A bis(squaraine) dye was synthesized by connecting two quinolinium-based squaraines *via* Yamamoto coupling. The head-to-tail chromophore arrangement leads to *intra*molecular J-type exciton coupling, resulting in an absorption maximum at 961 nm and a fluorescence peak at 971 nm with a quantum yield of 0.33% in chloroform. In less polar toluene, the bis-chromophore self-assembles into nanofibers, affording a pronounced bathochromic spectral shift with absorption maximum at 1095 nm and a fluorescence peak at 1116 nm due to *inter*molecular J-type coupling.

5.1 Introduction

Near-infrared (NIR) emitters with fluorescence in the second NIR window (NIR-II, 1000−1700 nm) are highly desired for applications ranging from noninvasive bio-imaging up to NIR OLEDs. For the former applications, the deeper penetration depth of NIR-II light in biological tissue is highly beneficial because of reduced photon scattering and diminished autofluorescence.[75,120,152] For the latter, NIR-II emitters enable new perspectives for security applications, biomedical sensors and night vision.[153] Low-bandgap organic molecules, however, suffer from significantly lower luminescence efficiency due to the fast non-radiative relaxation by the $S_1 \rightarrow S_0$ internal conversion (IC) process. For low-bandgap organic solid state materials, the situation is even worse due to additional non-radiative relaxation pathways originating from *inter*molecular interactions including charge transfer or a decrease of the transition dipole moment as observed in cofacial H-aggregates.[154] To overcome these

deficiencies, we herein introduce a double J-coupling strategy that involves both *intra*molecular J-coupling by the head-to-tail connection of two dipolar squaraine dyes ("J-dimer") and the self-assembly of these dyes into *inter*molecularly J-coupled dye aggregates. It is noteworthy that J-coupling appears so far indeed as the only approach that is able to enhance the radiative rate due to the increase of the transition dipole moment of the lowest excited state[120,155] whilst all other strategies utilized for improving NIR luminescence rely on reducing the rates for non-radiative processes, e.g. by rigidification of the π-scaffold.[156,157,158]

To demonstrate the successful application of this concept, we chose an emissive squaraine dye (**SQ**) from our earlier work[31] and designed the bis-chromophore **BisSQ3** bearing two solubilizing trialkoxyphenyl substituents (Figure 62). We selected this quinoline based squaraine not only because of the pronounced absorption and emission at long wavelengths, but also the rather linear molecular shape to fulfill the head-to-tail arrangement of the transition dipole moments *intra*molecularly (Figure 62). Squaraine dyes are known as fluorophores with intense narrow absorption bands and emission at rather long wavelengths,[22] accordingly positioning them together with BODIPY,[159] cyanine[160] and rylene[161] dyes among the brightest emitters in the NIR-I spectral range (NIR-I, 700−900 nm).[27]

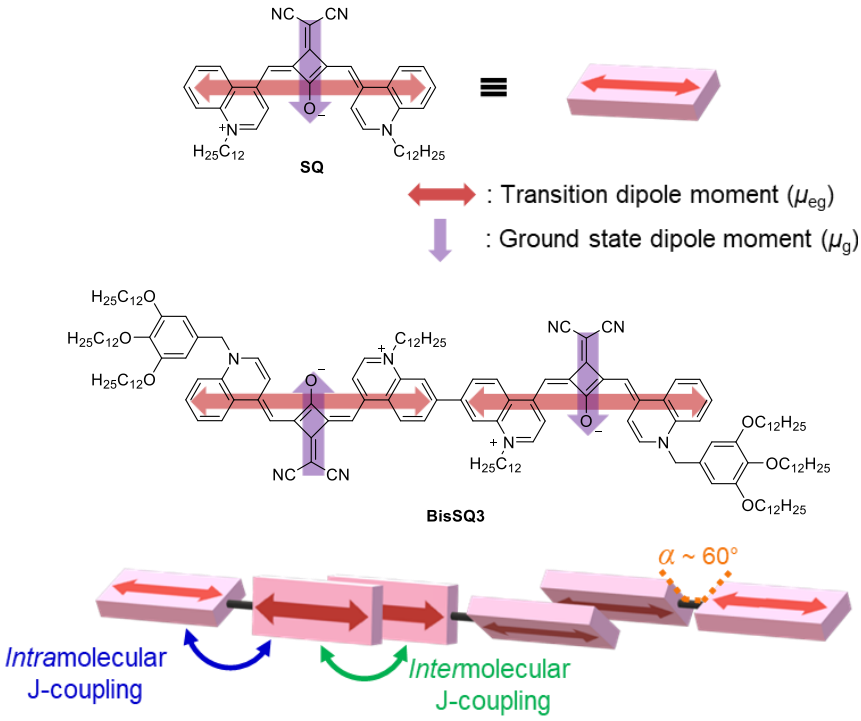

Figure 62. SQ[31] and **BisSQ3** molecules investigated in this work. Also shown is a schematic representation of the proposed aggregate structure of **BisSQ3** with the concept for double *intra*molecular (blue arrow) and *inter*molecular (green arrow) J-coupling. The orientations of the transition dipole moments and ground state dipole moments are illustrated by red and purple arrows, respectively.

5.2 Results and Discussion

5.2.1 Synthesis

Bis(squaraine) dye **BisSQ3** was synthesized as illustrated in Scheme 9 by a three-step condensation sequence starting with 1-dodecyl-7-iodo-4-methylquinolinium-iodide (**1**) and 1,2-diethoxycyclobutenedione (**2**). Subsequent reaction with malononitrile, followed by condensation with 1,2,3-tridodecyloxybenzyl-quinoliniumbromide (**5**) and final Ni-catalyzed Yamamoto coupling of two squaraine dyes **6** afforded the desired product **BisSQ3** in good yields of 42% . For details on the syntheses of the new molecules, see *Appendix* (*Chapter 9.3*).

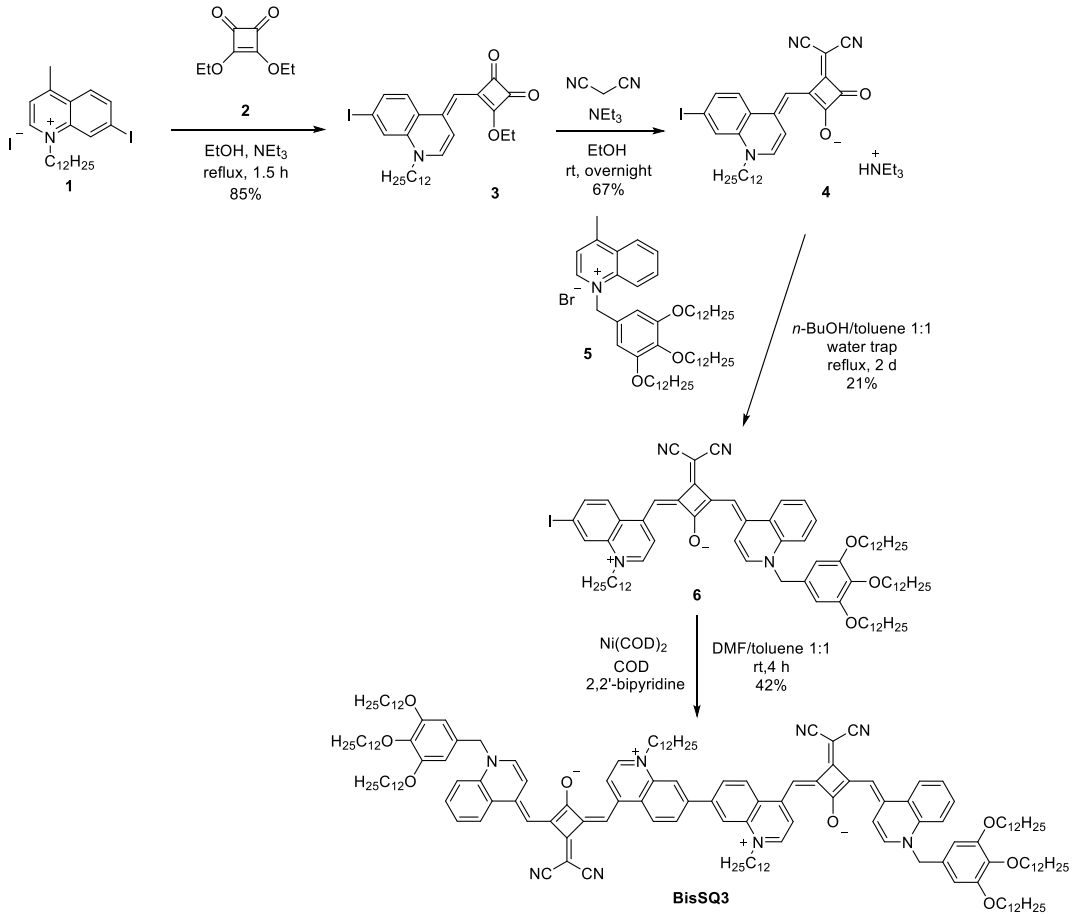

Scheme 9. Synthetic route to bis(squaraine) dye **BisSQ3**. COD = 1,5-cyclooctadiene.

5.2.2 Molecular Optical Properties

The UV/Vis/NIR absorption properties of molecular dissolved dipolar **SQ**[31] and **BisSQ3** were studied under dilute conditions ($c_0 < 1.0 \times 10^{-6}$ M) in polar $CHCl_3$ to ensure complete dissociation of the molecules. As shown in Figure 63, **SQ** exhibits an absorption maximum (λ_{max}) at 875 nm (black solid line) while the one of **BisSQ3** is already located at 961 nm in

$CHCl_3$ (blue solid line). This proves that the approach of *intra*molecular J-type coupling *via* head-to-tail connection of two squaraine dyes indeed results in a significant bathochromic shift of about 86 nm (1020 cm^{-1}) for the lowest-energy transition (Table 5). This *intra*molecular J-type coupling originates from the head-to-tail orientation of the two transition dipole moments (μ_{eg}) of covalently connected chromophores within **BisSQ3**, as μ_{eg} is parallel to the long molecular axis of **SQ** (Figure 62). As expected, the covalent connection of two squaraine units leads to an increase in the molar absorption coefficient (ε_{max} = 385000 $M^{-1}cm^{-1}$) for **BisSQ3** (Figure S51). The observed band broadening for **BisSQ3** can be assigned to the conformational flexibility due to the rotation around the covalent bond between the two respective chromophores and accordingly reduced π-conjugation.[39,127,131] As shown in Table 5, μ_{eg}^2 increases significantly from **SQ** (163 D^2) to **BisSQ3** (382 D^2) in $CHCl_3$, showing a doubled transition strength, which further indicates the strong *intra*molecular J-type coupling.[162]

The fluorescence spectra of both **SQ** (λ_{em} = 885 nm) and **BisSQ3** (λ_{em} = 971 nm) in $CHCl_3$ exhibit very small Stokes shifts ($\Delta\tilde{\nu}_{Stokes}$ = 110 – 130 cm^{-1}) with mirror-image behavior with respect to their absorption profiles (Figure 63). This is a strong indication for only minor changes of the molecular structure as well as solvent shell in the excited state. The absolute fluorescence quantum yield (Φ_{FL}) could be determined to be 1.30% for **SQ** and 0.33% for **BisSQ3** in $CHCl_3$ at RT after correction for reabsorption[163] (for details, see *Appendix*, *Chapter 9.3*). The slight decrease in Φ_{FL} for **BisSQ3** can be attributed to the lower optical bandgap facilitating internal conversion to the ground state and additional non-radiative pathways caused by rotation around the single bond which connects the two squaraine dyes. Nevertheless, this value is comparable with literature known NIR-II dyes[164,165,166] and even higher than a reported squaraine dye[42] in the similar spectral range. Hence, despite the non-radiative process caused by bond rotation and the small optical band gap, a decent Φ_{FL} is retained by the approach of *intra*molecular J-type exciton coupling. Due to the low Φ_{FL} and poor excitation by a pulsed laser diode (EPL) in combination with high signal-to-noise ratio of the NIR detector of our fluorescence setup, no fluorescence decay curves for lifetime determination could be obtained. The molecular optical properties of **SQ** and **BisSQ3** in $CHCl_3$ are summarized in Table 5.

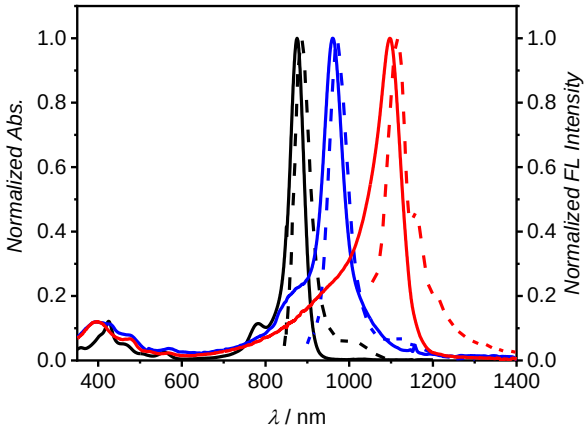

Figure 63. Normalized UV/Vis/NIR absorption (solid lines) and fluorescence (dashed lines) spectra of **SQ** in $CHCl_3$ (black, λ_{ex} = 815 nm), **BisSQ3** in $CHCl_3$ (blue, λ_{ex} = 870 nm), and aggregates of **BisSQ3** in toluene (red, λ_{ex} = 985 nm) at 293 K.

Table 5. Summarized optical properties of squaraine dyes **SQ** and **BisSQ3** obtained by absorption and fluorescence spectroscopy in specified solvent at 293 K.

	Solvent	λ_{max} (nm)	ε_{max} ($M^{-1}cm^{-1}$)	μ_{eg}[c] (D)	μ_{eg}^2 (D^2)	$FWHM_{abs}$ (cm^{-1})	λ_{em} (nm)	$\Delta\tilde{\nu}_{Stokes}$ (cm^{-1})	Φ_{FL}[e] (%)
SQ	$CHCl_3$	875	274000	12.8	163	485	885	130	1.30 ± 0.22
BisSQ3	$CHCl_3$[a]	961	385000	19.5	382	630	971	110	0.33 ± 0.01
BisSQ3	Toluene[b]	1095	335000	20.3	411	500	1116[d]	160	n.d.[f]

[a] $c_0 = 1.0 \times 10^{-6}$ M, dissociated species. [b] $c_0 = 5.5 \times 10^{-5}$ M, aggregated species. [c] Calculated from the integral of the designated absorption bands (λ_{max}) according to eq. S24 (see *Appendix*, *Chapter 9.3*). [d] Fluorescence spectrum was measured with a front-face setup (1 cm cell thickness; $c_0 = 4.0 \times 10^{-6}$ M; OD = 0.1) without polarizers and was not corrected from reabsorption. [e] Absolute fluorescence quantum yields were determined by a calibrated integrating sphere system (F-M01, accessory of FLS980 spectrometer; 1 cm cell thickness, OD = 0.1). The values were corrected for reabsorption (for details, see *Appendix*, *Chapter 9.3*).[f] Not determined due to limitations of the experimental setup as well as the required high concentrations for complete aggregation (OD > 0.3).

Optical brightness is another important quantity that determines the quality of fluorophores. The optical brightness is defined as the product of the fluorescence quantum yield and the molar absorption coefficient at the absorption maximum ($\Phi_{FL} \times \varepsilon_{max}$). Notably, **BisSQ3** exhibits an outstanding molar absorption coefficient (ε_{max} = 385000 $M^{-1}cm^{-1}$) compared to recently reported organic NIR-II emitters in organic solvents.[165, 167, 168] Therefore, upon excitation at 961 nm, **BisSQ3** exhibits appreciable high optical brightness (1270 $M^{-1}cm^{-1}$).[31,167,169]

5.2.3 Self-Assembly Studies

By changing the solvent from $CHCl_3$ to less polar toluene, *inter*molecular aggregation of **BisSQ3** can be induced. Upon increasing the percentage of toluene, the absorption maximum at 961 nm in $CHCl_3$ decreases, while a new, strongly bathochromically shifted absorption band located at 1095 nm emerges (Figure 64a). The same phenomenon can also be observed upon cooling down a hot toluene solution of **BisSQ3** ($c_0 = 2.5 \times 10^{-6}$ M) from 358 K to 293 K (Figure 64b). Furthermore, cooling experiments of **BisSQ3** in toluene at different concentrations revealed a concentration dependency (Figure S55a), confirming that the spectral change is indeed due to *inter*molecular aggregation. This aggregation in low polar solvent is presumably guided by a combination of dispersion and dipole-dipole interactions of each squaraine chromophore's ground state dipole moments (μ_g, see Figure 62).[27] Notably, the slope of the aggregate absorption band (Figure 63, red solid line) at the long wavelength end of the spectrum is significantly sharpened compared to the dissociated state in $CHCl_3$ (Figure 63, blue solid line), indicating an ordered packing of molecules within a more rigid aggregate structure. Moreover, the aggregate absorption band (Figure 63, red solid line) shows a remarkable bathochromic shift by 134 nm (1270 cm^{-1}, see Figure S52) with respect to the dissociated state in $CHCl_3$ as well as a band narrowing (*FWHM* = 500 cm^{-1}), indicating pronounced J-type exciton coupling resulting from *inter*molecular aggregation. Compared to the single reference **SQ**, the shift is even larger (2300 cm^{-1}, see Figure S52). It is important to note that these aggregation-induced changes of the optical properties are entirely different from those observed for the solid-state self-assembled **SQ** where two main absorption bands originated from *inter*molecular charge transfer (ICT) mediated coupling due to significant donor-acceptor overlap.[170] Such spectral feature caused by ICT within squaraine aggregates leads to the quenching of the fluorescence as discussed in *Chapter 4*.[131] Here, **BisSQ3** aggregates show only one bathochromically shifted absorption band, indicating less contribution of ICT. This further implied a more slipped arrangement between the neighboring squaraine units where the distance between donor and acceptor is larger, which will be discussed below in more detail.

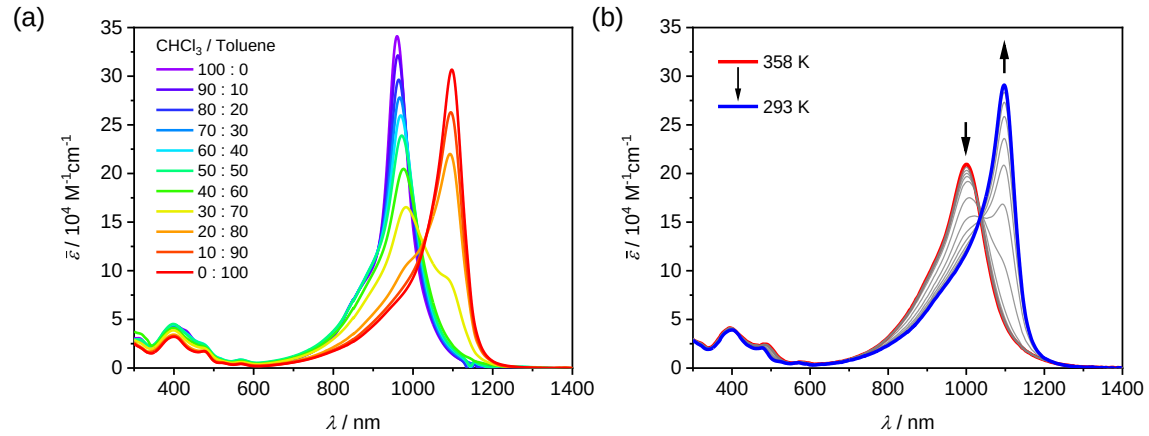

Figure 64. (a) UV/Vis/NIR spectra of **BisSQ3** in $CHCl_3$/toluene mixtures at specified ratios (c_0 = 2.5 × 10^{-6} M, T = 293 K). (b) Temperature-dependent UV/Vis/NIR spectra of **BisSQ3** in toluene (c_0 = 2.5 × 10^{-6} M) from 358 K (red) to 293 K (blue) with a cooling rate of 5 K/min.

In order to verify the absence of additional aggregation pathways, temperature-dependent measurements with different temperature ramps (5 K/min and 0.1 K/min) were carried out. As shown in Figure S55b, the heating and cooling profiles are similar regardless of the temperature ramp, which confirms that no out-of-pathway species is present. In addition, a minor hysteresis can be observed while cooling down the solution, implying a small kinetic effect of the aggregation process. The plot of apparent molar extinction coefficients at 1095 nm against temperature hints by the step rise upon aggregation toward a cooperative self-assembly process. However, upon decreasing the concentration from 5.5 × 10^{-5} M to 6.0 × 10^{-7} M, there is no significant change in the absorption band (Figure S56). Therefore, a quantitative analysis of the self-assembly mechanism of **BisSQ3** in pure toluene was not possible *via* concentration-dependent studies since the complete self-assembly process cannot be monitored by means of UV/Vis/NIR spectroscopy.

Aggregates with strong J-type coupling are expected to exhibit an enhanced fluorescence, therefore, we investigated the emission properties of **BisSQ3** aggregate in toluene. As shown in Figure 63, a weak emission at 1116 nm (dashed red line, λ_{ex} = 985 nm) with marginal Stokes shift of 160 cm^{-1} was detected. It is noteworthy that at the concentration (c_0 = 5.5 × 10^{-5} M) of the measured solution, the absorption spectrum revealed a nearly fully aggregated state of **BisSQ3**, indicating that the emission originating from the dissociated species is negligible. In combination with the significantly bathochromically shifted and narrowed absorption band, the J-aggregate excitonic characteristic is indeed confirmed. Unfortunately, a precise determination of Φ_{FL} was not possible due to the low signal-to-noise ratio with our fluorescence setup even without polarizers and maximum slit opening as well as due to the extremely small

Stokes shift. Detailed optical properties of **BisSQ3** aggregates in toluene are summarized in Table 5.

5.2.4 Structural Investigations

In order to gain structural insight into the **BisSQ3** aggregates, atomic force microscopy (AFM) measurements of **BisSQ3** on various substrates were performed. The spin-coating of the aggregated sample solution (c_0 = 1.5 × 10^{-5} M) from toluene onto hydrophobic silica wafer leads to the deposition of helical fiber-like aggregates (Figure 65) with the average diameter of 1.8 ± 0.3 nm and length of up to 150 nm and a helical pitch of 10–13 nm. Similar morphologies can be observed on HOPG as well as hydrophilic mica surfaces constituting either rod-like aggregates with a diameter of 1.6 ± 0.2 nm, (Figure S57) or fiber-like aggregates with a diameter of 2.1 ± 0.2 nm (Figure S58), respectively. Notably, the aggregates tend to co-agglomerate on HOPG and thus form sheet-like structures (Figure S57). A slight difference in the diameter of the aggregates on various substrates can be explained by the degree of the interaction, presumably guided by the trialkoxyphenyl wedges and the substrates of different surface energies. However, the dimensions and the same type of 1D morphologies can be observed regardless of the choice of the substrates, indicating only a minor influence of the substrates on the aggregate structures after deposition.

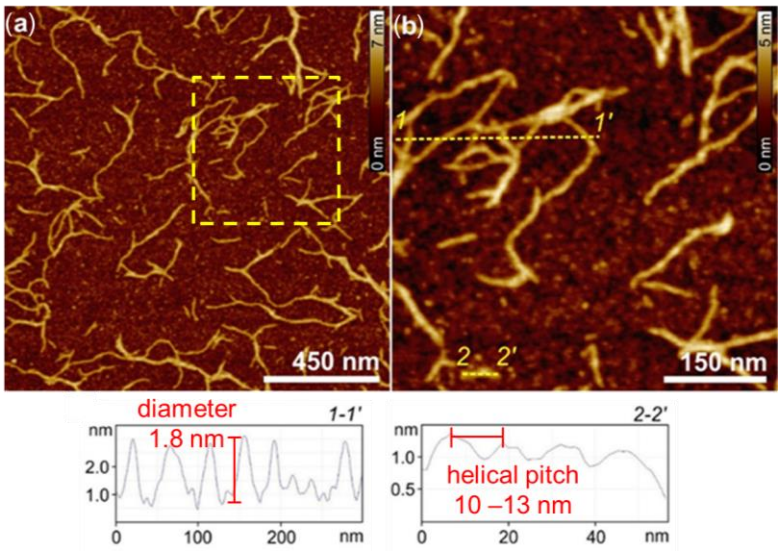

Figure 65. AFM height images of **BisSQ3** aggregates deposited by spin-coating from a toluene solution (c_0 = 1.5 × 10^{-5} M) onto silicon wafer at 2000 rpm. *Z* scales are 7 nm in (a), and 5 nm in (b). Image (b) is the enlargement of the dashed yellow box in image (a). The bottom image shows the cross-section analyses from the yellow dashed lines 1-1' and 2-2' in image (b).

To derive a packing model for the **BisSQ3** nanofiber, we first performed geometry optimization for the molecular structure of **BisSQ3** by varying the dihedral angle α between the dipolar squaraine units using the semi-empirical PM6 method (Figure S59).[171] The results reveal two energetic minimum structures for **BisSQ3** with different dihedral angles (α) of −126.8° (53.2°) and 133.1° (−46.9°), respectively, while always aiming for a cancellation of the two partial ground state dipole moments of the two covalently linked dipolar dyes. The length along the long axis of the molecule is about 3.0 nm (Figure S59). In less polar solvent, the self-assembly of squaraine dyes is strongly driven by the dipole-dipole interactions due to their μ_g as well as the π-π interactions, therefore, an antiparallel π-stacking of the squaraine chromophores to cancel the respective partial μ_g (Figure 66a, purple arrows) is rationally proposed. Owing to the structural distortion between the chromophores[118] and the additional steric hindrance contributed by the bulky trialkoxyphenyl substituents, we suggest a strongly slip-stacked arrangement of the **BisSQ3** molecules enabling J-type exciton coupling (Figure 66a, red arrows), which is in line with the significant bathochromic shift of the absorption spectrum of **BisSQ3** aggregates. This spectral feature is in contrast to the solid-state self-assembly of **SQ**[170] and many other NIR absorbing but non-emissive squaraine-based solid-state materials[98,99] that exhibit two characteristic main peaks in the absorption spectrum originated from *inter*molecular charge transfer mediated coupling. Hence, a more slipped arrangement between the interacting squaraine units is suggested to give weaker donor-acceptor interactions while manifesting the J-type coupling, which can be further supported by the smaller slip angle ($\theta \sim 23°$) shown in Figure 66b and Figure S60 (for details, see *Appendix*, *Chapter 9.3*).

Taking the size of the molecule elucidated from the calculated structure and the helical pitch revealed by AFM into account, one turn of the helical fiber should contain six molecules (Figure 66b), which in turn yields the ideal dihedral angle α to be 60° (for more details, see *Appendix*, *Chapter 9.3*). Considering the slight conformation change due to *inter*molecular interactions, this is in good agreement with the calculated minimum energy structure where a dihedral angle α is about 53.2° (Figure S59).

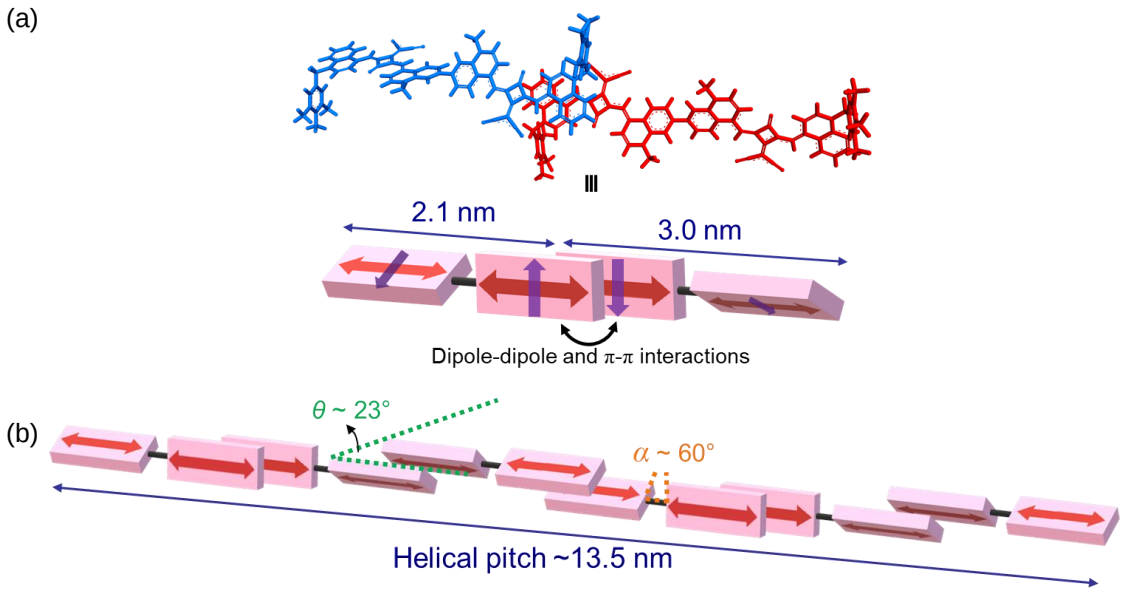

Figure 66. (a) Slip-stacked packing motif of two **BisSQ3** molecules. The red double head arrow represents the transition dipole moment, while the purple arrow the ground state dipole moment in the schematic representation. (b) Proposed packing motif of six molecules of **BisSQ3** to form one helical pitch within the nanofibers of **BisSQ3**.

Our tentative packing model reveals that the strategy of connecting two squaraine dyes in a head-to-tail fashion successfully triggered the formation of an aggregate with J-type exciton coupling in less polar solvents. Although there are halogenated squaraine dyes analogous to **SQ** reported which tend to aggregate in toluene, they all form cofacially stacked H-type aggregates driven by the anti-parallel alignment of their μ_g as well as dispersion forces, thus resulting in blue-shifted absorption spectra.[28] In contrast, **SQ** exhibits no aggregation behavior in toluene[28] but forms *inter*molecular charge transfer mediated J-type coupling in thin films (λ_{abs} = 1040 nm) which could be successfully applied in ultra-narrow bandwidth NIR organic photodiodes.[170] However, like for other previously utilized squaraine aggregates,[69,131] this kind of bathochromically shifted lowest energy excited state is non-fluorescent and should be distinguished from the fluorescent one reported for **BisSQ3**.

Moreover, the choice of donor moiety for the squaraine core structure is crucial. Dicyanomethylene substituted squaraine dyes are known to possess a C_{2v} symmetry, which mostly leads to a bent structure.[27] In *Chapter 3*, we have reported a bis(squaraine) dye based on benzothiazole donors with bent chromophores,[118] which gives rise to a *transoid* S-shaped and a *cisoid* folded conformation that exist as minimal energy structures in solution.[39,126,127,172] The former leads to an *intra*molecular J-type coupling, but the coupling strength is weaker compared to **BisSQ3** due to the larger distances between the two chromophores as well as not completely collinear alignment, resulting in a smaller spectral shift (800 cm^{-1}). In addition, the

cisoid conformation exhibits a side-to-side arrangement of the transition dipole moments, thus contributes to an undesired blue shift in the absorption spectrum due to H-type exciton coupling.[39,118] In contrast, the geometry optimization scan for **BisSQ3** reveals that at the two potential energy minima, both conformations exhibit an almost head-to-tail arrangement between the two chromophores (Figure S59, bottom), facilitating strong *intra*molecular J-type coupling that causes a significant bathochromic shift (1020 cm^{-1}) with respect to **SQ**. This head-to-tail arrangement is due to the proper choice of the donor moiety for **BisSQ3**, i.e., a quinoline moiety, leading to a linear alignment of the chromophores.

5.3 Conclusion

In conclusion, we have designed a new bis(squaraine) dye **BisSQ3** composed of two collinearly aligned dipolar chromophores which shows a strongly bathochromically shifted absorption maximum at 961 nm with respect to the single squaraine dye due to *inter*molecular J-type coupling. The narrow fluorescence with only 110 cm^{-1} Stokes shift shows an emission maximum at 971 nm with a quantum yield of 0.33% in chloroform. In less polar toluene, this **BisSQ3** self-assembles into helical nanofibers with a diameter of 1.8 nm and a helical pitch of 10 – 13 nm according to AFM studies. Remarkably, the absorption spectrum of the self-assembled species exhibits a pronounced bathochromic spectral shift into the NIR-II window with an absorption maximum as high as 1095 nm and emission maximum at 1116 nm due to additional *inter*molecular J-type coupling. Combining the experimental results of absorption spectroscopy and AFM studies with geometry optimization calculations, we were able to derive a packing model for the **BisSQ3** nanofibers, in which a slip-stacked arrangement of the antiparallel aligned and π-stacked chromophores is proposed. To sum up, we have demonstrated that connecting two quinoline-based squaraine dyes in a head-to-tail fashion leads to both *intra*- and *inter*molecular J-type exciton coupling. This double J-coupling strategy appears as the most rational for designing organic NIR-II emitters with decent luminescence efficiency.

§ Note added in proof:

Whilst this thesis was under evaluation from May to July 2021, an advanced version of this chapter including a theory part has been published: C.-A. Shen, M. Stolte, J. H. Kim, A. Rausch, F. Würthner, *J. Am. Chem. Soc.* **2021**, *143*, 11946–11950. Reprinted with permission. Copyright 2021 American Chemical Society. (https://pubs.acs.org/articlesonrequest/AOR-Y75USPGUZGCTAYXW7PMU)

Chapter 6

–

Selective Parallel G-quadruplex Recognition by a NIR-to-NIR Two-Photon Squaraine

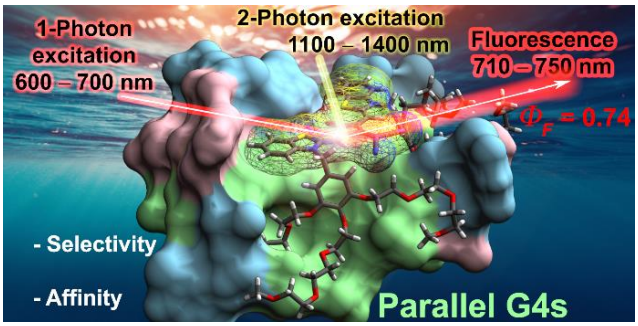

This chapter was published in: V. Grande, C.-A. Shen, M. Deiana, M. Dudek, J. Olesiak-Banska, K.Matczyszyn, F. Würthner, *Chem. Sci.* **2018**, *9*, 8375–8381.
Reprinted with permission from reference 173.
Copyright 2018 Royal Society of Chemistry (Great Britain)

Abstract: Fluorescence imaging probes for specific G-quadruplex (G4) conformations are of considerable interest in biomedical research. Herein, we present the synthesis and the binding properties of a new water-soluble near-infrared (NIR) amphiphilic squaraine dye (**CAS-C1**) which is capable of selective detection of parallel over non-parallel and non G4 topologies. The striking changes in its linear optical response upon binding to parallel G4s give rise to high fluorescence quantum yields ($\Phi_{FL} \approx 0.7$) and one-photon molecular brightness in the far-red-NIR region. The outstanding recognition process of **CAS-C1** for parallel G4s via end-stacking provides binding constants in the nanomolar regime ($K_b = 10^7 – 10^9\ M^{-1}$) awarding it as one of the most potent parallel G4 binders currently available. Moreover, the **CAS-C1**-parallel G4

system exhibits large two-photon absorption (TPA) cross-sections and molecular brightness in the second NIR biological transparency window ($\lambda \approx 1275$ nm), making it an ideal candidate for NIR-to-NIR ultrasensitive two-photon procedures.

6.1 Introduction

Single-stranded guanine-rich oligonucleotides can fold into noncanonical compact, highly stable four-stranded helices known as G-quadruplexes (from here denoted as G4s).[174] Recent studies have demonstrated the occurrence of G4s in human cells and their implication in several key biological events especially those that are disease- and aging-related.[175,176] As a consequence, they are recognized as potential drug targets. To date, over 700000 G4s have been identified across the human genome,[177] especially located in the telomeres at the ends of chromosomes and in the promoter regions of oncogenes. Although indisputable progresses have been made over the past years in the design of G4-binders,[178] the development of more complex multitasking compounds that combine the optimization of both optical performances (excitation and emission wavelengths > 600 nm and high brightness) and G4 structural selectivity/affinity (G4 over duplex binding and among the G4 topologies, Figure 67) remains highly challenging.[179] Indeed, the overwhelming majority of the small optical imaging probes for G4 detection are commonly photoexcited by relatively high-to-moderate energy light (330 – 600 nm)[180,181] in order to generate the emission between the visible and far-red region of the electromagnetic spectrum. Such energies, in particular UV or blue, are in themselves deleterious to cells as they can irreversibly damage DNA and/or induce formation of cytotoxic reactive oxygen species.[182] Furthermore, their excitation and emission wavelengths are confined outside the first and second near-infrared (NIR) biological transparency windows (BTWs, NIR-I: 700 – 950 nm and NIR-II: 1000 – 1350 nm)[183] where absorption and scattering from tissues and oxy/deoxygenated blood is significant, limiting their relevance to 2-D cell cultures and precluding their use in more realistic diagnosis environments, such as in thick tissues or *in vivo* models. The lack of biocompatible fluorescent organic probes in the BTWs has prevented the use of these highly sensitive spectral ranges for in-depth imaging.[183] In addition, the dynamic nature of the G4 structure enable a range of different topologies (e.g. parallel, hybrid and antiparallel) to potentially form under different physiological conditions, making molecular recognition particularly arduous. In our research on G4-probes, we have recently shown that a dicyanovinyl squaraine dye (**SQgI**, Figure 67a)[33] could behave as G4-specific NIR light-up probe. In the complexed state, **SQgl** is emissive at 700 nm upon

excitation at 661 nm through one-photon absorption (OPA) with an impressive quantum yield of $\Phi_{FL} \approx 0.6$. The probe exhibited good selectivity of G4 over duplex, with the dicyanovinyl squaraine dye capable to impart outstanding selectivity over non-G4 structures and remarkable specificity toward parallel G4 topologies. However, this probe presented inherent optical, practical and affinity limitations including: i) moderate solubility, ii) moderate binding constants (K_b values comprised between 105 – 106 M^{-1}) [32,33,88] and iii) excitation wavelengths outside the BTWs. Thus, we speculated that exploring the chemical space around the squaraine core should enable optimization of both optical and DNA binding performances and we decided to decorate the dicyanovinylene squaraine moiety with bulkier water-soluble brush-type groups.

Herein, we present the first example of a water-soluble amphiphilic squaraine dye (hereafter **CAS-C1**, Figure 67a) exhibiting G4-selective fluorescence light-up upon photoexcitation both within the NIR-I ($\lambda_{max} \approx 720$ nm and $\Phi_{FL} \approx 0.7$) through OPA, and within the NIR-II (two-photon absorption cross-section, σ_2, of ≈ 300 GM and two-photon molecular brightness, $\sigma_2 \times \Phi_{FL}$, of ≈ 200 GM at 1275 nm) through TPA. Moreover, the unprecedented nonlinear optical properties of **CAS-C1** are combined with the outstanding selectively for parallel over non-parallel G4 architectures and duplex morphologies of any length and composition awarding it as the best two-photon parallel G4-specific probe currently available.

6.2 Results and Discussion

6.2.1 Design and Synthesis

With the aim to increase the binding selectivity and the solubility of ligand **SQgl**, we decorated the dicyanovinylene squaraine core scaffold with brush substituents carrying six triethylene glycol chains (detailed syntheses and characterizations, see *Appendix, Chapter 9.4*). The massive presence of oligoethylene glycol chains is not only beneficial for the solubility of the ligand, but it is also known to strengthen the affinity of the ligand toward the parallel G4s upon noncovalent interactions within the grooves: this approach is reported in the literature and has been exploited in the design of selective G4-ligands.[184] The molecular design of dicyanovinyl squaraine revealed a suitable choice in terms of affinity and selectivity with G4s.[33] Additionally, the donor-acceptor-donor (D-A-D) nature of the chromophores[27] appeared very promising for multi-photon absorption processes at long-infrared wavelengths. The synthesis according to the route shown in Figure 67a starts from the reported brush precursor **C1**, which was

brominated to give the corresponding bromide **C2** which underwent a nucleophilic substitution with methyl-benzothiazole to give **C3**. Following the reported synthetic procedure for dicyanovinyl squaraines,[27] **CAS-C1** was obtained after condensation of the squaric ester **C4** with two equivalents of methyl-benzothiazolium **C3**. Squaraine **CAS-C1** revealed fairly good solubility in various organic solvents. The absorption and emission spectra in these solvents revealed a moderate negative solvatochromism (Figure S76) and can be assigned to monomeric species (Figure S75).

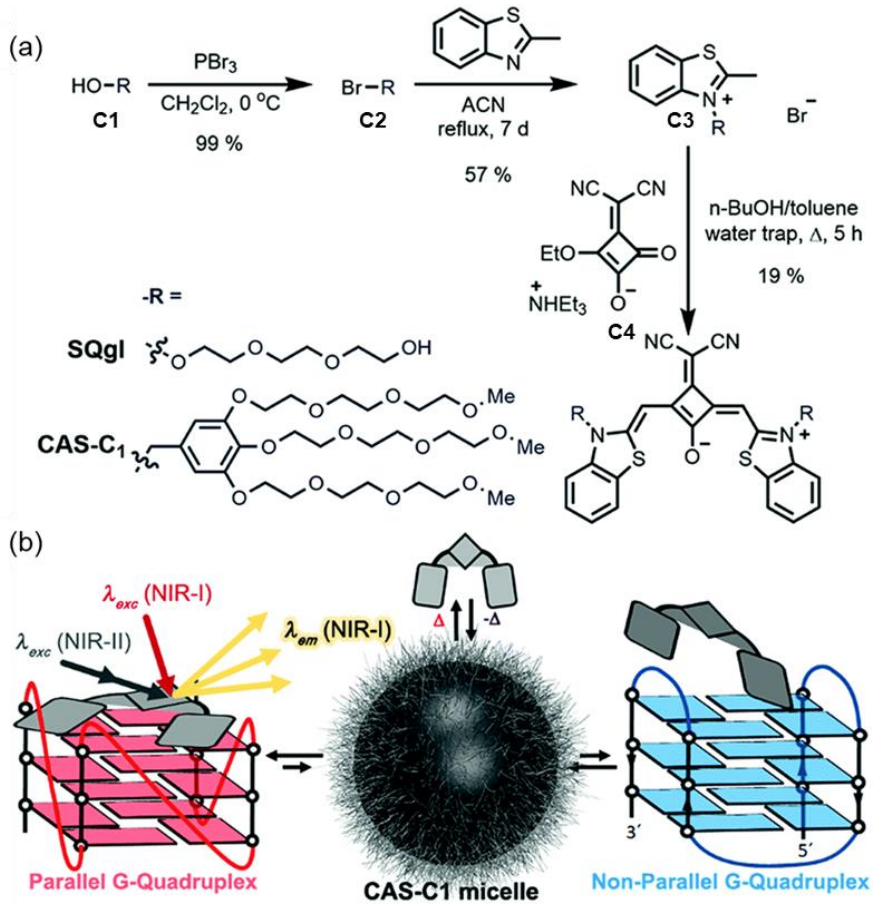

Figure 67. (a) Synthetic route to **CAS-C1**. (b) Schematic illustration of the multiphotonic selective detection mechanism: the squaraine shows amphiphilic assembly in water into micelles. The formation of a stable complex with parallel G-quadruplex (left) is able to displace the squaraine from the micellar aggregate and trigger the fluorescent emission in the NIR-I biological window upon both monophotonic excitation in the NIR-I and biphotonic excitation in the NIR-II. **CAS-C1** bestows high selectivity of interactions over non-quadruplex and non-parallel G4 structures (right).

6.2.2 Aggregation in Water

In aqueous solution, **CAS-C1** absorption spectra reveal a different band shape and a strongly blue-shifted absorption maximum at 632 nm with an apparent extinction coefficient

ε_{max} = 6.2 × 10^4 M^{-1} (Figure 68a, red line) which are first evidences for an H-type exciton coupling between aggregated dyes.[130]

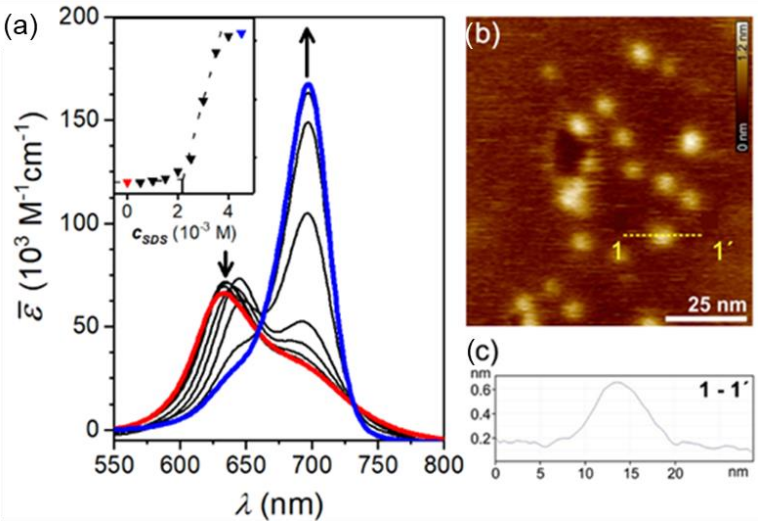

Figure 68. (a) UV/Vis absorption spectra of an aqueous **CAS-C1** solution (c_0 = 3.0 × 10^{-6} M, 25 °C, red line) and upon addition of increasing amounts of SDS. The inset shows the incorporation of the squaraine dye in the SDS micelle upon addition of the surfactant with a critical concentration of 2.1 × 10^{-3} M. (b) AFM height images on mica after spin coating the **CAS-C1** aqueous solution (3.0 × 10^{-6} M). *Z* scale is 1.2 nm. (c) Cross-section from yellow dashed lines 1−1'.

Atomic force microscopy (AFM) revealed the presence of small particles with an irregular diameter of 10 – 30 nm and a height of 0.6 – 3.0 nm (Figure 68b) which suggests the formation of micellar structures. The blue-shifted absorption band indicates a cofacial stacking of **CAS-C1** molecules, most likely in an antiparallel fashion in order to cancel the dyes' large dipole moment.[32] Such arrangement explains well the strong H-type excitonic coupling and the quenched fluorescence emission. Due to the massive presence of ethylene glycol chains, **CAS-C1** is particularly suited to form such micellar structure where the hydrophilic parts are predominantly directed to the outside (Figure 67b).

Upon heating to 95 °C, **CAS-C1** micellar aggregates become disfavored for entropic reasons leading to a new band at 676 nm with isosbestic point at 653 nm. These changes are reversible and are ascribed to the formation of the monomeric species in water, with the typical fluorescence emission peaked at 699 nm (Figure S77A). Global fitting of the temperature-dependent measurement in the range 550 – 750 nm is in good agreement with an isodesmic aggregation mechanism (Figure S77B). Despite the fact that the pure monomeric state is not fully reached in water, the extrapolation of the fitting at 676 nm predicts a reasonable value for monomeric **CAS-C1** of ε_{max} = 9.0 × 10^4 $M^{-1}cm^{-1}$. In accordance with the disaggregation model,

a fluorescence emission in water lights-up at 699 nm (Figure S77A, dotted line). In contrast, the emission profile of **CAS-C1** in its aggregated form is fully quenched due to nonradiative relaxation pathways in its H-aggregate state. In order to investigate the photophysical properties of the excited states, time-correlated single photon counting (TCSPC) measurements of **CAS-C1** in water at 80 °C were performed. The time-dependent decay fitted better with the biexponential function (Eq. S31) suggesting the coexistence of two different species: one with longer lifetime (τ_1 = 4.76 ns), consistently ascribed to the excited state of the free monomer in solution; the other one with shorter lifetime (τ_2 = 1.35 ns), ascribed to the species aggregated in the micellar structure (Figure S78). The dramatic decrease of both the lifetime and the emission intensity is therefore in accordance with the formation of additional radiationless pathways in the aggregated form.

A more efficient approach to disassemble **CAS-C1** into monomeric dyes is provided by the addition of surfactant molecules. Thus, we performed titration with sodium dodecyl sulfate (SDS) (Figure 68a). The surfactant affects moderately the formation of the micelles at lower SDS concentration. Above the critical concentration of 2.1×10^{-3} M, SDS induces a marked breakup of **CAS-C1** micelles by dissolving the **CAS-C1** monomer within the SDS micelles (Figure 68a).

6.2.3 G4 Binding

In a similar fashion to the disaggregation induced by SDS, molecular recognition of **CAS-C1** to suitable π-surfaces should also cause the disassembly of the micelle. This idea prompted us to study the recognition process of the squaraine toward a large panel of biologically relevant G4 topologies such as those found in the human telomeres (Tel-22) and minisatellite (Ceb25), in the proto-oncogene involved in the tumorigenesis of urinary bladder cancer (hRAS1), in the promoter region of myc, kit, KRAS, bcl2, and vav genes (c-myc, c-kit2, c-kit87up, KRAS 32, KRAS 22, bcl2 VAV1), in the vascular endothelial growth factor (VEGF) gene, in the telomeric transcripts (TERRA) and the thrombin-binding DNA aptamer (TBA) (see *Appendix*, *Chapter 9.4*, for details concerning the G4 topologies and their folding process). Indeed, upon addition of parallel G4s (e.g. VAV-1, c-myc and VEGF) the disappearance of the absorption band of **CAS-C1** aggregate along with the formation of a new bathochromically shifted band centered at ≈ 700 nm indicate the formation of G4 (parallel):**CAS-C1** complexes (Figure 69 and S80, S81). Concomitant with absorption changes, the steady-state emission of the squaraine fluorophore upon excitation at λ_{ex} = 660 nm, almost fully quenched in its aggregated

unbound state (λ_{em} = 698 nm), lights-up in the NIR-I at λ_{em} ≈ 720 nm (Figure 69a and S82, S83).

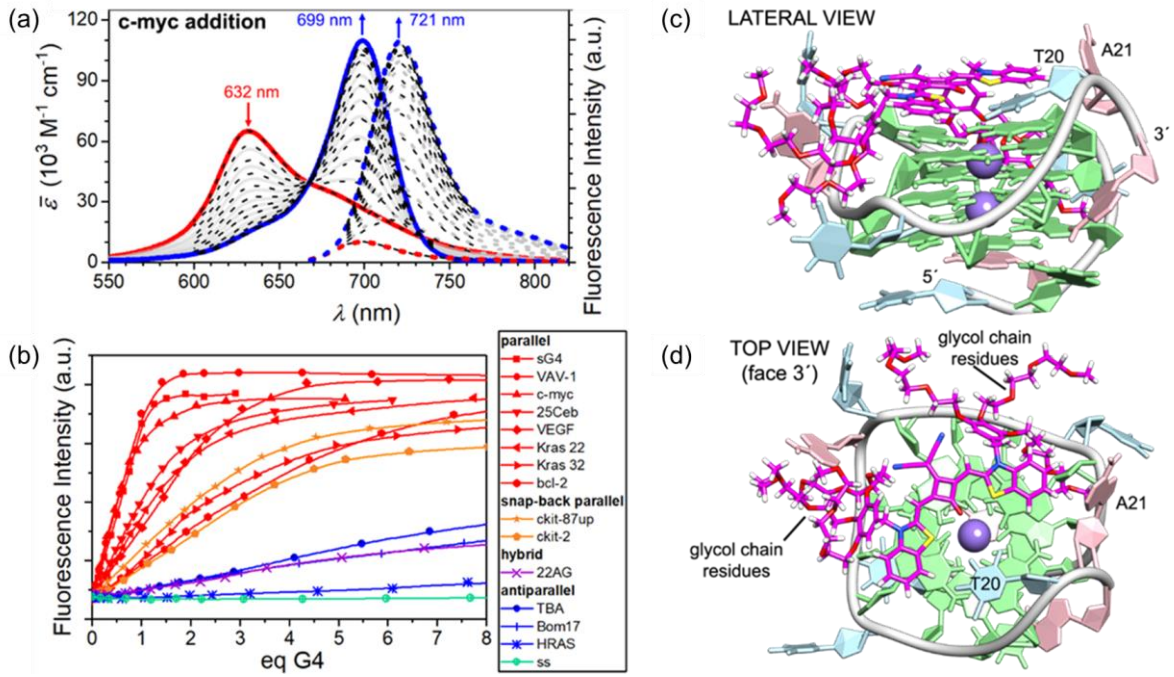

Figure 69. (a) Visible/NIR absorption (solid lines) and fluorescence spectra (dotted lines, excitation on the isosbestic point at 660 nm) of a **CAS-C1** buffered solution in water (1.66×10^{-6} M, TRIS buffer c = 10 mM, pH = 7.2, KCl c = 100 mM) upon addition of c-myc G4 at 25 °C (red and blue lines correspond to the spectra at 0 eq and 3.4 eq respectively. Superimposed black dotted line results from a global fitting with a 1:1 binding model ($K_b = 9.7 \times 10^6$ M−1). (b) Fluorescence titrations of the **CAS-C1** buffered solution in water upon addition of various G4s sequences at 25 °C: the plots show a clear-cut preference of the squaraine for the parallel G4s (in red). (c-d) Docking lowest energy binding models for **CAS-C1** with c-myc (score function $\Delta E = -5.9$ kcal mol^{-1}).

Notably, both the absorption and the emission bands are ≈ 20 nm redshifted compared to the spectrum of the monomeric squaraine in water (Figure S77). This is a clear indication of a direct interaction of the cyanine π-surface of **CAS-C1** with the guanines of the parallel quadruplexes. The excitation spectra and the lifetime decays recorded for **CAS-C1** in the presence of G4s indicate that the strong photoluminescence observed arises mainly from the **CAS-C1**:G4 complex through geometrical and structural restrictions which inhibit the nonradiative relaxation pathways, hence the increased lifetime and Φ_{FL} (Figure S84–S86). TCSPC decay trace of the **CAS-C1**:G4 excited states (Figure S85–S86) showed the presence of only one species, ascribed to the complexed squaraine, in accordance with the monoexponential function (Eq. S30). The singlet state lifetimes obtained by fitting of time-resolved fluorescence decays of the **CAS-C1**:G4 complexes are generally longer than the ones in organic solvents and comprised in the range 5 – 6 ns (Figure S76B). This relatively

long lifetimes with outstanding Φ_{FL} in the 700 – 800 nm range makes **CAS-C1** particularly intriguing candidate as a fluorescence lifetime-based probe for G4 live-cell visualization by fluorescence lifetime imaging microscopy (FLIM).

Comparison of absorption and fluorescence responses between parallel and antiparallel G4s as well as single- and double-stranded DNA of any length and composition indicates a clear-cut binding preference of **CAS-C1** for G4 parallel topologies (Figure 69b). This was further confirmed by duplex DNA competition titration assays (Figure S93, S94) which revealed very modest interference of interaction with c-myc and VAV-1, even in the presence of 50 eq of the ds-DNA.

It turned out that probe accommodation within the hydrophobic G4 scaffolds exert changes in the polarity of the surrounding that well-match an E_T^N value of 0.6 (Figure S76). The optical changes arising in the absorption and emission profiles of the **CAS-C1**-parallel G4 systems result in excellent one-photon brightness (defined as the product $\varepsilon \times \Phi_{FL}$) in the NIR region with values comprised between 56 and 84 × 10^3 M^{-1} cm^{-1} (Table 6).

As suggested by recent publications,[185,186,187] the issue of the binding stoichiometry of the complexes in solution was assessed by Job´s plot titration assays (Figure S87–S89), the tangent method and a global fitting based on both the 2:1, 1:1 and 1:2 binding models (Figure S90–S92). If compared with the previously reported **SQgl**, **CAS-C1** also showed multiple binding with the G4s, except for sG4, VAV-1 and c-myc.

A detailed quantitative binding data analysis that takes into account 1:1 and 1:2 **CAS-C1**:G4 stoichiometries with associated (anti-)cooperative effects indicates that **CAS-C1** exhibits higher binding constants for parallel topologies such as c-myc (Figure 69 c,d) with respect to antiparallel and non-G4 topologies with values that exceed by two-orders of magnitude those for the previously reported squaraine **SQgI** (see *Appendix, Chapter 9.4*, for details concerning the quantitative binding data analysis).[33] These results are ascribed to the highly accessible parallel G-quartets which, being devoid of adjacent lateral or diagonal loops, provide better π-stacking platforms for the accommodation of the squaraine core, thereby resulting in a better planarity and thus in a more efficient rigidification as desired for a fluorescence increase. On the other hand, the negative effect of the external quartets surrounded by loops in antiparallel G4s such as 22AG and c-kit hampers to some extent the end-stacking ability of **CAS-C1** inducing a lower overall optical response. The aforementioned rationale is confirmed by using the closely related c-myc G4 analogue sG4, featuring no flanking overhang residues at both 5´

and 3´ ends that limit the steric hindrance, to enhance the light-up ability of **CAS-C1**. Indeed, complexation of the squaraine with sG4 provides a Φ_{FL} of 0.74 which is among the highest values reported for nucleic acid complexes within comparable spectral range (Table 6).[188,189]

Table 6. Summary of the spectroscopic properties and the binding constants of the complexes of **CAS-C1** with various G4s.

G-Quadruplex	λ_{max} (nm)	ε_{max} (10^3 M^{-1} cm^{-1})	λ_{em} (nm)	K_{11} (M^{-1})	K_{12} (M^{-1})	τ (ns)	Φ_{FL}	$\varepsilon_{max} \times \Phi_{FL}$ (10^3 M^{-1} cm^{-1})
sG4	699	114	722	8.1×10^6	-	5.8	0.74±0.07	84
VAV-1	699	118	722	1.2×10^7	-	5.6	0.67±0.02	79
c-myc	699	108	721	9.7×10^6	-	5.5	0.52±0.03	56
25Ceb	698	108	719	3.2×10^7	1.1×10^6	6.0	0.66±0.01	71
VEGF	699	113	721	1.4×10^2	6.5×10^9	5.7	0.74±0.08	84
Kras 22	699	116	721	2.7×10^8	9.2×10^5	5.4	-	-
Kras 32	699	103	721	3.6×10^6	3.5×10^5	5.6	-	-
bcl-2	699	113	721	4.3	8.1×10^9	-	-	-
ckit-87up	699	103	721	1.2×10^4	1.0×10^7	5.5	-	-
ckit-2	699	92	720	3.0×10^2	4.6×10^8	-	-	-

Structural insights into the binding mode of **CAS-C1** with G4s were provided by docking binding analysis on the G4s whose structures in solution had been derived by NMR studies under similar experimental conditions. The elucidated structures of G4s are referenced in Table S5. In the case of c-myc, the squaraine chromophore is the recognition unit leading to a perfect complementary match with the 3´-quartet (Figure 69c). However, the substitution of side groups at the squaraine chromophore has surely an impact in the binding. On one side, the massive number of glycol chains are responsible for the enhanced interaction compared to **SQgl** by establishing strong electrostatic interactions with the polar backbone of the G4. Presumably, the glycol chains displace water molecules from the grooves and thereby provide an entropic contribution to the stability of the G4-**CAS-C1** complex, especially for the parallel ones,[190] which explains the strengthening of the binding affinity compared with **SQgl**. On the

other hand, it is reasonable to assume that the steric hindrance of the benzyloxy unit, which is accommodated in the hydrophobic pockets in the side of the quartet (Figure 69c,d), largely contribute to the selectivity of the interaction. It is noteworthy that the binding constant for the 1:1 binding of Kras 22 is ≈ 20-times higher than for other high-affinity parallel G4 (e.g. c-myc, VAV-1 and c-myc). Despite the structure of Kras 22 is not yet fully elucidated in solution, structural comparison shown in Table S6 suggests that the extra thymine located within one of the G-runs in the Kras 22 may be responsible for an apparent stabilization of the complex with **CAS-C1**.

6.2.4 Two-Photon Absorption

A fundamental optical limitation is encountered at the nanoscale level owing to Abbe's law of diffraction, which limits the maximum spatial resolution to approximately half the wavelength of light used to image the specimen.[191] One way to overcome this limitation involves the use of nonlinear optical procedures based on multi-photon absorption processes. In this approach, the excitation of a chromophore is performed by the simultaneous absorption of two-photons with half the energy required for the corresponding one-photon absorption process. As a result, the excitation wavelength is confined in the first and second NIR biological transparency windows where the diffusion and absorption of light by inherently biological matrices is minimized, and thus allowing deep tissue penetration. Moreover, the low-energy excitation prevents photobleaching and cellular damages in biological samples. Importantly, the TPA is limited to a small femtoliter volume and occurs only at the focal point of a focused laser beam resulting in 3D image resolution. Despite the lower energy of the IR light compared to visible and UV light, this excitation mode has been proven to induce damage to the samples when using classical fluorophore that possess low TPA cross-section (σ_2 < 50 GM).[192] It turns out that, besides having significant photoluminescence properties in the NIR, a chromophore should also possess high σ_2 values to be considered as a suitable probe for two-photon microscopy procedures in NIR-to-NIR configurations. The TPA spectra of **CAS-C1** complexed with parallel G4s including VAV1, VEGF and c-myc were measured by two-photon excited fluorescence (TPEF) method in the range 1000 − 1550 nm and are reported in Figure 70 as $\sigma_2 \times \Phi_{FL}$.

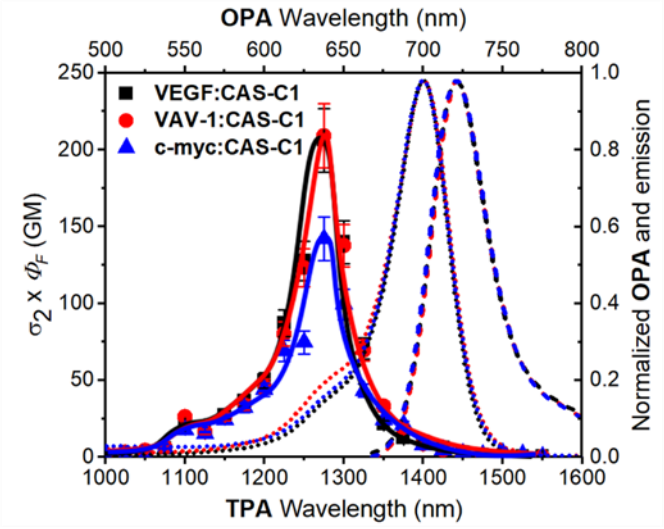

Figure 70. Two-photon molecular brightness ($\sigma_2 \times \Phi_{FL}$) plot of **CAS-C1** in the presence of VEGF, VAV-1 and c-myc (10 mM Tris, 100 mM K^+, pH 7.2) at molar ratio (r) = 7. The values of the Φ_{FL} used are tabulated in Table 6. As a comparison, the OPA corresponding to the double of the energy of the TPA is shown (top and right axis): the absorption (dotted lines) and emission (dashed line) spectra corresponding to the **CAS-C1** complexes with the G4s are shown.

In general, all the complexes show similar TPA spectra composed of an intense high energy TPA band blue shifted compared to the one-photon transition energy and a weak low energy TPA band that matches well the wavelength-doubled 1PA spectra. These spectral features are usually associated with centrosymmetric quadrupolar molecules, in which selection rules for 1PA and 2PA electronic transitions are mutually exclusive. **CAS-C1** presents a non-centrosymmetric character with a quasi-C_{2v} symmetry and can be treated as bent quadrupolar chromophores, of which the quadrupolar conformation gives rise to an intense hypsochromically shifted TPA while the residual dipolar character results in a weak TPA transition overlapped with the 1PA maximum. Similar conclusions were recently reported for extended Michler's ketone, heptamethine, diarylboryl and anthracenyl derivatives.[193] The TPA cross-section (σ_2) values for the **CAS-C1**:G4 systems follow the order: **CAS-C1**:VAV1 σ_2 = 312 GM, **CAS-C1**:VEGF σ_2 = 278 GM and **CAS-C1**:c-myc σ_2 = 273 GM at 1275 nm (Figure S99). Interestingly, the **CAS-C1** aggregate also shows TPA absorption close to half energy of the corresponding OPA, in agreement with a centrosymmetric aggregate (Figure S100).

The high values of σ_2 combined with the associated 2PA maximum are an optimal combination for NIR-to-NIR configurations since excitation of **CAS-C1**:G4 systems can be performed within the NIR-II window by TPA (λ_{ex}(2PA) = 1275 nm) with emissions centered within the

NIR-I spectral region ($\lambda_{em} \approx 720$ nm). In line with the trend depicted for σ_2 also the two-photon molecular brightness ($\sigma_2 \times \Phi_{FL}$), as a result of the strong fluorescent enhancement of **CAS-C1** bound to parallel G4s, follow the same order (i.e., **CAS-C1**:VAV1 $\sigma_2 \times \Phi_{FL}$ = 209 GM, **CAS-C1**:VEGF $\sigma_2 \times \Phi_{FL}$ = 206 GM and **CAS-C1**:c-myc $\sigma_2 \times \Phi_{FL}$ = 142 GM at 1275 nm) indicating the suitability of **CAS-C1** to be used as a nonlinear biomarker for parallel G4 detection by using ultrasensitive fluorescence microscopy techniques. These values are nevertheless lower than those observed for monomeric **CAS-C1** in organic solvent ($\sigma_2 \times \Phi_{FL}$ = 386 GM in isopropanol, Figure S98). This result is in agreement with recent results from Goodson and co-workers[194] and some of us[195,196] that relate the changes in the TPA cross-section to the different DNA binding modes. In particular, groove binders exhibit an enhanced TPA cross-section due to the DNA electric field induced enhancement of the transition dipole moment, while intercalators or end-stackers show a decrease in the TPA cross-section when complexed with DNA. Accordingly, this finding also supports our proposal that **CAS-C1** binds to parallel G4s mainly *via* end-stacking mode in agreement with the docking results. The end-stacking ability of **CAS-C1** was further confirmed through electronic circular dichroism (ECD) measurements (Figure S101).[197] Indeed, the native conformation of the parallel G4s was almost not affected by the presence of the squaraine dye indicating no or very weak perturbation on the quadruplex morphologies. By analogy with previously reported data for a G4 intercalator,[196] the absence of conformational changes observed for **CAS-C1**-parallel G4 systems constitutes a definitive evidence of the ability of **CAS-C1** to coordinate the external G-tetrads, ruling out the possible intercalative binding behavior of our probe known to give rise to pronounced structural changes associated with a partially disruption of the stacking interactions that govern G4 formation.

6.3 Conclusions

In conclusion, the herein reported results on a new squaraine dye **CAS-C1** with outstanding binding strength and selectivity towards parallel G4 motif open up a new research line for this fascinating class of NIR fluorophores and functional dyes[183,198] beyond previous applications in organic electronics,[25] photovoltaics[26a] and exciton transport.[199] The **CAS-C1** probe once complexed with parallel G4s exhibits a NIR light-up fluorescence response with quantum yields that go beyond 0.7. As a result, close-to-optimal one-photon molecular brightness in the far red-NIR region can be obtained. The parallel G4 preference of **CAS-C1** is accompanied by binding constants that exceed by two-orders of magnitude those calculated for the previously

reported squaraine **SQgI**. The selectivity of the probe is tested toward a large panel of anti-parallel G4s and single- and double-stranded morphologies of any size and composition making **CAS-C1** a highly discriminatory parallel G4-binder. The docking results showed that the squaraine chromophore bestows the necessary selectivity for the interactions with the G4s. The molecular design of **CAS-C1** allowed us, on the one hand, to increase the selectivity of the interaction by exploiting the more easily accessible G-quartet surface of parallel G4s and, on the other hand, the massive presence of glycol chains in the hydrophobic pocket of the G4 imparted strong affinity. The complexes of **CAS-C1** with parallel G4s also possess strong two-photon absorption with maxima centered at 1275 nm, which make them ideally suited for NIR-to-NIR imaging procedures. Ultimately, the enhanced fluorescence quantum yields and the two-photon absorption cross-section enable one to obtain exceptionally high two-photon molecular brightness values within the NIR-II window that are desired for virtually all ultrasensitive fluorescence spectroscopy and microscopy techniques. These overall findings award **CAS-C1** as the best two-photon parallel G4-specific probe currently available.

Chapter 7

—

Summary and Conclusion

Squaraine dyes have attracted more and more attention in the past decade due to their outstanding optical properties, i.e., typical cyanine-like behavior with strong and narrow absorption and fluorescence along with the easily functionalized molecular structure.[22] One successful approach of core functionalization is to replace one oxygen of the squaric carbonyl group with a dicyanomethylene group, which shifts the absorption and emission into the near-infrared (NIR) region and at the same time leads to a rigid, planar structure with C_{2v} symmetry, resulting in a ground state dipole moment.[27] These characteristics are proven to be beneficial for the π-π aggregation of these squaraines with G-quadruplex (G4) structures, as described in *Chapter 6*. However, such squaraines tend to form dimeric or small aggregates in solution with cofacial chromophore arrangements due to dispersion forces and dipole-dipole interactions, usually leading to H-type exciton coupling with undesired blue-shifted absorption bands and quenched fluorescence.[28] Therefore, the goal of this thesis was the design of dicyanomethylene-substituted squaraine dyes that self-assemble into extended aggregates in solution with J-type coupling, in order to retain or even enhance their outstanding optical properties. Toward this goal, bis(squaraine) dyes were envisioned with two squaraine units covalently linked to trigger a slip-stacked packing motif within the aggregates to enable J-type coupling.

As shown in *Chapter 3*, bis(squaraine) dye **BisSQ1** was synthesized (Figure 71a), in which two dicyanomethylene squaraine chromophores are covalently linked without spacer unit. Aliphatic and hydrophilic side chains were incorporated to provide phase segregation in order to enhance aggregation. Concentration and temperature-dependent UV/Vis/NIR spectroscopy experiments reveal that **BisSQ1** undergoes cooperative self-assembly resulting in J-type aggregates in a solvent mixture of toluene/1,1,2,2-tetrachloroethane (TCE) (98:2, *v*/*v*). The

J-type exciton coupling is evident from the significantly red shifted absorption maximum at 886 nm (Figure 71b) and the fluorescence peak at 904 nm. AFM studies reveal a sheet-like morphology for the aggregates and a tentative packing model could be proposed accordingly. The model indeed suggests a slip-stacked arrangement of the chromophores, which is most likely due to the structural distortion between the squaraine units within the bis-chromophore. In conclusion, this was a first example to direct squaraine dye aggregation in solution to the more desired slip-stacked packing leading to J-type exciton coupling by simply connecting two dyes in a head-to-tail bis-chromophore structure.

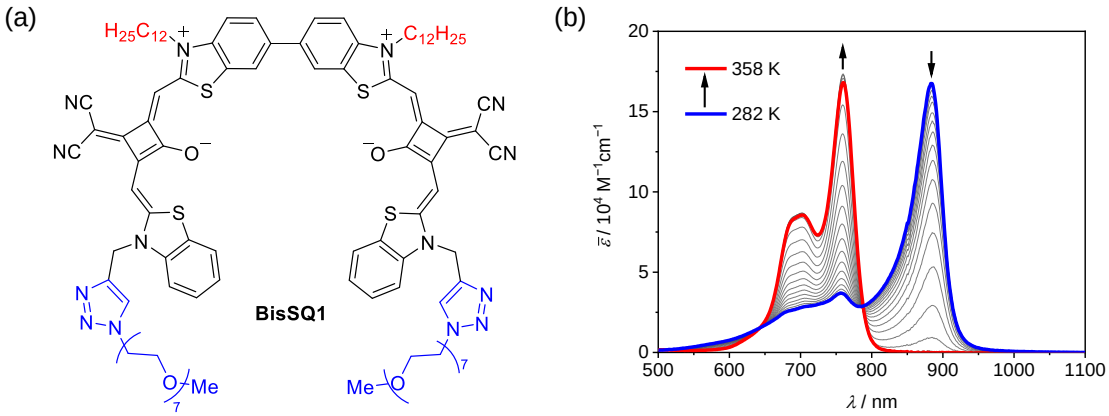

Figure 71. (a) Molecular structure of **BisSQ1** and (b) temperature-dependent UV/Vis/NIR absorption spectra of **BisSQ1** in toluene/TCE 98:2 (*v*/*v*) at $c_0 = 5.0 \times 10^{-6}$ M. The arrows indicate the spectral changes with increasing temperature.

Connecting two squaraine dyes with an additional phenylene spacer (**BisSQ2**) leads to two different polymorphs with very distinct morphologies and absorption spectra upon cooling down a solution of **BisSQ2** in a solvent mixture of toluene/TCE (98:2, *v*/*v*) depending on the cooling rate (Figure 72). Accordingly, rapid cooling resulted in rigid helical nanorods (**BisSQ2-AggI**) with an absorption spectrum showing a panchromatic feature with maxima at 605, 737 and 783 nm, while slow cooling led to a sheet-like structure (**BisSQ2-AggII**) with a significant bathochromic shift in the absorption spectrum (Figure 72, top). Concentration-dependent UV/Vis/NIR studies reveal that the self-assembly processes can be described by the cooperative K_2/K model. Hence, a cooperativity factor of $\sigma = 0.016$ (0.00038) and binding constants for the nucleation of $K_2 = 3.56 \times 10^3\ M^{-1}$ ($2.42 \times 10^2\ M^{-1}$) and for the elongation of $K = 2.18 \times 10^5\ M^{-1}$ ($6.37 \times 10^5\ M^{-1}$) were determined for **BisSQ2-AggI** (**BisSQ2-AggII**). In consequence, **BisSQ2-AggI** is the kinetically favored species, while **BisSQ2-AggII** is the thermodynamically stable aggregate.

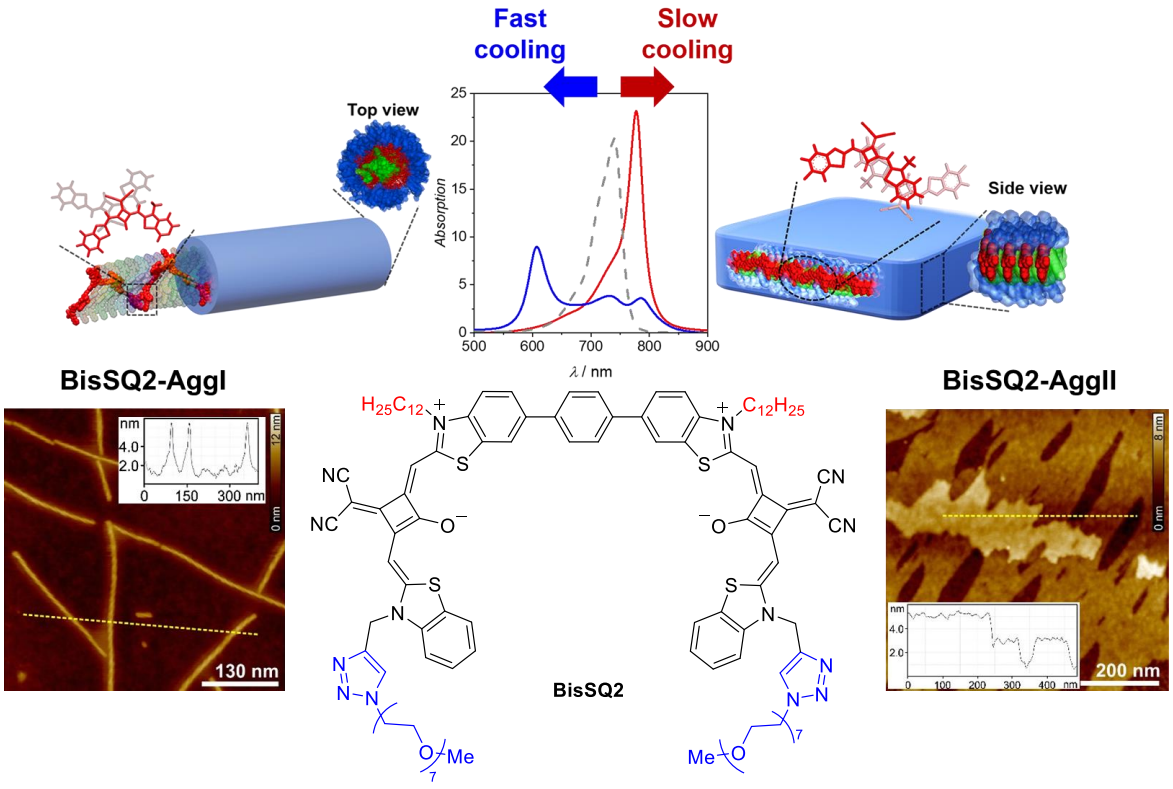

Figure 72. Top: UV/Vis/NIR spectra (middle) of a solution of **BisSQ2** (c_0 = 2.5 × 10^{-5} M, toluene/TCE 98:2) at 85 °C (gray) and those at 25 °C obtained upon rapid cooling (blue: **AggI**) and slow cooling (red: **AggII**). Also shown are the proposed packing models for **AggI** (left) and **AggII** (right). Bottom: Molecular structure of **BisSQ2** (middle) and height AFM image of **BisSQ2-AggI** (left) and **BisSQ2-AggII** (right). The insets display the cross-section analysis from yellow dashed line shown in the AFM images.

According to the morphological information given by AFM and WAXS experiments, packing arrangements for both the thermodynamically stable **BisSQ2-AggII** nanosheets (Figure 72, top right) and the **BisSQ2-AggI** nanorods (Figure 72, top left) could be derived, which further enabled the elucidation of the impact of the chromophore packing on the UV/Vis/NIR absorption spectra of these dye aggregates. It was discovered that the conventional molecular exciton model failed to explain the broad absorption features of **BisSQ2-AggI** for the given packing arrangement, therefore more profound theoretical investigations based on the Essential States Model (ESM) were applied to unveil the importance of *inter*molecular charge transfer (ICT) to adequately describe the panchromatic absorption spectrum of **BisSQ2-AggI**. Moreover, the red-shift observed in the **BisSQ2-AggII** absorption spectrum can be assigned to the interplay of Coulomb coupling and ICT-mediated coupling.

Inspired by the promising results obtained for the bis(squaraine) dyes shown in *Chapter 3* and *4*, *Chapter 5* adopted the same bis-chromophore strategy for the purpose of constructing an NIR

emitter with a bathochromically shifted spectrum. Accordingly, the molecular optical properties and aggregation behaviors of **BisSQ3** based on 4-methylquinolinium donors and two solubilizing trialkoxyphenyl substituents were presented (Figure 73). In chloroform, **BisSQ3** exhibits an absorption maximum at 961 nm with a significant bathochromic shift (1020 cm^{-1}) compared to the reference mono-squaraine **SQ**, indicating *intra*molecular J-type coupling *via* head-to-tail arrangement of two squaraine dyes. Moreover, **BisSQ3** shows a fluorescence peak at 971 nm with a decent quantum yield of 0.33%. In less polar toluene, **BisSQ3** self-assembles into nanofibers with additional *inter*molecular J-type coupling, causing a pronounced bathochromic shift with absorption maximum at 1095 nm and a fluorescence peak at 1116 nm. Thus, it could be shown that connecting two quinoline-based squaraines in a head-to-tail fashion leads to not only *intra*-, but also *inter*molecular J-type exciton coupling (Figure 73), which serves as a promising strategy to shift the absorption and emission of organic fluorophores into the NIR-II window while retaining decent quantum yields.

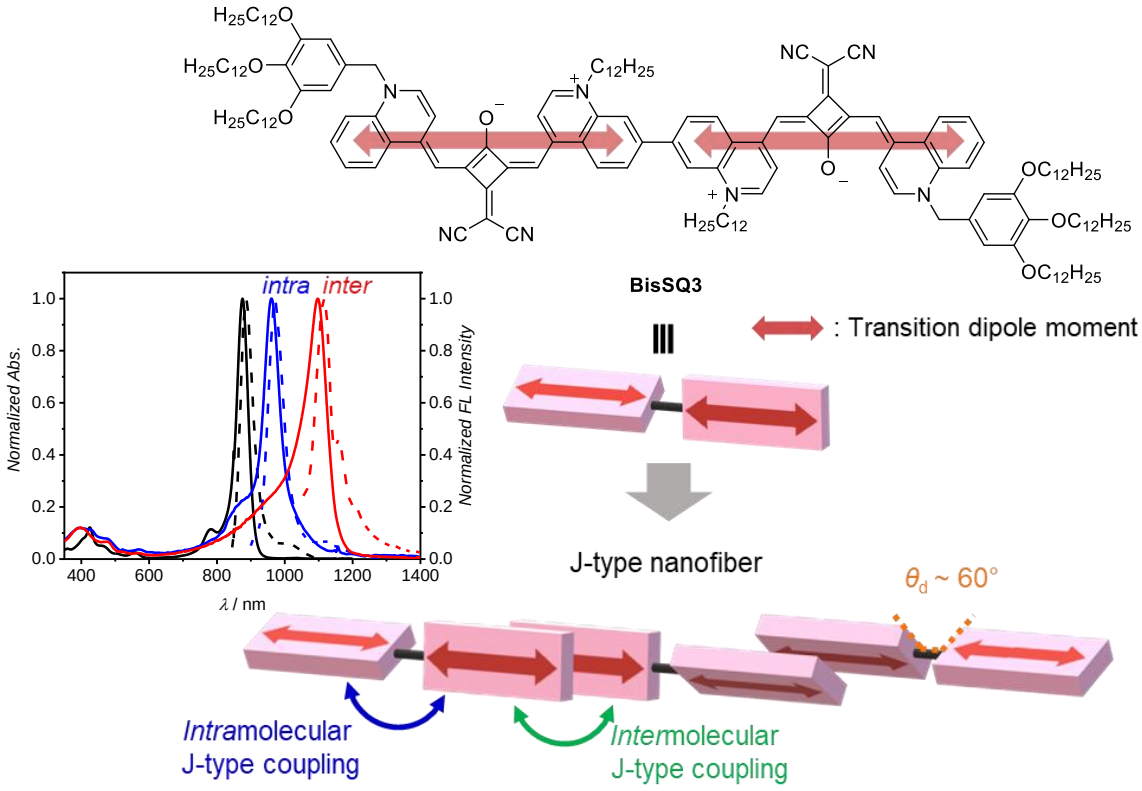

Figure 73. Molecular structure of **BisSQ3** (top) and normalized UV/Vis/NIR absorption (solid lines) and fluorescence (dashed lines) spectra (left) of reference **SQ** in $CHCl_3$ (black, λ_{ex} = 815 nm), **BisSQ3** in $CHCl_3$ (blue, λ_{ex} = 870 nm), and aggregates of **BisSQ3** in toluene (red, λ_{ex} = 985 nm) at 293 K. Also shown is a schematic representation of the proposed aggregate structure of **BisSQ3** (bottom) with the concept for double *intra*molecular (blue arrow) and *inter*molecular (green arrow) J-type coupling. The orientation of the transition dipole moments is illustrated by double-headed red arrows.

In *Chapter 6*, the binding of dicyanomethylene-substituted squaraine **CAS-C1** to G-quadruplex (G4) was described (Figure 74). The water-soluble amphiphilic squaraine dye carries six triethylene glycol chains, providing excellent solubility in water. Its planar core structure interacted well with parallel G4s ($K_b = 10^7 – 10^9\ M^{-1}$) and exhibited an "NIR light-up" fluorescence response with quantum yields > 70%. Moreover, **CAS-C1** manifests outstanding selectivity to parallel G4s according to binding experiments toward a large panel of anti-parallel G4s and single- and double-stranded nucleic acids. The docking results further proved that not only the planar squaraine core facilitates the interaction with the G-quartet surface of parallel G4s, but also the massive presence of glycol chains provides an entropic contribution to the stability of the G4-**CAS-C1** complex. In addition, the complexes also possess strong two-photon absorption with the maximum centered at 1275 nm, which enables NIR-to-NIR imaging procedures. These findings make **CAS-C1** the best two-photon parallel G4-specific probe currently available (Figure 74).

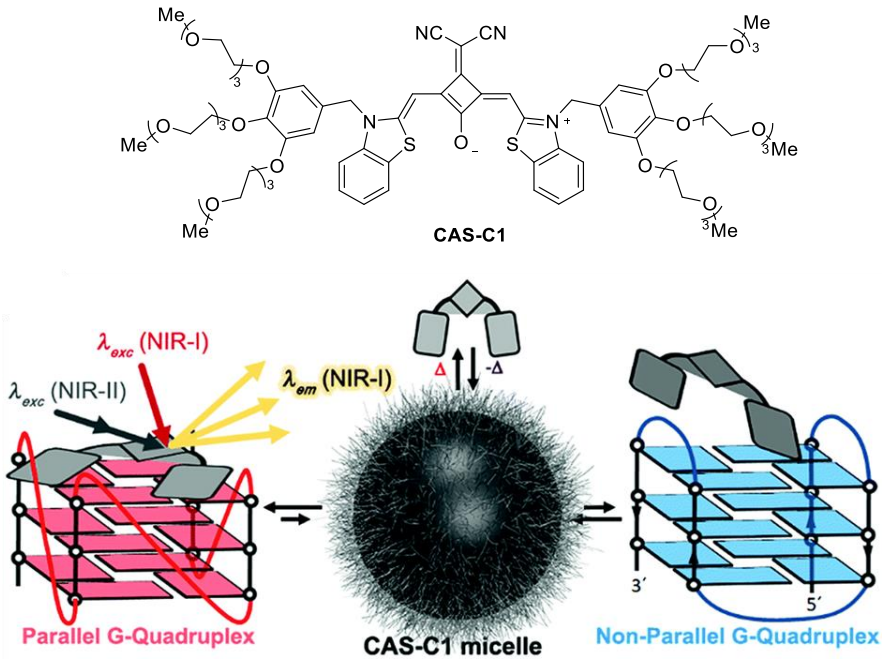

Figure 74. Top: Molecular structure of squaraine **CAS-C1**. Bottom: Schematic illustration of the multiphotonic selective detection mechanism.

In conclusion, this work illustrates based on squaraine dyes how a simple modification of the molecular structure can significantly affect the aggregation behavior and further alter the optical properties of dye aggregates. Elongated supramolecular structures based on dicyanomethylene substituted squaraine dyes were successfully established by covalently linking two squaraine units to form a bis-chromophore structure. Then, a simple but efficient

general approach was established to direct squaraine dye aggregation in solution from the common cofacial stacking with H-type exciton coupling to the more desired slip-stacked packing leading to J-type exciton coupling by directly connecting two squaraine dyes in a head-to-tail fashion without spacer units. Moreover, as shown in *Chapter 4*, the additional spacer between the squaraine dyes in **BisSQ2** allowed different molecular conformations, which leads to two different morphologies depending on the cooling rates for a hot solution. Hence, this is a promising strategy to realize supramolecular polymorphism.

In general, it is expected that the concept of constructing J-aggregates by the bis-chromophore approach can be extended to entirely different classes of dyes since J-aggregates possess a variety of features such as spectral shifts into the NIR window, fluorescence enhancement, light harvesting, and efficient exciton migration, which are commonly observed and utilized for numerous fundamental studies and applications. Moreover, the insights on short-range charge transfer coupling for squaraine dyes is considered of relevance for all materials based on alternating donor-acceptor π-systems. The panchromatic spectral feature is in particular crucial for acceptor-donor-acceptor (ADA) dyes, which are currently considered as very promising materials for the development of bulk heterojunction solar cells.[151]

Chapter 8

—

Zusammenfassung und Fazit

Squarainfarbstoffe haben in den letzten Jahren aufgrund ihrer hervorragenden optischen Eigenschaften, zu denen ein Cyanin-ähnliches Absorptions- und Fluoreszenzverhalten zählt, in Kombination mit einer leicht funktionalisierbaren Molekülstruktur immer mehr Aufmerksamkeit auf sich gezogen.[22] Ein erfolgreicher Ansatz der Kernfunktionalisierung besteht darin, ein Sauerstoffatom der Quadratsäure-Carbonylgruppe durch eine Dicyanomethyleneinheit zu ersetzen, was die Absorption und Emission in den nahen infraroten (NIR-) Bereich verschiebt und gleichzeitig zu einer starren planaren Struktur mit C_{2v} Symmetrie und einem Grundzustandsdipolmoment führt.[27] Diese Eigenschaften haben sich als vorteilhaft für die π-π-Aggregation von diesen Squarainen auf G-Quadruplex (G4) Strukturen erwiesen, wie in *Kapitel 6* beschrieben. Solche Squaraine neigen jedoch zur Bildung von Dimeren oder kleinen Aggregaten in Lösung mit kofazialen Chromophoranordnungen aufgrund Dispersionskräften und Dipol-Dipol-Wechselwirkungen. Dies resultiert in der Regel zu einer H-artigen exzitonischen Kopplung mit unerwünschten, blauverschobenen Absorptionsbanden und gelöschter Fluoreszenz.[28] Daher war das Ziel dieser Dissertation, Dicyanomethylen-substituierte Squarainfarbstoffe zu entwickeln, die sich in Lösung zu verlängerten Aggregaten mit J-artiger Kopplung selbst organisieren. Auf diese Weise sollten die ausgezeichneten optischen Eigenschaften der Squarainfarbstoffe erhalten oder sogar verbessert werden. Zu diesem Zweck, wurden Bis(squarain)-Farbstoffe synthetisiert, in denen zwei Squarain-Einheiten kovalent verbunden sind, was zu einer gestapelten Anordnung mit longitudinalem Versatz innerhalb der Aggregate und damit zu einer J-artigen Kopplung führt.

Wie in *Kapitel 3* gezeigt, wurde Bis(squarain) **BisSQ1** synthetisiert (Abbildung 1), bei dem zwei Dicyanomethylen-substituierte Squaraine ohne Brückeneinheit kovalent verknüpft sind. Aliphatische und hydrophile Seitenketten wurden eingebaut, um eine Phasentrennung

bereitzustellen und so die Aggregation zu verbessern. Konzentrations- und temperaturabhängige UV/Vis/NIR-spektroskopische Experimente zeigten, dass **BisSQ1** in einem Lösungsmittelgemisch aus Toluol/1,1,2,2-Tetrachlorethan (TCE) (98:2, *v*/*v*) J-Aggregate nach einem kooperativen Mechanismus bildet. Die *J*-artige exzitonische Kopplung ist aus dem signifikant rotverschobenen Absorptionsmaximum bei 886 nm (Abbildung 1) und der Fluoreszenzbande bei 904 nm ersichtlich. AFM-Studien enthüllten eine blattartige Morphologie der Aggregate, sodass ein Packungsmodell vorgeschlagen werden konnte, in dem eine gestapelte Anordnung der Chromophore mit Versatz vorliegt, was höchstwahrscheinlich auf die strukturelle Verzerrung zwischen den Squarain-Einheiten innerhalb des Bis-Chromophors zurückzuführen ist. Damit stellt dieses System das erste Beispiel dar, in dem Squarainfarbstoffaggregate mit J-artiger exzitonischen Kopplung in Lösung realisiert wurden.

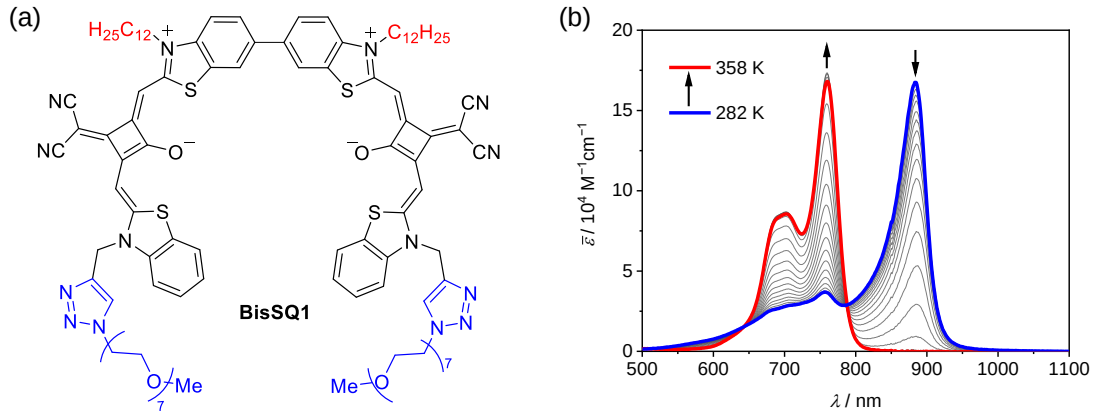

Abbildung 1. (a) Darstellung der Molekülstruktur von **BisSQ1** und (b) temperaturabhängige UV/Vis/NIR-Absorptionsspektren von **BisSQ1** in Toluol/TCE 98:2 (*v*/*v*) bei $c_0 = 5.0 \times 10^{-6}$ M. Die Pfeile geben die spektralen Änderungen mit ansteigende Temperatur an.

Das Verbinden von zwei Squarainfarbstoffen mit einer zusätzlichen Phenyl-Brückeneinheit (**BisSQ2**) führt abhängig von der Abkühlrate beim Kühlen einer Lösung von **BisSQ2** in einem Lösungsmittelgemisch aus Toluol/TCE (98:2, *v*/*v*) (Abbildung 2) zu zwei Polymorphen mit sehr unterschiedlichen Absorptionsspektren. Dementsprechend entstanden beim schnellen Abkühlen starre, helikale Nanostäbe (**BisSQ2-AggI**) mit einem panchromatischen Absorptionsspektrum mit Maxima bei 605, 737 und 783 nm, während ein langsames Abkühlen zu einer blattartigen Struktur (**BisSQ2-AggII**) mit einer signifikanten bathochromen Verschiebung des Absorptionsmaximums führte (Abbildung 2, oben Mitte). Konzentrationsabhängige UV/Vis/NIR-Studien zeigten, dass die Selbstorganisationsprozesse durch das kooperative K_2/*K*-Modell beschrieben werden können. So wurde eine Kooperativität

von σ = 0.016 (0.00038) und eine Bindungskonstante von $K_2 = 3.56 \times 10^3$ M^{-1} (2.42×10^2 M^{-1}) für die Nukleation und von $K = 2.18 \times 10^5$ M^{-1} (6.37×10^5 M^{-1}) für den supramolekularen Polymerisationsprozess von **BisSQ2-AggI** (**BisSQ2-AggII**) bestimmt. Folglich ist **BisSQ2-AggI** die kinetisch bevorzugte Spezies, während **BisSQ2-AggII** das thermodynamisch stabile Aggregat ist.

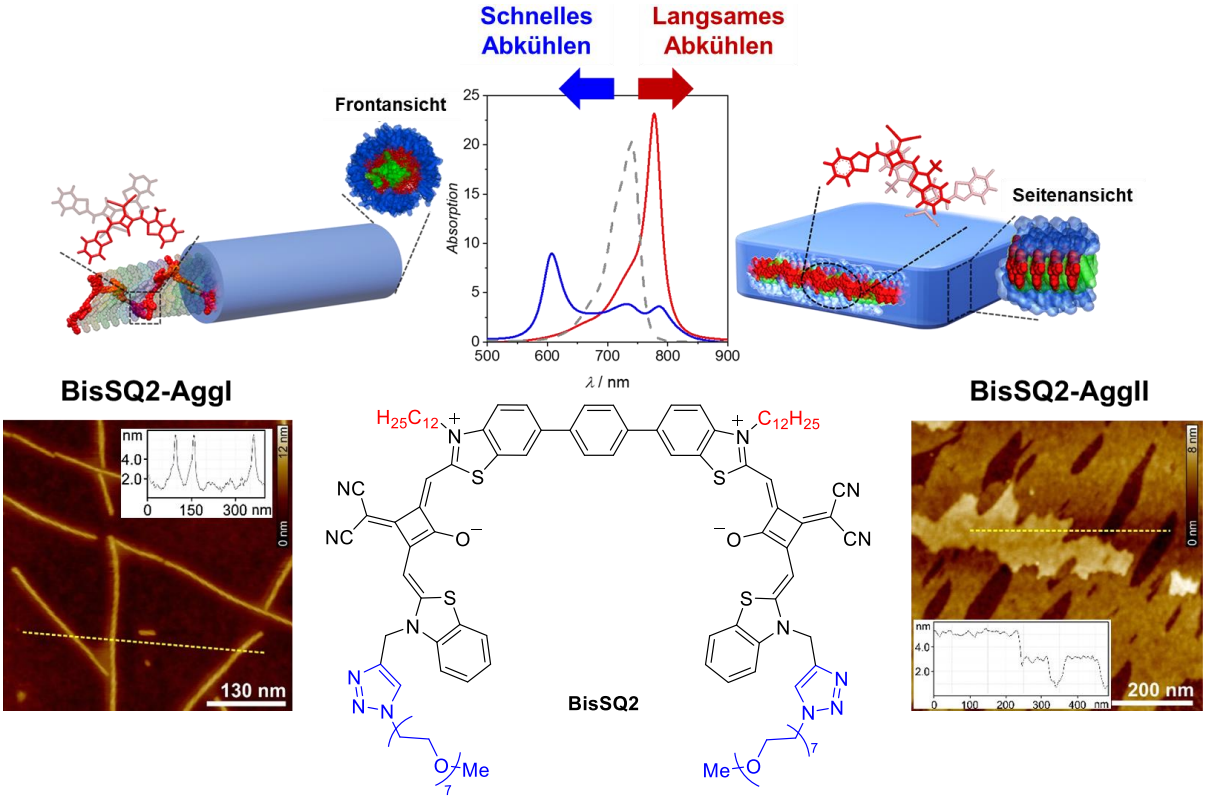

Abbildung 2. Oben: UV/Vis/NIR-Spektren (Mitte) einer Lösung von **BisSQ2** ($c_0 = 2.5 \times 10^{-5}$ M, Toluol/TCE 98:2) bei 85 °C (grau) und bei 25 °C, die beim schnellen Abkühlen (blau: **AggI**) und langsamen Abkühlen (rot: **AggII**) erhalten wurden. Auch gezeigt sind die vorgeschlagenen Packungsmodelle für **AggI** (links) und **AggII** (rechts). Unten: Molekülstruktur von **BisSQ2** (Mitte) und Höhen-AFM-Bild von **BisSQ2-AggI** (links) und **BisSQ2-AggII** (rechts). Die Einfügungen in den AFM-Bildern zeigen die Querschnittsanalysen der gelben gestrichelten Linie.

Basierend auf den Informationen aus den AFM- und WAXS-Experimenten konnten Packungsanordnungen sowohl für die thermodynamisch stabilen **BisSQ2-AggII**-Nanoblätter (Abbildung 2, oben rechts) als auch für die **BisSQ2-AggI**-Nanostäbe (Abbildung 2, oben links) erstellt werden. Dies ermöglichte die Aufklärung des Einflusses der Chromophorpackung auf die UV/Vis/NIR-Absorptionsspektren der Farbstoffaggregate. So konnte gezeigt werden, dass die konventionelle molekulare Exzitonentheorie die breiten Absorptionsmerkmale von **BisSQ2-AggI** für die gegebene Packungsanordnung nicht erklären konnte. Daher wurden tiefgreifendere theoretische Untersuchungen auf der Grundlage des *Essential States Model*

(ESM) durchgeführt, und die Bedeutung des *inter*molekularen Ladungstransfers (*inter*molecular charge transfer, ICT) wurde aufgedeckt, um das panchromatische Absorptionsspektrum von **BisSQ2-AggI** angemessen zu beschreiben. Darüber hinaus konnte die im **BisSQ2-AggII**-Absorptionsspektrum beobachtete Rotverschiebung dem Zusammenspiel von Coulomb- und ICT-vermittelter Kopplung zugeordnet werden.

Inspiriert von den vielversprechenden Ergebnissen für die in *Kapitel 3* und *4* gezeigten Bis(squarain)-Farbstoffe, wurde dieselbe Bis-Chromophor-Strategie zur Realisierung eines NIR-Emitters mit einem bathochrom verschobenen Spektrum genutzt. Dementsprechend wurden die optischen Eigenschaften und das Aggregationsverhalten von **BisSQ3** basierend auf 4-Methylchinolinium-Donoren und zwei solubilisierenden Trialkoxyphenyl-Substituenten vorgestellt (Abbildung 3). In Chloroform zeigt **BisSQ3** ein Absorptionsmaximum bei 961 nm mit einer signifikanten bathochromen Verschiebung (1020 cm^{-1}) im Vergleich zum Referenz-Monosquarain **SQ**, was auf eine *intra*molekulare J-artige Kopplung über die Kopf-Schwanz-Anordnung der zwei Squarainfarbstoffe hinweist. Darüber besitzt **BisSQ3** ein Fluoreszenzmaximum bei 971 nm mit einer Quantenausbeute von 0.33%. Im weniger polaren Lösungsmittel Toluol ordnet sich **BisSQ3** zu Nanofasern an mit zusätzlicher *inter*molekularer J-artiger Kopplung, was eine ausgeprägte bathochrome Verschiebung mit einem Absorptionsmaximum bei 1095 nm und einem Fluoreszenzmaximum bei 1116 nm zur Folge hat. Somit konnte gezeigt werden, dass die Kopf-Schwanz Verknüpfung der zwei Chinolinsquaraine nicht nur zu einer *intra*-, sondern auch zu einer *inter*molekularen J-artigen exzitonischen Kopplung führt (Abbildung 3), was als vielversprechende Strategie zur Verschiebung der Absorption und Emission von organischen Fluorophoren ins NIR-II-Fenster unter Beibehaltung anständiger Quantenausbeuten erscheint.

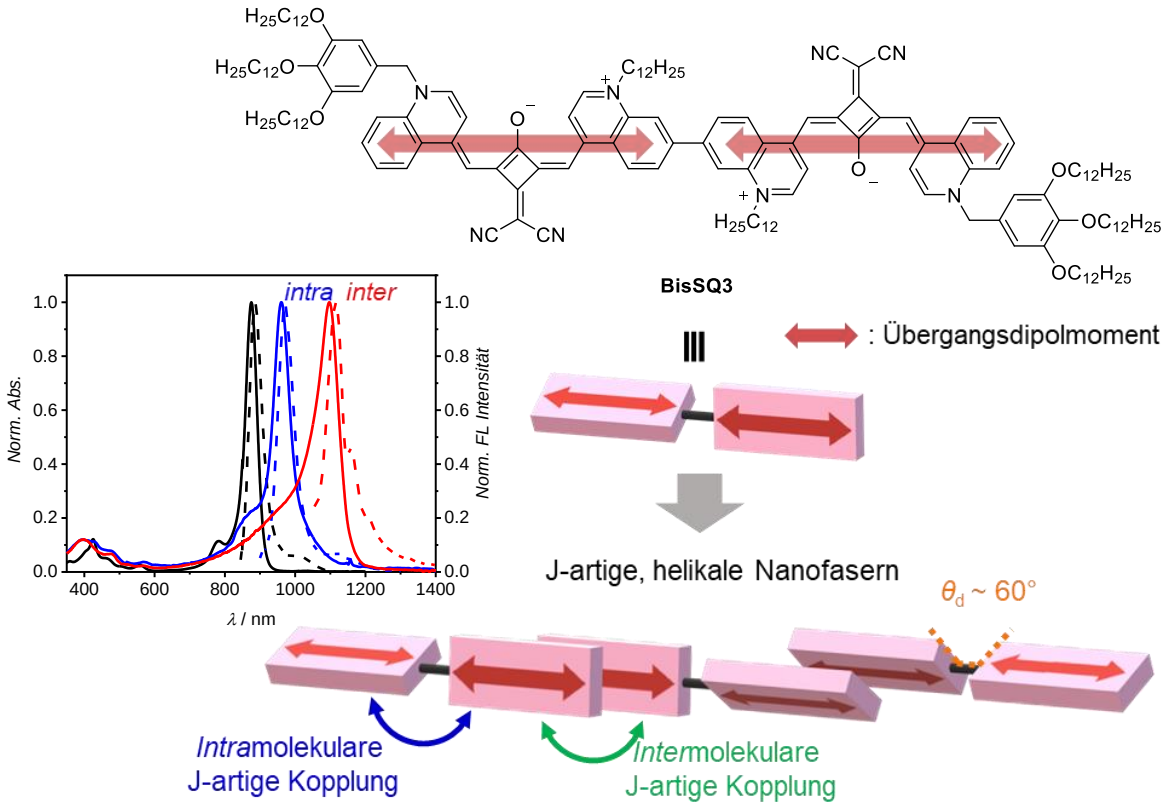

Abbildung 3. Molekülstruktur von **BisSQ3** (oben) und normierte UV/Vis/NIR-Absorptions- (durchgezogene Linien) und Fluoreszenzspektren (gestrichelte Linien) (links) des Referenz-**SQ** in $CHCl_3$ (schwarz, λ_{ex} = 815 nm), **BisSQ3** in $CHCl_3$ (blau, λ_{ex} = 870 nm) und Aggregate von **BisSQ3** in Toluol (rot, λ_{ex} = 985 nm) bei 293 K. Ebenfalls gezeigt ist eine schematische Darstellung der vorgeschlagenen Aggregatstruktur von **BisSQ3** (unten) mit dem Konzept der doppelten *intra*molekularen (blauer Pfeil) und *inter*molekularen (grüner Pfeil) J-artigen Kopplung. Die Ausrichtung der Übergangsdipolmomente ist durch rote Doppelpfeile dargestellt.

In *Kapitel 6* wurde die Bindung des Dicyanomethylen-substituierten Squarains **CAS-C1** an G-Quadruplex (G4) beschrieben. Der wasserlösliche amphiphile Squarainfarbstoff trägt sechs Triethylenglykolketten und bietet eine ausgezeichnete Löslichkeit in Wasser (Abbildung 4). Seine planare Kernstruktur interagierte sehr gut mit parallelen G4s ($K_b = 10^7 - 10^9$ M^{-1}) und zeigte ein „NIR-Aufleuchten“ mit Quantenausbeuten von über 70%. Darüber hinaus zeigte **CAS-C1** eine herausragende Selektivität für parallele G4s gemäß Bindungsexperimenten gegenüber einer großen Gruppe von antiparallelen G4s und einzel- und doppelsträngigen Nukleinsäuren. Die Ergebnisse der Docking-Studie zeigten zusätzlich, dass nicht nur der planare Squarain-Kern die Wechselwirkung mit der G-Quartett-Oberfläche paralleler G4 erleichtert, sondern auch das massive Vorhandensein von Glykolketten einen entropischen Beitrag zur Stabilität des G4-**CAS-C1**-Komplexes leistet. Außerdem besitzen die Komplexe auch eine starke Zwei-Photonen-Absorption mit einem Maximum bei 1275 nm, was NIR-zu-

NIR-Bildgebungsverfahren ermöglicht. Diese Ergebnisse machen **CAS-C1** zur derzeit besten verfügbaren Zwei-Photonen-Parallel-G4-spezifischen Sonde (Abbildung 4).

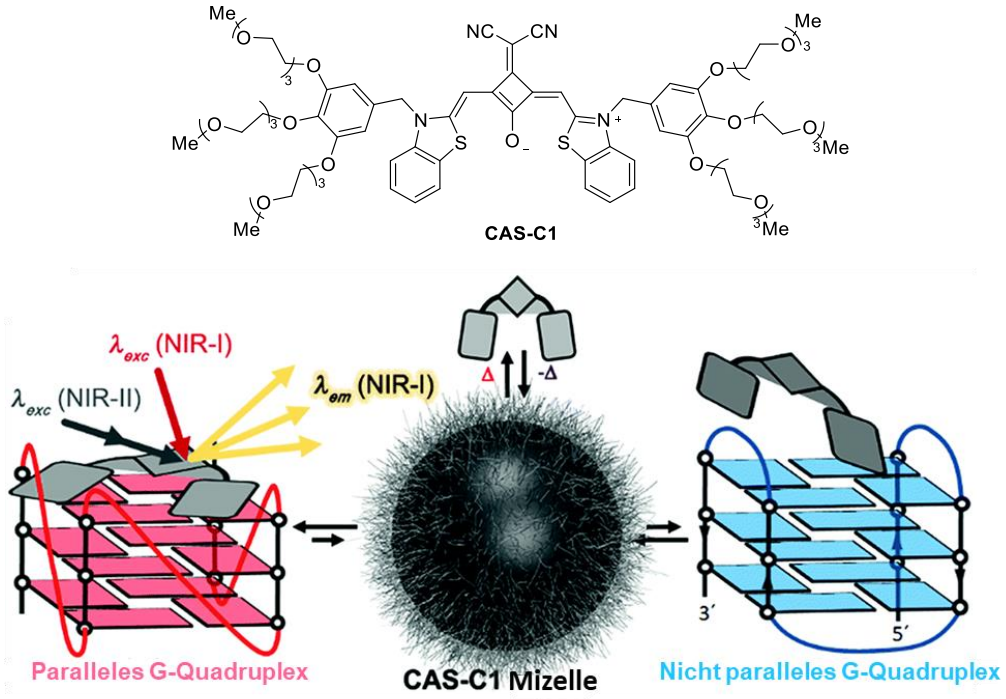

Abbildung 4. Oben: Strukturformel von Squarain **CAS-C1**. Unten: Schematische Darstellung des multiphotonischen selektiven Detektionsmechanismus.

Zusammenfassend zeigt diese Dissertation über Squarainfarbstoffe, wie eine einfache Modifikation der Molekülstruktur das Aggregationsverhalten signifikant beeinflussen und die optischen Eigenschaften von Farbstoffaggregaten verändern kann. Verlängerte supramolekulare Strukturen auf der Basis von Dicyanomethylen-substituierten Squarainfarbstoffen wurden erfolgreich etabliert, indem zwei Squarain-Einheiten kovalent zu einer Bis-Chromophor-Struktur verknüpft wurden. Dann wurde ein einfacher, aber effizienter allgemeiner Ansatz etabliert, um die Aggregation von Squarainfarbstoffen in Lösung von der üblichen kofazialen Stapelung mit H-artiger exzitonischer Kopplung zu der gewünschten gestapelten Anordnung mit longitudinalem Versatz und J-artiger Kopplung zu erhalten. Darüber hinaus ermöglichte, wie in *Kapitel 4* gezeigt, die zusätzliche Brückeneinheit zwischen den Squarainfarbstoffen in **BisSQ2** unterschiedliche molekulare Konformationen, was in Abhängigkeit der Abkühlraten einer heißen Lösung von **BisSQ2** zu zwei unterschiedlichen Morphologien führte. Daher ist dies eine vielversprechende Strategie zur Realisierung von supramolekularem Polymorphismus.

J-Aggregate weisen verschiedene Merkmalen auf, die für zahlreiche grundlegende Studien und Anwendungen verwendet werden können, wie z. B. spektrale Verschiebungen ins NIR-Fenster, Fluoreszenzverstärkung, Lichtsammlung und effiziente Exzitonenmigration. Im Allgemeinen kann davon ausgegangen werden, dass das Konzept der Konstruktion von J-Aggregaten nach dem Bis-Chromophor-Ansatz auf völlig unterschiedliche Farbstoffklassen ausgedehnt werden kann. Darüber hinaus werden die Erkenntnisse zur Ladungstransferkopplung für Squarainfarbstoffe für alle Materialien, die auf alternierenden Donor-Akzeptor-π-Systemen basieren, als relevant betrachtet. Das panchromatische Absorptionsverhalten ist insbesondere für Akzeptor-Donor-Akzeptor (ADA)-Farbstoffe wichtig, die derzeit als vielversprechende Materialien für die Entwicklung von Heteroübergangssolarzellen angesehen werden.[151]

Chapter 9

–

Appendix

9.1 Supporting Information for *Chapter 3*: NIR-Emitting Squaraine J-Aggregate Nanosheets[118]

9.1.1 Materials and Methods

General

All solvents and reagents were purchased from commercial sources and used as received without further purification. Column chromatography was performed using silica gel 60M (0.04 – 0.063 mm).

Gel permeation chromatography (GPC)

For the GPC purification method, the preparative recycling-GPC LaboACE from Japan Analytical Industry Co., Ltd. (JAI) with PLgel Prep columns (from Agilent Technologies) were used.

NMR spectroscopy

NMR spectra were recorded on a Bruker Avance 400 or Bruker Avance DMX 600 at 295 K. The spectra were calibrated to the residual solvent peak and the chemical shifts δ are given in ppm. Multiplicities are denoted as follows: s = singlet, d = doublet, t = triplet, q = quartet, quint = quintet, dd = doublet of doublets, td = triplet of doublets, m = multiplet, br = broad. Diffusion ordered NMR spectroscopy (DOSY) data were measured at 295 K with a Bruker Avance III HD 600MHz spectrometer and a 5 mm BBFO probe containing a z-axis gradient coil with a maximum gradient strength of 50 G cm^{-1}.

Mass spectrometry

High-resolution mass spectra (ESI) were recorded on a microTOF focus instrument (Bruker Daltonik GmbH).

Optical spectroscopy

For all spectroscopic measurements, spectroscopic grade solvents (Uvasol®) were used. The absorption spectra were recorded on JASCO V-670 or V-770 UV/Vis-NIR spectrophotometers. The spectral band width and the scan rate were 1 nm and 400 nm min^{-1}, respectively. Stock solutions in $CHCl_3$ or 1,1,2,2-tetrachloroethane (TCE) were accurately freshly prepared for all measurements and continuously diluted for absorption measurements by taking into account the solubility and the absorbance. The UV/Vis-NIR measurements were performed in quartz cell cuvettes with path lengths of 0.1, 1.0, 5.0, 10.0 and 100.0 mm. For temperature-dependent measurements, absorption spectra have been corrected for the density change. Fluorescence spectra were recorded on a FLS 980 Edinburgh fluorescence spectrometer. Fluorescence quantum yields were determined by a calibrated integrating sphere system (C9920, Hamamatsu, Japan). Time-resolved measurements were performed with a ps laser diode at 670 nm and a TCSPC detection unit.

Atomic force microscopy (AFM)

AFM measurements were performed under ambient conditions using a Bruker Multimode 8 SPM system operating in tapping mode in air. Silica cantilevers (OMCL-AC200TS, Olympus) with a resonance frequency of ~150 kHz and a spring constant of ~10 Nm^{-1} were used. The samples were prepared by spin-coating of solutions in toluene/TCE mixture (98:2, $c_0 = 2 \times 10^{-5}$ M) onto highly ordered pyrolytic graphite (HOPG), silicon waver (SiO_x) or mica with 2000 rpm.

Computational Studies

Geometry optimization was performed for **BisSQ1** on the level of density functional theory (DFT) using the B3LYP functional[200,201] in combination with the 6-31G* basis set[202] as implemented in the Gaussian 09 program package.[203]

9.1.2 Synthesis and Characterizations

Synthesis of compound **3**

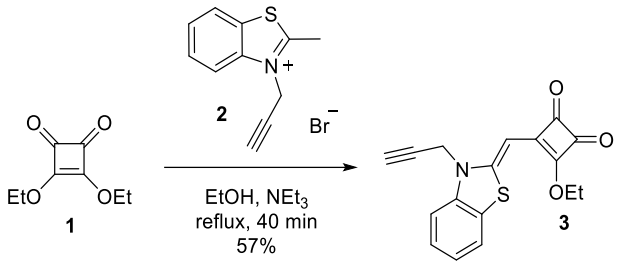

2-Methyl-3-propargylbenzothiazolium bromide (**2**) (839 mg, 3.13 mmol) was dissolved in 5.5 mL ethanol and 1.4 mL triethylamine. 1,2-diethoxycyclobutenedione (**1**) (0.53 mL, 3.7 mmol) was then added dropwise. The mixture was heated to reflux for 40 minutes. Afterwards, the reaction was cooled down to room temperature and the solvent was removed under reduced pressure. The crude product was purified by column chromatography (silica gel, eluent: pure CH_2Cl_2 to CH_2Cl_2/EtOAc 92:8) to obtain **3** as a yellow solid (554 mg, 1.78 mmol, 57%).

^{1}H NMR (400 MHz, DMSO-d_6): δ = 7.82 (dd, J = 8.0, 1.0 Hz, 1H), 7.51 (d, J = 8.0, 1H), 7.42 (td, J = 7.4, 1.0 Hz, 1H), 7.23 (t, J = 7.4 Hz, 1H), 5.68 (s, 1H), 5.11 (d, J = 2.4 Hz, 2H), 4.76 (q, J = 7.0 Hz, 2H), 3.46 (t, J = 2.4 Hz, 1H), 1.44 (t, J = 7.0 Hz, 3H) ppm.
^{13}C NMR (101 MHz, DMSO-d_6): δ = 192.2, 185.8, 185.3, 172.1, 158.3, 140.1, 127.2, 125.6, 123.8, 122.6, 111.8, 80.1, 76.9, 76.1, 69.5, 34.7, 15.7 ppm.
HRMS (ESI, pos. mode, MeOH): m/z: 334.05024 $[M+Na]^+$ (calcd. for $C_{17}H_{13}NNaO_3S^+$: 334.05084).
Mp: > 200 °C (decomp.)

Synthesis of compound **4**

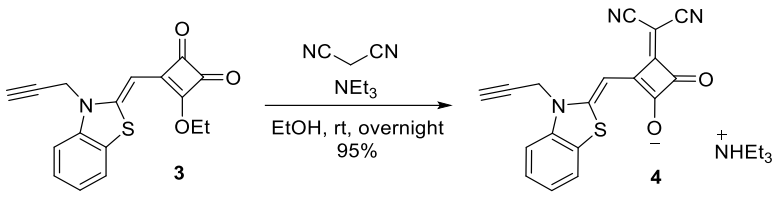

Compound **3** (491 mg, 1.58 mmol) was dissolved in 300 mL ethanol and malononitrile (522 mg, 7.90 mmol) was added while stirring. Triethylamine (1.1 mL, 7.9 mmol) was added dropwise. The mixture was stirred at room temperature overnight. The solvent was removed under

reduced pressure and the solid was washed with diethyl ether to yield a dark orange powder (651 mg, 1.51 mmol, 95%).

^{1}H NMR (400 MHz, DMSO-d_6): δ = 7.65 (d, J = 7.3 Hz, 1H), 7.31 – 7.29 (m, 2H), 7.11 – 7.06 (m, 1H), 5.94 (s, 1H), 4.76 (d, J = 2.1 Hz, 2H), 3.37 (t, J = 2.3 Hz, 1H), 3.09 (m, 6H), 1.17 (t, J = 7.2 Hz, 9H) ppm.
^{13}C NMR (101 MHz, DMSO-d_6): δ = 191.1, 185.8, 174.4, 167.5, 152.4, 140.5, 126.6, 125.8, 122.6, 122.0, 118.9, 118.3, 110.5, 82.6, 79.2, 76.8, 75.5, 45.8, 34.2, 8.7 ppm.
HRMS (ESI, neg. mode, MeCN/$CHCl_3$): m/z: 330.03208 $[M-NHEt_3]^-$ (calcd. for $C_{18}H_8N_3O_2S^-$: 330.03427).
Mp: > 200 °C (decomp.)

Synthesis of compound **5a**

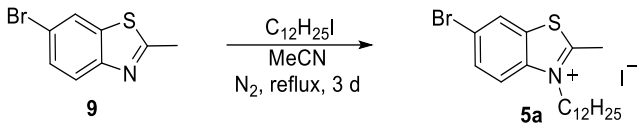

6-Bromo-2-methylbenzothiazole (**9**) (4.4 g, 19 mmol) and 1-iodododecane (14 mL, 57 mmol) was dissolved in 10 mL acetonitrile under nitrogen atmosphere and stirred during reflux for three days. After the reaction mixture was cooled down to room temperature, the solvent was removed under reduced pressure. The resulting residue was subsequently washed with ethyl acetate and diethyl ether to yield a yellow viscous material (2.5 g, 4.8 mmol, 25%). The synthesis was continued without further purification.

Synthesis of compound **6a**

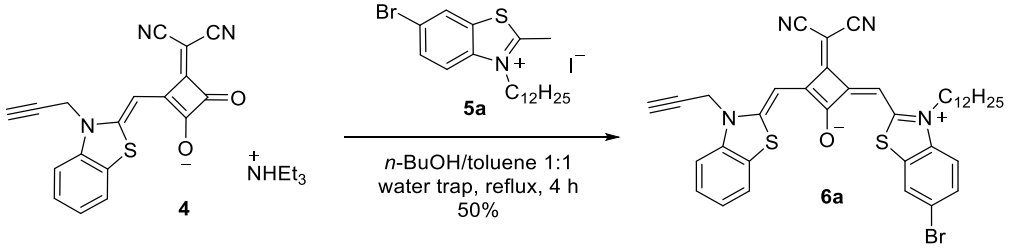

Compound **4** (35.6 mg, 82.0 µmol) and **5a** (88.0 mg, 168 µmol) were mixed in 2 mL *n*-butanol and 2 mL toluene and heated to reflux with a water-removing Dean-Stark apparatus for 4 h. Then the reaction mixture was cooled to room temperature and the solvent was removed under reduced pressure. The crude product was purified by column chromatography (silica gel, eluent:

pure $CHCl_3$) to obtain a dark green solid. The solid was further washed with methanol. The solid was collected and dried to give a dark green powder (29.0 mg, 40.8 µmol, 50%).

^{1}H NMR (400 MHz, $CDCl_3$): δ = 7.65 (d, J = 1.8 Hz, 1H), 7.57 (dd, J = 8.0, 1.2 Hz, 1H), 7.53 (dd, J = 8.7, 1.8 Hz, 1H), 7.46 (td, J = 8.0, 1.2 Hz, 1H), 7.30 (m, 2H), 7.09 (d, J = 8.7 Hz, 1H), 6.40 (s, 1H), 6.38 (s, 1H), 4.84 (d, J = 2.4 Hz, 2H), 4.11 (t, J = 7.8 Hz, 2H), 2.46 (t, J = 2.4 Hz, 1H), 1.83 (quint, J = 7.8 Hz, 2H), 1.48 – 1.41 (m, 2H), 1.39 – 1.21 (m, 16H), 0.87 (t, J = 7.0 Hz, 3H) ppm.

^{13}C NMR (151 MHz, $CDCl_3$): δ = 174.2, 165.2, 164.7, 163.1, 160.8, 160.4, 140.17, 140.15, 130.9, 130.4, 128.2, 127.8, 125.1, 124.9, 122.5, 118.7, 118.5, 117.8, 113.3, 112.0, 87.9, 87.6, 75.4, 74.3, 47.4, 41.5, 36.0, 32.1, 29.75, 29.74, 29.65, 29.54, 29.49, 29.43, 27.7, 26.9, 22.9, 14.3 ppm.

HRMS (ESI, pos. mode, $MeCN/CHCl_3$): m/z: 708.1576 $[M]^+$ (calcd. for $C_{38}H_{37}BrN_4OS_2^+$: 708.1587).

Mp: > 225 °C (decomp.)

Synthesis of compound **6b**

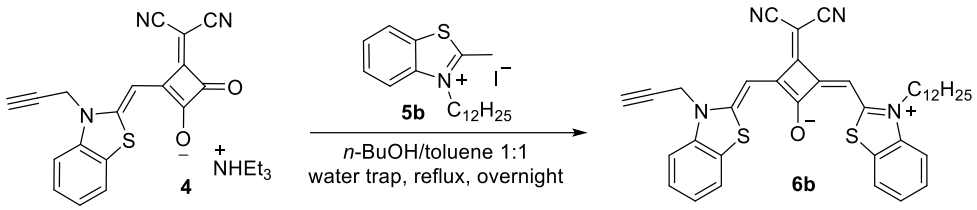

Compound **4** (202 mg, 467 µmol) and 2-methyl-3-dodecylbenzothiazolium iodide (**5b**) (473 mg, 1.06 mmol) were mixed in 15 mL *n*-butanol and 15 mL toluene and heated to reflux with a water-removing Dean-Stark apparatus overnight. Then the reaction mixture was cooled to room temperature and the solvent was removed under reduced pressure. The crude product was purified by column chromatography (silica gel, eluent: pure $CHCl_3$) and the obtained solid was washed with methanol. The solid was collected and dried to give a dark green powder. This compound was applied for the next step without further purification.

Synthesis of compound **7**

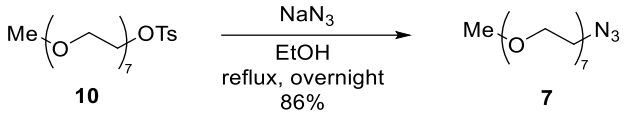

Hepta(ethylene glycol) monotosyl monomethyl ether (1.54 g, 3.11 mmol), and sodium azide (1.01 g, 15.6 mmol) were dissolved in 15 mL EtOH and heated to reflux overnight. After the reaction mixture was cooled down to room temperature, the solvent was removed under reduced pressure. The crude mixture was dissolved in CH_2Cl_2 (100 mL) and extracted with water (20 mL × 2) and brine (20 mL × 1). The combined organic layers were dried over $MgSO_4$ and evaporated to obtain a yellow oil (0.97 g, 2.7 mmol, 86%).

^{1}H NMR (400 MHz, $CDCl_3$): δ = 3.68 – 3.63 (m, 24H), 3.55 – 3.53 (m, 2H), 3.38 (t, J = 5.2 Hz, 2H), 3.37 (s, 3H) ppm.
^{13}C NMR (101 MHz, $CDCl_3$): δ = 72.1, 70.83, 70.80, 70.76, 70.74, 70.71, 70.65, 70.2, 59.2, 50.8 ppm.
HRMS (ESI, pos. mode, MeCN/$CHCl_3$): *m*/*z*: 388.20575 $[M+Na]^+$ (calcd. for $C_{15}H_{31}N_3NaO_7^+$: 388.20542).

Synthesis of compound **8a**

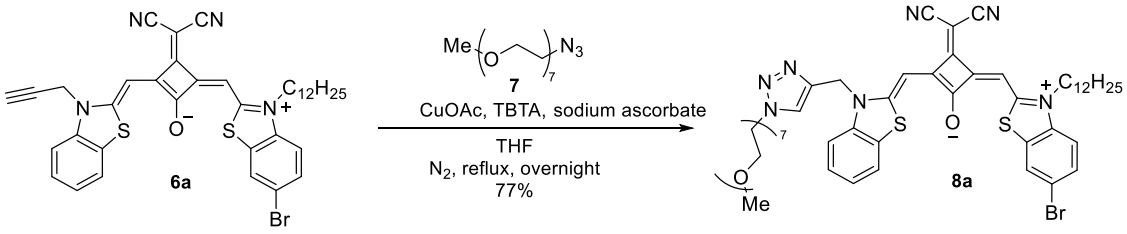

Copper (I) acetate (0.54 mg, 4.4 µmol) and sodium ascorbate (17 mg, 88 µmol) were suspended in 1 mL THF and stirred under nitrogen atmosphere for ca. 15 minutes until the color turned green. Precursors **6a** (15.7 mg, 22 µmol) and **7** (20.2 mg, 55 µmol) were dissolved in 1 mL THF and TBTA (4.7 mg, 8.8 µmol) and the Cu(I) catalyst solution were added. The reaction mixture was then heated to reflux overnight under nitrogen atmosphere. Inorganic salts were filtered off and THF was removed under reduced pressure. Preparative recycling GPC ($CHCl_3$/MeOH = 9:1) was applied to isolate the pure product **8a** as a dark green solid (18.4 mg, 17 µmol, 77%).

^{1}H NMR (400 MHz, $CDCl_3$): δ = 8.37 (s, 1H), 7.94 (d, J = 8.3 Hz, 1H), 7.63 (d, J = 1.9 Hz, 1H), 7.57 – 7.49 (m, 3H), 7.31 (t, J = 7.5 Hz, 1H), 7.05 (d, J = 8.6 Hz, 1H), 6.43 (s, 1H), 6.31 (s, 1H), 5.39 (s, 2H), 4.56 (t, J = 5.3 Hz, 2H), 4.07 (t, J = 7.5 Hz, 2H), 3.91 (t, J = 5.3 Hz, 2H), 3.64 – 3.61 (m, 22 H), 3.55 – 3.52 (m, 2H), 3.37 (s, 3H), 1.82 (quint, J = 7.4 Hz, 2H), 1.48 – 1.40 (m, 2H), 1.37 – 1.25 (m, 16H), 0.87 (t, J = 6.8 Hz, 3H) ppm.

^{13}C NMR (101 MHz, CD_2Cl_2): δ = 173.8, 164.8, 164.4, 162.5, 161.1, 160.4, 141.3, 140.6, 140.0, 130.8, 130.6, 128.3, 128.0, 125.4, 125.3, 125.0, 122.4, 119.7, 118.6, 117.5, 114.0, 113.7, 113.5, 87.4, 72.2, 70.95, 70.86, 70.83, 70.81, 70.76, 70.7, 69.5, 59.0, 50.8, 47.6, 42.1, 32.3, 30.1, 30.0, 29.92, 29.87, 29.74, 29.66, 27.7, 27.2, 23.1, 14.3 ppm.

HRMS (ESI, pos. mode, MeCN/$CHCl_3$): m/z: 1073.37388 $[M]^+$ (calcd. for $C_{53}H_{68}BrN_7O_8S_2^+$: 1073.37487).

Mp: 174 – 175 °C.

Synthesis of compound **SQ1**

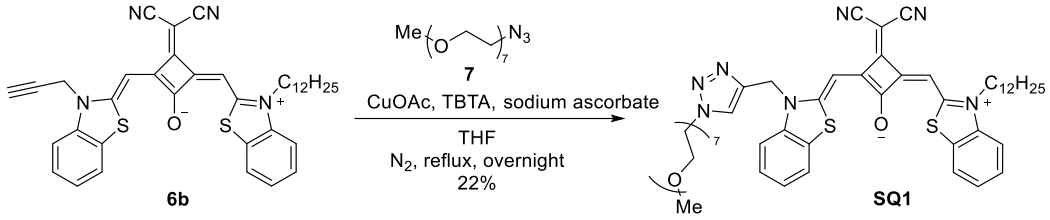

Copper (I) acetate (2.43 mg, 19.8 µmol) and sodium ascorbate (78.5 mg, 396 µmol) were suspended in 3 mL THF and stirred under nitrogen atmosphere for ca. 15 minutes until the color turned green. Precursors **6b** (62 mg, 99 µmol) and **7** (72.3 mg, 198 µmol) were dissolved in 10 mL THF, and TBTA (21.0 mg, 39.6 µmol) and the Cu(I) catalyst solution were added. The reaction mixture was stirred under reflux overnight under nitrogen atmosphere. Inorganic salts were filtered off and THF was removed under reduced pressure. Preparative recycling GPC ($CHCl_3$/MeOH = 9:1) was applied to isolate the pure product **SQ1** as a dark green solid (22.3 mg, 22.3 µmol, 22%).

^{1}H NMR (400 MHz, $CDCl_3$): δ = 8.36 (s, 1H), 7.90 (d, J = 8.3 Hz, 1H), 7.60 – 7.43 (m, 4H), 7.31 – 7.24 (m, 3H), 6.39 (s, 1H), 6.38 (s, 1H), 5.35 (s, 2H), 4.56 (t, J = 5.2 Hz, 2H), 4.15 (t, J = 7.5 Hz, 2H), 3.91 (t, J = 5.2 Hz, 2H), 3.65 – 3.61 (m, 22 H), 3.55 – 3.52 (m, 2H), 3.37 (s, 3H), 1.85 (quint, J = 7.4 Hz, 2H), 1.52 – 1.43 (m, 2H), 1.40 – 1.20 (m, 16H), 0.87 (t, J = 6.8 Hz, 3H) ppm.

^{13}C NMR (151 MHz, $CDCl_3$): δ = 174.3, 164.9, 163.7, 162.8, 161.4, 160.3, 141.2, 141.0, 139.8, 130.2, 129.9, 128.6, 127.9, 127.7, 125.2, 125.0, 124.9, 122.5, 122.1, 119.8, 118.8, 113.7, 112.3, 87.4, 86.5, 72.0, 70.8, 70.7, 70.6, 69.2, 59.2, 50.5, 47.2, 41.7, 40.5, 36.0, 32.1, 29.84, 29.80, 29.74, 29.66, 29.57, 29.51, 29.48, 29.44, 27.8, 27.0, 22.8, 14.3 ppm.

HRMS (ESI, pos. mode, MeCN/$CHCl_3$): *m*/*z*: 1018.45371 $[M+Na]^+$ (calcd. for $C_{53}H_{69}N_7NaO_8S_2^+$: 1018.45412).

Mp: 165 °C.

Synthesis of **BisSQ1**

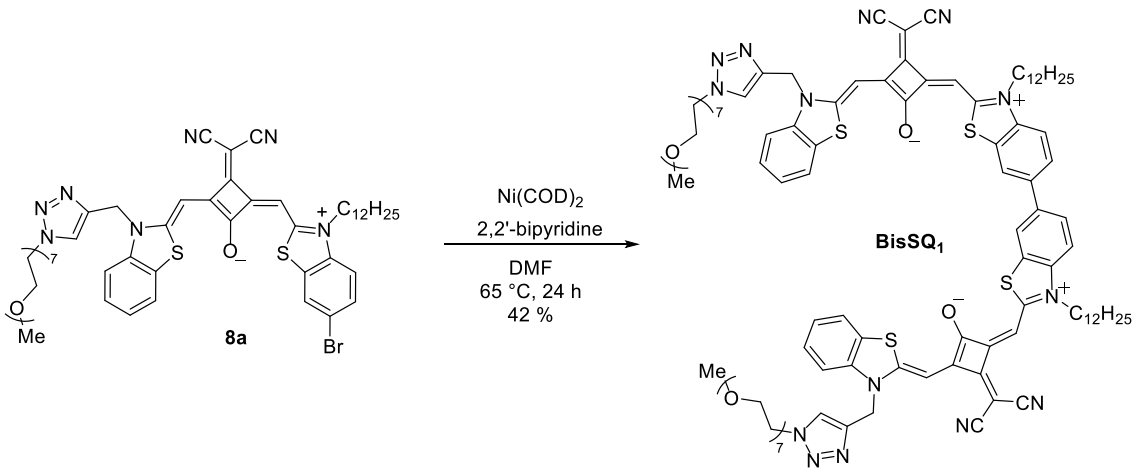

Squaraine **8a** (36.4 mg, 33.85 µmol), 2,2'-bipyridine (2.64 mg, 16.93 µmol), and bis-(1,5-cyclooctadiene)nickel(0) (4.66 mg, 16.93 µmol) were mixed in a Schlenk tube under N_2 atmosphere. Anhydrous DMF (10 mL) was added through a syringe into the reaction mixture and it was stirred at 65 °C for 24 hours. Afterwards, the reaction was cooled to room temperature and then diluted with 30 mL CH_2Cl_2. The solution was washed with water (30 mL × 3). The combined organic phase was dried over $MgSO_4$ and the solvent was removed under reduced pressure. Preparative recycling GPC ($CHCl_3$/MeOH = 9:1) was applied, giving pure **BisSQ1** as a dark green waxy solid (14.2 mg, 7.13 µmol, 42%).

^{1}H NMR (400 MHz, $CDCl_3$): δ = 8.37 (s, 2H), 7.92 (d, *J* = 8.2 Hz, 2H), 7.69 (d, *J* = 1.6 Hz, 2H), 7.59 (d, *J* = 8.6 Hz, 2H), 7.55 (d, *J* = 8.2 Hz, 2H), 7.50 (t, *J* = 8.0 Hz, 2H), 7.29 – 7.24 (m, 4H), 6.39 (s, 2H), 6.33 (s, 2H), 5.37 (s, 4H), 4.57 (t, *J* = 5.1 Hz, 4H), 4.13 (br, 4H), 3.92 (t, *J* = 5.1 Hz, 4H), 3.64 – 3.52 (m, 48H), 3.37 (s, 6H), 1.88 – 1.84 (m, 4H), 1.49 – 1.19 (m, 32H), 0.89 – 0.83 (m, 6H) ppm.

^{13}C NMR (151 MHz, $CDCl_3$): δ = 174.2, 164.3, 164.2, 162.8, 160.9, 160.4, 141.1, 140.8, 139.7, 136.2, 130.2, 129.9, 129.8, 128.0, 126.7, 126.6, 125.2, 124.3, 123.5, 122.1, 120.2, 119.7, 118.7,

113.9, 112.5, 87.5, 87.0, 72.1, 70.8, 70.73, 70.68, 70.65, 69.2, 59.2, 50.5, 47.3, 41.8, 40.6, 32.1, 29.85, 29.81, 29.76, 29.69, 29.60, 29.51, 29.49, 27.8, 27.0, 22.8, 14.3 ppm.

HRMS (ESI, pos. mode, MeCN/$CHCl_3$): *m/z*: 2011.8988 $[M+Na]^+$ (calcd. for $C_{106}H_{136}N_{14}NaO_{16}S_4$: 2011.9034).

Mp: > 285 °C (decomp.)

9.1.3 UV/Vis Absorption and Fluorescence Spectroscopy

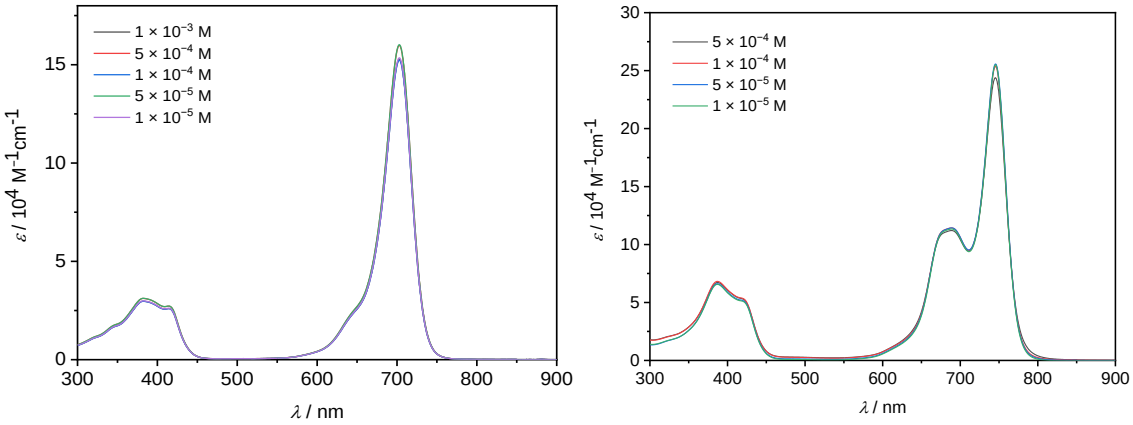

Figure S1. UV/Vis absorption spectra of **SQ1** (left) and **BisSQ1** (right) in $CHCl_3$ at different concentrations at 25 °C.

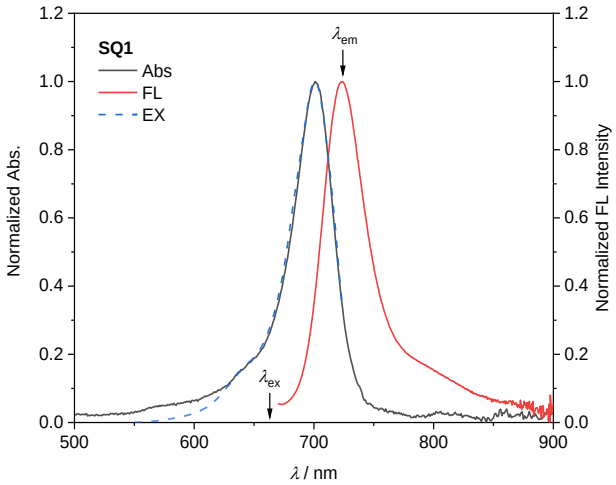

Figure S2. Normalized UV/Vis (solid black line), fluorescence (solid red line, λ_{ex} = 660 nm) and excitation (dashed blue line, λ_{em} = 724 nm) spectra of **SQ1** in $CHCl_3$ at $c_0 = 5\times10^{-6}$ M, 25 °C.

9.1.4 Determination of Absolute Fluorescence Quantum Yield

During the fluorescence quantum yield investigation of **SQ1** and **BisSQ1** utilizing an integrating sphere, strong reabsorption took place, which was identified by the broadening and decrease of the fluorescence intensity and the shift of the fluorescence maximum to lower wavelength upon dilution. The reabsorption contaminated spectrum were adjusted at the red edge to the reabsorption-free fluorescence spectrum (Figure S3) and the corrected absolute quantum yields were determined using the approach of Ahn *et al.*[163]

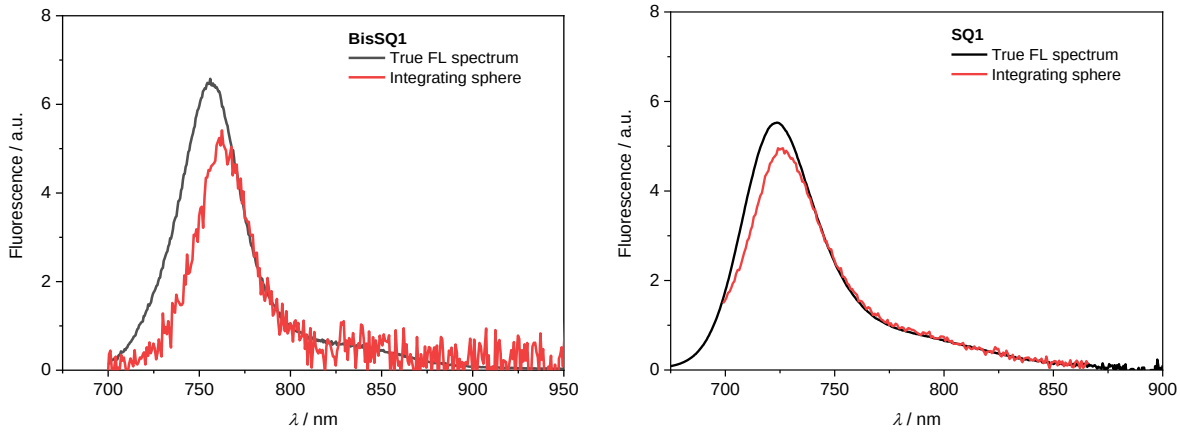

Figure S3. Left: Fluorescence spectrum of **BisSQ1** in $CHCl_3$ solution measured with the integrating sphere (c_0 = 2 × 10^{-6} M, red line) adjusted to the red edge of the reabsorption-free spectrum (c_0 = 2 × 10^{-6} M, black line). Right: Fluorescence spectrum of **SQ1** in $CHCl_3$ solution measured with the integrating sphere (c_0 = 5×10^{-6} M, red line) adjusted to the red edge of the reabsorption-free spectrum (c_0 = 5×10^{-6} M, black line).

9.1.5 Self-Assembly Studies

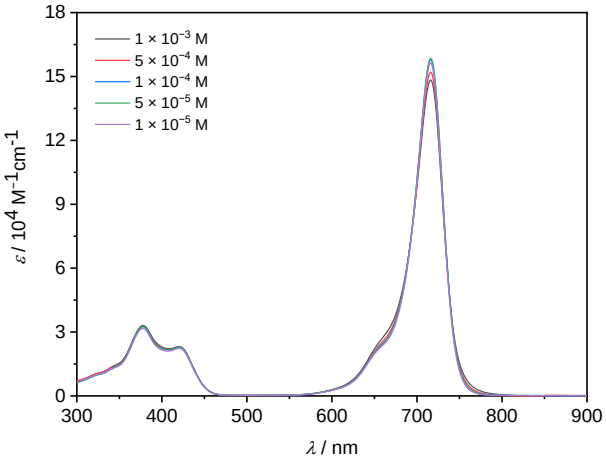

Figure S4. UV/Vis absorption spectra of **SQ1** in toluene/TCE 98:2 at different concentrations at 25 °C (λ_{max} = 716 nm).

Data Evaluation

For the thermodynamic analysis of the self-assembly processes, literature known procedures were applied. The temperature-dependent analyses were performed according to the procedures recently reported by Meijer, Schenning and Van der Schoot.[128,204] The equations used to fit the concentration-dependent UV/Vis data are according to the monomer-dimer,[205] isodesmic (equal-*K*)[206] and the cooperative K_2/K model.[93]

Determination of the Degree of Aggregation Based on UV/Vis Data

The degree of aggregation α_{agg} was calculated from the data obtained by concentration and temperature-dependent UV/Vis measurements according to Equations (S1) and (S2)

$$\alpha_{agg}(c) = \frac{\varepsilon(c)-\varepsilon_M}{\varepsilon_A-\varepsilon_M} \quad (S1)$$

$$\alpha_{agg}(T) = \frac{\varepsilon(T)-\varepsilon_M}{\varepsilon_A-\varepsilon_M}, \quad (S2)$$

where $\varepsilon(c)$ is the measured apparent absorption coefficient at concentration c, ε(T) is the measured apparent absorption coefficient at temperature T, and ε_M and ε_A are the respective absorption coefficients of the monomer (M) and fully aggregated state (A). ε_M and ε_A could be determined directly from the spectroscopic data at high and low concentrations and temperatures.

Nucleation-Elongation Model of Meijer, Schenning and Van der Schoot[128,204]

In the elongation regime, the fraction of aggregated species (α_{agg}) can be defined by

$$\alpha_{agg} = \alpha_{SAT}\left(1 - exp\left[\frac{-\Delta H_e}{RT_e^2}(T - T_e)\right]\right), \quad (S3)$$

in which ΔH_e is the enthalpy corresponding to the aggregation (elongation) process, T the absolute temperature, T_e the elongation temperature, R the ideal gas constant and α_{SAT} is a parameter introduced to ensure that $\alpha_{agg}/\alpha_{SAT}$ does not exceed unity.
On the other hand, in the nucleation regime, α_{agg} can be defined by

$$\alpha_{agg} = K_a^{1/3} exp\left[\left(2/3K_a^{-1/3} - 1\right)\frac{\Delta H_e}{RT_e^2}(T - T_e)\right], \quad (S4)$$

where K_a is the dimensionless equilibrium constant of the activation step at the elongation temperature.

As presented in the main text in *Chapter 3*, temperature-dependent UV/Vis absorption measurement of **BisSQ1** was carried out in a solvent mixture of toluene/1,1,2,2-tetrachloroethane (TCE) = 98:2 (*v*/*v*) from 282 K to 358 K at the concentration of 5×10^{-6} M. The heating process led to a transition from aggregated (λ_{max} = 886 nm) to monomeric (λ_{max} = 757 nm) species. However, under the measurement conditions, the fully aggregated state was not achieved. Thus, we could only determine the value of ε_M. For ε_A, a very concentrated solution of **BisSQ1** in toluene/TCE 98:2 at $c_0 = 1.0 \times 10^{-3}$ M was prepared and measured separately at low temperatures, namely 278 and 283 K. Since both UV/Vis absorption spectra looked identical (Figure S5), we assume **BisSQ1** to be fully aggregated at this condition. Hence, ε_A can be deduced from these spectra at the desired wavelength λ = 886 nm and thus the degree of aggregation α_{agg} can be calculated in order to perform the analysis using the nucleation-elongation model (Figure 54 in *Chapter 3*).[128]

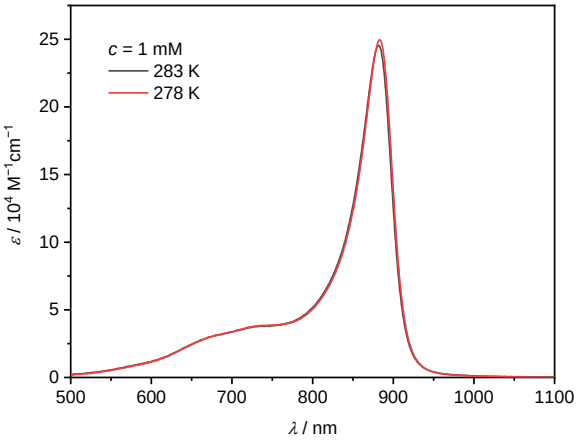

Figure S5. UV/Vis spectra of **BisSQ1** in toluene/TCE 98:2 (*v*/*v*) at $c_0 = 1.0 \times 10^{-3}$ M, 278 and 383 K.

Concentration-dependent UV/Vis measurements were carried out to complement our investigation of the cooperative self-assembly process of **BisSQ1**. Therefore, **BisSQ1** solutions in a solvent mixture of toluene/$CHCl_3$ = 95:5 (*v*/*v*) from $c_0 = 2 \times 10^{-7}$ M to 1×10^{-4} M at 25 °C were prepared and measured. $CHCl_3$ was used as an additive to increase the solubility of **BisSQ1** in order to cover a broad concentration range. As shown in Figure S6, an increase of the concentration from $c_0 = 2 \times 10^{-7}$ M to 1×10^{-4} M at 25 °C results in a transition from monomeric species (λ_{max} = 757 nm) to nearly totally aggregated species (λ_{max} = 886 nm). The degree of aggregation was calculated according to the experimental data extracted at 886 nm and plotted against the concentration (Figure S7). Indicated by the abrupt decrease of the apparent absorption at 739 nm, the monomer-dimer[205] or isodesmic (equal-*K*)[206] model failed to describe the aggregation process (Figure S7 left). By applying the cooperative K_2/K model,[93]

a pronounced cooperativity of 0.08 with the elongation constant $K = 7.5 \times 10^5$ M^{-1} were yielded, which is in good agreement with the temperature-dependent measurements (Figure S7 right).

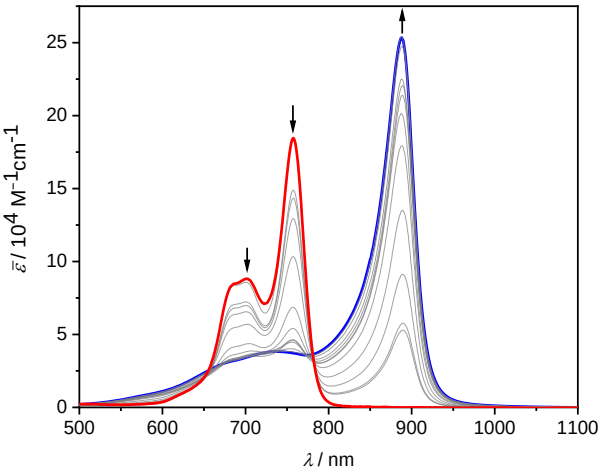

Figure S6. Concentration-dependent UV/Vis spectra of **BisSQ1** in toluene/$CHCl_3$ 95:5 (*v*/*v*) at $c_0 = 1.0 \times 10^{-4} – 2.0 \times 10^{-7}$ M, 25 °C. The arrows indicate the spectral changes with increasing concentration.

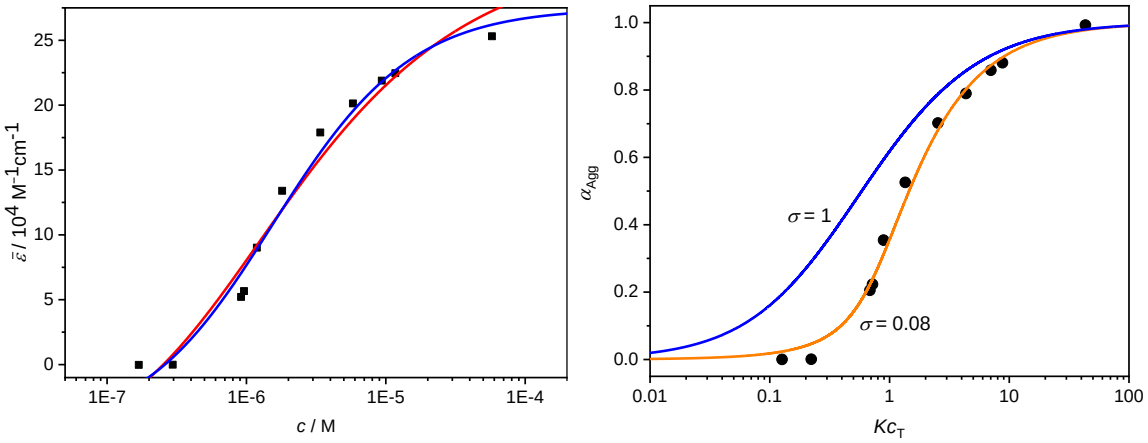

Figure S7. Left: apparent molar absorption at 886 nm as a function of concentration of **BisSQ1** in toluene/$CHCl_3$ 95:5 fitted with the monomer-dimer[205] (red line, $r^2 = 0.9712$) and the isodesmic model[206] (blue line, $r^2 = 0.9833$). Right: plot of fractions of aggregate against Kc_T and fitting with the cooperative K_2/K model[93] with different σ values.

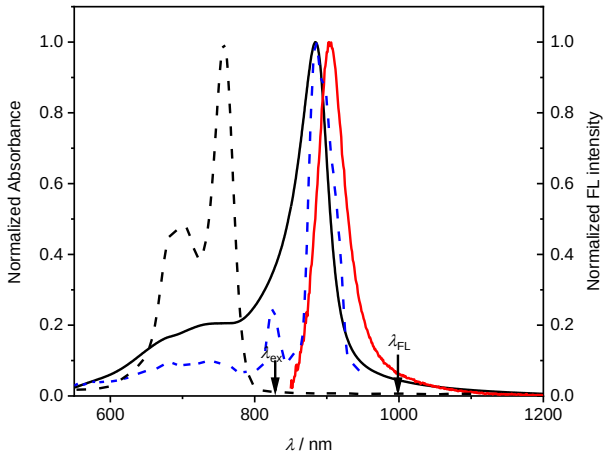

Figure S8. Normalized absorption (solid black line), fluorescence (solid red line) and excitation spectra (dashed blue line) of aggregated **BisSQ1** in toluene/$CHCl_3$ 95:5 (*v*/*v*) at c_0 = 6.0 × 10^{-5} M, 25 °C and the absorption spectrum of **BisSQ1** in $CHCl_3$ at c_0 = 1 × 10^{-5} M, 25 °C (dashed black line).

Table S1. Summarized absorption and fluorescence data of aggregated **BisSQ1** in toluene/$CHCl_3$ 95:5 (*v*/*v*) at c_0 = 6.0 × 10^{-5} M, 25 °C.

λ_{max} (nm)	λ_{FL}[a] (nm)	$\Delta\tilde{\nu}_{Stokes}$ (cm^{-1})	*FWHM* (cm^{-1})
886	904	225	620

[a] λ_{ex} = 820 nm. Fluorescence spectrum was measured with a front-face setup (1 mm cell thickness) and the polarizer at magic angle; excitation spectrum was measured with a front-face setup (1 mm cell thickness) without polarizers.

9.1.6 DOSY NMR

DOSY NMR studies were performed in toluene-d_8 (Figure S9, the selected peaks (*) correspond to the proton signals of **BisSQ1**). In order to avoid the influence of convection effects due to temperature gradients in the coil of the probe, two different pulse sequences, a stimulated echo BPP-LED pulse sequence with sample rotation and a corresponding double stimulated echo pulse sequence without sample rotation were used. No differences in diffusion data obtained from the two pulse sequences were observed, which confirms the absence of convection effects. The diffusion coefficients were obtained by fitting the decay curves of the signal area versus the gradient strength with a monoexponential function. The decay curves with the respective fit and the resulting hydrodynamic radii are shown in Figure S10 a–d.

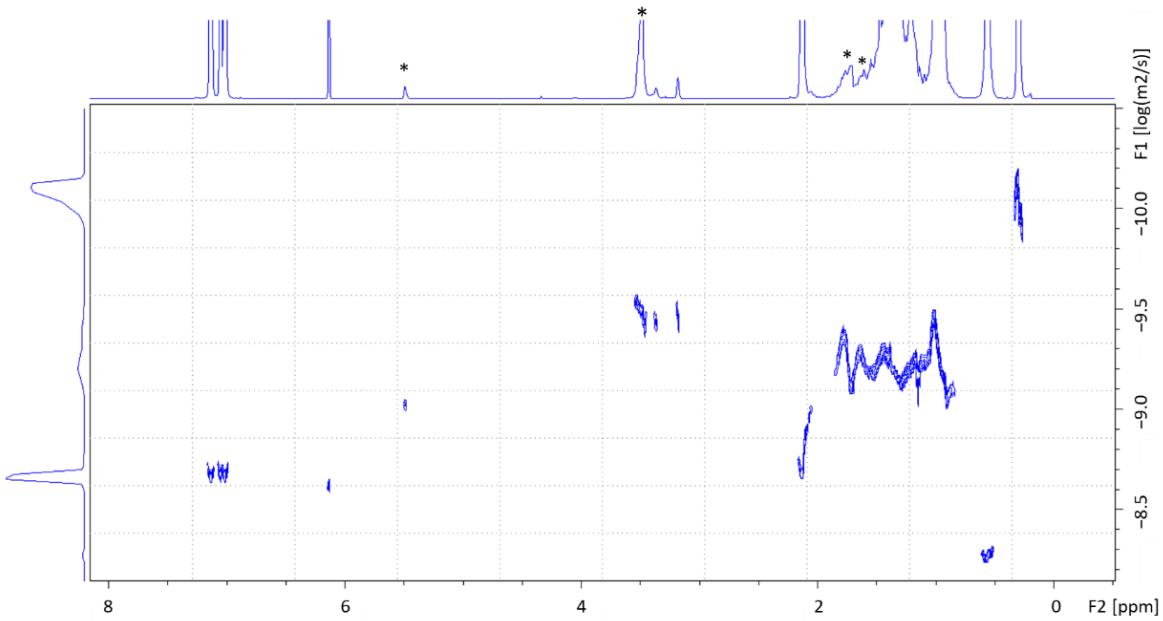

Figure S9. DOSY NMR spectrum of **BisSQ1** in toluene-d_8 (c_0 = 5 × 10^{-4} M, 295 K, 600 MHz). The selected signals (*) correspond to the **BisSQ1** moieties.

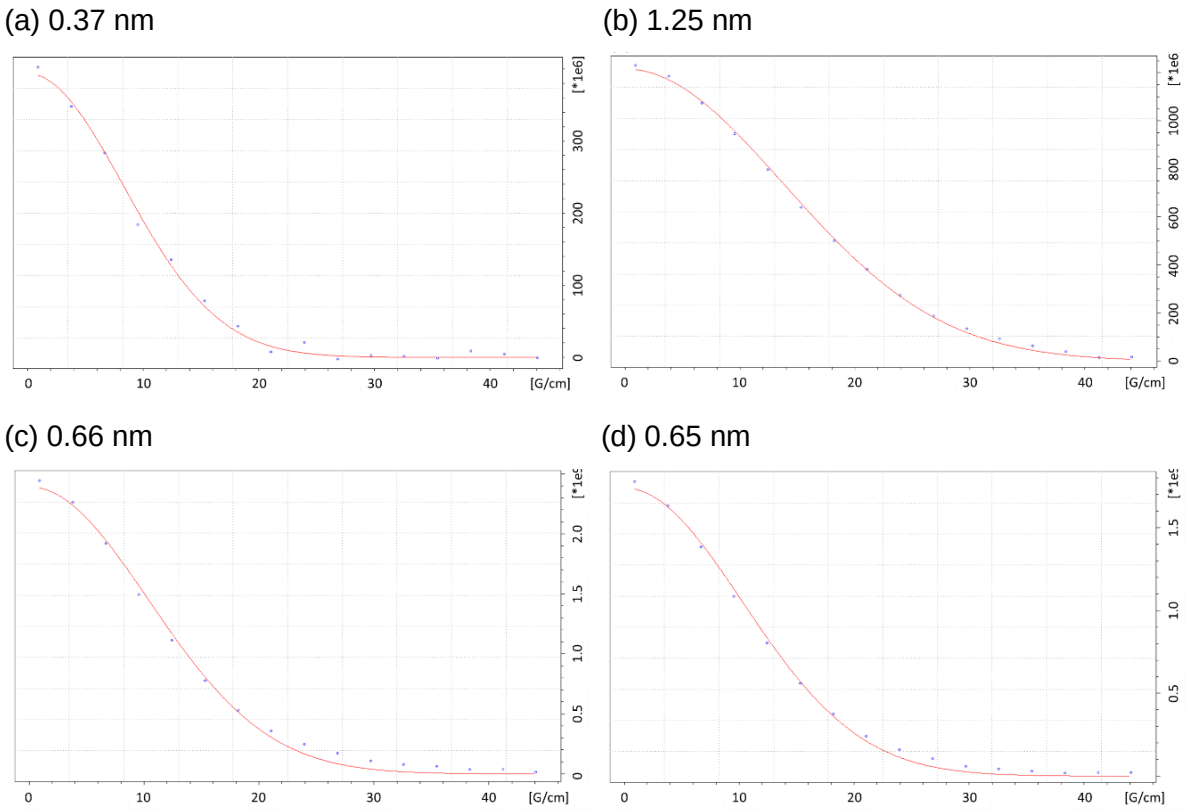

Figure S10. Decay curves and corresponding monoexponential fit for the selected signals as obtained from the Topspin fitting routine for **BisSQ1**. (a) 5.58 – 5.36 ppm, diffusion coefficient = 9.88 × 10^{-10} m^2/s; (b) 3.60 – 3.43 ppm, diffusion coefficient = 2.93 × 10^{-10} m^2/s; (c) 1.86 – 1.68 ppm, diffusion coefficient = 5.50 × 10^{-10} m^2/s; (d) 1.68 – 1.55 ppm, diffusion coefficient = 5.68 × 10^{-10} m^2/s. The corresponding hydrodynamic radii are given on the top of the respective decay curves.

Unfortunately, an unambiguous interpretation was not possible. The data showed different diffusion coefficients (which correspond to various hydrodynamic radii) for the different functional groups within the same molecule. This can be due to a distribution of sizes of the sheet-like aggregates in solution. The selected ^{1}H NMR signals may originate from aggregates of different size, thus causing a variation in the observed diffusion coefficient. Additionally, the strong aggregation and reduced mobility of some functional groups within the aggregate results in signal broadening and is the reason why only few signals of the aggregated species can be observed (Figure S9). The reported diffusion coefficients (see caption of Figure S10) were obtained from pseudo-2D measurements with the BPP-LED pulse sequence and converted to approximate radii by using the dynamic viscosity of toluene at 295 K. We also want to emphasize that the DOSY analysis and the corresponding equations are generally designed for spherical particles with a uniform size. In our case, we assume sheet-like structures (see AFM studies) and the growth of the aggregate cannot be controlled, resulting in an unknown size distribution.

9.1.7 AFM Studies

The thin film consisting of the sheet-like structures was observed on hydrophobic silicon wafer (Figure S11 left) as well as on hydrophilic mica (Figure S11 right). The height of the sheets was measured to be 2.0 ± 0.2 nm. The width varies between 10 – 40 nm and the length is up to 200 nm. The observed dimensions are comparable with that of the sheet-like structures on HOPG, as described in the main text (Figure 55a and b).

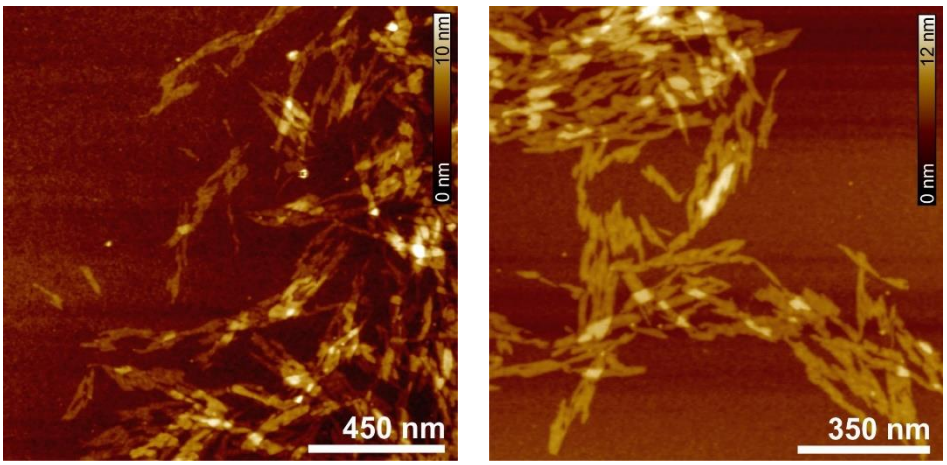

Figure S11. Height AFM images of sample **BisSQ1** prepared by spin-coating of toluene/TCE 98:2 (*v*/*v*) solution on SiO_x (left, *Z* scale is 10 nm); mica (right, *Z* scale is 12 nm.)

9.1.8 Proposed Packing Model

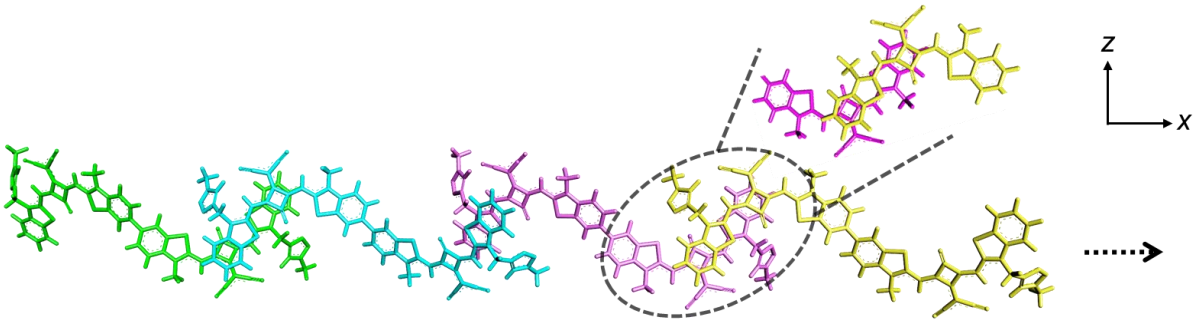

Figure S12. Proposed chromophore arrangement with each molecule colored differently within the nanosheet of self-assembled **BisSQ1** simulated and visualized using the program suite *BIOVIA Materials Studio 2017R2*. The geometry of the monomers was optimized at the level of density functional theory (B3LYP/6-31G*). Dashed arrow shows the supramolecular polymerization in x-axis. (Side chains are neglected for simplicity.)

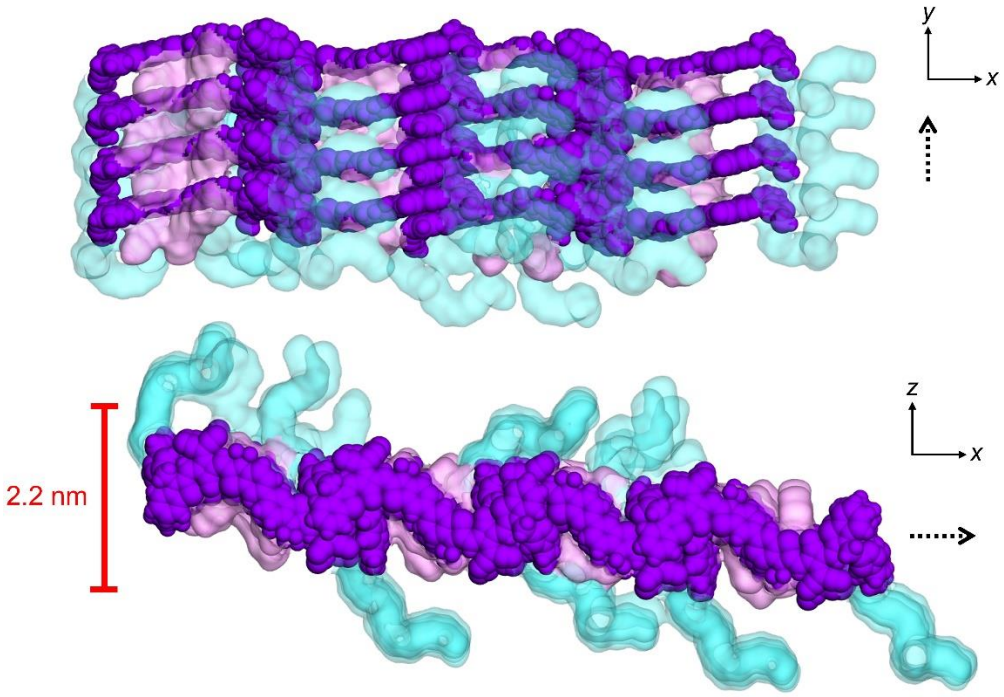

Figure S13. Proposed packing model of the nanosheets of self-assembled **BisSQ1**. Side view (top) and top view (bottom) of the nanosheet with the chromophores colored in violet. The geometry of the individual chromophores was optimized at the level of density functional theory (B3LYP/6-31G*). Oligoethyleneglycol chains are colored in cyan and aliphatic chains in pale violet, respectively. The model was created and optimized using the program suite *BIOVIA Materials Studio 2017R2* with the Forcite module in combination with the force field COMPASSII. Dashed arrows show the direction of two-dimensional supramolecular polymerization.

9.1.9 NMR Spectra

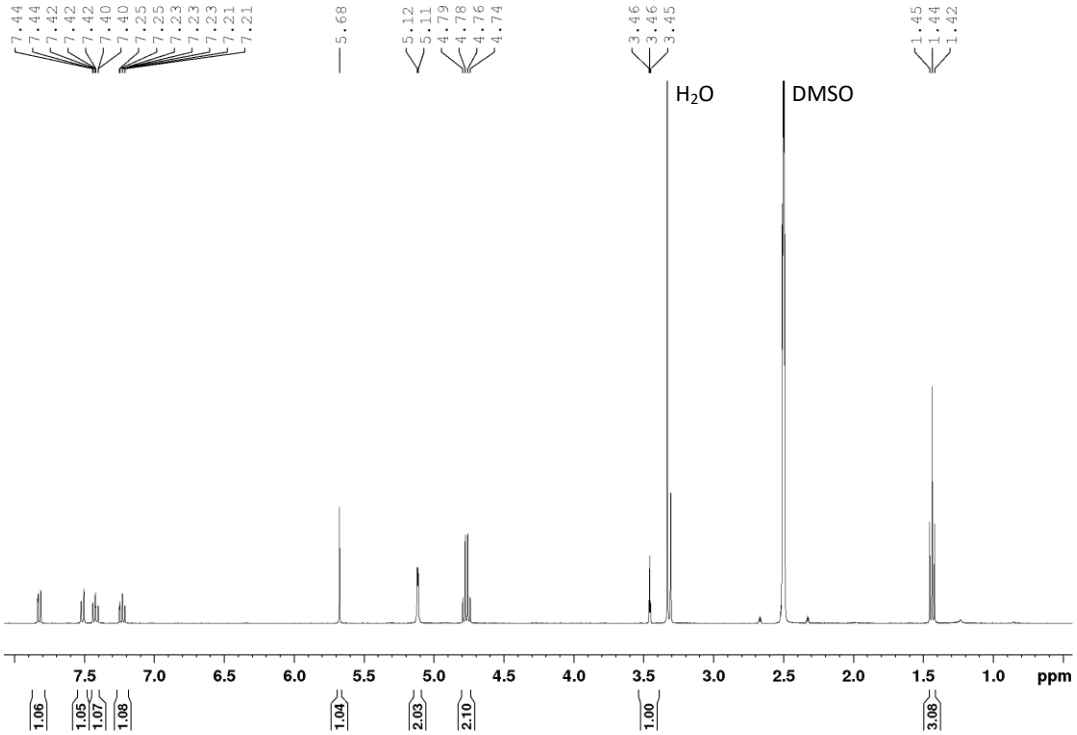

Figure S14. ^{1}H NMR (400 MHz, 295 K) spectrum of compound **3** in DMSO-d_6.

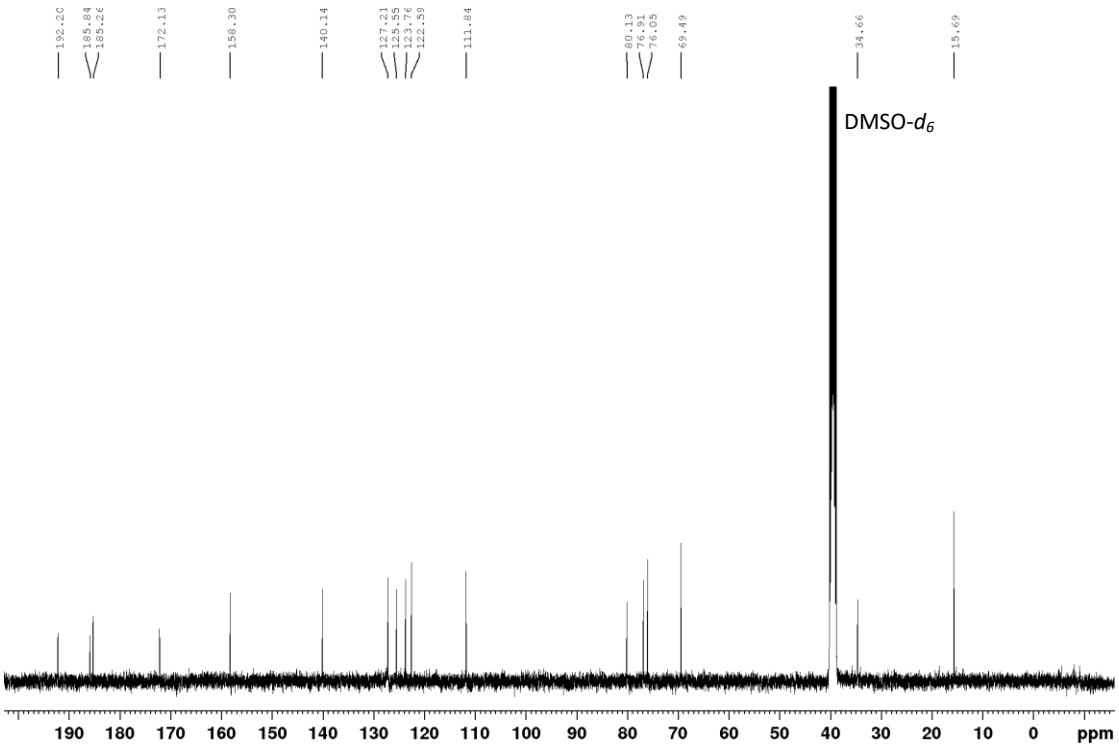

Figure S15. ^{13}C NMR (101 MHz, 295 K) spectrum of compound **3** in DMSO-d_6.

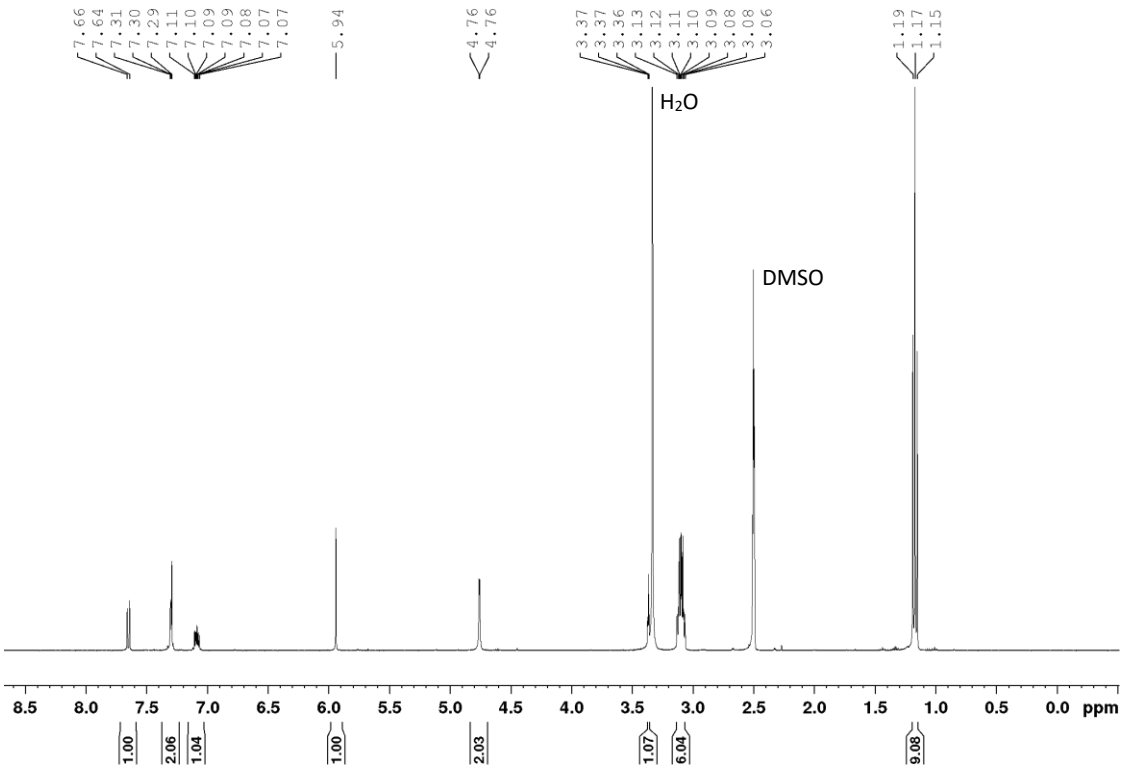

Figure S16. ^{1}H NMR (400 MHz, 295 K) spectrum of compound **4** in DMSO-d_6.

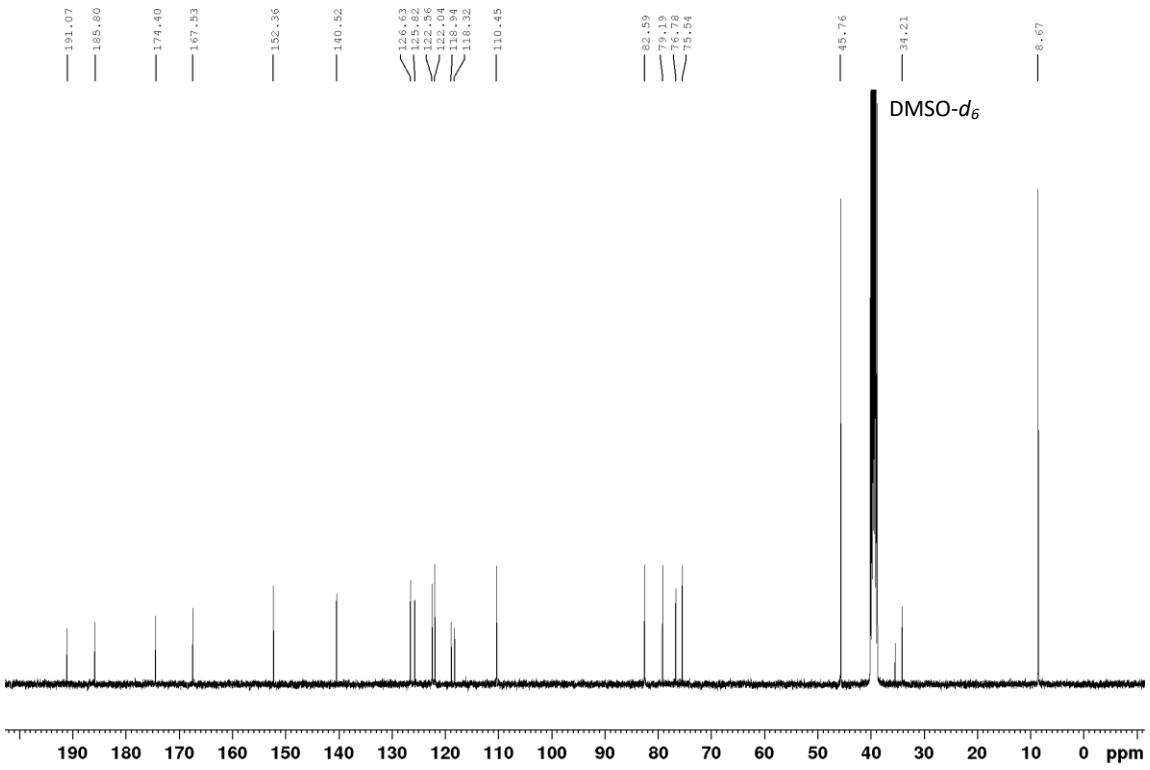

Figure S17. ^{13}C NMR (101 MHz, 295 K) spectrum of compound **4** in DMSO-d_6.

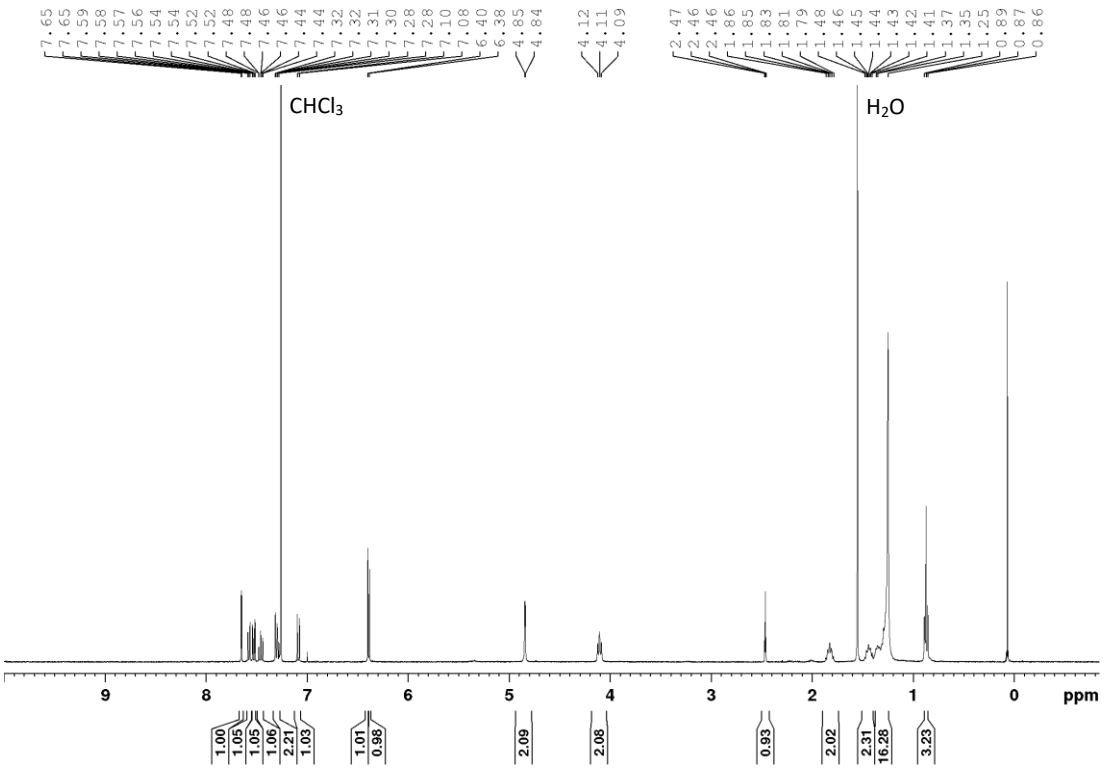

Figure S18. ^{1}H NMR (400 MHz, 295 K) spectrum of compound **6a** in $CDCl_3$.

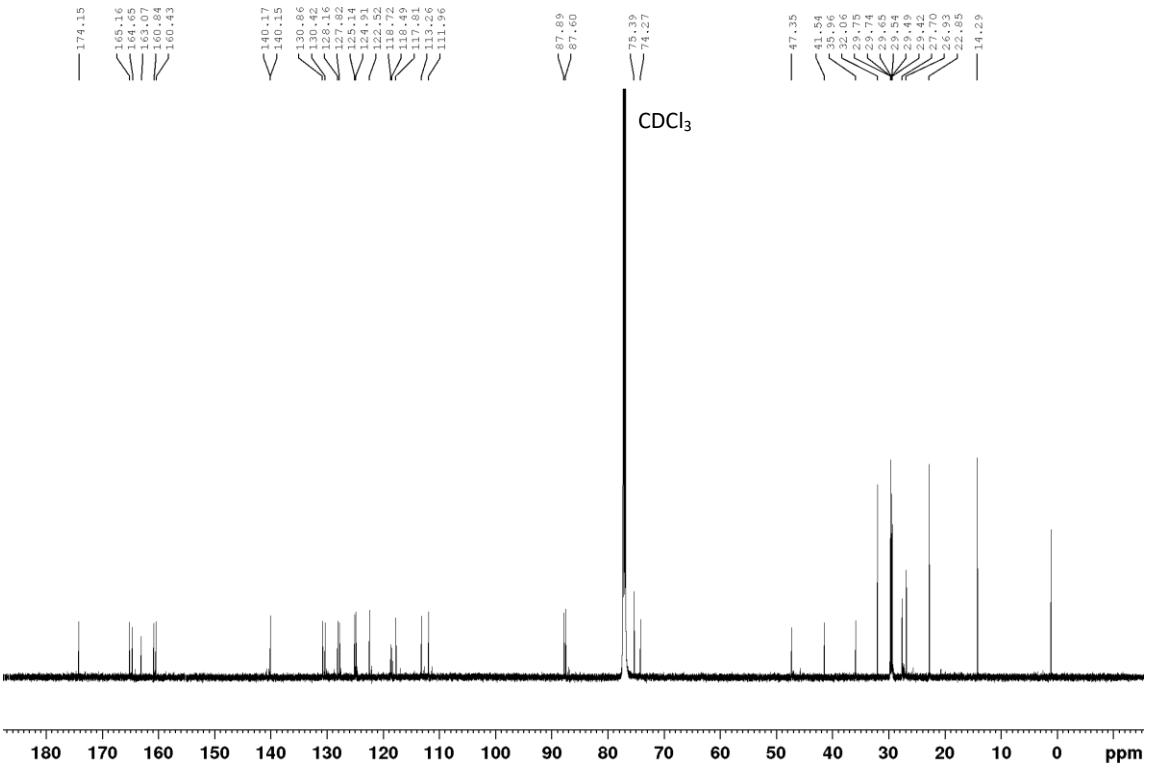

Figure S19. ^{13}C NMR (151 MHz, 295 K) spectrum of compound **6a** in $CDCl_3$.

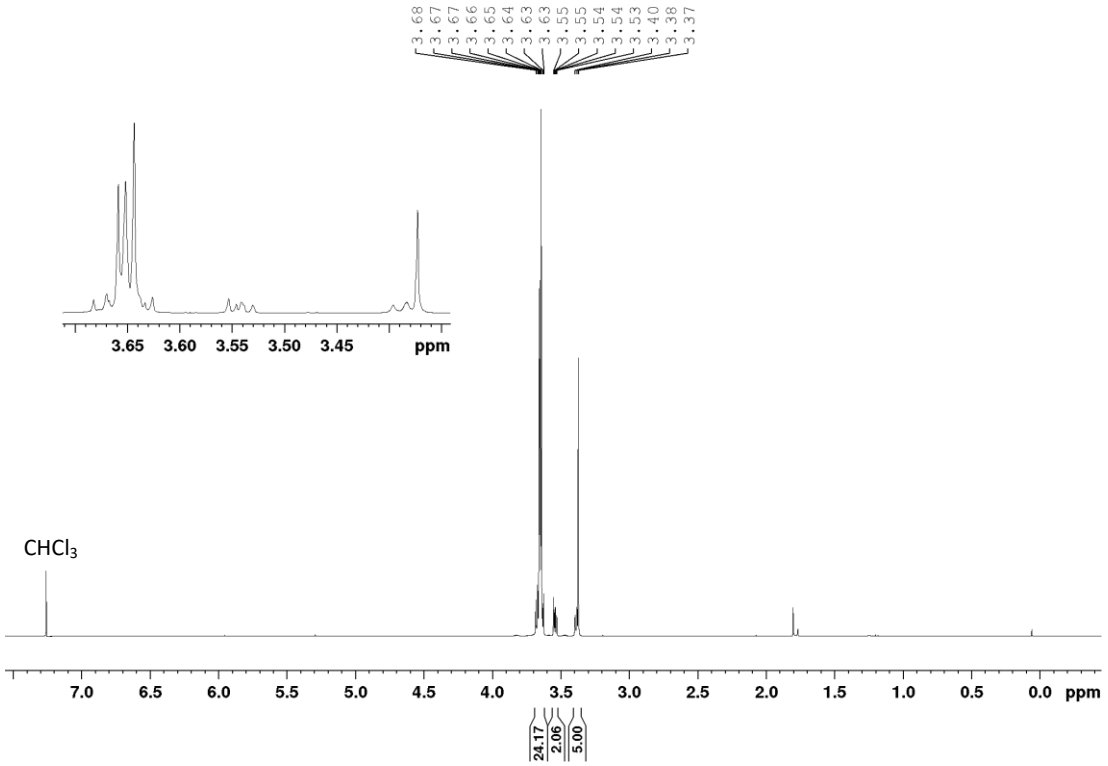

Figure S20. ^{1}H NMR (400 MHz, 295 K) spectrum of compound **7** in $CDCl_3$.

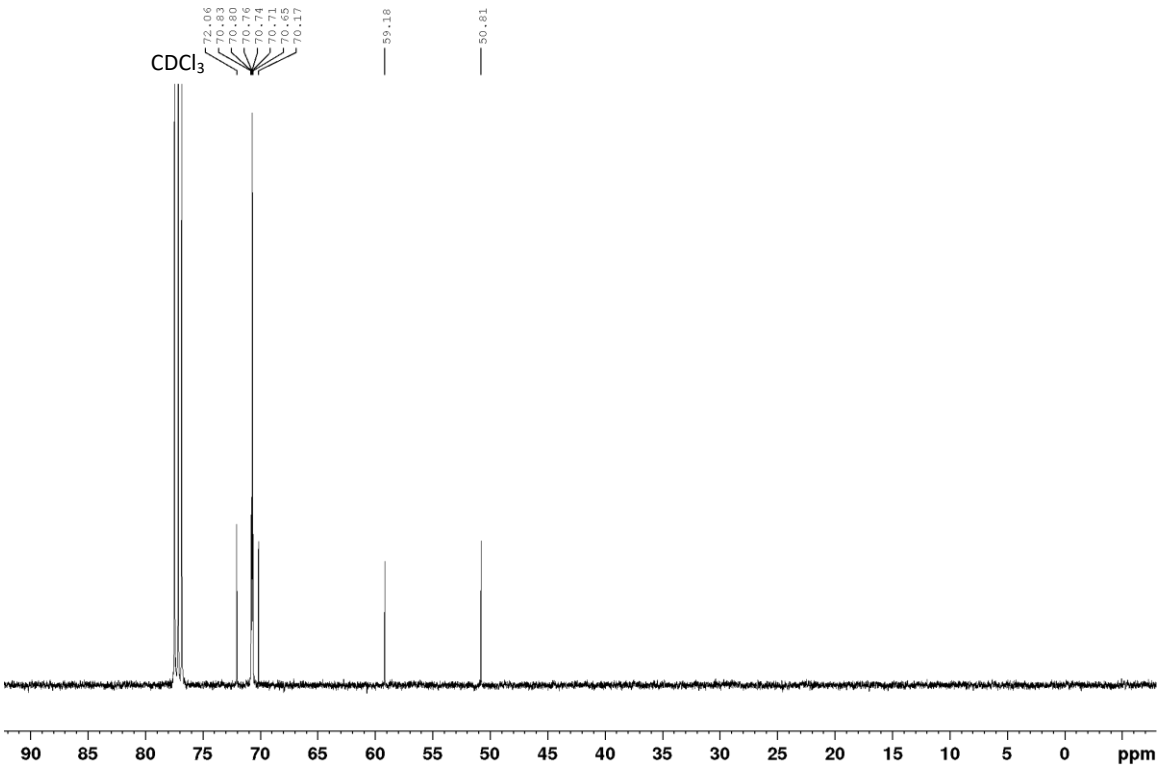

Figure S21. ^{13}C NMR (101 MHz, 295 K) spectrum of compound **7** in $CDCl_3$.

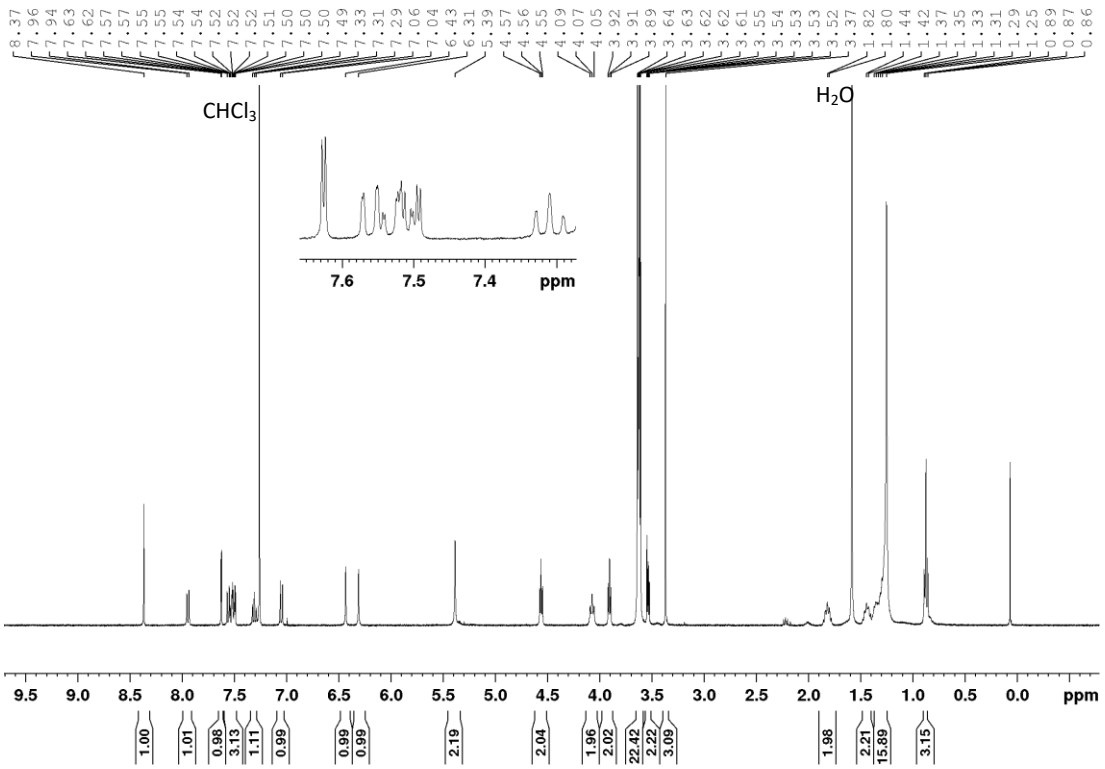

Figure S22. ^{1}H NMR (400 MHz, 295 K) spectrum of compound **8a** in $CDCl_3$.

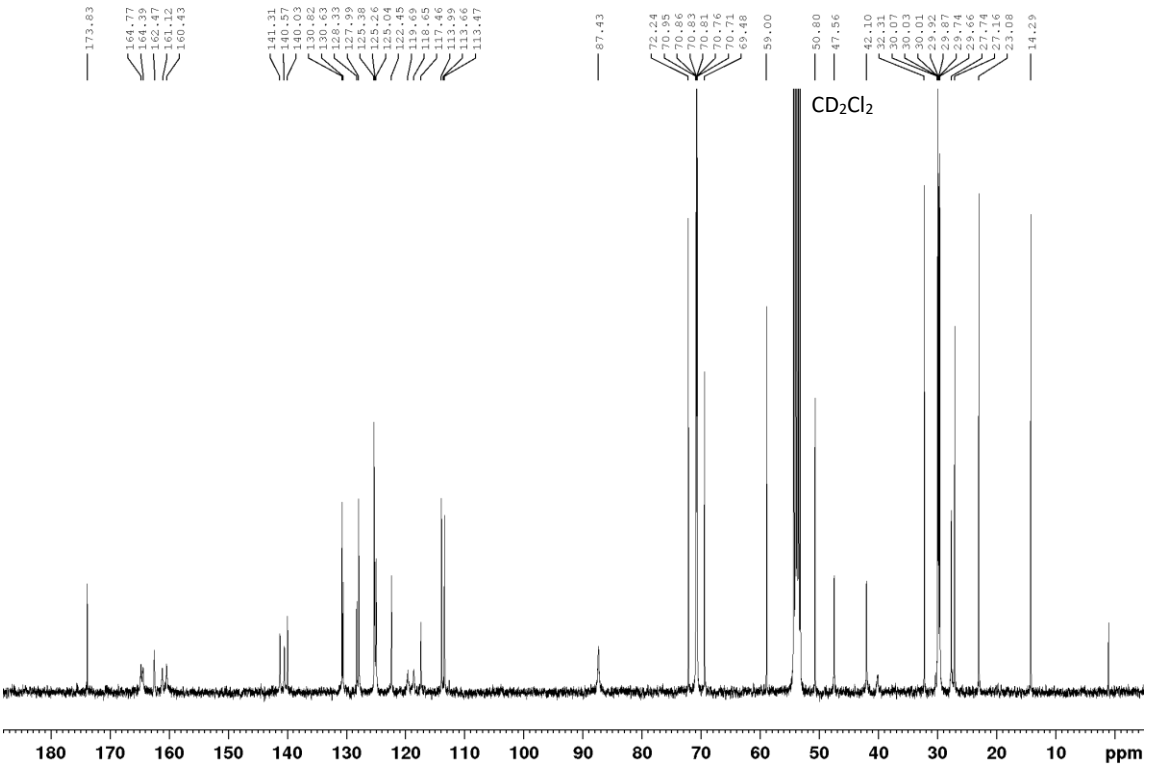

Figure S23. ^{13}C NMR (101 MHz, 295 K) spectrum of compound **8a** in CD_2Cl_2.

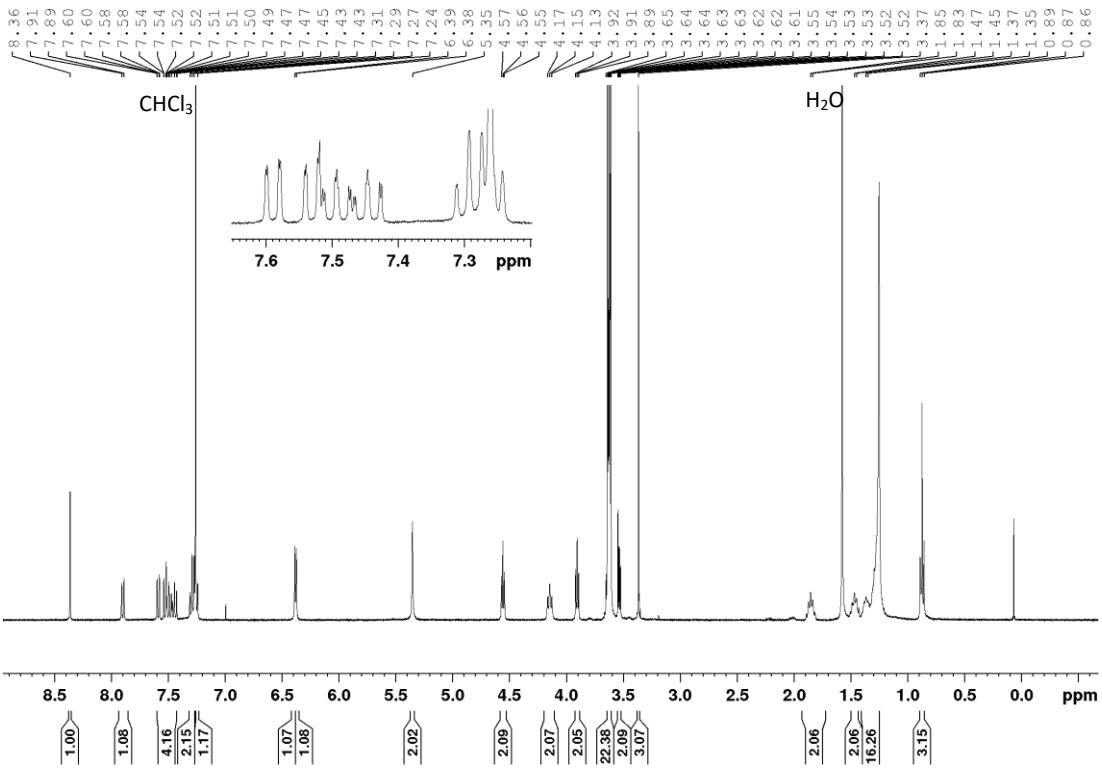

Figure S24. ^{1}H NMR (400 MHz, 295 K) spectrum of compound **SQ1** in $CDCl_3$.

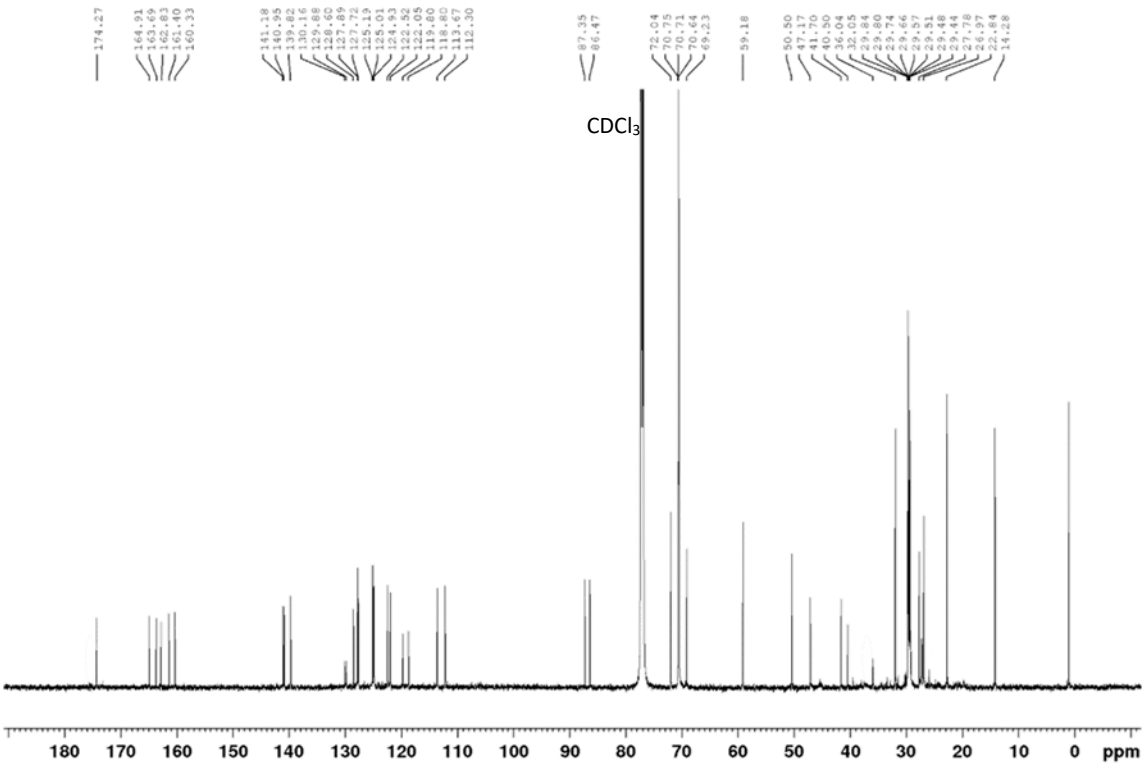

Figure S25. ^{13}C NMR (151 MHz, 295 K) spectrum of compound **SQ1** in $CDCl_3$.

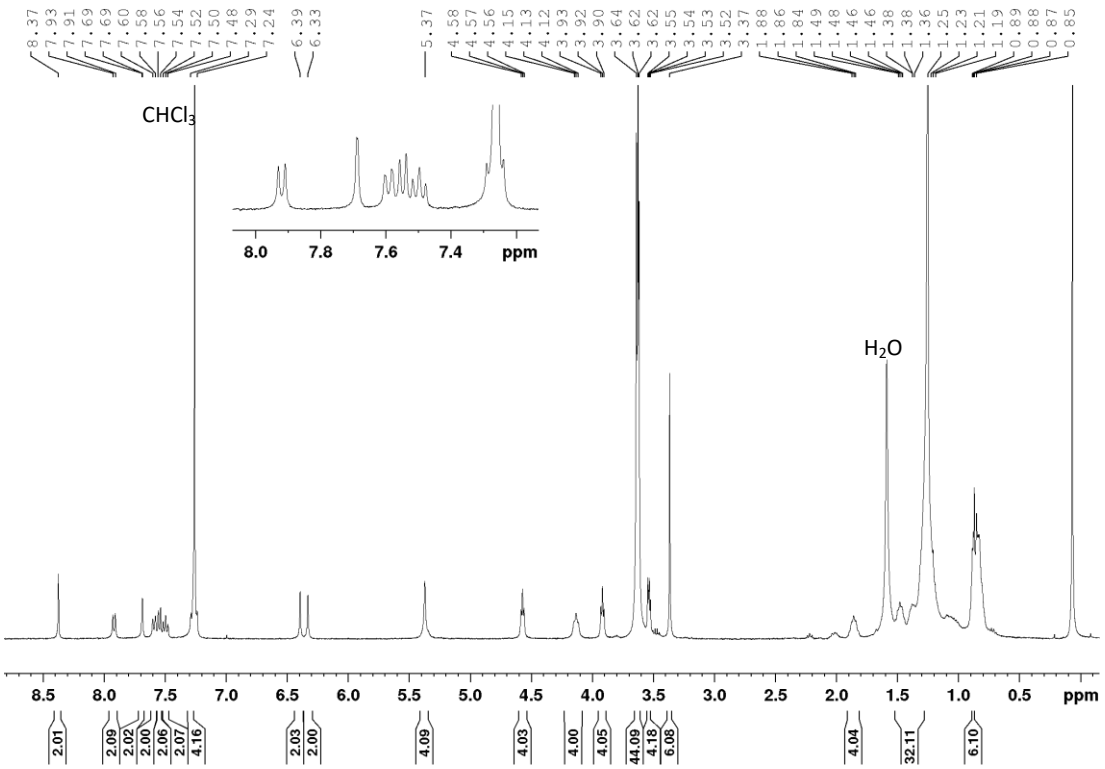

Figure S26. ^{1}H NMR (400 MHz, 295 K) spectrum of compound **BisSQ1** in $CDCl_3$.

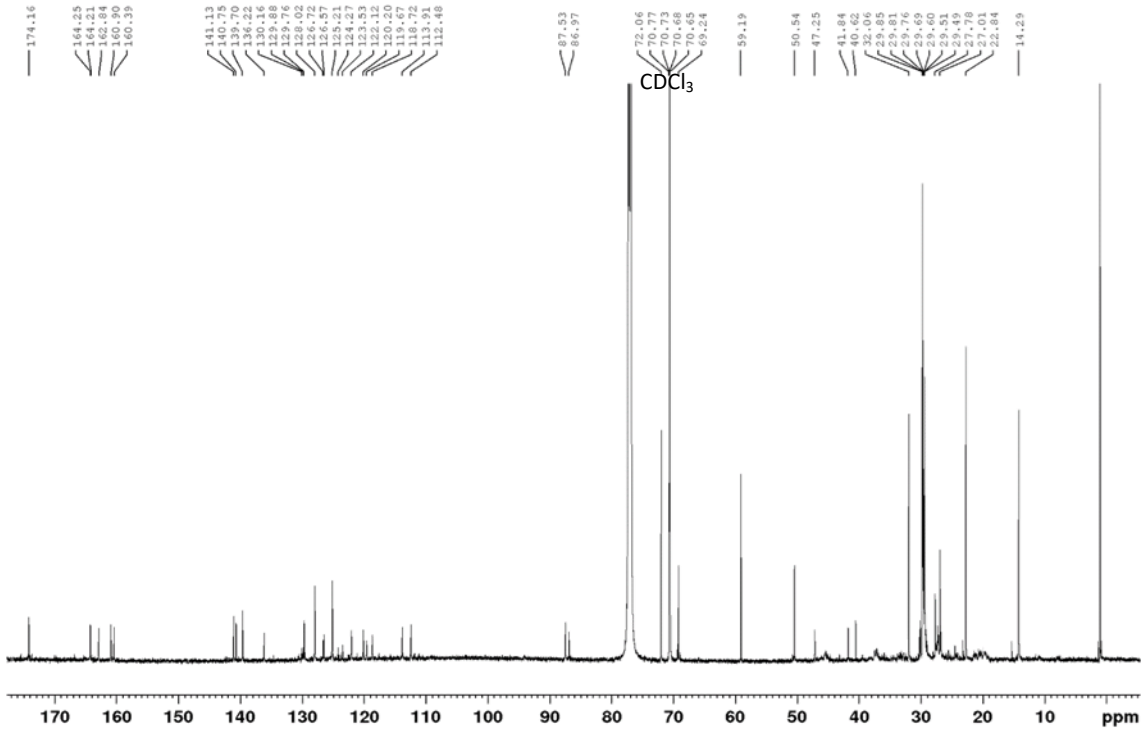

Figure S27. ^{13}C NMR (151 MHz, 295 K) spectrum of compound **BisSQ1** in $CDCl_3$.

9.2 Supporting Information for *Chapter 4*: Polymorphism in Squaraine Dye Aggregates by Self-Assembly Pathway Differentiation: Panchromatic Tubular Dye Nanorods versus J-Aggregate Nanosheets[131]

9.2.1 Materials and Methods

General

All solvents and reagents were purchased from commercial sources and used as received without further purification. Column chromatography was performed using silica gel 60M (0.04 – 0.063 mm).

Gel permeation chromatography (GPC)

For the GPC purification method, the preparative recycling-GPC LaboACE from Japan Analytical Industry Co., Ltd. (JAI) with PLgel Prep columns (from Agilent Technologies) were used.

NMR spectroscopy

NMR spectra were recorded on a Bruker Avance 400 or Bruker Avance DMX 600 at 295 K. The spectra were calibrated to the residual solvent peak and the chemical shifts δ are given in ppm. Multiplicities are denoted as follows: s = singlet, d = doublet, t = triplet, q = quartet, quint = quintet, dd = doublet of doublets, td = triplet of doublets, m = multiplet, br = broad.

Mass spectrometry

High-resolution mass spectra (ESI) were recorded on a microTOF focus instrument (Bruker Daltonik GmbH).

Optical spectroscopy

For all spectroscopic measurements, spectroscopic grade solvents (Uvasol®) were used. The absorption spectra were recorded on JASCO V-670 or V-770 UV/Vis/NIR spectrophotometer. The spectral band width and the scan rate were 1 nm and 400 nm min^{-1}, respectively. Stock solutions in $CHCl_3$ or 1,1,2,2-tetrachloroethane (TCE) were accurately freshly prepared for all measurements and continuously diluted for absorption measurements by taking into account the solubility and the absorbance. The UV/Vis/NIR measurements were performed in quartz cell cuvettes with path lengths of 0.1, 1.0, 5.0, 10.0 and 100.0 mm. Fluorescence spectra were recorded on a FLS 980 Edinburgh fluorescence spectrometer. Fluorescence quantum yields

were determined by a calibrated integrating sphere system (C9920, Hamamatsu, Japan). Time-resolved measurements were performed with a ps laser diode at 670 nm and a TCSPC detection unit.

Sample preparation for self-assembly studies

Stock solutions are prepared by dissolving **BisSQ2** in TCE first and then diluting with toluene. The as-prepared solutions with specified concentration (toluene/TCE 98:2) are heated to 85 °C for 20 minutes to achieve a fully monomeric state.

Stock solution of AggI: The hot solution is transferred immediately into a pre-cooled 25 °C chamber and equilibrated for 1 hour.

Stock solution of AggII: The hot solution is slowly cooled down to 25 °C with a rate of 2 °C/min and then sonicated for 20 minutes at 25 °C.

For concentration-dependent UV/Vis/NIR measurements, the stock solution is diluted into a series of sample solutions with various concentrations and equilibrated for one day prior to the measurements.

Atomic force microscopy (AFM)

AFM measurements were performed under ambient conditions using a Bruker Multimode 8 SPM system operating in tapping mode in air. Silica cantilevers (OMCL-AC200TS, Olympus) with a resonance frequency of ~150 kHz and a spring constant of ~10 Nm^{-1} were used. The samples were prepared by spin-coating of solutions in toluene/TCE mixture (98:2, $c_0 = 2.5 \times 10^{-5}$ M) onto silica wafer (SiO_x) with 2000 rpm.

Wide-angle X-ray scattering (WAXS)

WAXS measurements were performed on a Bruker Nanostar (Detector Vantec2000, Microfocus copper anode X-ray tube Incoatec). Samples were prepared on aluminium foil by multistep evaporation of a 5.0 g L^{-1} solution of **BisSQ2-AggI** or **BisSQ2-AggII** in toluene/TCE 98:2. The measurements were carried out with the sample positioned perpendicular to the incident X-ray beam. WAXS experiments were performed at a sample-detector distance of 21 cm, with the detector tilted by 14° upwards in order to study the angular range of $2q = 0.8° - 28°$. Silver behenate was used as calibration standard for WAXS. All X-ray data were processed and evaluated with the program datasqueeze.

9.2.2 Synthesis and Characterizations

Synthesis of compound **BisSQ2**

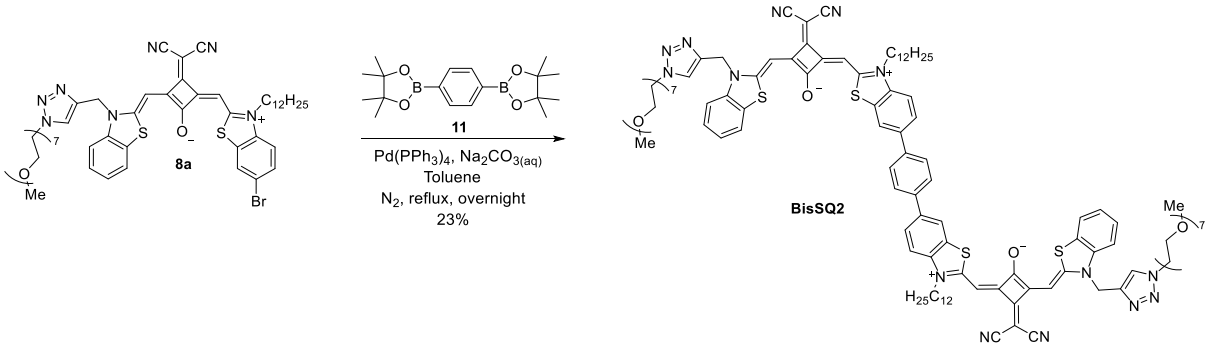

Compound **8a** (55.0 mg, 51.5 µmol), tetrakis(triphenylphosphine)palladium(0) ($Pd(PPh_3)_4$) (3.78 mg, 3.27 µmol) and 1 M Na_2CO_3 aqueous solution (0.6 mL) were mixed in 2 mL anhydrous toluene under nitrogen atmosphere. 1,4-phenyldiboronic acid bis(pinacol) ester (7.60 mg, 23.0 µmol) was dissolved in 2 mL anhydrous toluene and added dropwise into the above mixture *via* syringe pump (rate: 1 mL/h) and heated to reflux overnight. Inorganic salts were filtered off and toluene was removed under reduced pressure. Preparative recycling GPC ($CHCl_3$/MeOH = 9:1) was applied, giving pure **BisSQ2** as a dark green waxy solid (11.0 mg, 5.32 µmol, 23%).

^{1}H NMR (400 MHz, $CDCl_3$): δ = 8.37 (s, 2H), 7.88 (d, J = 8.6 Hz, 2H), 7.75 (d, J = 1.9 Hz, 2H), 7.67 (dd, J = 8.6 Hz, 1.9 Hz, 2H), 7.61 (s, 4H), 7.53 (d, J = 7.7 Hz, 2H), 7.47 (t, J = 8.6 Hz, 2H), 7.31 – 7.24 (m, 4H), 6.38 (s, 2H), 6.35 (s, 2H), 5.34 (s, 4H), 4.57 (t, J = 5.4 Hz, 4H), 4.17 (br, 4H), 3.91 (t, J = 5.4 Hz, 4H), 3.64 – 3.61 (m, 44H), 3.55 – 3.52 (m, 4H), 3.37 (s, 6H), 1.89 – 1.84 (m, 4H), 1.53 – 1.18 (m, 32H), 0.87 (m, 6H) ppm.

^{13}C NMR (151 MHz, $CDCl_3$): δ = 174.2, 164.4, 163.9, 162.8, 160.7, 160.6, 141.2, 140.5, 139.8, 138.8, 137.3, 130.2, 130.1, 130.0, 129.9, 129.6, 128.0, 127.9, 127.6, 126.7, 125.2, 125.0, 122.1, 120.3, 119.7, 118.8, 113.8, 112.5, 87.5, 86.8, 72.1, 70.8, 70.73, 70.72, 70.70, 70.68, 70.67, 70.64, 69.2, 59.2, 50.5, 47.3, 41.8, 40.5, 32.1, 29.9, 29.77, 29.76, 29.69, 29.60, 29.50, 29.48, 27.8, 27.0, 22.8, 14.3 ppm.

HRMS (ESI, pos. mode, MeCN/$CHCl_3$): m/z: 2087.93841 $[M+Na]^+$ (calcd. for $C_{112}H_{140}N_{14}NaO_{16}S_4^+$: 2087.93468).

Mp: > 285 °C (decomp.)

9.2.3 UV/Vis/NIR Absorption and Fluorescence Spectroscopy

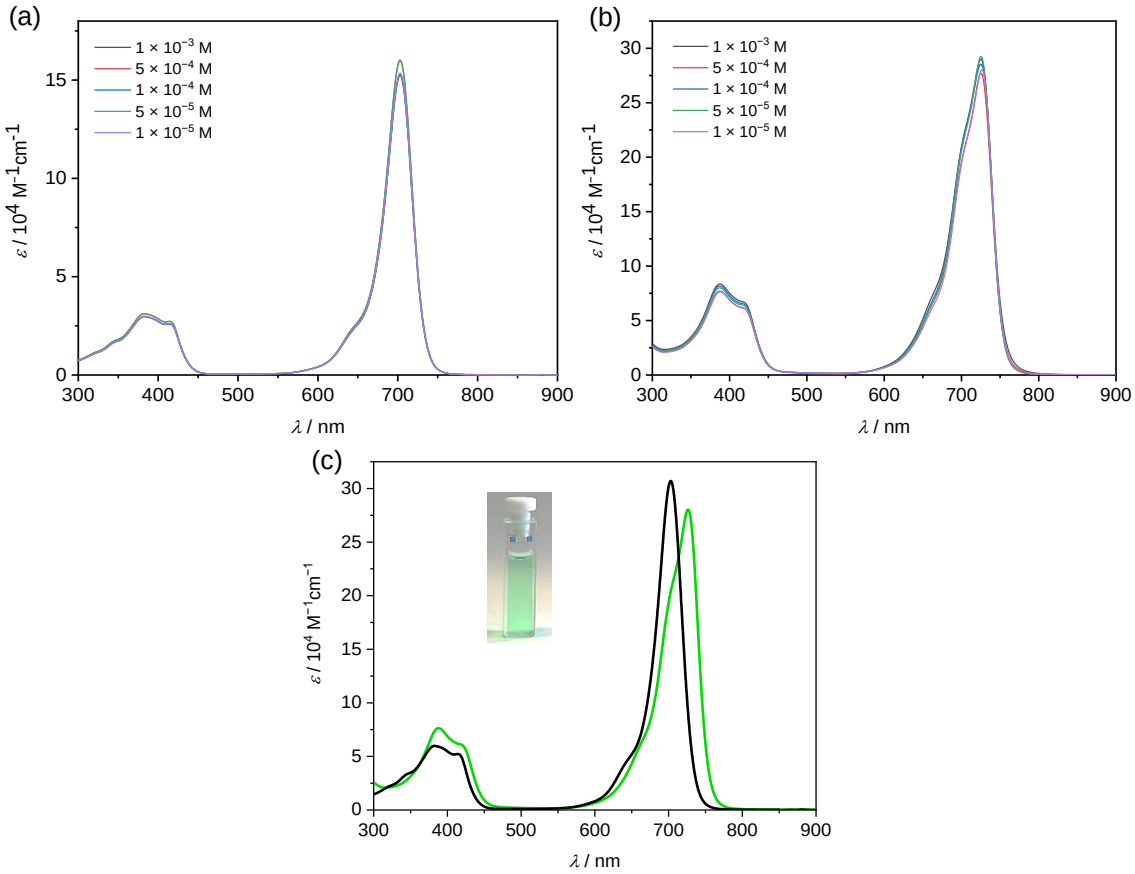

Figure S28. UV/Vis/NIR absorption spectra of (a) **SQ1** and (b) **BisSQ2** in $CHCl_3$ at different concentrations at 25 °C. (c) UV/Vis/NIR absorption spectra of **SQ1** (black line) and **BisSQ2** (green line) in $CHCl_3$ at $c_0 = 1 \times 10^{-5}$ M, 25 °C. The extinction coefficient ε for **SQ1** was doubled for better comparison. Inset of (c): **BisSQ2** solution in $CHCl_3$ at $c_0 = 1 \times 10^{-5}$ M, 25 °C.

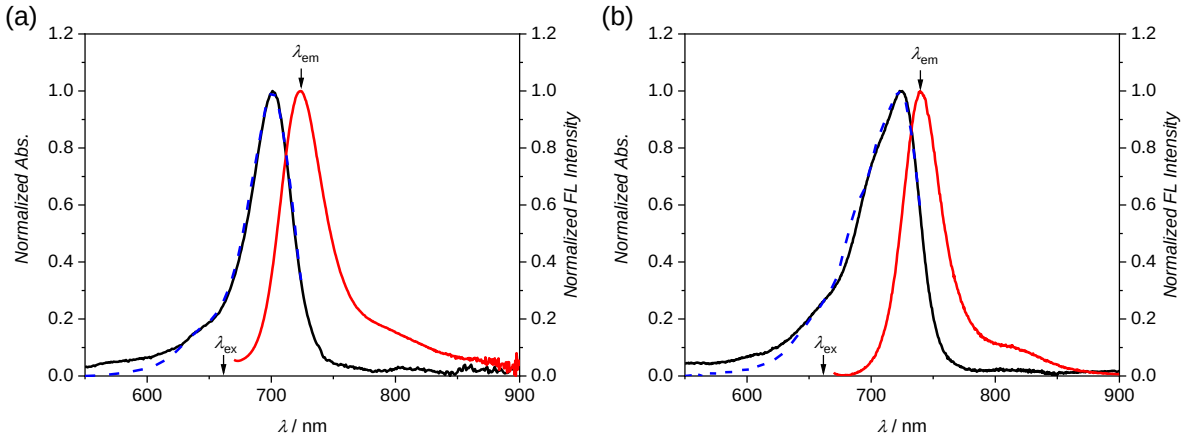

Figure S29. Normalized UV/Vis/NIR absorption (solid black lines), fluorescence (solid red lines, λ_{ex} = 660 nm) and excitation (dashed blue lines, λ_{em} = 724 nm for **SQ1**, λ_{em} = 740 nm for **BisSQ2**) spectra of (a) **SQ1** and (b) **BisSQ2** in $CHCl_3$ at 25 °C.

Table S2. Summarized absorption and emission data of **BisSQ2** and **SQ1** in $CHCl_3$.

	λ_{max} (nm)	ε_{max} ($M^{-1}cm^{-1}$)	λ_{em} (nm)	$\Delta\tilde{\nu}_{Stokes}$ (cm^{-1})	Φ_{FL}[a] (%)	τ_{FL}[b] (ns)	k_{FL}[c] (10^8 s^{-1})	k_{nr}[c] (10^8 s^{-1})
SQ1	703	150000	724	410	79 ± 0.36 (81 ± 0.17)	4.78 ± 0.01	1.65 ± 0.01 (1.69 ± 0.01)	0.44 ± 0.02 (0.40 ± 0.01)
BisSQ2	726	280000	740	260	42 ± 1.3 (46 ± 0.75)	3.01 ± 0.01	1.41 ± 0.42 (1.59 ± 0.02)	1.92 ± 0.43 (1.78 ± 0.27)

[a] Fluorescence quantum yields were determined by a calibrated integrating sphere system. The value corrected from re-absorption are given in brackets.
[b] Φ_{FL} were determined by tail fit analysis of the data obtained from time-correlated single photon counting measurements with ps laser diode at 670 nm using a magic angle setup.
[c] Determined according to $k_{FL} = \Phi_{FL}/\tau_{FL}$ and $k_{nr} = 1/\tau_{FL} - k_{FL}$. The value calculated from corrected QY is given in brackets.

9.2.4 Determination of Absolute Fluorescence Quantum Yield

During the fluorescence quantum yield investigations of **BisSQ2** and **SQ1** utilizing an integrating sphere, strong reabsorption took place, which was identified by the broadening and decrease of the fluorescence intensity and the shift of the fluorescence maximum to lower wavelength upon dilution. The reabsorption contaminated spectra were adjusted at the red edge to the reabsorption-free fluorescence spectra (Figure S30) and the corrected absolute quantum yields were determined using the approach of Ahn *et al.*[163]

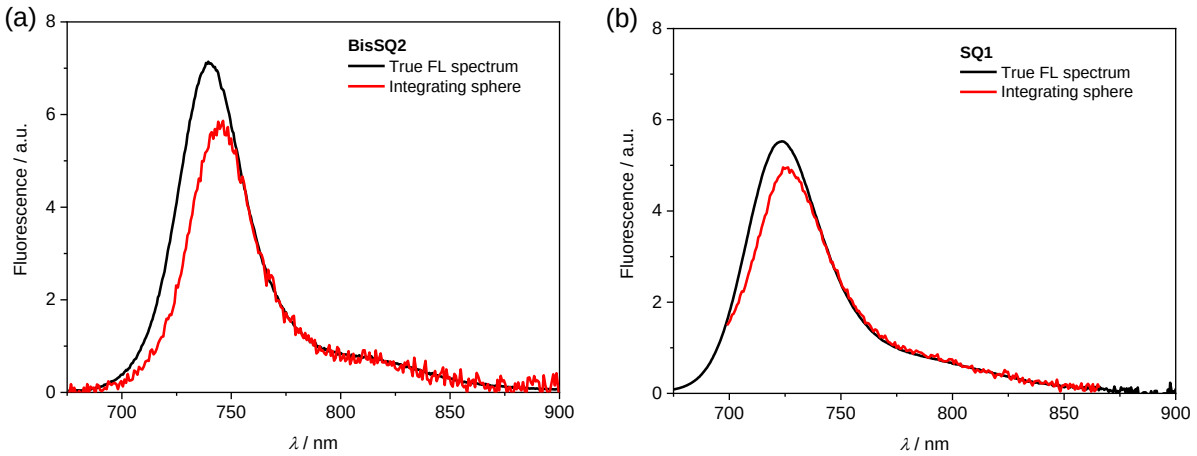

Figure S30. (a) Fluorescence spectrum of **BisSQ2** in $CHCl_3$ solution measured with the integrating sphere ($c_0 = 8 \times 10^{-6}$ M, red line) adjusted to the red edge of the reabsorption-free spectrum ($c_0 = 2 \times 10^{-7}$ M, black line). (b) Fluorescence spectrum of **SQ1** in $CHCl_3$ solution measured with the integrating sphere ($c_0 = 5 \times 10^{-6}$ M, red line) adjusted to the red edge of the reabsorption-free spectrum ($c_0 = 5 \times 10^{-6}$ M, black line).

9.2.5 Self-Assembly Studies

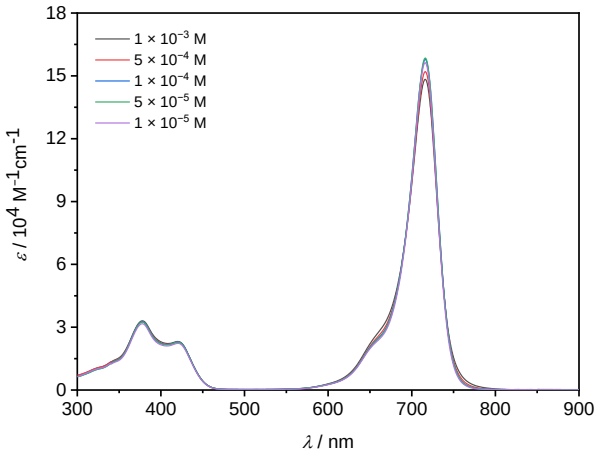

Figure S31. UV/Vis/NIR absorption spectra of **SQ1** in toluene/TCE 98:2 at different concentrations at 25 °C.

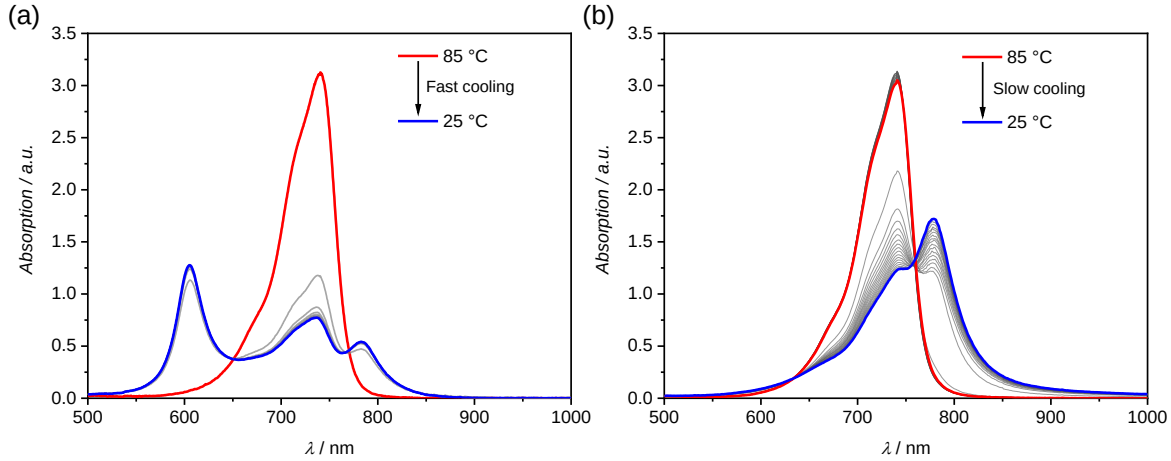

Figure S32. UV/Vis/NIR absorption spectra showing the formation of (a) **BisSQ2-AggI** *via* fast cooling (transferring the hot solution immediately into a pre-cooled chamber at 25 °C) and (b) **BisSQ2-AggII** *via* slow cooling (2 °C/min) in toluene/TCE 98:2, $c_0 = 2.5 \times 10^{-5}$ M. Red lines: spectra at 85 °C; blue lines: spectra at 25 °C.

9.2.6 Proposed Packing Models

To derive the number of strands intertwined within the nanorods, the volume of one single molecule (V_{mol}) was determined as follows:

$$V_{\mathrm{mol}} = \frac{M}{\rho \times N_{\mathrm{A}}} = 3.432\ \mathrm{nm}^3 \qquad \text{(S5)}$$

(Molar mass, M = 2066.67 g/mol; molecular density, ρ = 1 g/cm^3 (estimated); Avogadro constant, $N_A = 6.022 \times 10^{23}$ mol^{-1}).

The volume of one pitch of the nanorod (V_{rod}) can be calculated based on the AFM experimental data (Figure 57d):

$$V_{\mathrm{rod}} = \pi \times r^2 \times h = 245\ \mathrm{nm}^3 \quad \text{(S6)}$$

(r = 0.5 × diameter = 2.5 nm, h = helical pitch = 12.5 nm).

Hence, the number of molecules (N) that constitute one helical pitch can be estimated by:

$$N = \frac{V_{rod}}{V_{mol}} \cong 72 \quad \text{(S7)}$$

Based on our modelling studies, nine molecules are required to form one helical pitch of a single strand (Figure S33). Therefore, it is reasonable to assume the formation of eight intertwining strands (8 × 9 = 72 molecules) in the rod-like aggregate as displayed in Figure 58c in the main text.

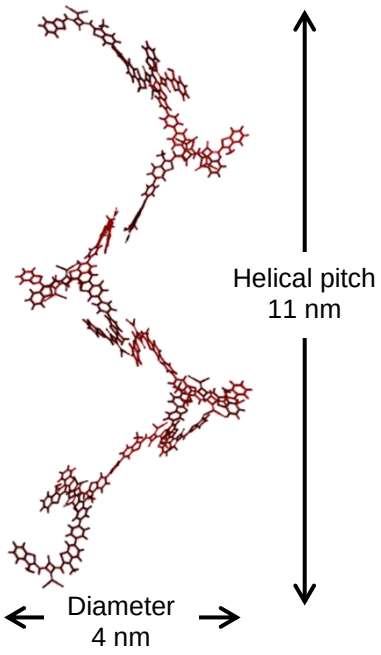

Figure S33. Proposed structural model of one single strand of **BisSQ2-AggI** nanorod, which shows the side view. The model was constructed and visualized with the program suite *BIOVIA Materials Studio 2017R2* and the side chains were omitted for clarity.

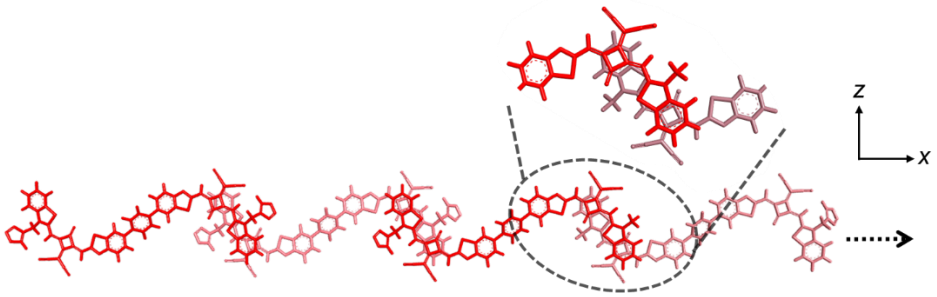

Figure S34. Proposed chromophore arrangement with each molecule colored differently within the nanosheet of **BisSQ2-AggII** simulated and visualized using the program suite *BIOVIA Materials Studio 2017R2*. The dashed arrow shows the supramolecular polymerization in x-axis. (Side chains are neglected for simplicity.)

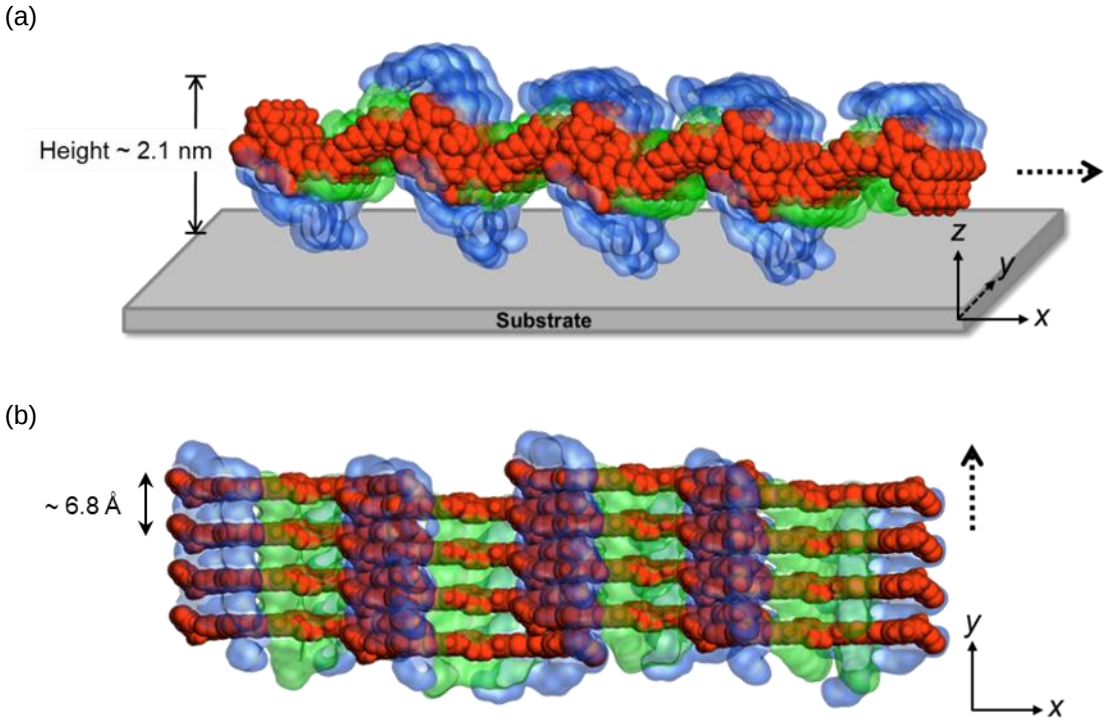

Figure S35. Proposed packing model of the nanosheets of **BisSQ2-AggII**. (a) Front view and (b) top view of the nanosheet with the chromophores colored in red. Oligoethyleneglycol chains are colored in blue and dodecyl chains in green, respectively. The model was created and optimized using the program suite *BIOVIA Materials Studio 2017R2* with the Forcite module in combination with the force field COMPASSII. The dashed arrows show the direction of two-dimensional supramolecular polymerization into nanosheets.

9.2.7 Data Evaluation

For the concentrated stock solution of **BisSQ2-AggI** ($c_0 = 2.2 \times 10^{-4}$ M), which was prepared for the concentration-dependent UV/Vis/NIR experiments (Figure 59 in *Chapter 4*), we observed that the dye aggregates adsorbed on the inner wall of the glass vial. This is in line with our proposed packing model (Figure 58c in *Chapter 4*) where the hydrophilic oligo

ethylene glycol chains are on the outside of the nanorods, therefore the nanorods tend to interact with the hydrophilic glass surface. As a consequence, the real concentration of **BisSQ2-AggI** in the stock solution was unknown and lower than that calculated, causing an underestimation of the molar absorptivity of all the samples. Noteworthy is that an isosbestic point is visible (Figure 59a in *Chapter 4*), indicating that the dilution process was correct and reliable. In addition, we confirmed that **BisSQ2** in its monomeric form under diluted condition (toluene/TCE 98:2, $c_0 = 2.0 \times 10^{-6}$ M) was not adsorbed on the glass surface. We measured the absorption spectrum for the diluted solution and determined the molar absorptivity at 739 nm (Figure S36). This molar absorptivity was used to calibrate the measured spectrum of the fully monomeric state (sample with the lowest concentration) in the concentration-dependent experiment. Afterwards, all the other measured spectra were calibrated accordingly (Figure 59 in *Chapter 4*), thus the real concentrations of all samples could be calculated for further thermodynamic analyses.

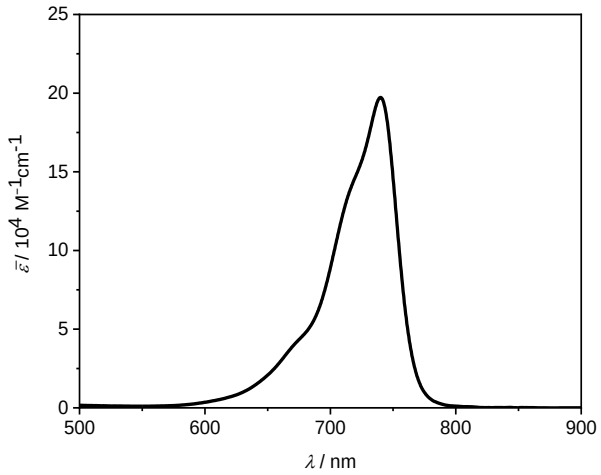

Figure S36. UV/Vis/NIR absorption spectrum of **BisSQ2** in toluene/TCE 98:2, $c_0 = 2.0 \times 10^{-6}$ M at 25 °C.

For the thermodynamic analysis of the self-assembly processes, literature known procedures were applied. Accordingly, we have used the monomer-dimer,[205] isodesmic[206] and cooperative K_2/K model[93] to fit the concentration-dependent UV/Vis/NIR spectra. The results are depicted in Figure S37.

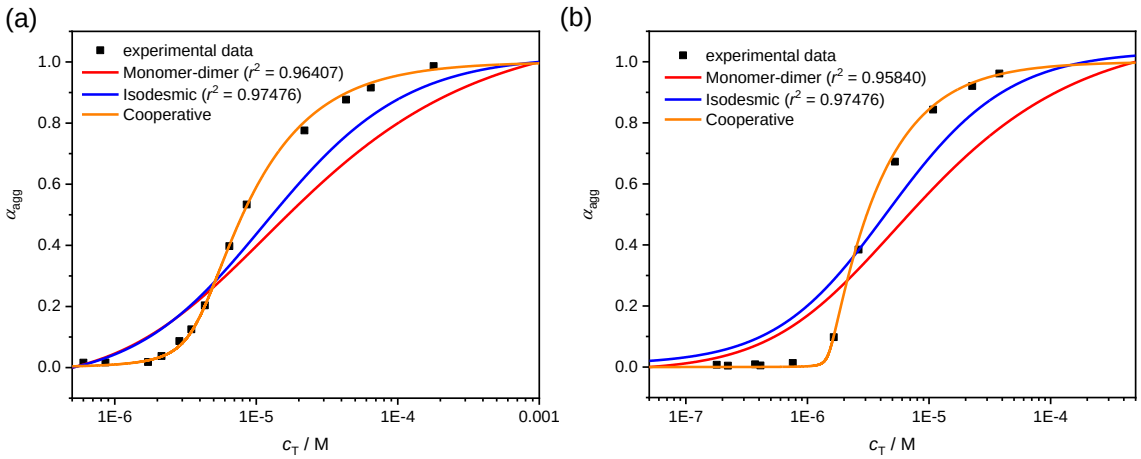

Figure S37. Plot of fractions of aggregate against c_T and fitting with the monomer-dimer model (red line), isodesmic model (blue line) and cooperative K_2/K model (orange line) of (a) **BisSQ2-AggI** at 739 nm; (b) **BisSQ2-AggII** at 780 nm in toluene/TCE 98:2 (25 °C).

Cooperative K_2/K Model[93]

In this model, two states of the aggregation process are differentiated: the nucleation regime, described by the equilibrium constant K_2 for the dimerization, and the elongation regime, being characterized by the equilibrium constant K.[93] The absorption spectra of **BisSQ2** were globally fitted[146] and in this way the aggregation constants K_2 and K as well as the absorption spectra of ideal monomer and aggregate were obtained.

Determination of the Degree of Aggregation Based on UV/Vis/NIR Data

The degree of aggregation α was calculated from the data obtained by concentration-dependent UV/Vis/NIR measurements according to Equation (S8):

$$\alpha(c) = \frac{\varepsilon(c) - \varepsilon_M}{\varepsilon_A - \varepsilon_M}, \quad \text{(S8)}$$

where $\varepsilon(c)$ is the measured apparent absorption coefficient at concentration c and ε_M and ε_A are the respective absorption coefficients of the monomer (M) and fully aggregated state (A). ε_M and ε_A were determined from the ideal monomer and aggregate spectra obtained from the global fit analysis using the K_2/K model.

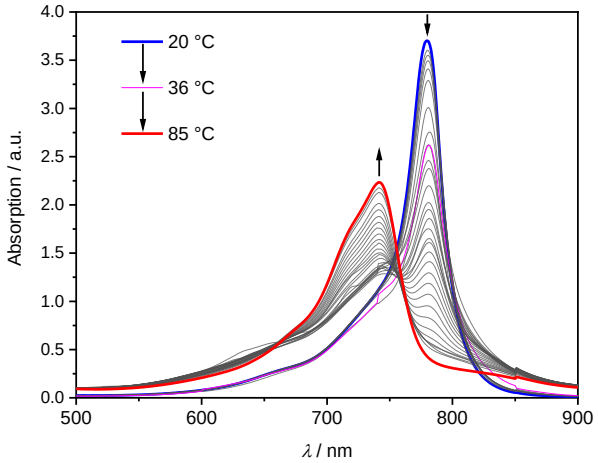

Figure S38. Temperature-dependent UV/Vis/NIR absorption spectra of **BisSQ2-AggII** in toluene/TCE 98:2 (c_0 = 2.5 × 10^{-5} M, 20 – 85 °C, ramp: 5 °C/min, stirring rate: 500 rpm). The curve in magenta indicates the temperature at which precipitation started to occur.

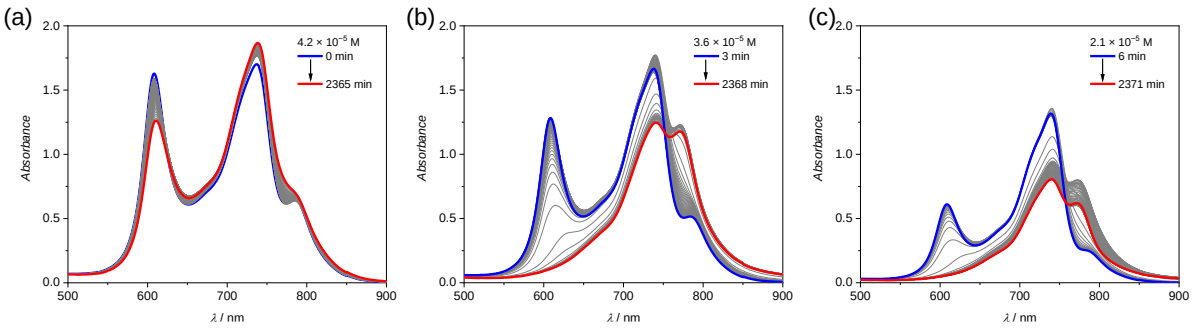

Figure S39. Time-dependent UV/Vis/NIR absorption spectra of **BisSQ2-AggI** (blue curves) in toluene/TCE 98:2, (a) c_0 = 4.2 × 10^{-5} M, (b) c_0 = 3.6 × 10^{-5} M, (c) c_0 = 2.1 × 10^{-5} M at 30 °C, stirring rate = 500 rpm.

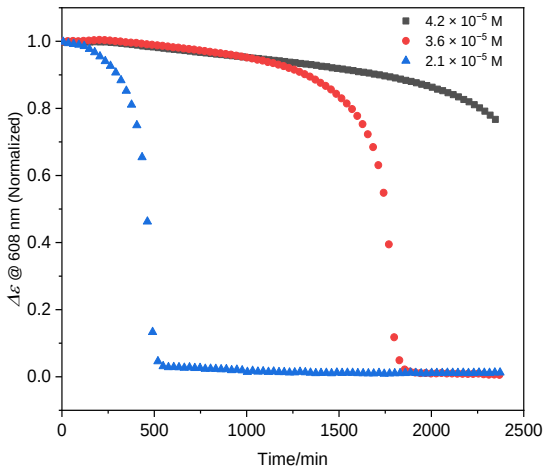

Figure S40. Normalized absorption profile at 608 nm as a function of time of the time-dependent UV/Vis/NIR measurements of **BisSQ2** in toluene/TCE 98:2 at 30 °C (c_0 = 4.2 × 10^{-5} M, 3.6 × 10^{-5} M, 2.1 × 10^{-5} M, stirring rate: 500 rpm).

9.2.8 Computational Chemistry

Geometry optimizations were performed for **SQ1** at the level of density functional theory (DFT) employing the long-range corrected CAM-B3LYP functional[207] in combination with the def2-SVP basis set.[208] For this purpose, the Gaussian 09 program package[203] was used and the dodecyl and oligoethylene glycol side chains were replaced by methyl groups. The existence of a real minimum was confirmed by frequency calculations revealing the absence of an imaginary frequency. The electrostatic potential surface (Figure S41) was visualized using the UCSF Chimera program.[209]

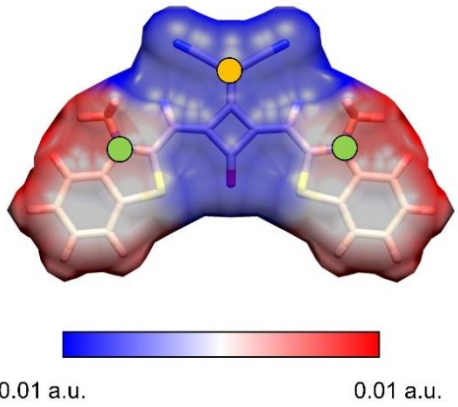

Figure S41. Electrostatic potential surface of the geometry-optimized structure of **SQ1** (CAM-B3LYP/def2-SVP, surface offset = 1.4 Å). The green and orange filled circles represent the position of the positive and negative point-integer charges used for the simulation of the absorption spectra within the Essential States Model.

9.2.9 Essential States Model

Monomer

The absorption properties of monomeric **SQ1** and **BisSQ2** aggregates were investigated based on the Essential States Model (ESM) pioneered by Painelli and coworkers.[115] In addition, we followed the approach of Spano and coworkers, who extended the model by including the effect of vibronic coupling and *inter*molecular charge transfer (ICT) states.[114c] Accordingly, the monomeric squaraine chromophore is described by three essential states, i.e., two zwitterionic states $|Z_1>$ and $|Z_2>$ as well as the neutral state $|N>$ (Figure 61a in *Chapter 4*). The electronic Hamiltonian is described by

$$\widehat{H}_{el}^{mon} = \eta_Z \sum_{i=1,2} |Z_i >< Z_i| + t_Z \sum_{i=1,2} (|N >< Z_i| + h.c.), \tag{S9}$$

where η_Z is the energy of the two zwitterionic states, which are coupled to the neutral state by the transfer integral t_Z describing the *intra*molecular electron transfer from the donor to the acceptor subunit. The energy of the neutral state is set to zero. Diagonalization of the Hamiltonian leads to three adiabatic states, i.e., the ground state $|g\rangle$ and two excited states $|e_1\rangle$ and $|e_2\rangle$. The latter is responsible for the absorption in the UV region, whereas transition from the ground to excited state $|e_1\rangle$ causes the absorption in the Vis/NIR region.[39]

In order to account for vibronic coupling, we employ a Holstein-type Hamiltonian, where each donor-acceptor arm is described by one harmonic oscillator with frequency ω_{vib}. The charges in the zwitterionic states will affect the geometry of the "left" ($|Z_1\rangle$) and "right" ($|Z_2\rangle$) side arm, which is considered by employing a shift of the respective potential along the vibrational coordinate by λ in the corresponding zwitterionic state (with λ^2 being the Huang-Rhys factor). Accordingly, the Hamiltonian has the form:

$$\hat{H}_{vibronic}^{mon} = \hbar\omega_{vib} \sum_{i=1,2} b_i^\dagger b_i + \hbar\omega_{vib}\lambda \sum_{i=1,2} (b_i^\dagger + b_i + \lambda)|Z_i\rangle\langle Z_i|. \quad \text{(S10)}$$

ħ is the reduced Planck constant and the operator $b_i^\dagger$ and b_i create and annihilate a vibrational excitation on side arm *i*, respectively. Thus, the first term in equation S10 reflects the vibrational part, whereas the second term describes the coupling of electronic and nuclear coordinates. The absorption spectrum of **SQ1** was simulated (Figure S42) using the parameters listed in Table S3, which are in agreement with simulations for a similar squaraine dye.[39] The absorption in the UV region arises from transition to higher excited states[39] and is significantly broader in the experimental spectrum due to the presence of several excited states, which are not considered by the three-state model.

The positive charge in the zwitterionic states was placed on the nitrogen atom of the corresponding donor moiety and the negative charge on the centric carbon atom of the dicyanomethylene group, respectively. This is in line with the electrostatic ground state potential surface (Figure S41) calculated by density functional theory. Furthermore, the maximum number of vibrational quanta was limited to six with all possible combinations among the two oscillators in order to reduce computational effort. This is a legitimate approximation, since the spectrum is already converged employing a cap of five for the total numbers of vibrational quanta (Figure S42).

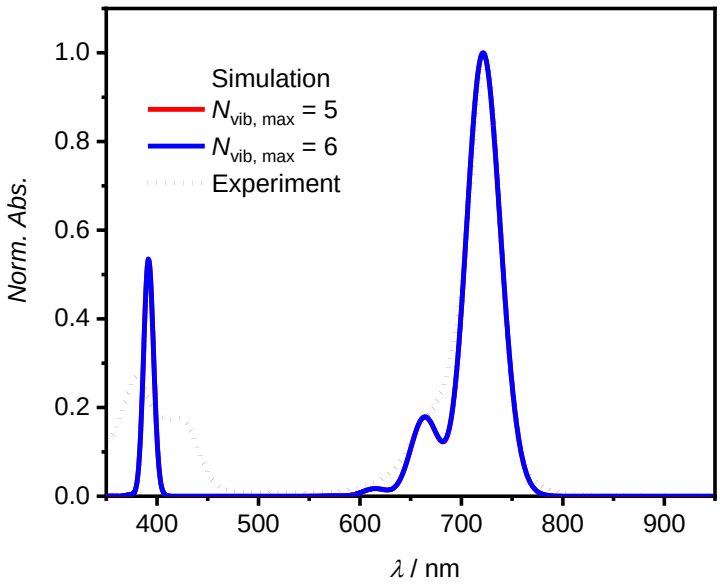

Figure S42. Experimental (black dotted line, toluene /TCE 98:2, c_0 = 1 x 10^{-5} M) and simulated absorption spectra of monomeric **SQ1** with a cap for the vibrational quanta per molecule of five (red solid line) and six (blue solid line). All further parameters used for the calculations are listed in Table S3.

The intensity ratio of the 0–1 and 0–0 absorption band can be estimated from the adiabatic Huang-Rhys factor λ^2_{adiab} by[114e]

$$\frac{I_{0-1}}{I_{0-0}} \approx \lambda^2_{adiab} = \frac{(1-\rho)^2}{2}\,\lambda^2. \tag{S11}$$

This results in a value of λ^2_{adiab} = 0.17, which is in good agreement with the intensity ratio of 0.18 determined from the absorption spectrum.

Coulombically Coupled Dimers

The Hamiltonian of the Coulombically coupled dimer can be written as

$$\hat{H}^{dimer}_{Coul} = \sum_{n=1,2} \hat{H}^{mon,n} + \hat{V}_{Coul}\,, \tag{S12}$$

where $\hat{H}^{mon,n}$ represents the total monomer Hamiltonian of chromophore *n*:

$$\hat{H}^{mon,n} = \hat{H}^{mon,n}_{el} + \hat{H}^{mon,n}_{vibronic}\,. \tag{S13}$$

The second term in equation S12 accounts for the Coulomb interaction of the point-integer charges between the two chromophores in the respective essential state:

$$\hat{V}_{Coul} = \frac{1}{4\pi\varepsilon\varepsilon_0}\sum_S \sum_{B=1,2,3} \frac{q_{1,B}(S)\cdot q_{2,B}(S)}{|\mathrm{r}_{1,B}-\mathrm{r}_{2,B}|} |\, S >< S|, \qquad \text{(S14)}$$

where S runs over all possible combinations of essential states ($|Z_1Z_1>$, $|Z_1Z_2>$ etc.). B indicates the "left" (B = 1) and "right" (B = 2) donor unit as well as the acceptor moiety (B = 3) of the chromophore with the corresponding point integer charges $q_{1,B}$(S) and $q_{2,B}$(S) of the two chromophores 1 and 2. In addition, $\mathrm{r}_{1,B}$ and $\mathrm{r}_{2,B}$ represent the position vector of the respective charges in chromophore 1 and 2. ε_0 is the vacuum permittivity and ε the screening factor, which is used to consider also solvent effects. Furthermore, the use of point integer charges instead of more delocalized charge densities leads to an overestimation of the coupling strength that is additionally taken into account by the screening factor. In doing so, a screening factor of ε = 2.9 was used to account for solvent effects and the overestimation of the Coulomb interaction due to the use of point-integer charges, in accordance with earlier work on squaraine[114c] and merocyanine dyes.[210]

Table S3. Parameters used for the simulation of the UV/Vis/NIR absorption spectra of monomeric squaraine **SQ1** within the Essential States Model as well as of the dimer of **BisSQ2-AggI** and **BisSQ2-AggII** with and without *inter*molecular charge transfer (ICT).

		BisSQ2-AggI		**BisSQ2-AggII**	
	SQ1	Coulomb coupl.	Coulomb. coupl. + ICT	Coulomb coupl.	Coulomb coupl. + ICT
t_Z (cm^{-1})	8950	8950	8950	8950	8950
η_Z (cm^{-1})	1850	1850	1850	1850	1850
λ^2	1.21	1.21	1.21	1.21	1.21
ω_{vib} (cm^{-1})	1200	1200	1200	1200	1200
σ (cm^{-1})	450	600	600	375	375
ε	–	2.9	2.9	2.9	2.9
t_{CT} (cm^{-1})	–	–	2550	–	1800
η_{CT} (cm^{-1})	–	–	8600	–	9500
λ^2_{CT}	–	–	0.74	–	0.74
$v_{\max}$	6	6	6	6	6

Dimer Including *Inter*molecular Charge Transfer (ICT) States

The close spatial proximity of the donor and acceptor unit between the two chromophores is indicative of *inter*molecular charge transfer (ICT). Hence, in order to consider the effect of ICT states, we have extended the dimer Hamiltonian following the approach by Hestand *et al.*[114c]

$$\hat{H}^{dimer}_{Coul+ICT} = \sum_{n=1,2} \hat{H}^{mon,n} + \hat{V}_{Coul} + \hat{H}^{ICT}. \tag{S15}$$

The Coulomb operator $\hat{V}_{Coul}$ now considers all possible combinations of essential states including ICT states (*vide infra*).

The Hamiltonian $\hat{H}^{ICT}$ can be divided into two parts:

$$\hat{H}^{ICT} = \hat{H}^{CS} + \hat{H}^{inter}, \tag{S16}$$

where $\hat{H}^{CS}$ represents the Hamiltonian for the charge separated states and consists of a pure electronic and a vibronic contribution:

$$\hat{H}^{CS} = \hat{H}^{CS}_{el} + \hat{H}^{CS}_{vibronic}\,. \tag{S17}$$

The electronic part is defined as

$$\hat{H}^{CS}_{el} = \eta_{CT} \sum_{n=1,2} |A_n >< A_n| + \eta_Z \sum_{n=1,2} |Z_{3,n} >< Z_{3,n}|$$

$$+ t_Z \sum_{n=1,2} \sum_{a=1,2} (|\, Z_{3,n} >< C_{a,n}| + h.c.), \tag{S18}$$

where η_{CT} is the energy of a charge separated state that is characterized by one chromophore in the anionic state and the other one in the cationic state, respectively. By doing so, we extend the diabatic basis by four additional essential states |C_1>, |C_2>, |A> and |Z_3> as shown in Figure S43a. The first term in equation S18 counts the number of charge separated states considering that only states are allowed, which exhibit a net charge of zero (e.g. |C_1A>, |C_2A> etc.). Note that |C_2A> indicates that chromophore 1 is in the cationic state |C_2> with a positive charge at the "right" donor unit, whereas chromophore 2 is in the anionic state |A> as depicted in Figure S43b. A pair of the cationic (|C_1> or |C_2>) and anionic state |A> results from *inter*molecular charge transfer between two chromophores in the neutral state and are coupled by t_{CT}. In

addition, we also consider a zwitterionic state |Z_3> (Figure S43a), which is formed upon *inter*molecular charge transfer between two chromophores in state |Z_1N> (Figure 61b) leading to state |Z_3A>. In addition, a charge separated state of the form |Z_3A> occurs upon *intra*molecular charge transfer from the donor to the acceptor moiety of a chromophore in a cationic state of the pair |C_1A> or |C_2A>. The energy of the pair |Z_3A> is set to $\eta_{CT} + \eta_Z$ and is therefore increased by η_Z with respect to |C_1A> or |C_2A> to account for the additional energy needed for the *intra*molecular charge separation. This is fulfilled by the second term in equation S18 and the off-diagonal term (third term in equation S18) couples the respective states

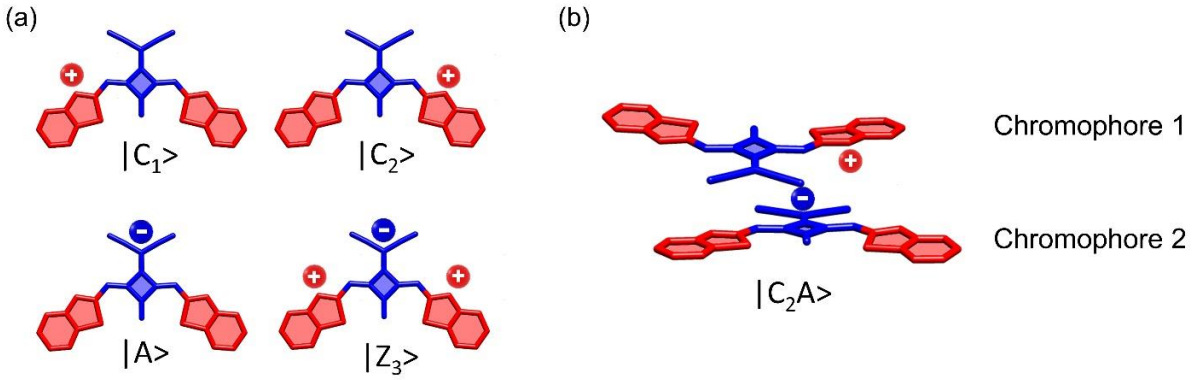

Figure S43. (a) Cationic (|C_1> and C_2>), anionic (|A>) and zwitterionic (|Z_3>) diabatic ICT states. (b) Squaraine dimer in the state |C_2A> with chromophore 1 in the cationic state |C_2> and chromophore 2 in the anionic state |A>, respectively. Note that the positive charge is located at the "right" donor unit of chromophore 1 and that chromophore 2 is slipped towards the "right".

The vibronic part of the Hamiltonian describing ICT states is written as

$$\hat{H}^{CS}_{vibronic} = \hbar\omega_{vib}\lambda_{CT}\sum_{n=1,2}\sum_{i=1,2}(b^{\dagger}_{i,n} + b_{i,n} + \lambda_{CT})(|A_n><A_n| + |C_{i,n}><C_{i,n}|) + \hbar\omega_{vib}\lambda\sum_{n=1,2}\sum_{i=1,2}(b^{\dagger}_{i,n} + b_{i,n} + \lambda)(|Z_{3,n}><Z_{3,n}|. \quad \text{(S19)}$$

This assumes that in the anionic state both side arms are affected by the negative charge at the central acceptor unit. Hence, the potential of both oscillators are shifted by λ_{CT} with respect to the neutral state. However, in a cationic state only the potential of the side arm is shifted by λ_{CT}, which contains the positive charge. In addition, the charges on the two side arms in the zwitterionic state |Z_3> should affect both potentials. Therefore, the potential of both arms are shifted by λ, which is set equal to the displacement in the zwitterionic states |Z_1> and |Z_2> (see equation S10) to reduce the amount of adjustable parameters.

The last term in equation S16 describes the *inter*molecular electron transfer by coupling the ICT states with the respective initial state as displayed in Figure S44. The reverse process is taken into account by the Hermitian conjugate:

$$\widehat{H}^{inter} = t_{CT}(|NN >< AC_1| + |NN >< C_2A| + |Z_2Z_1 >< AC_1| + |Z_1Z_1 >< C_1A| + |Z_2Z_1 >< C_2A| + |Z_2Z_2 >< AC_2| + |Z_1N >< Z_3A| + |NZ_2 >< AZ_3| + h.c.). \quad \text{(S20)}$$

For the simulations of the absorption spectrum (Figure 61c,d in *Chapter 4*), the parameters listed in Table S3 were used. Hence, the same values were employed for t_Z, η_Z, λ^2, and ω_{vib} as for the monomer. The parameters for ICT were adjusted to obtain best agreement with the experimental absorption spectrum resulting in values of t_{CT} = 2250 cm^{-1}, η_{CT}= 8700 cm^{-1} and λ^2_{CT} = 0.71 for **BisSQ2-AggI**, which is consistent with the simulations by Hestand *et al.*[114c] considering that a different squaraine chromophore is used in our studies. The cap for the total number of vibrational quanta was set to six with all possible distributions among the side arms of the two chromophores. This is a reasonable approximation, since the spectrum already shows convergence when a cap of five vibrational quanta is used (Figure S45).

Following the same approach, we have simulated the absorption spectrum of **BisSQ2-AggII** with and without ICT states (Figure 61d and Figure S48). Best agreement with the experimental spectrum was achieved when a lower *inter*molecular donor-acceptor interaction (t_{CT} = 1800 cm^{-1}) was assumed compared to **BisSQ2-AggI** (t_{CT} = 2550 cm^{-1}). This is in agreement with the larger *inter*molecular distance for **BisSQ2-AggII** (~6.0 Å) between the nitrogen atom of the donor moiety of one chromophore and the centric carbon atom of the dicyanomethylene group of the other chromophore in comparison to **BisSQ2-AggI** (~4.5 Å). Hence, the donor-acceptor interaction is weaker for **BisSQ2-AggII**. Furthermore, the larger distance also results in a larger energy of the charge-separated state of η_{CT} = 9500 cm^{-1} (for **BisSQ2-AggI**: η_{CT} = 8600 cm^{-1}).

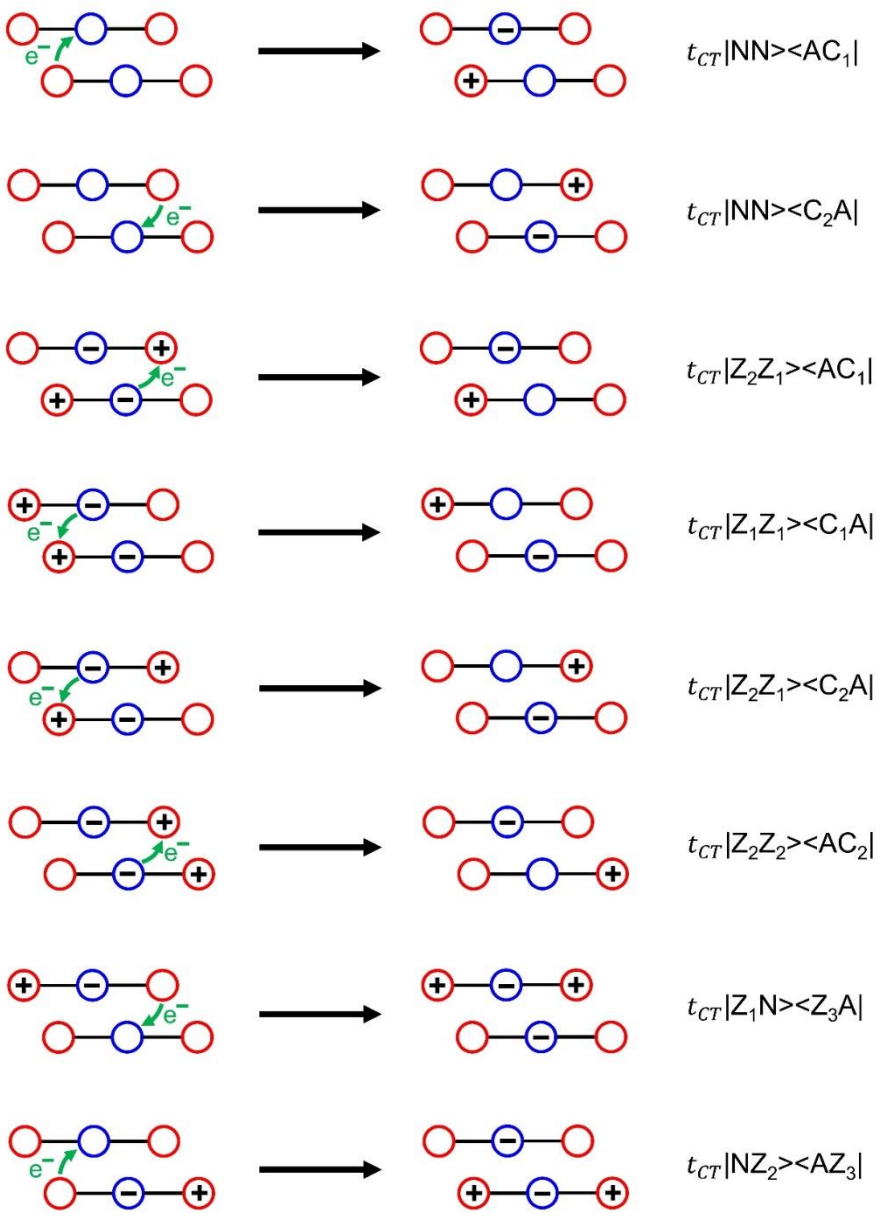

Figure S44. Schematic representation of the *inter*molecular electron transfer processes for a squaraine dimer leading to ICT states, which are coupled by the initial states through the transfer integral t_{CT}. The acceptor and donor moieties of the squaraine chromophores are displayed as blue and red circles, respectively. The corresponding off-diagonal elements of the electronic Hamiltonian are also given.

Simulation of Absorption Spectra

The absorption spectra were calculated by

$$A(E) = \sum_{e} |< \Psi_g |\hat{\mu}| \Psi_e > |^2 \cdot E_{eg} \cdot exp\left(- \frac{\left(E - E_{eg}\right)^2}{\sigma^2} \right), \qquad \text{(S21)}$$

where $A(E)$ is the absorption at the photon energy E. Ψ_g and Ψ_e represent the ground and excited state wave function, while E_{eg} is the transition energy from the ground to the respective excited state. The last term in equation S21 describes a Gaussian line broadening with full width σ at 1/e of the absorbance. The dipole moment operator $\hat{\mu}$ is defined as

$$\hat{\mu} = \sum_S \mu(S)|S><S|, \tag{S22}$$

where S runs over all possible combinations of essential states ($|NN>$, $|NZ_1>$, $|NZ_2>$, etc. in the case of a dimer) and $\mu(S)$ is the respective dipole moment in state S:

$$\mu(S) = \sum_n \sum_B r_{n,B} \cdot q_{n,B}(S), \tag{S23}$$

where B denotes the "right" (B = 1) and "left" (B = 2) side arm as well as the acceptor moiety (B = 3) of the squaraine chromophores. $q_{n,B}(S)$ stands for the point-integer charge of chromophore n residing at the respective donor or acceptor unit (defined by B) in state S. Furthermore, $r_{n,B}$ is the corresponding position vector of charge $q_{n,B}(S)$.

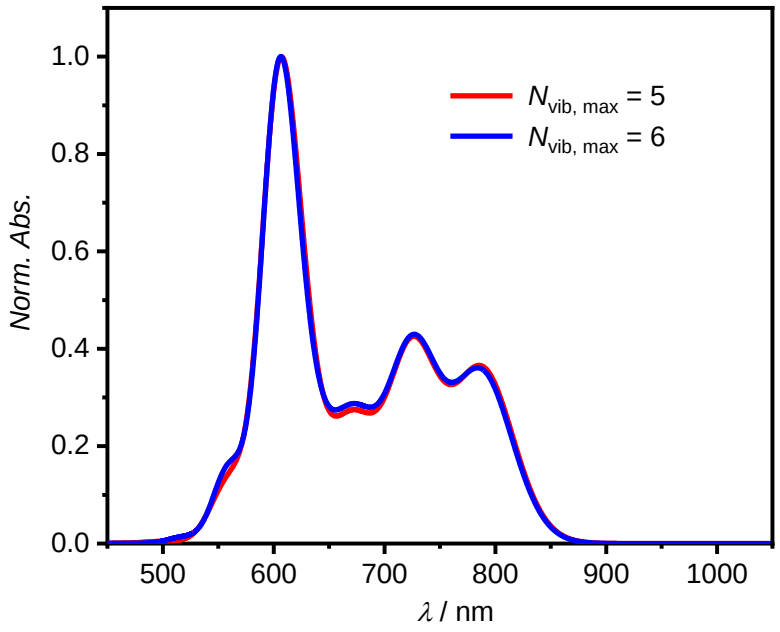

Figure S45. Simulated absorption spectrum of **BisSQ2-AggI** dimer including ICT states with a cap for the vibrational quanta per molecule of five (red solid line) and six (blue solid line). All further parameters used for the calculations are listed in Table S3. The spectra were shifted by 200 cm^{-1} towards higher energies.

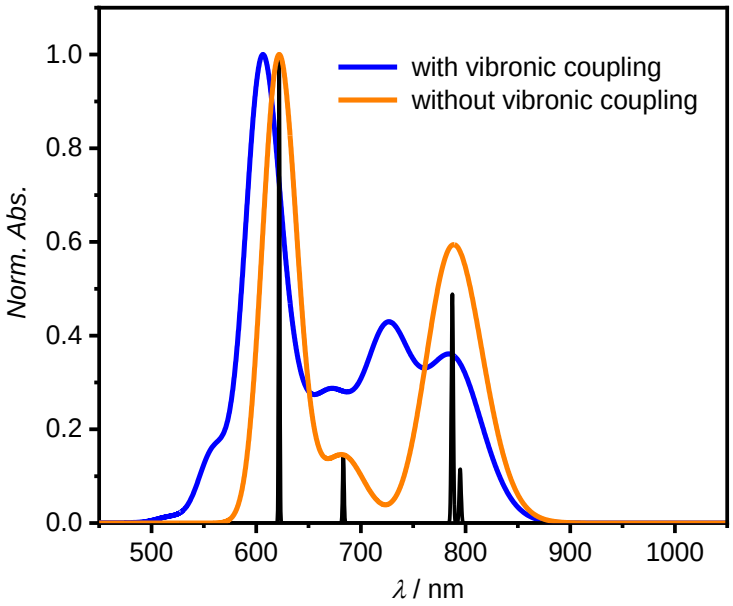

Figure S46. Simulated absorption spectrum of **BisSQ2-AggI** dimer including ICT states with (blue solid line) and without vibronic coupling (orange solid line). All other parameters used for the simulations are listed in Table S3. The spectrum without vibronic coupling is shown with a decreased full width (σ = 20 cm^{-1}, black solid line) to illustrate the allowed pure electronic transitions. The spectra were shifted by 200 cm^{-1} towards higher energies.

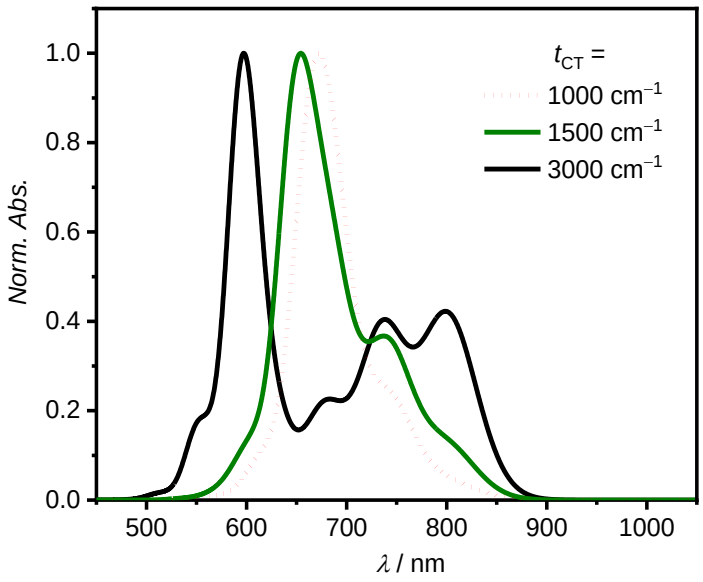

Figure S47. Simulated absorption spectrum of **BisSQ2-AggI** dimer including ICT states using the parameters shown in Table S3. The spectra were calculated for different values of the *inter*molecular charge transfer integral: t_{CT} = 1000 cm^{-1} (red dotted line), t_{CT} = 1500 cm^{-1} (green solid line) and t_{CT} = 3000 cm^{-1} (black solid line).

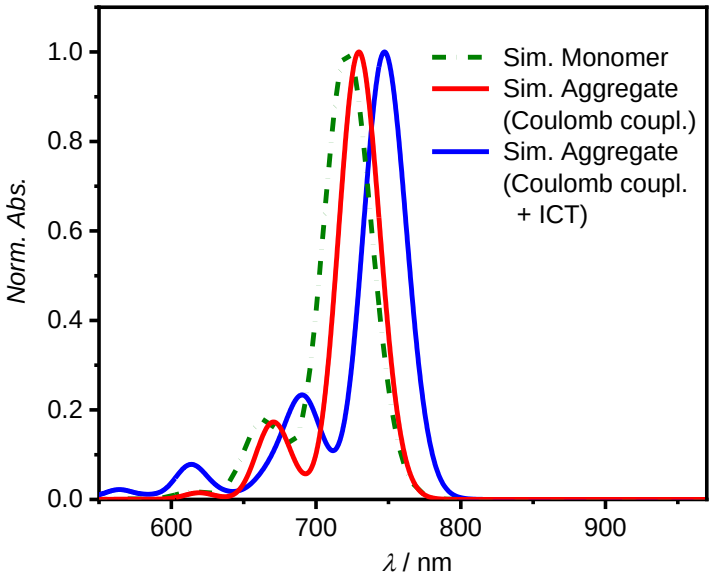

Figure S48. Simulated absorption spectrum of **BisSQ2-AggII** considering only Coulomb coupling (red solid line) as well as both ICT states and Coulomb coupling (blue solid line). In addition, the simulated absorption spectrum of reference **SQ1** is shown (green dash-dotted line).

9.2.10 NMR Spectra

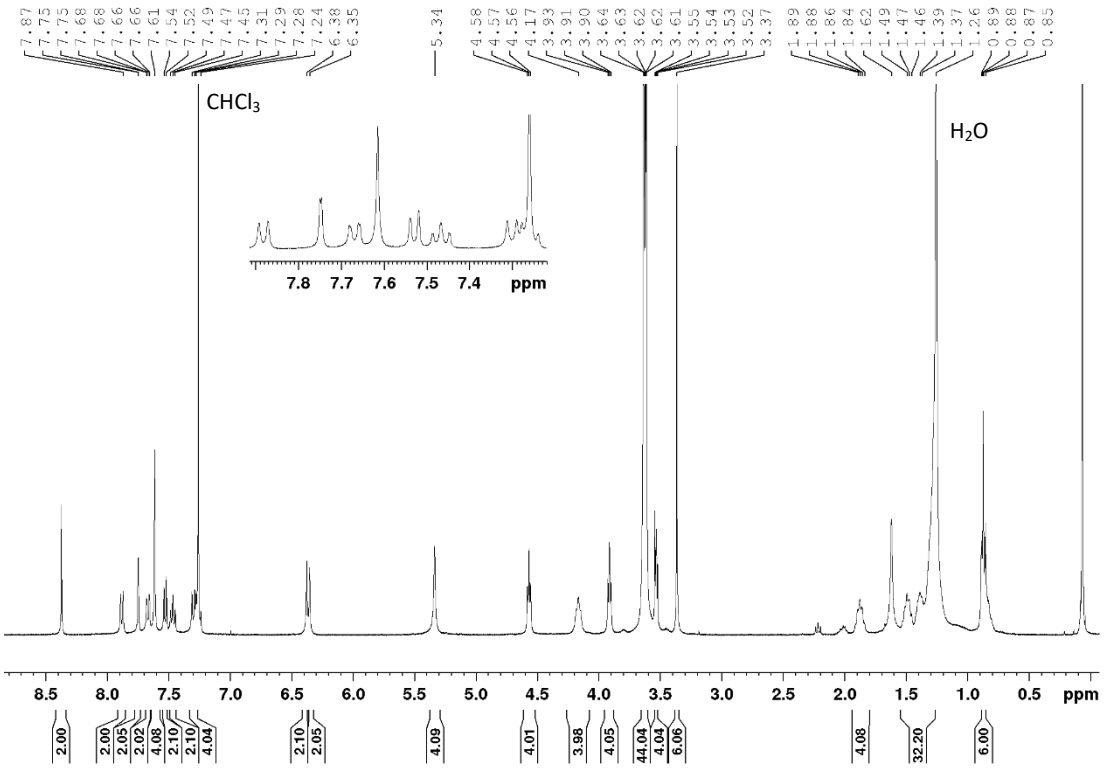

Figure S49. ^{1}H NMR (400 MHz, 295 K) spectrum of compound **BisSQ2** in $CDCl_3$.

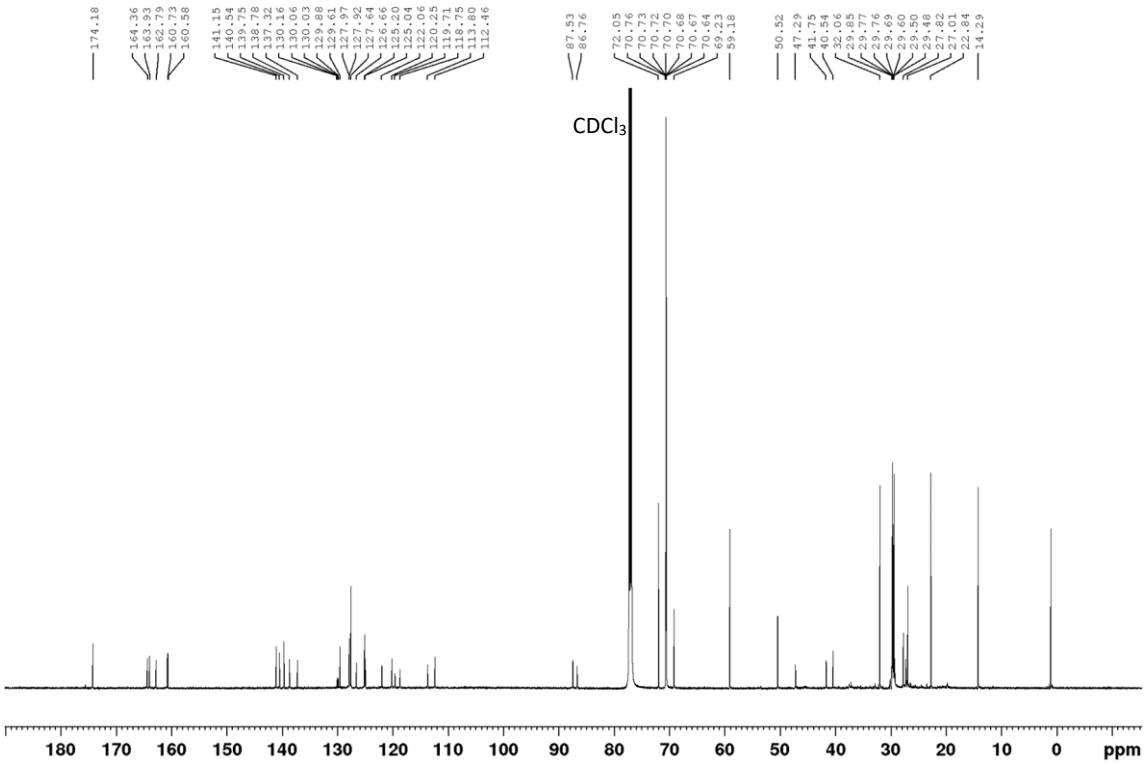

Figure S50. ^{13}C NMR (151 MHz, 295 K) spectrum of compound **BisSQ2** in $CDCl_3$.

9.3 Supporting information for *Chapter 5*: A Double J-Coupling Strategy for Near Infrared Emitters

9.3.1 Materials and Methods

General

All solvents and reagents were purchased from commercial sources and used as received without further purification. Column chromatography was performed using silica gel 60M (0.04 – 0.063 mm).

NMR spectroscopy

NMR spectra were recorded on a Bruker Avance 400 or Bruker Avance DMX 600 at 295 K (if not specified). The spectra were calibrated to the residual solvent peak and the chemical shifts δ are given in ppm. Multiplicities are denoted as follows: s = singlet, d = doublet, t = triplet, q = quartet, quint = quintet, dd = doublet of doublets, td = triplet of doublets, m = multiplet, br = broad.

Mass spectrometry

MALDI-TOF mass spectrometry was performed on a MALDI TOF MS ultrafleXtreme mass spectrometer (Bruker Daltonik GmbH). High-resolution mass spectra (ESI) were recorded on a microTOF focus instrument (Bruker Daltonik GmbH).

Optical spectroscopy

For all spectroscopic measurements in solution, spectroscopic grade solvents (Uvasol®) were used. The absorption spectra were recorded on JASCO V-670 or V-770 UV/Vis/NIR spectrophotometer. The spectral band width and the scan rate were 1 nm and 400 nm min^{-1}, respectively. Stock solutions in specified solvents were freshly prepared for all measurements and continuously diluted for absorption measurements by taking into account the solubility and the absorbance. The UV/Vis/NIR measurements were performed in quartz cell cuvettes (SUPRASIL, Hellma Analytics) with path lengths of 0.1, 1.0, 10.0 and 100.0 mm. For temperature-dependent measurements, absorption spectra have been corrected for the density change. Fluorescence spectra were recorded on a FLS980-D2D2-ST Edinburgh fluorescence spectrometer and were corrected against the photomultiplier sensitivity and the lamp intensity. Absolute fluorescence quantum yields were determined by a calibrated integrating sphere system (F-M01, accessory of FLS980-D2D2-ST spectrometer).

Atomic force microscopy (AFM)

AFM measurements were performed under ambient conditions using a Bruker Multimode 8 SPM system operating in tapping mode in air. Silica cantilevers (OMCL-AC240TS, Olympus) with a resonance frequency of ~70 kHz and a spring constant of ~1.7 Nm^{-1} were used. The samples for AFM were prepared as stated in the figure captions.

9.3.2 Synthesis and Characterizations

Synthesis of compound **3**

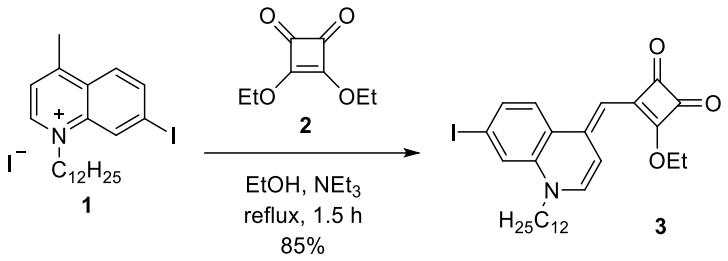

Compound **1** (1.70 g, 3.01 mmol) was dissolved in ethanol (20 mL) and trimethylamine (0.55 mL). Squaric acid diethyl ester **2** (600 mg, 3.53 mmol) was then added dropwise. The mixture was heated to reflux for 1.5 hours. Afterwards, the reaction was allowed to cool down to room temperature and the solvent was removed under reduced pressure. The crude product was purified by gravity column (eluent: CH_2Cl_2 : MeOH = 99 : 1) and a magenta fraction was isolated and dried as a magenta solid (1.43 g, 2.55 mmol, 85%).

^{1}H NMR (400 MHz, $CDCl_3$): δ = 7.88 (d, J = 7.6 Hz, 1H), 7.75 (d, J = 9.0 Hz, 1H), 7. 61 (d, J = 1.5 Hz, 1H), 7.56 (dd, J = 10.3, 7.1 Hz, 1H), 6.99 (d, J = 7.7 Hz, 1H), 5.99 (s, 1H), 4.85 (q, J = 7.1 Hz, 2H), 3.91 (t, J = 7.2 Hz, 2H), 1.78 (quint, J = 7.1 Hz, 2H), 1.51 (t, J = 7.1 Hz, 3H), 1.39 – 1.22 (m, 18H), 0.87 (t, J = 6.8 Hz, 3H) ppm.

^{13}C NMR (101 MHz, $CDCl_3$): δ = 193.6, 187.6, 186.5, 174.6, 145.9, 139.4, 137.2, 133.1, 127.1, 124.4, 123.2, 111.1, 97.9, 92.1, 70.0, 53.3, 32.0, 29.7 (two signals), 29.6, 29.5, 29.3, 28.6, 26.9, 22.8, 16.1, 14.3 ppm.

HRMS (ESI, pos. mode, $CHCl_3$/MeCN): m/z: 561.17349 $[M]^+$ (calcd. for $C_{28}H_{36}INO_3^+$: 561.17344).

Elemental analysis (%) calculated for $C_{28}H_{36}INO_3$: C, 59.89; H, 6.46; N, 2.49. Found: C, 59.90; H, 6.57; N, 2.56.

M.p.: 132 – 133 °C.

Synthesis of compound **4**

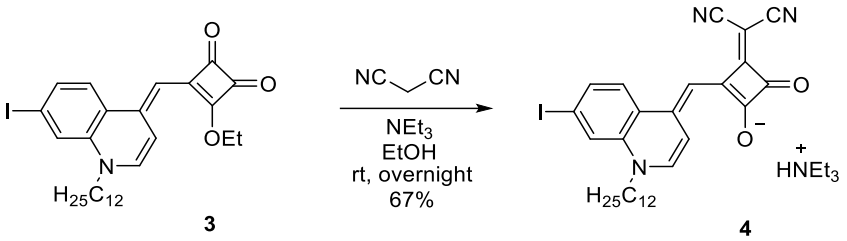

Compound **3** (1.40 g, 2.49 mmol) was dissolved in ethanol (75 mL) and malononitrile (337 mg, 5.10 mmol) was added while stirring. Triethylamine (650 µL, 4.66 mmol) was added dropwise and the mixture stirred at room temperature overnight. Solvent was removed under reduced pressure and the mixture was washed with diethyl ether to yield dark purple waxy solid. Compound **4** was used for the next step without further purification.

^{1}H NMR (400 MHz, DMSO-d_6): δ = 7.70 (d, J = 1.5 Hz, 1H), 7.66 (d, J = 7.8 Hz, 1H), 7.55 (dd, J = 8.6 Hz, 1.2 Hz, 1H), 7.44 (d, J = 9.0 Hz, 1H), 7.16 (d, 1H, J = 7.9 Hz), 6.35 (s, 1H), 3.94 (t, J = 7.0 Hz, 2H), 3.08 (m, 6H), 1.62 (m, 2H), 1.26 – 1.20 (m, 18H), 1.16 (t, J = 7.3 Hz, 9H), 0.84 (t, J = 6.8 Hz, 3H) ppm.
MS (MALDI, neg. mode, Matrix: DCTB 1:3 in Chloroform): m/z: 580.174 $[M-HNEt_3]^-$ (calcd. for $C_{29}H_{31}IN_3O_2^-$: 580.147).

Synthesis of compound **5**

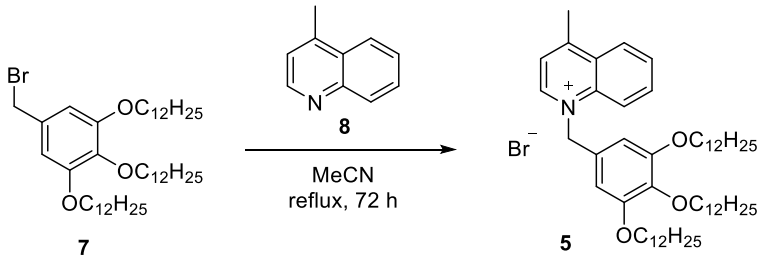

4-methylquinoline (**8**) (250 mg, 1.75 mmol) and compound **7** (3.80 g, 5.25 mmol) were dissolved in acetonitrile (100 mL) under nitrogen atmosphere and stirred for 72 h under reflux. After the reaction mixture was cooled down to room temperature, the solvent was removed under reduced pressure. The resulting residue was washed with diethyl ether to yield a white solid (1.50 g, 1.73 mmol, 66%).

^{1}H NMR (400 MHz, $CDCl_3$): 10.45 (d, J = 6.0 Hz, 1H), 8.59 (d, J = 8.9 Hz, 1H), 8.28 (dd, J = 8.5, 1.2 Hz, 1H), 8.08 (td, J = 8.0, 1.5 Hz, 1H), 7.95 (d, J = 6.0 Hz, 1H), 7.89 (t, J = 7.7 Hz,

1H), 6.65 (s, 2H), 6.52 (s, 2H), 3.86 (m, 6H), 3.00 (s, 3H), 1.73 – 1.63 (m, 6H), 1.44 – 1.37 (m, 6H), 1.34 – 1.21 (m, 48 H), 0.89 – 0.85 (m, 9H) ppm.

^{13}C NMR (101 MHz, $CDCl_3$): δ = 158.2, 153.8, 149.8, 138.8, 137.7, 135.3, 129.8, 129.6, 128.0, 126.5, 123.3, 120.3, 106.8, 73.5, 69.7, 60.9, 32.1, 30.4, 29.9 (two signals), 29.8 (three signals), 29.7, 29.6, 29.5, 26.3, 26.2, 22.8, 20.6, 14.3 ppm.

HRMS (ESI, pos. mode, $CHCl_3$/MeCN): *m*/*z*: 786.67665 $[M]^+$ (calcd. for $C_{53}H_{88}NO_3^+$: 786.67587).

M.p.: 127 – 128 °C.

Synthesis of compound **6**

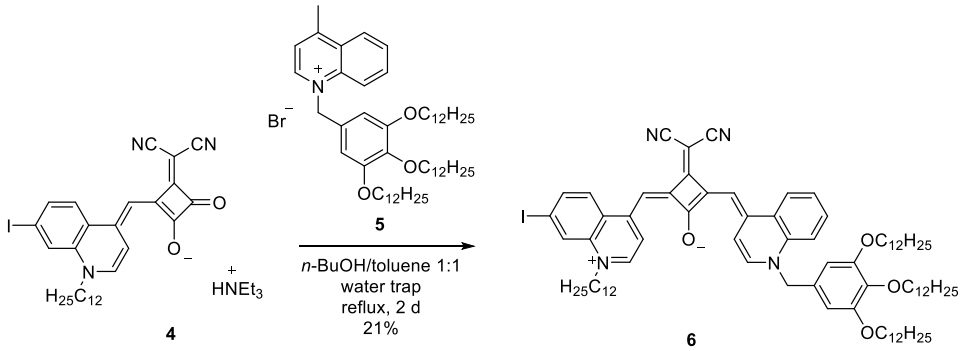

Semi-squaraine **4** (787 mg, 1.15 mmol) and compound **5** (2.00 g, 2.31 mmol) were mixed in *n*-butanol (25 mL) and toluene (25 mL) and heated to reflux with a water-removing Dean-Stark apparatus for 2 days. Then the reaction mixture was cooled to room temperature and the solvent was removed under reduced pressure. The crude product was purified by column chromatography (silica gel, eluent: 100% CH_2Cl_2 → CH_2Cl_2/MeOH 99:1) to obtain a brown solid. The solid was collected and further purified with size exclusion chromatography (eluent: CH_2Cl_2/MeOH 90:10) and the orange fraction was dried to give a dark green powder (337 mg, 250 μmol, 21%).

^{1}H NMR (400 MHz, THF-d_8, 330 K): δ = 8.88 (d, *J* = 7.3 Hz, 1H), 8.66 (d, *J* = 7.5 Hz, 1H), 8.19 (d, *J* = 8.3, 1H), 7.87 (d, *J* = 1.3 Hz, 1H), 7.81 (d, *J* = 9.0 Hz, 1H), 7.73 (d, *J* = 4.6 Hz, 1H), 7.71 (dd, *J* = 8.6, 1.5 Hz, 1H), 7.61 – 7.54 (m, 2H), 7.45 – 7.41 (m, 2H), 7.12 (s, 1H), 6.98 (s, 1H), 6.50 (s, 2H), 5.37 (s, 2H), 4.14 (t, *J* = 7.2 Hz, 2H), 3.90 (t, *J* = 6.3 Hz, 2H), 3.89 (t, *J* = 6.3 Hz, 4H), 1.86 – 1.78 (m, 6H), 1.53 – 1.30 (m, 74H), 0.90 – 0.86 (m, 12 H) ppm.

^{13}C NMR (151 MHz, THF-d_8, 330 K): δ = 176.8, 166.7, 164.5, 163.2, 154.7, 148.1, 146.1, 140.3, 140.1, 139.9, 138.8, 135.0, 132.4, 130.9, 127.3, 126.8, 126.4, 126.2, 126.1, 125.5, 118.8, 117.6, 115.7, 115.3, 106.6, 101.3, 100.7, 98.4, 73.6, 70.0, 57.7, 53.9, 41.9, 32.6 (two signals),

32.3, 31.2, 30.5 (two signals), 30.4 (three signals), 30.3 (three signals), 30.2, 30.1, 30.0, 29.9, 29.4, 27.4, 26.9 (two signals), 23.3, 23.2, 14.1 ppm.

HRMS (ESI, pos. mode, $CHCl_3$/MeCN): *m*/*z*: 1348.81159 $[M]^+$ (calcd. for $C_{82}H_{117}IN_4O_4^+$: 1348.81140).

Elemental analysis (%) calculated for $C_{82}H_{117}IN_4O_4$: C, 72.97; H, 8.74; N, 4.15. Found: C, 73.08; H, 8.79; N, 4.04.

M.p.: 193 – 195 °C.

Synthesis of **BisSQ3**

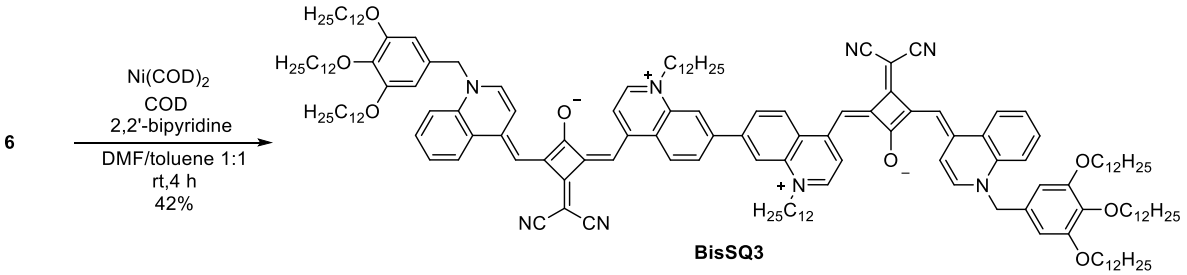

Squaraine **6** (90.0 mg, 66.7 µmol), 2,2'-bipyridine (25.0 mg, 160 µmol), 1,5-cyclooctadiene (19.6 µL, 160 µmol) and bis-(1,5-cyclooctadiene)nickel(0) (44.0 mg, 160 µmol) were mixed in a Schlenk tube under N_2 atmosphere. Anhydrous DMF (5 mL) and anhydrous toluene (5 mL) was added through a syringe into the reaction mixture and it was stirred at room temperature for 4 hours under N_2 flow. Afterwards, the solvent was removed under reduced pressure and then diluted with $CHCl_3$ (30 mL). The solution was washed with water (30 mL × 3). The combined organic phase was dried over K_2CO_3 and the solvent was removed under reduced pressure. The crude mixture was first flushed through a gravity column, where the silica gel is basified with triethylamine (NEt_3) with the eluent of $CHCl_3$/NEt_3 99:1. The main fraction eluted from the column was further concentrated and washed consecutively with acetone and *n*-hexane using a Soxhlet extractor. Each washing ran overnight. Finally, the black solid compound was dried with high vacuum (34.6 mg, 14.1 mmol, 42%). Due to aggregation of **BisSQ3** in solution, NMR measurements had to be performed at high temperature (T = 402 K) with low concentration. Therefore a ^{13}C NMR measurement was not possible. For ^1H-^1H COSY, TOCSY and ROESY spectra for the proton assignments, see Figures S69 – S72.

^1H NMR (600 MHz, *o*-dichlorobenzene-d_4, 402 K): δ = 8.80 (s, 2H), 8.72 (s, 2H), 8.15 – 8.11 (m, 4H), 7.64 (s, 2H), 7.45 (d, *J* = 8.0 Hz, 2H), 7.33 – 7.28 (m, 6H), 7.14 – 7.09 (m, 8H), 6.49 (s, 4H), 5.12 (s, 4H), 4.13 (br, 4H), 4.07 (t, *J* = 6.5 Hz, 4H), 3.94 (t, *J* = 6.4 Hz, 8H), 1.90 (quint,

J = 7.3 Hz, 4H), 1.82 (quint, *J* = 7.3 Hz, 4H), 1.73 (quint, *J* = 7.3 Hz, 8H), 1.54 (quint, *J* = 7.4 Hz, 4H), 1.47 – 1.37 (m, 12H), 1.34 – 1.27 (m, 128H), 0.86 (t, *J* = 6.8 Hz, 24H) ppm.
HRMS (ESI, pos. mode, $CHCl_3$/MeCN): *m*/*z*: 1221.91272 $[M]^{2+}$ (calcd. for $C_{164}H_{234}N_8O_8^{2+}$: 1221.90693).
M.p.: > 285 °C (decomp.)

9.3.3 Molecular Optical Properties

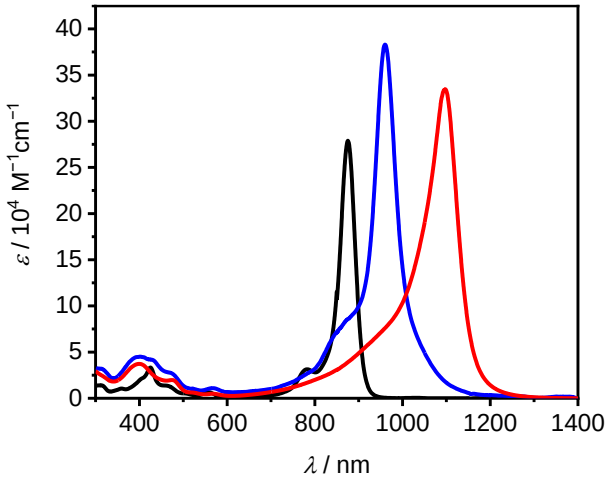

Figure S51. UV/Vis/NIR absorption spectra of **SQ** (black, $c_0 = 2.5 \times 10^{-6}$ M), **BisSQ3** (blue, $c_0 = 1.0 \times 10^{-6}$ M) in $CHCl_3$ and **BisSQ3** aggregate in toluene (red, $c_0 = 5.5 \times 10^{-5}$ M) at 293 K.

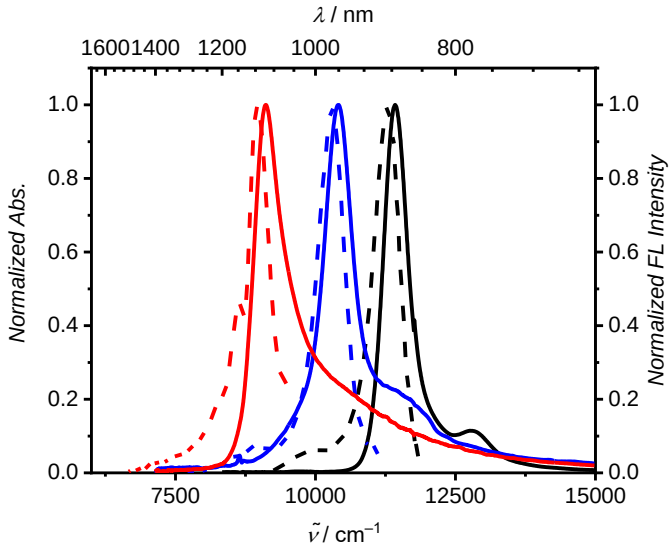

Figure S52. Normalized UV/Vis/NIR absorption (solid lines) and fluorescence (dashed lines) spectra (plotted with wavenumber linearly) of **SQ** in $CHCl_3$ (black, λ_{ex} = 815 nm), **BisSQ3** in $CHCl_3$ (blue, λ_{ex} = 870 nm), and aggregates of **BisSQ3** in toluene (red, λ_{ex} = 985 nm) at 293 K.

Transition Dipole Moment (μ_{eg}) Calculation

Transition dipole moments were calculated from the integral of the designated absorption bands (Figure S51) according to[162,211]

$$\mu_{eg}^2 = \frac{3\varepsilon_0 hc \ln 10}{20\pi^2 N_A} \cdot \frac{9n}{(n^2+2)^2} \cdot \int \frac{\varepsilon}{\tilde{\nu}} \, d\tilde{\nu}. \quad \text{(S24)}$$

(μ_{eg}: transition dipole moment; ε_0: permittivity of vacuum; h: Planck constant; c = speed of light; N_A: Avogadro constant; n: index of refraction of the solvent; ε: extinction coefficient in $M^{-1}cm^{-1}$; $\tilde{\nu}$: wavenumber in cm^{-1}).

Quantum Yield Determination

We applied the absolute method for the quantum yield determination[212] of **SQ** and **BisSQ3** with an integrating sphere setup. The absolute fluorescence quantum yield, Φ_{FL}, is, by definition, the ratio of the number of photons emitted (N^{em}) to the number of photons absorbed (N^{abs}):

$$\Phi_{FL} = \frac{N^{em}}{N^{abs}} \quad \text{(S25)}$$

The excitation profiles and the emission profiles of both the blank (pure solvent) and the sample solution was recorded (Figure S53). Notably, when recording the excitation profile, a neutral density filter (optical density: 2.0, NE220B from Thorlabs, Inc.) had to be employed to avoid saturating the NIR detector with the high intensity incident light. The transmittance of the filter is then used to scale the excitation profiles for the calculation of the quantum yield.

The absolute fluorescence quantum yield is then calculated as follows:

$$\Phi_{FL} = \frac{E_B - E_A}{S_A - S_B}, \quad \text{(S26)}$$

where E_A, E_B, S_A, and S_B refer to the integral of the scans (denoted in Figure S53). By applying equation (S26), the quantum yield of **SQ** in $CHCl_3$ is determined to be 1.30% ± 0.22% and for **BisSQ3** to be 0.33% ± 0.01% (with reabsorption correction, see below) as an average result of three independent samples.

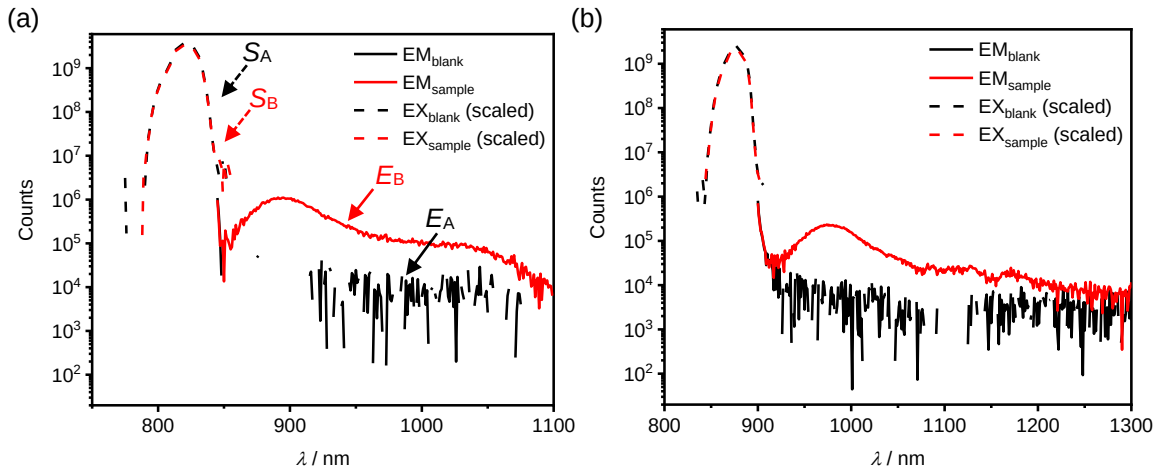

Figure S53. Excitation (dashed lines) and emission (solid lines) of the solvent (black lines) and sample in $CHCl_3$ (red lines). Sample (a) **SQ** (λ_{ex} = 815 nm); (b) **BisSQ3** (λ_{ex} = 870 nm). S_A, S_B, E_B, and E_A refer to the area under the specified curves.

During the fluorescence quantum yield investigations of **SQ** and **BisSQ3** utilizing an integrating sphere, reabsorption could not be avoided due to the low Φ_{FL}, a required optical density > 0.05 of the sample as well as low sensitivity of the NIR detector. Reabsorption can be identified by a broadening, deshaping and decrease of the fluorescence spectra and a bathochromic shift of the respective fluorescence maxima. The reabsorption contaminated spectra were adjusted at the red edge to the reabsorption-free fluorescence spectra (Figure S54) and the corrected absolute quantum yields were determined using the approach of Ahn *et al.*[163]

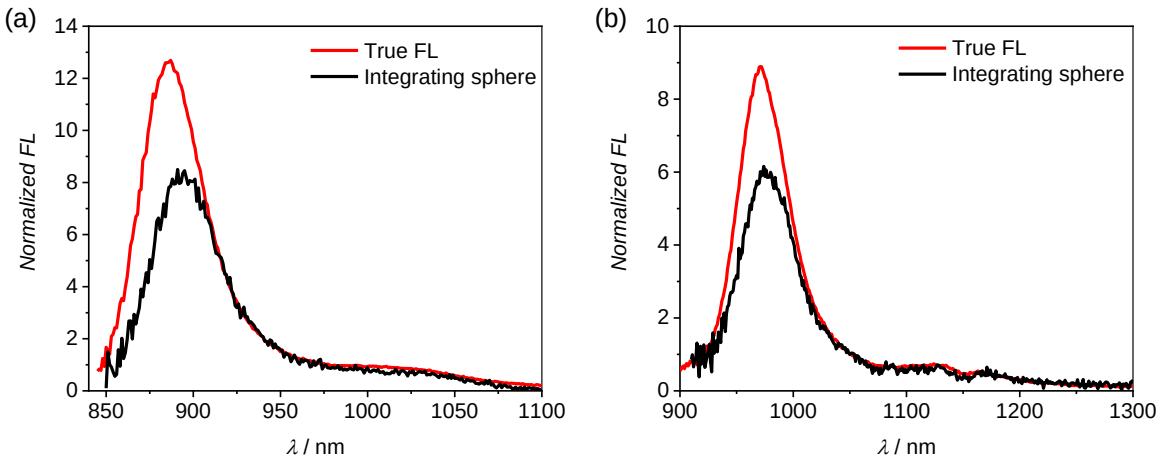

Figure S54. Fluorescence spectrum of (a) **SQ** (λ_{ex} = 815 nm) and (b) **BisSQ3** (λ_{ex} = 870 nm) in $CHCl_3$ solution measured with the integrating sphere (black line) adjusted to the red edge of the reabsorption-free spectrum (red line).

9.3.4 Aggregation of BisSQ3 in Toluene

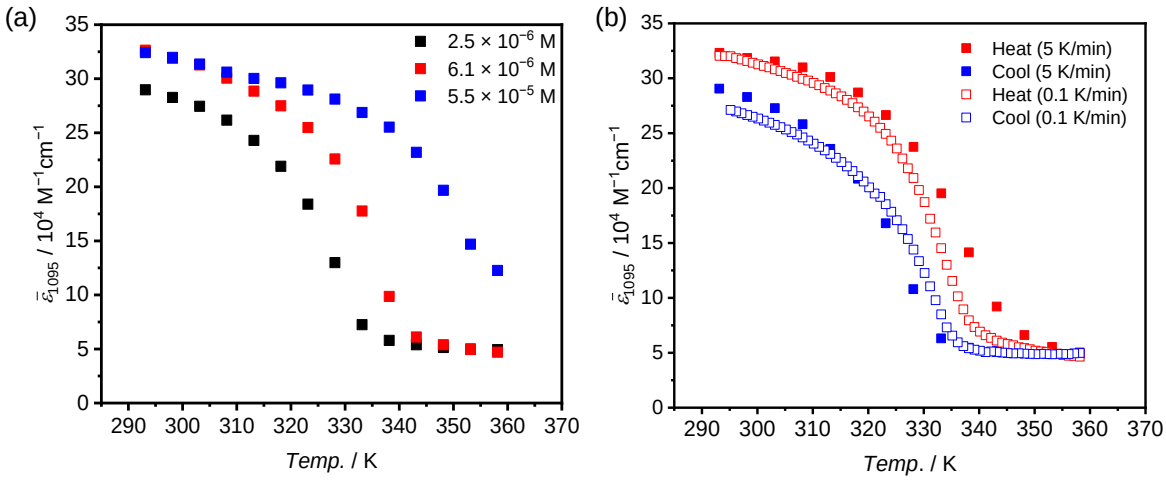

Figure S55. (a) Plot of apparent molar extinction coefficients at 1095 nm against temperature upon cooling of a solution of **BisSQ3** in toluene (black: c_0 = 2.5 × 10^{-6} M, red: c_0 = 6.1 × 10^{-6} M, blue: c_0 = 5.5 × 10^{-5} M). (b) Plot of apparent molar extinction coefficients at 1095 nm against temperature of a solution of **BisSQ3** in toluene with different temperature ramps. (c_0 = 2.5 × 10^{-6} M; solid dots: ramp = 5 K/min; hollow dots: ramp = 0.1 K/min).

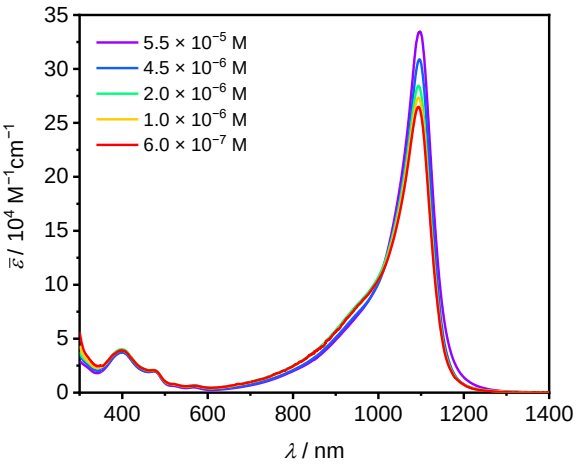

Figure S56. Concentration-dependent UV/Vis/NIR spectra of **BisSQ3** in toluene at 293 K (c_0 = 5.5 × 10^{-5} – 6.0 × 10^{-7} M).

9.3.5 AFM Images of BisSQ3 Aggregates

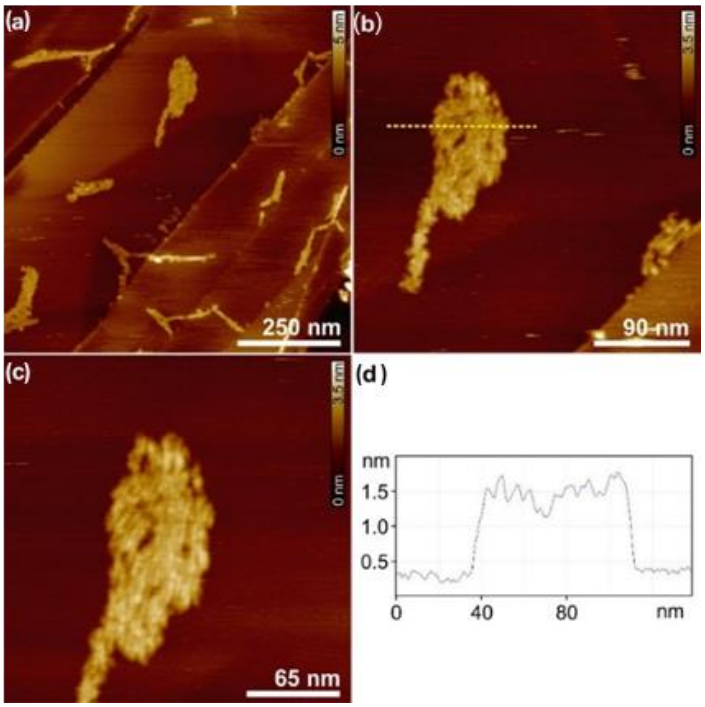

Figure S57. AFM height images of sample **BisSQ3** aggregates deposited by spin-coating of a toluene solution (c_0 = 1.5 × 10^{-5} M) onto HOPG with 5000 rpm. *Z* scale is 5 nm (a) and 3.5 nm (b,c). The image (d) shows the cross-section analysis from the yellow dashed line in image (b).

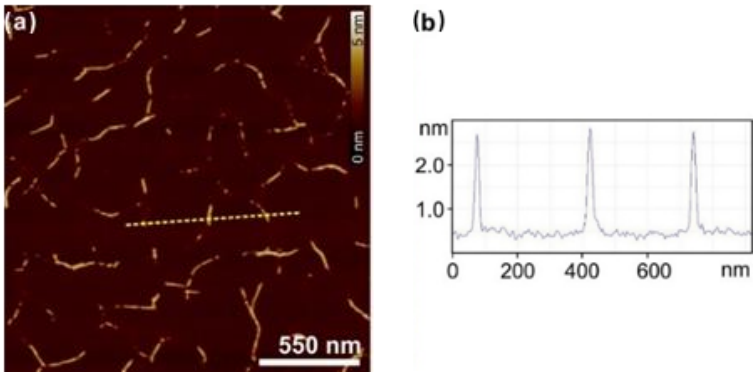

Figure S58. AFM height image of **BisSQ3** aggregates deposited by placing a drop of a toluene solution (c = 1.5 × 10^{-5} M) onto mica for 10 s with subsequent removal of the remaining solution. *Z* scale is 5 nm. The image (b) shows the cross-section analysis from the yellow dashed line in image (a).

9.3.6 Packing Model of BisSQ3 Nanofibers

9.3.6.1 Geometry Optimization Scan of BisSQ3

Geometry optimization scan of **BisSQ3** molecule was performed by varying the dihedral angle α with semi-empirical PM6[171] in Gaussain 09.D01 (Figure S59).[213] For simplicity, the dodecyl side chains were replaced by methyl groups. The bottom of Figure S59 shows the molecular structures with the lowest potential energy with a dihedral angle (α) of −126.8° (53.2°) and 133.1° (−46.9°).

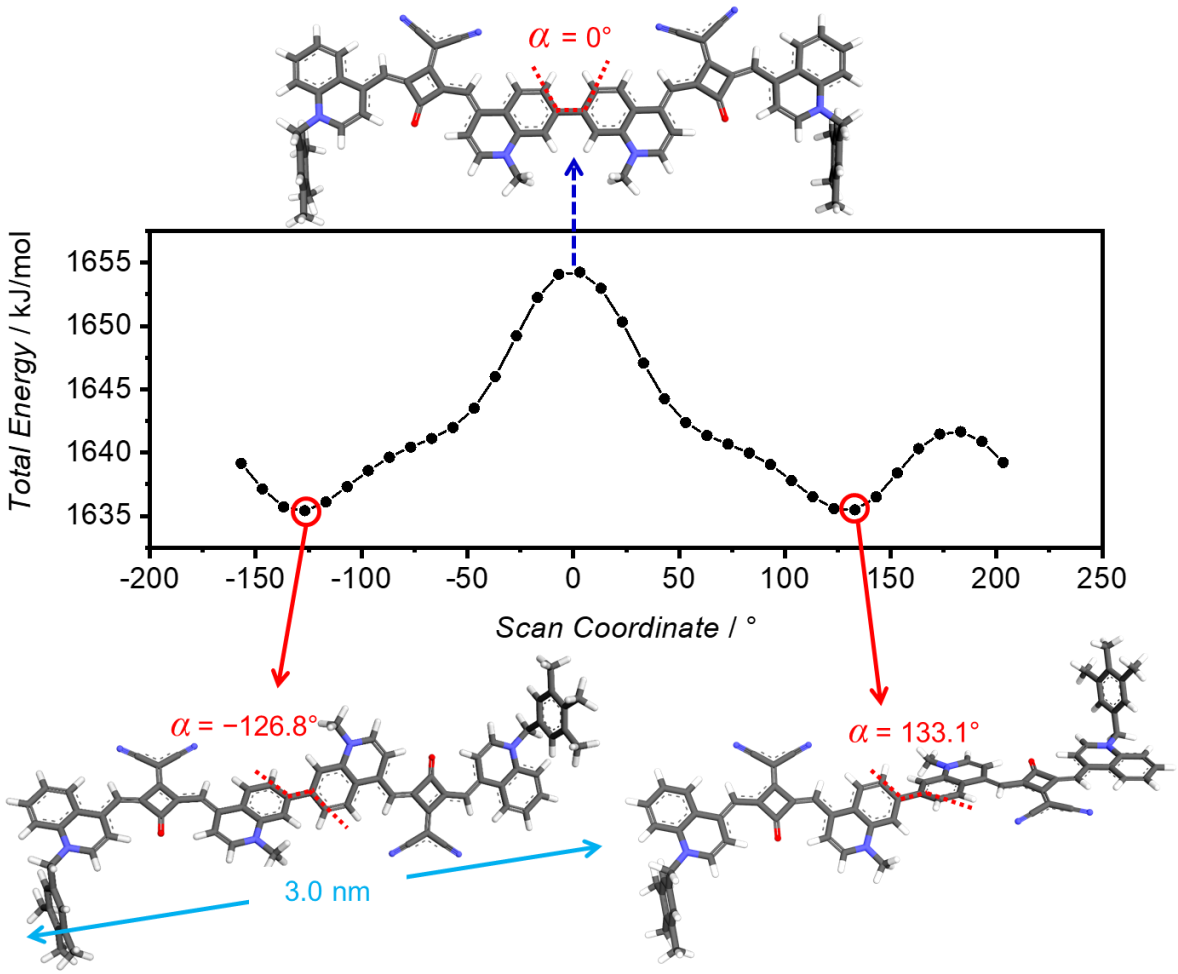

Figure S59. Top: Starting geometry of **BisSQ3**, where the dihedral angle (α) is defined to be 0°; middle: Geometry optimization scan of **BisSQ3** with different α by semi-empirical PM6 calculations.[171] Each point corresponds to the energy (y-axis) of a geometry-optimized structure with fixed dihedral angle (x-axis); bottom: Geometry-optimized structures of **BisSQ3** with the lowest energy obtained with semi-empirical PM6 method.[171]

9.3.6.2 Proposed Packing Model of BisSQ3 Nanofibers

Based on the packing motif of two **BisSQ3** molecules shown in Figure 66a (*Chapter 5*), the distance *r* between the centers of the two *inter*molecularly interacting squaraine units is

estimated to be 0.84 nm and considering ideal π-π stacking, the π-π distance is assumed to be 0.34 nm. Consequently, the slip angle (θ) between the centers of the neighboring chromophores in the arrangement can be calculated to be ~ 23°.

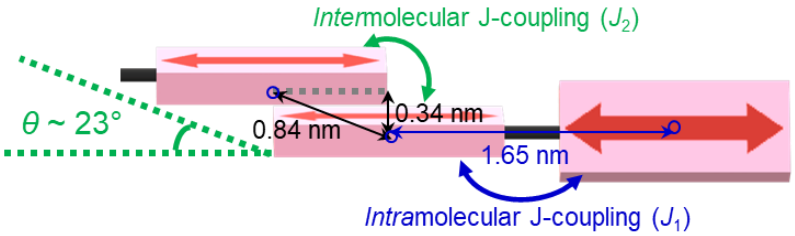

Figure S60. Schematic representation of the interacting chromophores within the **BisSQ3** aggregates.

On the other hand, the distance r between the centers of the two squaraine units within the molecule is estimated to be 1.65 nm (Figure S60), while θ is assumed to be 0° due to the head-to-tail alignment of the chromophores. Based on the above information and considering the transition dipole moment (μ_{eg}) of one squaraine unit to be 12.8 D (see Table 5 in *Chapter 5*) and α (rotational offset) always to be 0°, the exciton coupling energies J_1, J_2 (Figure S60 and Table S4) can be calculated within the point-dipole approximation following Kasha's theory (Equation 1 in *Chapter 2*).[43] Notably, both J_1 and J_2 are negative, indicating J-type exciton coupling, which is in line with the red-shifted absorption spectra (Figure 63 in *Chapter 5*). As shown in Table S4, the calculated J_1 (−367 cm^{-1}) deviates largely from the experimental spectral shift of −1020 cm^{-1}, while J_2 (−2146 cm^{-1}) is in good agreement with the experimental result (−2300 cm^{-1}). This indicates that the *inter*molecular J-type coupling within the **BisSQ3** aggregates can be rationally elucidated by conventional exciton theory, whereas a more precise model that considers other factors (eg. polarizability) is needed to interpret the *intra*molecular J-type coupling of **BisSQ3** molecules.

Table S4. Exciton coupling energies J calculated for neighboring squaraine units within **BisSQ3** aggregates corresponding to *intra*molecular (J_1) and *inter*molecular (J_2) J-type couplings based on Kasha's theory.[43]

BisSQ3	μ_{eg} (D)	r (Å)	θ (°)	J (cm^{-1})
*intra*molecular (J_1)	12.8	16.5	0	−367
*inter*molecular (J_2)		8.4	23	−2146

According to Figure 66a in *Chapter 5*, the helical pitch (*h*) can be estimated as follows:

$$h = 2.1 \times (n - 1) + 3.0 \text{ nm}, \quad \text{(S27)}$$

where *n* denotes the number of molecules per helical pitch. When *n* equals 5, a helical pitch (*h*) of 11.4 nm is obtained, while *h* = 13.5 nm is obtained when *n* = 6. Considering the AFM results where the observed helical pitch is around 10 – 13 nm (Figure 65b in *Chapter 5*), both *n* = 5 and *n* = 6 are reasonable.

Furthermore, the ideal dihedral angle (α) can be calculated as follows:

$$\alpha = \frac{360^\circ}{n}. \quad \text{(S28)}$$

Thus, in the case of *n* = 5, α equals 72°. On the other hand, when *n* = 6, α equals 60°. In combination with the minimal energy structure obtained from the geometry optimization scan (Figure S59), when *n* = 6, the dihedral angle α is closer to the calculated value of 53.2°. Therefore, we propose that one helical pitch should contain six molecules and accordingly illustrate the molecular packing motif of one helical pitch in Figure 66b (*Chapter 5*).

9.3.7 NMR and Mass Spectra

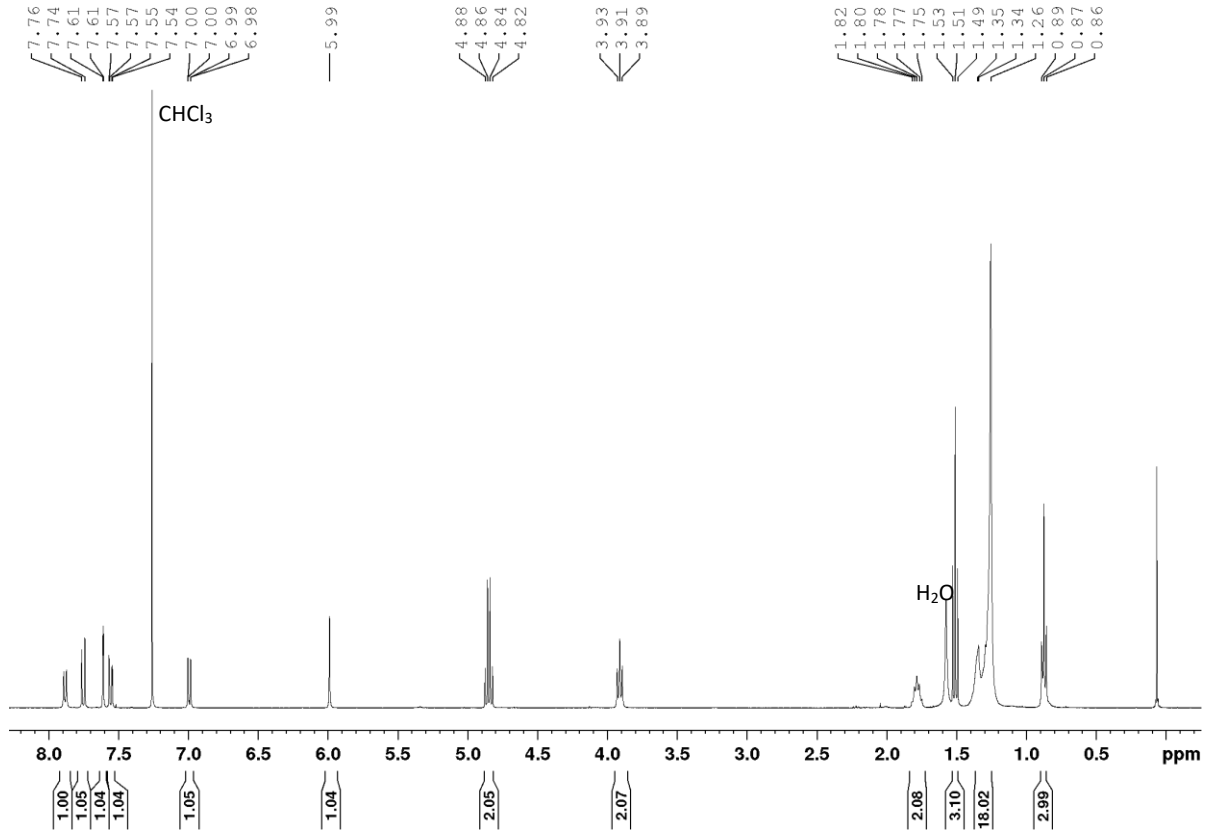

Figure S61. ^{1}H NMR (400 MHz, 295 K) spectrum of compound **3** in $CDCl_3$.

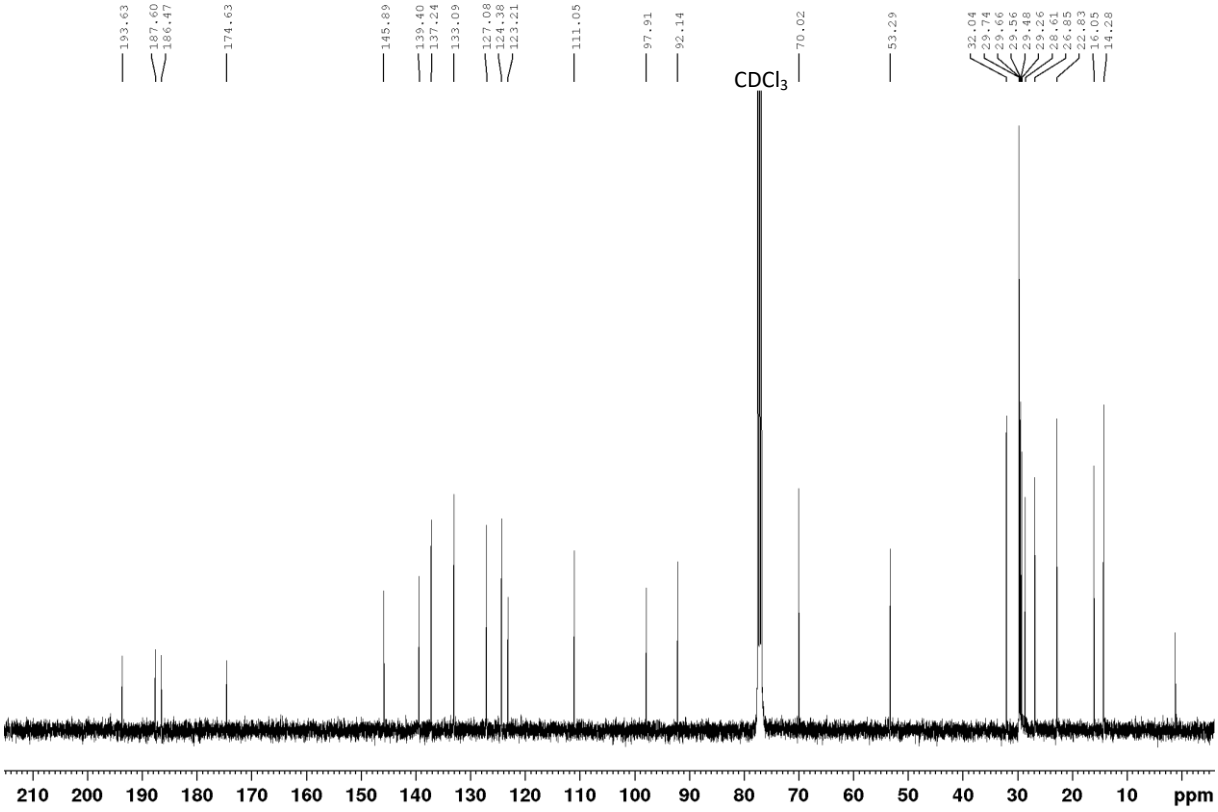

Figure S62. ^{13}C NMR (101 MHz, 295 K) spectrum of compound **3** in $CDCl_3$.

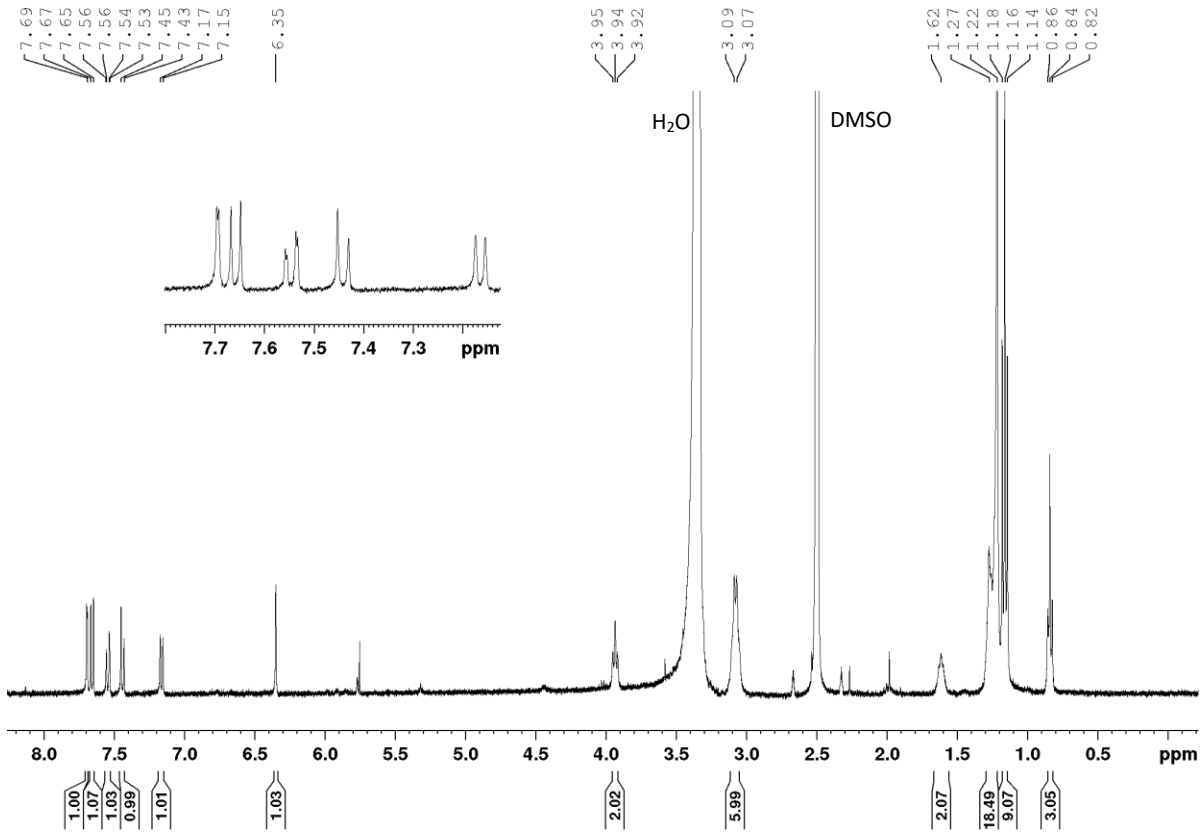

Figure S63. ^{1}H NMR (400 MHz, 295 K) spectrum of compound **4** in DMSO-d_6.

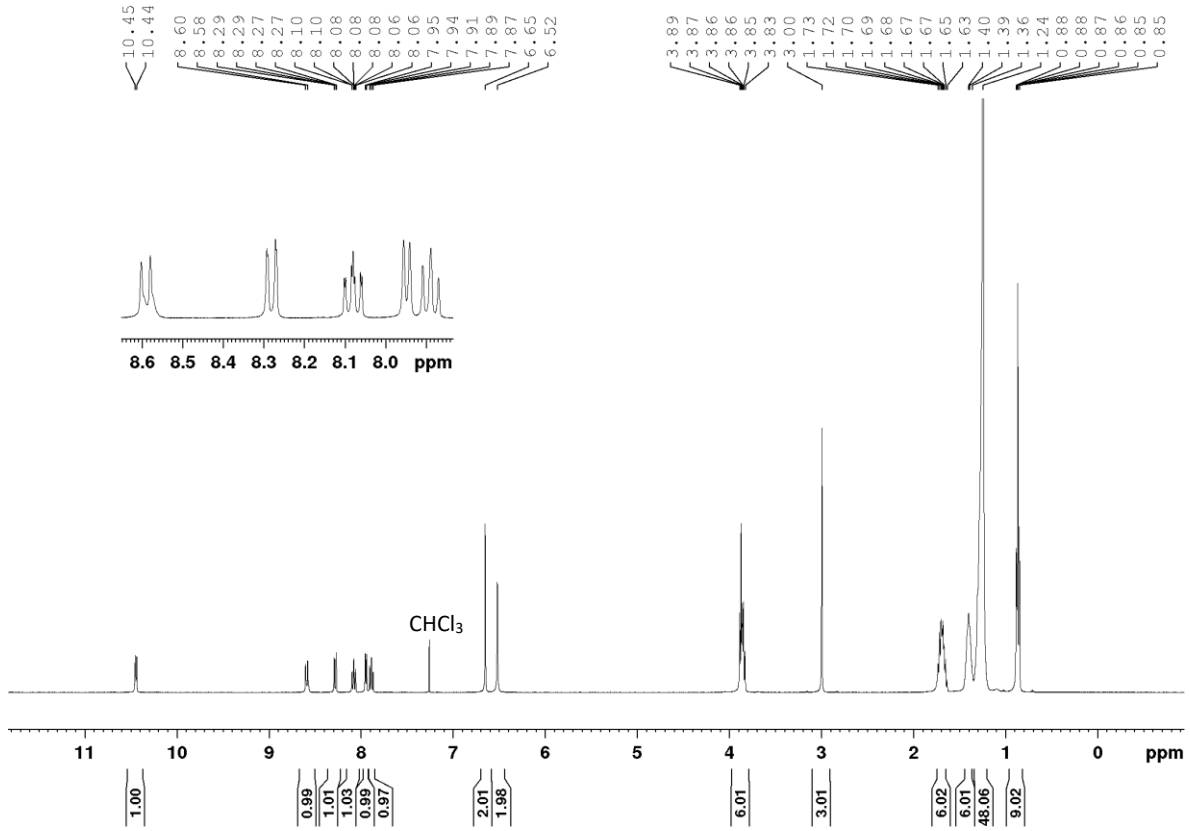

Figure S64. ^{1}H NMR (400 MHz, 295 K) spectrum of compound **5** in $CDCl_3$.

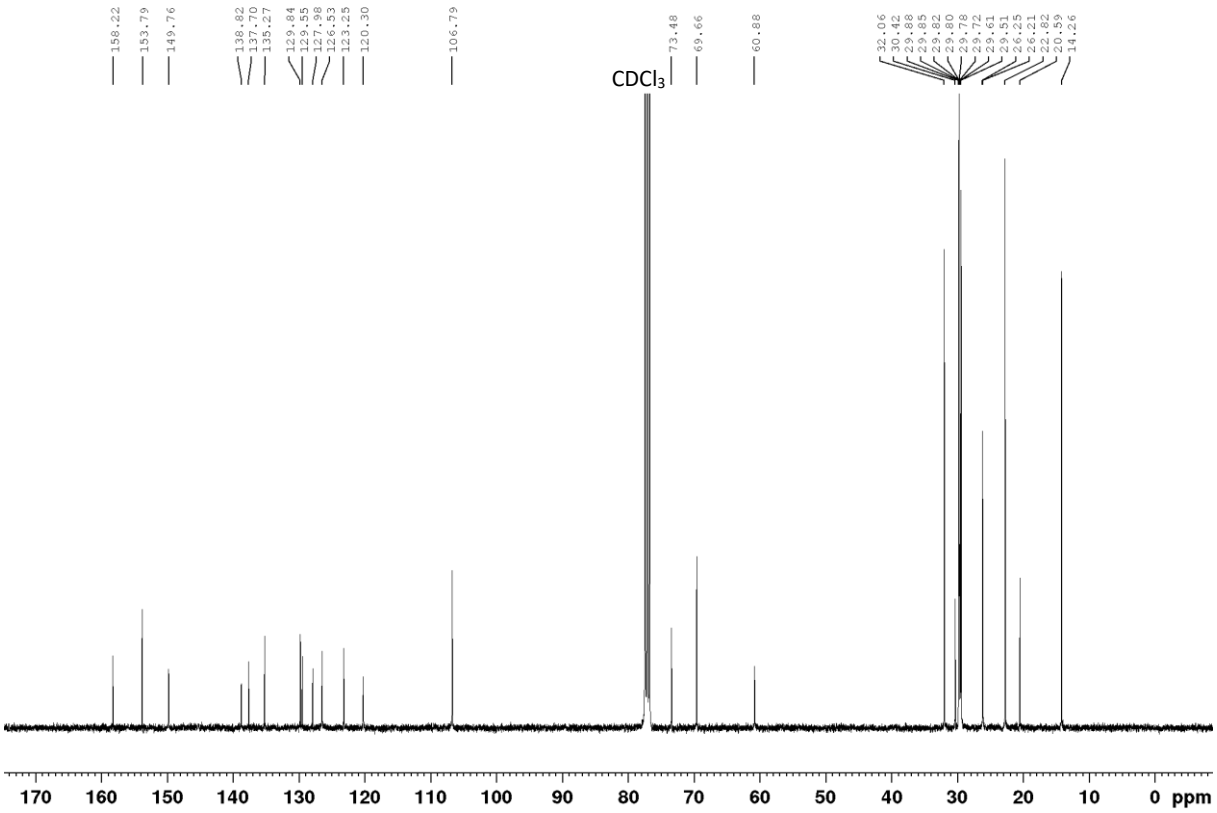

Figure S65. ^{13}C NMR (101 MHz, 295 K) spectrum of compound **5** in $CDCl_3$.

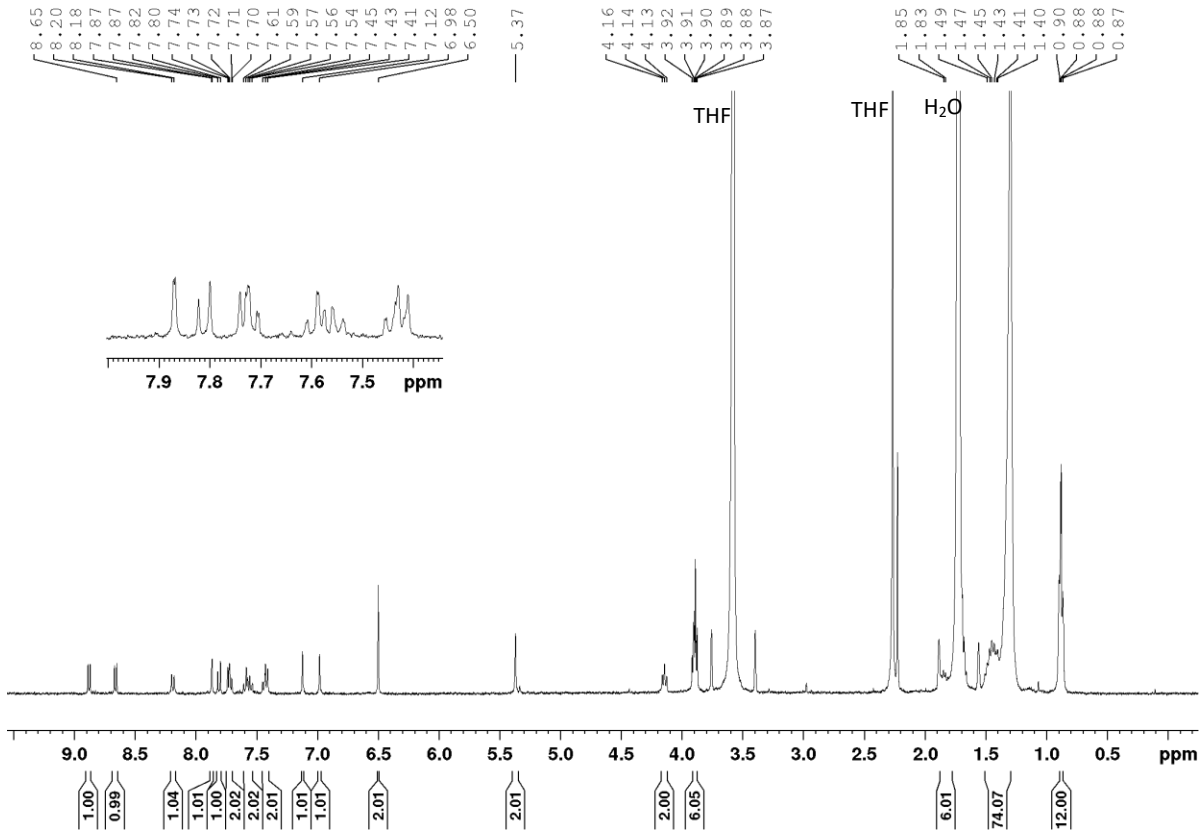

Figure S66. ^{1}H NMR (400 MHz, 330 K) spectrum of compound **6** in THF-d_8.

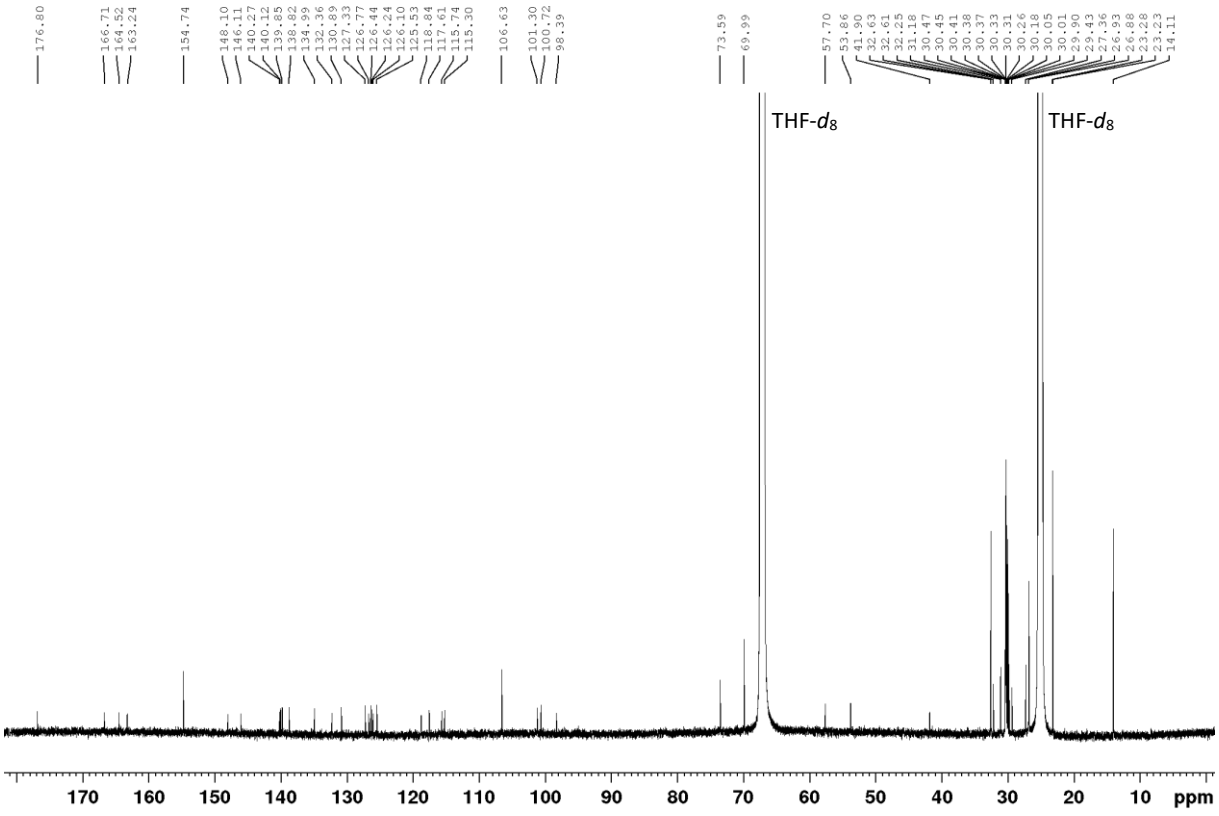

Figure S67. ^{13}C NMR (151 MHz, 330 K) spectrum of compound **6** in THF-d_8.

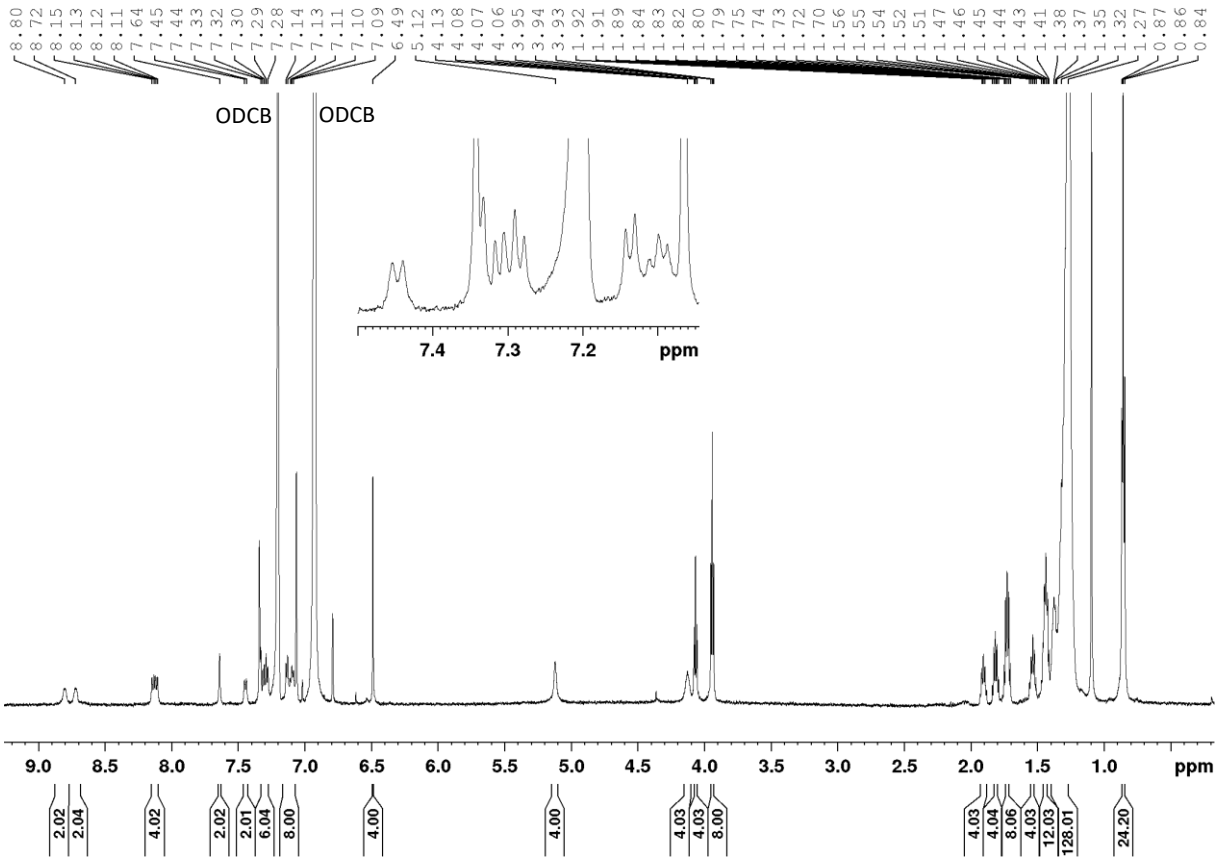

Figure S68. ^{1}H NMR (600 MHz, 402 K) spectrum of compound **BisSQ3** in *o*-dichlorobenzene-d_4 (ODCB).

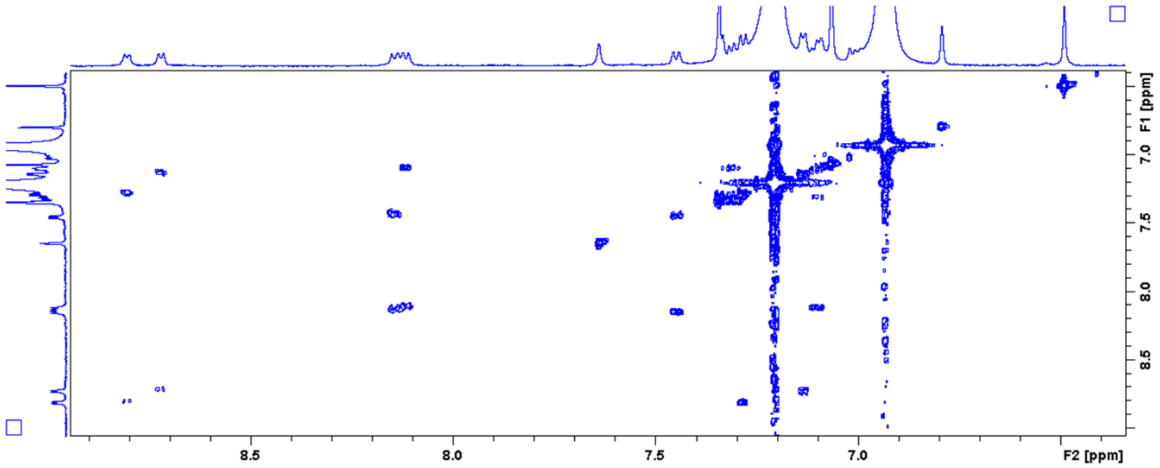

Figure S69. ^{1}H-^{1}H COSY NMR (600 MHz, 402 K) spectrum of compound **BisSQ3** in *o*-dichlorobenzene-d_4 (ODCB).

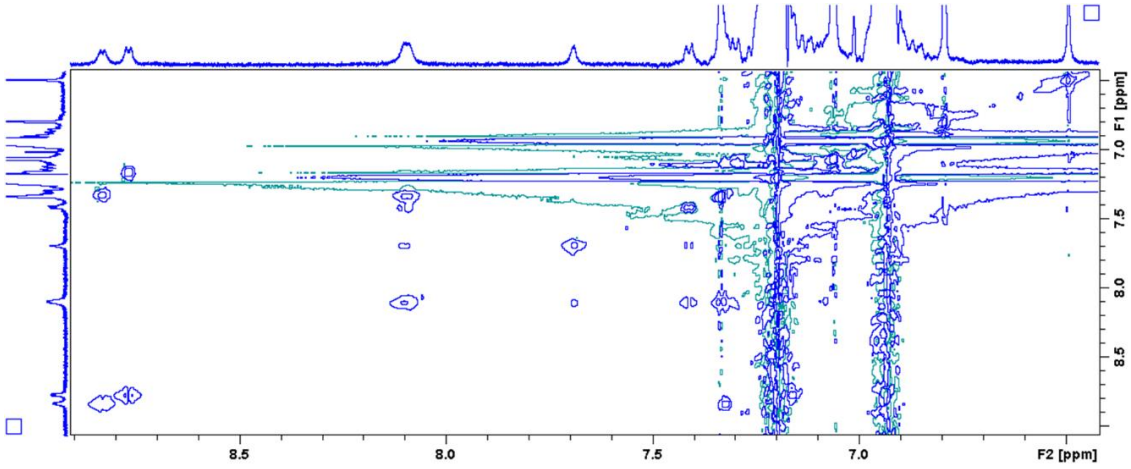

Figure S70. ^{1}H-^{1}H TOCSY NMR (600 MHz, 348 K) spectrum of compound **BisSQ3** in *o*-dichlorobenzene-d_4 (ODCB).

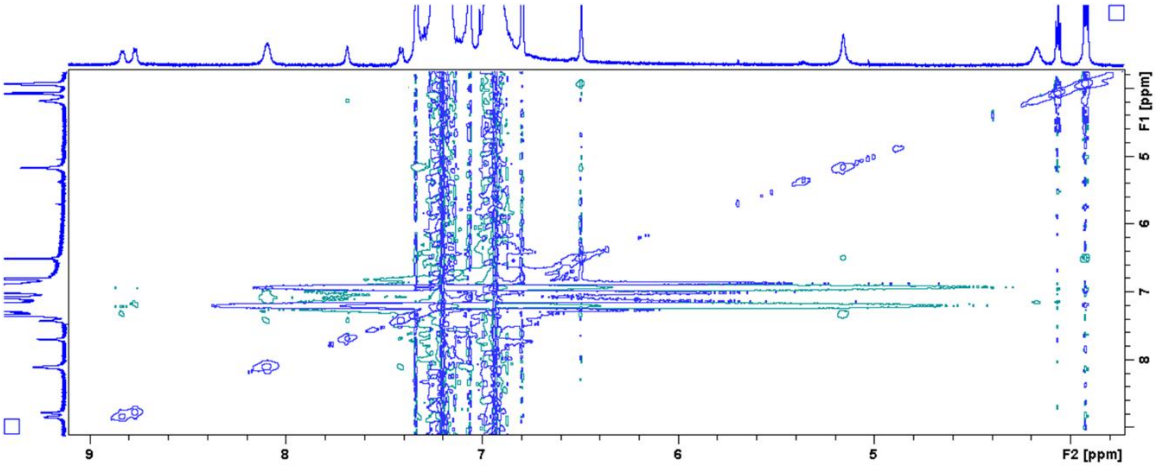

Figure S71. ^{1}H-^{1}H ROESY NMR (600 MHz, 348 K) spectrum of compound **BisSQ3** in *o*-dichlorobenzene-d_4 (ODCB).

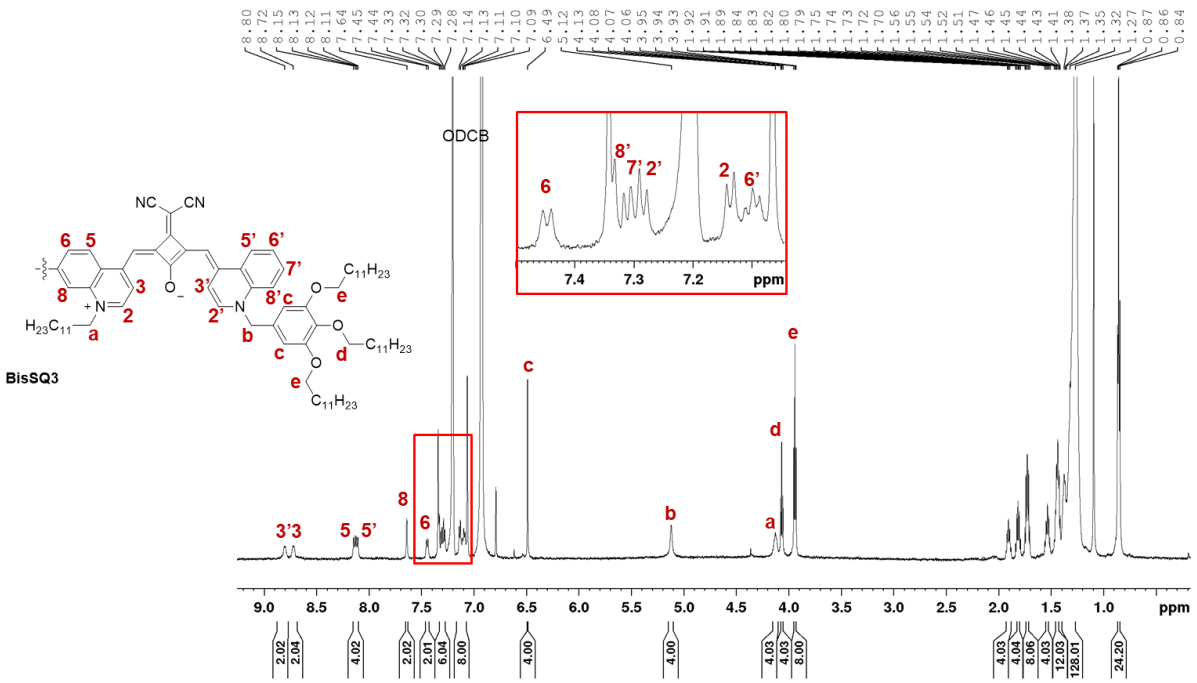

Figure S72. Assignment of the core protons of **BisSQ3** to the ^{1}H NMR (600 MHz, 402 K) spectrum of compound **BisSQ3** in *o*-dichlorobenzene-d_4 (ODCB) based on ^{1}H-^{1}H COSY, TOCSY, and ROESY NMR spectra.

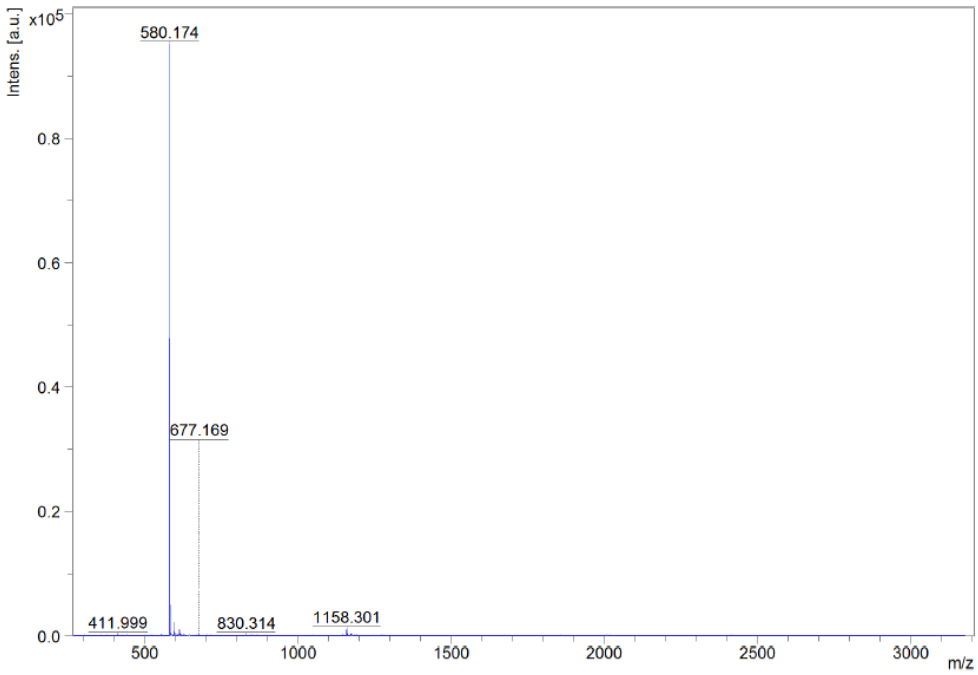

Figure S73. Mass spectrum (MALDI, neg. mode, matrix: DCTB 1:3 in chloroform) of compound **4**.

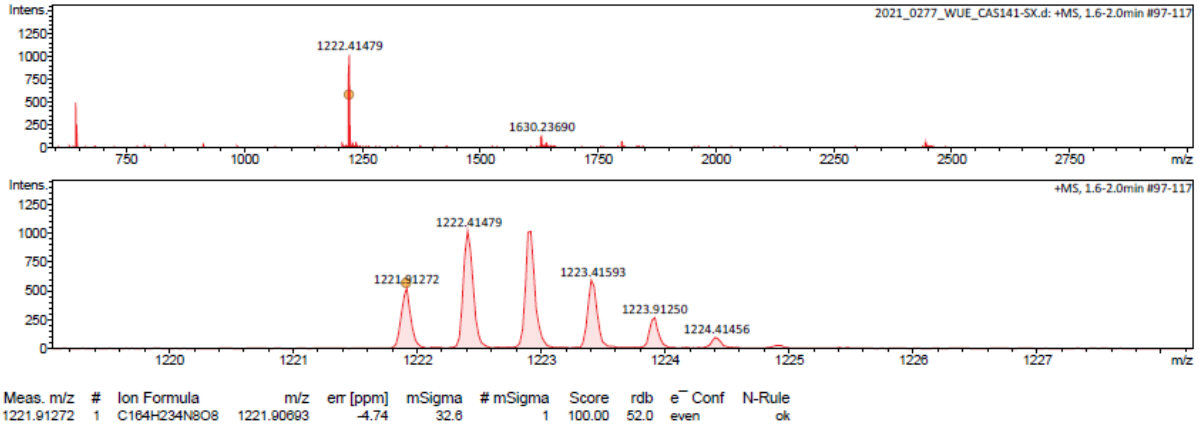

Meas. m/z	#	Ion Formula	m/z	err [ppm]	mSigma	# mSigma	Score	rdb	e⁻ Conf	N-Rule
1221.91272	1	C164H234N8O8	1221.90893	-4.74	32.6	1	100.00	52.0	even	ok

Figure S74. High resolution mass spectrum (ESI, pos. mode, $CHCl_3$/MeCN) of **BisSQ3**.

9.4 Supporting Information for *Chapter 6*: Selective Parallel G-Quadruplex Recognition by a NIR-to-NIR Two-Photon Squaraine[173]

9.4.1 Materials and Methods

Solvents and reagents were purchased from commercial suppliers (Sigma-Aldrich, ACROS, Alfa Aesar and Merck) and used as received, unless otherwise stated. All reactions were carried out under nitrogen atmosphere. Column chromatography was performed using silica gel 60M (0.04−0.063 mm). Oligonucleotides were purchased from Sigma Aldrich, diluted with water to a concentration of 2.00×10^{-3} M and stored at −15 °C. For all the experiments involving oligonucleotides, DNAse free water and transferring equipment were used. Ultrapure water type 1 was obtained by using a Millipore Simplicity® System (13.1 MΩ cm). A stock solution of 1.00 M KCl in water was prepared using solid KCl. The aqueous stock solution (1.00 M) of TRIS buffer was prepared by dissolving tris(hydroxymethyl)aminomethane in water and the pH was then adjusted to 7.42 ± 0.02 by adding KOH.

^{1}H and ^{13}C NMR spectra were generally recorded on a Bruker Avance III HD spectrometer operating at 400 MHz (^{1}H) or 101 MHz (^{13}C), with the residual protic solvent used as the internal standard. The chemical shifts are reported in parts per million (ppm). Multiplicities for proton signals are abbreviated as s, d, and m for singlet, doublet and multiplet, respectively.

High resolution mass spectra (HRMS) were recorded on an ESI micrOTOF focus spectrometer (Bruker Daltonic GmbH, Germany) and the matrix-assisted laser desorption/ionization (MALDI) spectra were obtained with a Bruker autoflex II spectrometer.

Optical spectroscopy. For all optical measurements spectroscopic grade solvents (Uvasol®) and ultra-pure water were used. Jasco V-770 UV-Vis-NIR spectrophotometer was used with spectral band width and the scan rate of 1 nm and 240 nm min^{-1}, respectively. For aqueous solution temperature-dependent absorption measurements, the concentration was corrected for the temperature-dependent density change by using the experimental equation for water ($d = 1.59 \times 10^{-3}\ T^3 - 5.97 \times 10^{-6}\ T^2 + 2.27 \times 10^{-5}\ T + 0.99994$, where T is the temperature in °C). Fluorescence spectra were recorded on PTI QM-4/2003 spectrometer with additional NIR add-on kit. Fluorescence quantum yields were determined by optical dilution method ($OD_{max} < 0.1$) as the average value of four different excitation wavelengths (630, 640, 650 and 660 nm) using Rhodamine 800 (λ_{max} = 681 nm, λ_{em} = 698 nm in ethanol, $\Phi_{FL} = 0.25 \pm 0.03$)[214] as reference. The signals were corrected for the different refractive indexes, according to the following equation:[215]

$$\Phi_{\mathrm{FL}} = \Phi_{\mathrm{FL}}^{\mathrm{ref}} \times \frac{I_\lambda}{I_\lambda^{\mathrm{ref}}} \frac{1-10^{-A_\lambda^{\mathrm{ref}}}}{1-10^{-A_\lambda}} \frac{n^2}{n_{\mathrm{ref}}^2} \quad \text{(S29)}$$

where I_λ is the fluorescence intensity area in the range 667 – 850 nm. The slits width of both monochromators were set fixed at 5.0 nm.[212]

The UV/Vis measurements were performed in conventional quartz cell cuvettes with path lengths of 0.01 – 50.0 mm.

ECD spectra were measured with a Jasco J-815 spectropolarimeter (JascoInc, USA) equipped with the JascoPeltier-type temperature controller (CDF-426S/15) and are presented as a sum of 3 accumulations. ECD measurements were performed at 25 °C in the wavelength range of 210 − 310 nm at different **CAS-C1** / G4 ratios. Before use, the optical chamber of the CD spectrometer was deoxygenated with dry nitrogen and was held under nitrogen atmosphere during the measurements. Appropriate references were subtracted from the obtained CD spectra.

TCSPC and singlet lifetime. The buffered solution of squaraine and G4 was prepared as for the titration studies. The suitable amount of G4 was added in order to obtain a complete formation of the complex. The formation of the complex was monitored by UV/Vis spectroscopy, then emission and excitation spectra were recorded. Lifetimes were obtained by monitoring the decay in the emission maximum upon irradiation of the pulsed laser at 670 nm (laser pulse 100 ns, emission slit 6.0 nm).

Data were fitted with a monoexponential function (Eq. S30) or a biexponential function (Eq. S31):

$$I = A + B_1 e^{-\frac{t}{\tau_1}} \quad \text{(S30)}$$

$$I = A + B_1 e^{-\frac{t}{\tau_1}} + B_2 e^{-\frac{t}{\tau_2}} \quad \text{(S31)}$$

Atomic Force Microscopy (AFM). AFM measurements were performed under ambient conditions using a Bruker Multimode 8 SPM system operating in tapping mode in air. Silica cantilevers (OMCL-AC160TS, Olympus) with a resonance frequency of ≈ 300 kHz and a spring constant of ≈ 40 Nm^{-1} were used. The samples were prepared by spin-coating a 1×10^{-5} M **CAS-C1** aqueous solution onto mica with 2000 – 4000 rpm.

Oligonucleotide annealing. A suitable amount of 2.00×10^{-3} M G4 stock solution was diluted with buffered water (c_{KCl} = 100 mM**,** tris(hydroxymethyl)aminomethane TRIS buffer 10.0 mM,

pH= 7.4), heated up at 95 °C for 10 min and then let it slowly cooled down to room temperature in nearly 3 hours. For UV/Vis titrations 500 μM solutions were used. The G4s used in these experiments, their sequence and topology is described in Table S5.

Table S5. Oligonucleotides utilized in this study purchased from Sigma Aldrich.

Name	Sequence[a]	Length	Topology and description
KRAS 32	AGGGCGGTGTGGGAAGAGGGAAGAGGGGGAGG	32	parallel[216]
KRAS 22	AGGGCGGTGTGGGAATAGGGAA	22	parallel[217]
sG4	GGGTGGGTAGGGTGGG	16	parallel
bcl2	GGGCGGGCGCGGGAGGAAGGGGGCGGG	27	parallel[218]
25CEB	AGGGTGGGTGTAAGTGTGGGTGGGT	25	parallel[219]
c-myc	TGAGGGTGGGTAGGGTGGGTAA	22	parallel[216]
VAV1	GGGCAGGGAGGGAACTGGG	19	parallel[220]
VEGF	GGGAGGGTTGGGGTGGG	17	parallel[218]
TERRA	AGGGUUAGGGUUAGGGUUAGGG	22	parallel[221]
c-kit2	CCCGGGCGGGCGCGAGGGAGGGGAGG	26	parallel (snap-back)[216]
c-kit87up	AGGGAGGGCGCTGGGAGGAGGG	22	parallel (snap-back)[222]
22AG (A-Tel21, wtTel22)	AGGGTTAGGGTTAGGGTTAGGG	22	hybrid/anti-parallel[223]
hRAS1	TCGGGTTGCGGGCGCAGGGCACGGGCG	27	anti-parallel[220]
Bom17	GGTTAGGTTAGGTTAGG	17	anti-parallel[219]
TBA 15	GGTTGGTGTGGTTGG	15	anti-parallel[218]
ss SCR	GGATGTGAGTGTGAGTGTGAGG	22	single strand[216]
ds26	CAATCGGATCGAATTCGATCCGATTG	26	duplex[216]

[a] Conventional 5' to 3' direction.

UV/Vis and fluorescence G4 titration. Aqueous solutions of squaraine **CAS-C1** were prepared by dissolving the compound in ultra-pure water and adding KCl and TRIS stock solutions (c_{KCl} = 100 mM, c_{TRIS} = 10.0 mM). The pH was checked by a Mettler Toledo Fivego® portable pH meter and adjusted to pH = 7.42 ± 0.04. The freshly prepared **CAS-C1** solution was titrated with the freshly annealed oligonucleotide buffered solution (500 μM). The titration experiments were followed by UV/Vis (UV/Vis bandwidth 2.0 nm, response 0.06 s, interval 0.5 nm, scan speed 400 nm/min) and fluorescence measurements (excitation at 660 nm, slit 4.00 nm, excitation polarizer at 0 °, emission polarizer at 54.8 °, iris setting 100, averaged on 3 repetitions) after each addition and nearly 25 min stirring in the dark (400 rpm, 25 °C). The concentration of the experiment was optimized to have $OD < 0.20$ to avoid reabsorption in the fluorescence emission.

Two-photon excited fluorescence studies. Two-photon absorption was determined from two-photon excited fluorescence (TPEF) spectra measured with a femtosecond laser system, which consisted of Ti:Sapphire laser Chameleon (Coherent Inc.) and an optical parametric oscillator Chameleon OPO (Coherent, Inc.) with an output signal tunable in the range 1000 – 1600 nm. The system produces pulses of the repetition rate equal 80 MHz and the pulse duration ≈ 200 fs. An output power was set to 100 – 120 mW for all the wavelengths, the same for each sample and a corresponding reference solution. The sample solution contained in a cuvette was illuminated with a microscope objective (Nikon Plan Fluor, 40x, NA 0.75) and collected in an epi-fluorescence mode. TPEF spectra were measured with Shamrock 303i spectrometer (Andor) equipped with iDus camera (Andor). The TPA spectra were obtained by tuning the wavelength of OPO and measuring the corresponding intensity of TPEF. The absolute 2PA cross-sections were calculated using relative fluorescence technique [224] where TPEF of the sample is compared with the signal of a standard under the same experimental conditions. We used styryl 9M as a standard.[225]

Data processing. All the data were corrected for the dilution upon titration with the G4 stock solution (500 μM). Binding constants were obtained by using multiple global fitting methods (Nelder-Mead method) for UV/Vis data in the range of 600 – 740 nm and fluorescence data in the range 690 – 764 nm by including dilution corrections. The procedure was repeated according to the method described in the references.[186,187]

Molecular modelling. Structural optimization of **CAS-C1** was carried out on its methylated precursor by Density Functional Theory (DFT) utilizing Gaussian09[226] suite of programs. The monomeric forms were optimized using B3LYP/6-311+G** and the solvent effect (THF, unless specified) was taken into account as PCM. Excited state was modelled using TD-DFT method.

For molecular docking, the coordinates of the structures were retrieved from the Protein Data Bank.[227] All structures were inferred from NMR studies in solution, under similar conditions (concentration, ionic strength, pH and temperature) of the experimental ones.

Docking studies were carried out with the Lamarckian genetic algorithm following the procedure developed for G-quadruplex DNA/RNA and ligand locking using Auto-dock Vina v1.1.2.[228] The dimensions of the active site box, that was placed always at the center of the G-quadruplex, were set to 80 Å x 80 Å x 80 Å, with a grid space of 0.375 Å. **CAS-C1** was optimized before using Gaussian suite of program (B3LYP/6-31+G** level, in water modelled

as polarizable continuum model with UAHF atomic radii). Two rounds of simulation were performed. In the first round, simulated annealing was used to find a rough binding mode of **CAS-C1** with 50 runs while keeping all other parameters default. The search space was subsequently reduced and another 200 runs were conducted to get a more precise result. Following the docking studies of **CAS-C1** with G-quadruplexes DNA/RNA, molecular graphics and analyses were performed with the UCSF Chimera package. Chimera is developed by the Resource for Biocomputing, Visualization, and Informatics at the University of California, San Francisco (supported by NIGMS P41-GM103311).[209]

9.4.2 Synthesis and Characterizations

Squaraine **CAS-C1** was synthesized according to the route depicted in Scheme S1. The staring compounds **C1** [229] and **C4**[27] were synthesized by literature-known procedures and 2-methylbenzothiazole was obtained from commercial supplier.

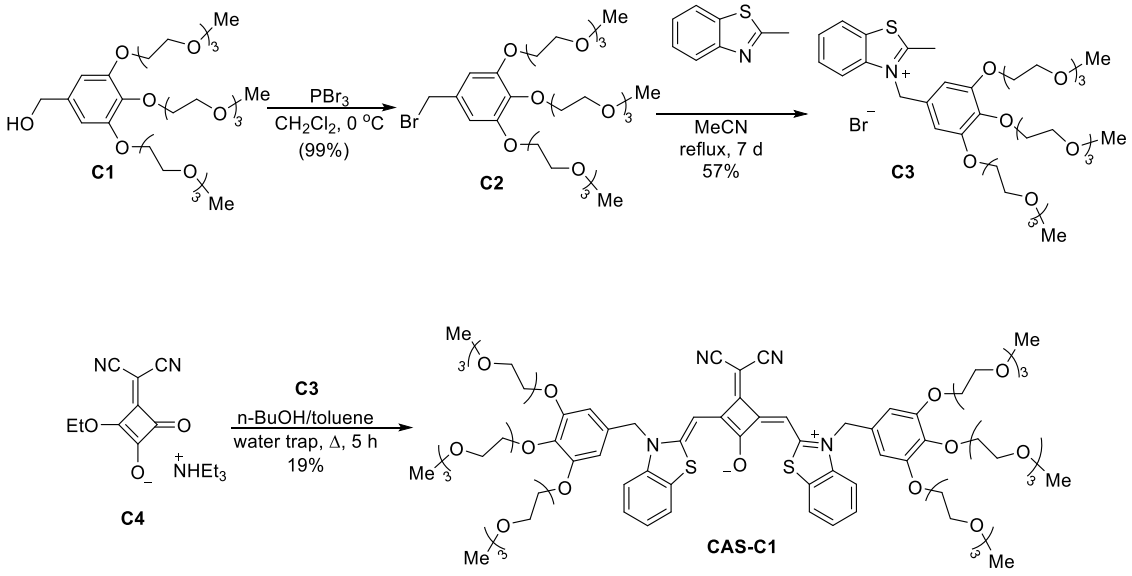

Scheme S1. Synthetic route to **CAS-C1**.

Synthesis of C2

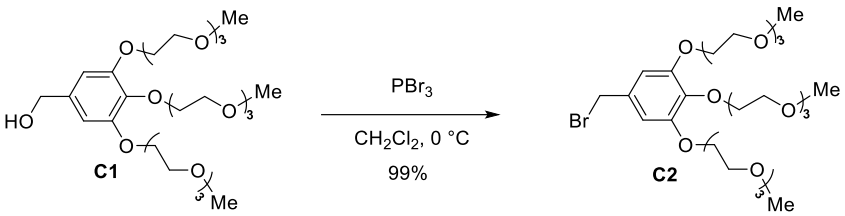

To a solution of benzyl alcohol derivative **C1** (1.03 g, 1.73 mmol) in anhydrous dichloromethane (5 mL) PBr_3 (0.086 mL, 0.905 mmol) was added at 0 °C under nitrogen atmosphere. The reaction mixture was stirred for 2 h at 0 °C. Afterwards, water (50 mL) was added and the organic layer was separated. The aqueous phase was extracted with dichloromethane (100 mL × 3). The combined organic layer was washed with brine and dried over sodium sulfate. The solvent was removed under reduced pressure to obtain benzyl bromide **2** as a light brown liquid in nearly quantitative yield (1.14 g, 99%).

^{1}H NMR (400 MHz, $CDCl_3$): δ = 6.62 (s, 2H), 4.40 (s, 2H), 4.12−4.16 (m, 6H), 3.84 (t, J = 5.2 Hz, 4H), 3.77 (t, J = 5.0 Hz, 2H), 3.70−3.73 (m, 6H), 3.64−3.67 (m, 12H), 3.52−3.55 (m, 6H), 3.38 (s, 9H) ppm; ^{13}C NMR (101 MHz, $CDCl_3$): δ = 152.5, 138.5, 132.9, 108.6, 70.7, 70.65, 70.63, 70.5, 70.49, 70.47, 70.45, 69.6, 68.8, 59.01, 58.9, 34.0 ppm. MS (MALDI, pos. mode, matrix: DCTB 1:3, $CHCl_3$): *m*/*z*: 679.228 $[M+Na]^+$ (calcd for $C_{28}H_{49}BrNaO_{12}$: 679.231).

Synthesis of C3

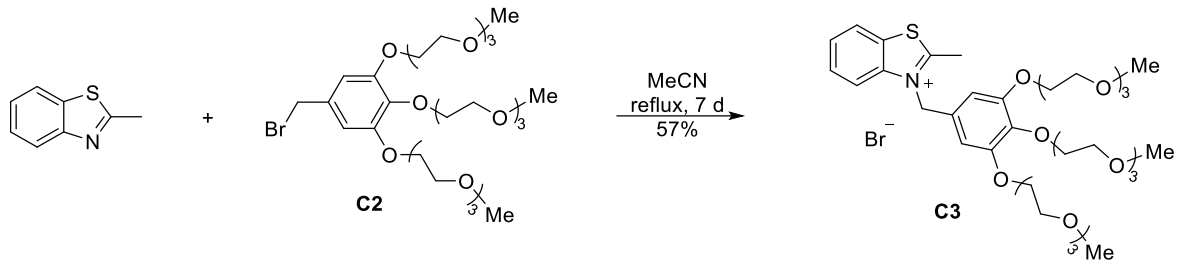

2-Methylbenzothiazole (50 µL, 392 µmol) and **C2** (1.03 g, 1.57 mmol) were mixed in 5 mL anhydrous acetonitrile (MeCN) and heated to reflux for seven days under nitrogen atmosphere. The reaction mixture was then cooled down to room temperature and the solvent was removed under reduced pressure. The residue was dissolved in methanol (1 mL) and a large amount of diethyl ether (100 mL) was added to induce precipitation. The precipitate was collected by filtration, washed with diethyl ether, and dried under high vacuum to yield compound **C3** as a viscous brown oil (182 mg, 58%).

^{1}H NMR (400 MHz, MeOD): δ = 8.34 (d, J = 8.2 Hz, 1H, H_{arom}), 8.21(d, J = 8.0 Hz, 1H, H_{arom}), 7.88 (td, J = 7.9 Hz, 1.2 Hz, 1H, H_{arom}), 7.82 (td, J = 7.9 Hz, 1.2 Hz, 1H, H_{arom}), 6.60(s, 2H, H_{arom}), 5.98 (s, 2H, N-CH_2), 4.10 (m, 6H, CH_2), 3.77 (m, 6H, CH_2), 3.63 (m, 18H, CH_2), 3.52 (m, 6H, CH_2), 3.34 (s, 3H, O-CH_3), 3.33 (s, 6H, O-CH_3), 3.29 (s, 3H, CH_3) ppm. ^{13}C NMR (101 MHz, MeOD): δ = 154.8, 142.9, 131.2, 129.9, 125.5, 118.3, 107.8, 73.7, 73.5, 73.0, 72.9, 71.8, 71.7, 71.6, 71.5, 71.4, 71.3, 70.8, 70.3, 62.2, 59.1, 53.7, 17.6 ppm. HRMS (ESI, pos. mode, MeOH): m/z: 726.3526 [M^+] (calcd for $C_{36}H_{56}NO_{12}S$: 726.3518).

Synthesis of CAS-C1

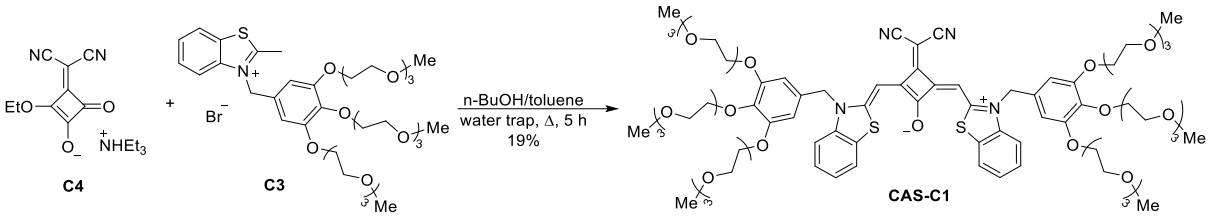

A round-bottom flux, equipped with a water-removing Dean-Stark apparatus, was charged with 4 mL *n*-butanol and 4 mL toluene. Subsequently, dicyanomethylene squaric ester **C4** (13.0 mg, 44.6 µmol) and compound **C3** (168 mg, 208 µmol) were added and the mixture was heated to reflux at 180 °C for 5 h. After being cooled down to room temperature, solvent was removed under reduced pressure. The residue was dissolved in CH_2Cl_2/MeOH = 4/1 solvent mixture (3 mL) and added dropwise into 500 mL of pre-cooled diethyl ether. After 1 h of vigorous stirring, the precipitate was collected by filtration and washed with diethyl ether. The crude product was further purified by flash chromatography ($CHCl_3$/MeOH = 97/3) to yield a viscous green solid (13.8 mg, 20%).

^{1}H NMR (400 MHz, $CDCl_3$): δ = 7.59 (dd, J = 7.8, 0.6 Hz, 2H, H_{arom}), 7.42 (td, J = 7.8 Hz, 1.1Hz, 2H, H_{arom}), 7.30 (m, 4H, H_{arom}), 6.48 (s, 4H, H_{arom}), 6.31 (s, 2H, $CH_{methylene}$), 5.18 (s, 2H, N-CH_2), 4.11 (m, 12H, CH_2), 3.79 (t, J = 5 Hz, 8H, CH_2), 3.75 (t, J = 5.0 Hz, 4H, CH_2), 3.68 (m, 12H, CH_2), 3.61 (m, 24H, CH_2), 3.52 (m, 12H, CH_2), 3.351 (s, 6H, O-CH_3), 3.347 (s, 12H, O-CH_3) ppm; ^{13}C NMR (101 MHz, $CDCl_3$): δ = 174.2, 164.5, 162.7, 161.0, 153.1, 141.3, 138.4, 128.9. 128.2, 127.9, 125.0, 122.4, 112.3, 106.8, 87.7, 72.2, 71.8, 70.6, 70.5, 70.4, 70.3, 69.6, 68.9, 59.0, 49.9 ppm; HRMS (ESI, pos. mode, MeCN/$CHCl_3$): m/z: 1577.68018 [M+H]$^+$ (calcd for $C_{79}H_{109}N_4O_{25}S_2$: 1577.68168). Elemental analysis (%) calculated for $C_{79}H_{108}N_4O_{25}S_2$: C 60.14, H 6.9, N 3.55, S 4.06; found: C 60.14, H 7.04, N 3.76, S 3.78.

9.4.3 Optical Studies in Organic Solvents

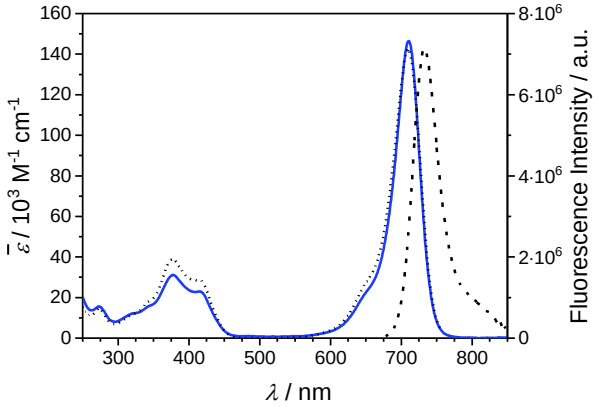

Figure S75. Absorption (filled), emission (dashed) and excitation (dotted) spectra of **CAS-C1** in chloroform solution.

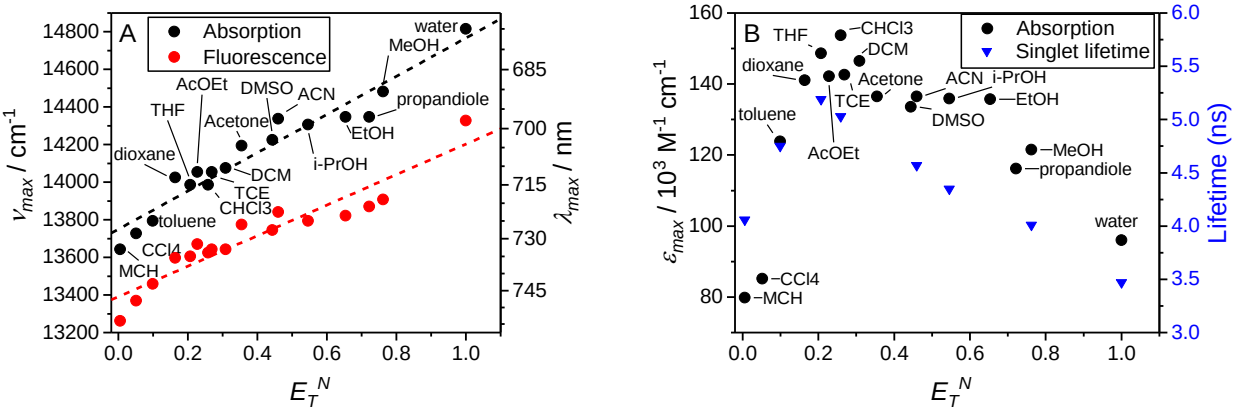

Figure S76. (A) Change of the absorption (black) and emission (red) maxima for the optical spectra of **CAS-C1** depending on the solvent polarity. (B) Change of the extinction coefficient (left axis, black) and fluorescence lifetime (right axis, blue) with the solvent polarity.

9.4.4 Optical Studies in Aqueous Media

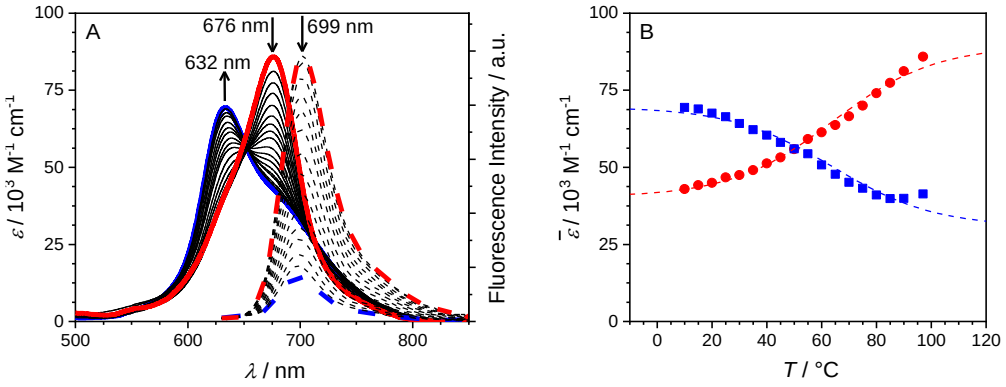

Figure S77. (A) UV/Vis (filled line) and fluorescence (dotted line) spectrum of an aqueous **CAS-C1** solution (5.8×10^{-7} M) upon decreasing the temperature from 95 (red) to 10 °C (blue). (B) Plot of the apparent extinction coefficient $\bar{\varepsilon}$ at 632 and 676 nm against the temperatures. Dotted lines correspond to a fitting with the isodesmic model (T_m = 64 °C, $\Delta H^{pol} = -55.9$ kJ mol^{-1}, R^2 = 0.985).

The apparent extinction coefficient was plotted against the temperature and fitted well with a temperature-dependent isodesmic aggregation model (Eq. S32),[128] with an estimated T_m = 64 °C and assuming an enthalpy of each step of polymerization of $\Delta H^{pol} = -55.9$ kJ mol^{-1}.

$$\alpha_{agg}^{\lambda} = \frac{\varepsilon_{(T)}^{\lambda} - \varepsilon_{(low)}^{\lambda}}{\varepsilon_{(high)}^{\lambda} - \varepsilon_{(low)}^{\lambda}} = \frac{1}{1+e^{-0.908\,\Delta H^{pol}\frac{T-T_m}{R\,(T_m+273.15)^2}}} \qquad \text{(S32)}$$

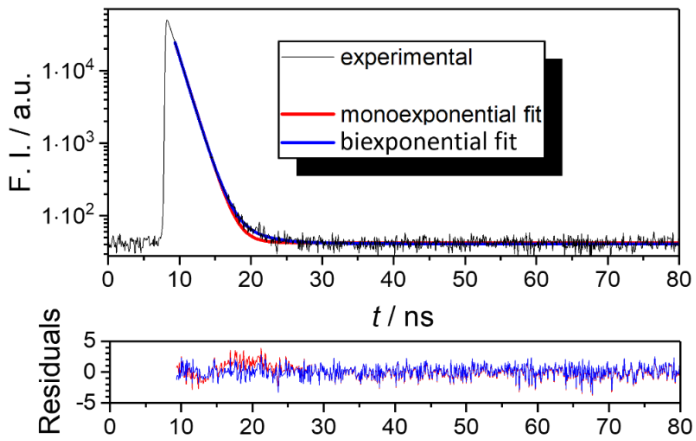

Figure S78. Time-correlated single photon counting decay (excitation at 670 nm) for **CAS-C1** in water at 80 °C. In red the fitting with a monoexponential function (Eq. S30); the fitting with a biexponential function (Eq. S31, τ_1 = 4.76 ns, τ_2 = 1.35 ns). The fitting with the biexponential function better describes the decay in the range 15 – 25 s (R^2 = 0.9998) compared with the monoexponential function (R^2 = 0.9972).

9.4.5 G-Quadruplex Studies

Kinetics

The binding of **CAS-C1** with various G4s revealed no significant kinetics.

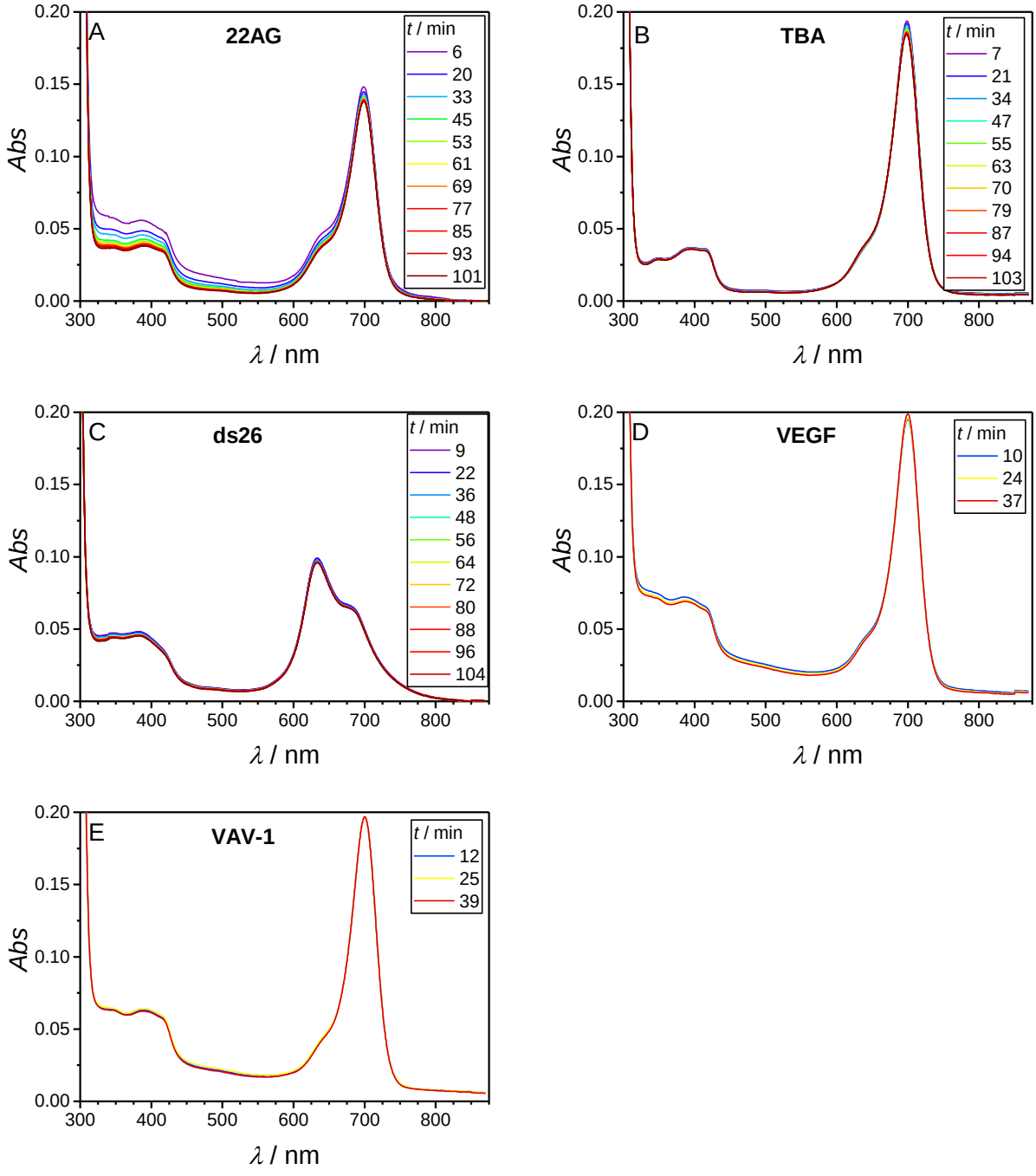

Figure S79. Kinetics of interaction between **CAS-C1** and: (A) 22AG; (B) TBA; (C) ds26; (D) VEGF and (E) VAV-1. (TRIS buffer c = 10 mM, pH = 7.2, KCl c = 100 mM, 25 °C). After addition of G4, the sample was measured at different time intervals as indicted in the insets.

G-Quadruplex Titrations

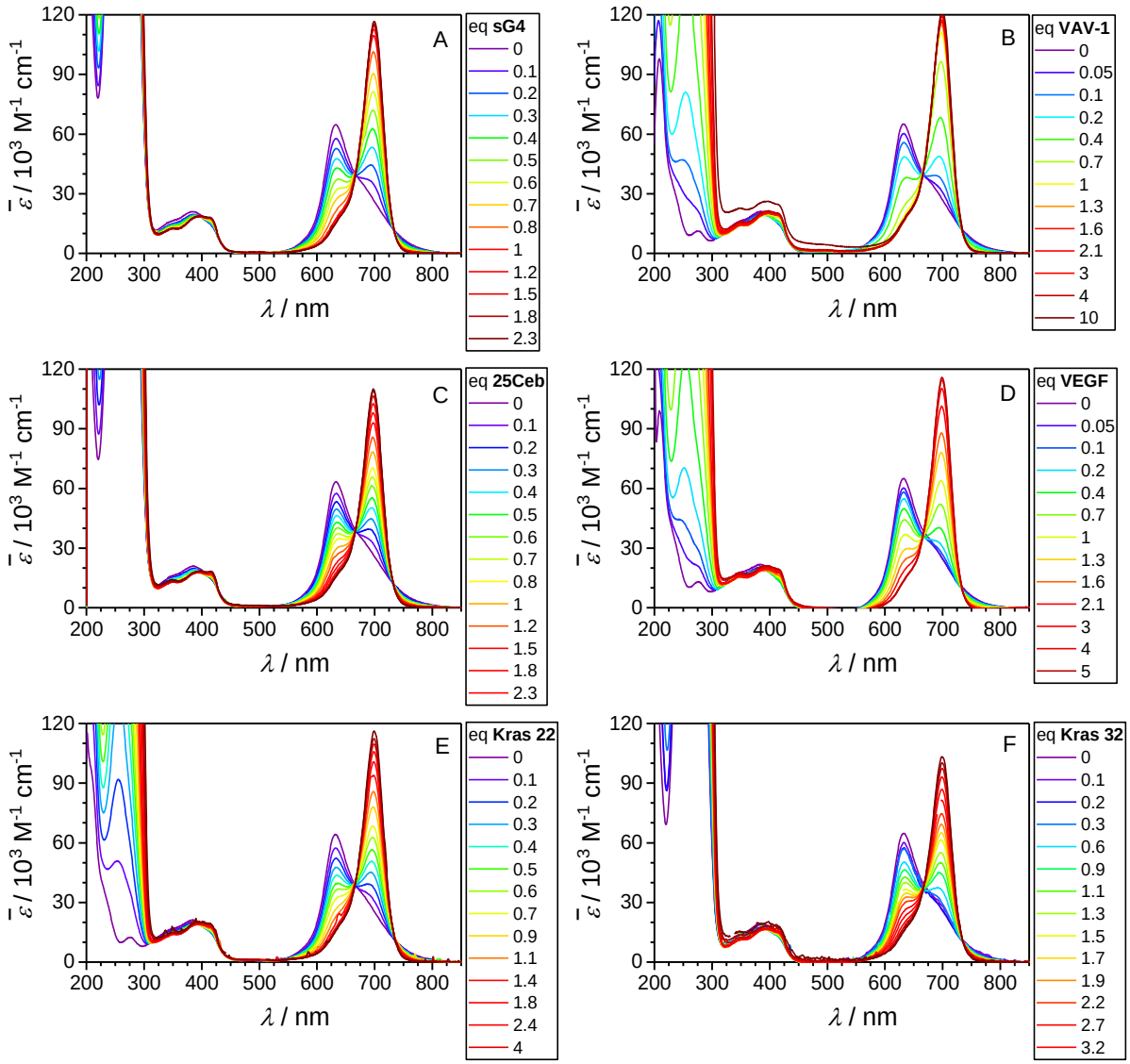

Figure S80. UV/Vis spectra of **CAS-C1** in buffered water solution (1.66×10^{-6} M, TRIS buffer c = 10 mM, pH = 7.2, KCl c = 100 mM) upon addition of various G4s (500 µM, buffered solution) at 25 °C: (A) sG4, (B) VAV-1, (C) 25Ceb, (D) VEGF, (E) Kras 22 and (F) Kras 32.

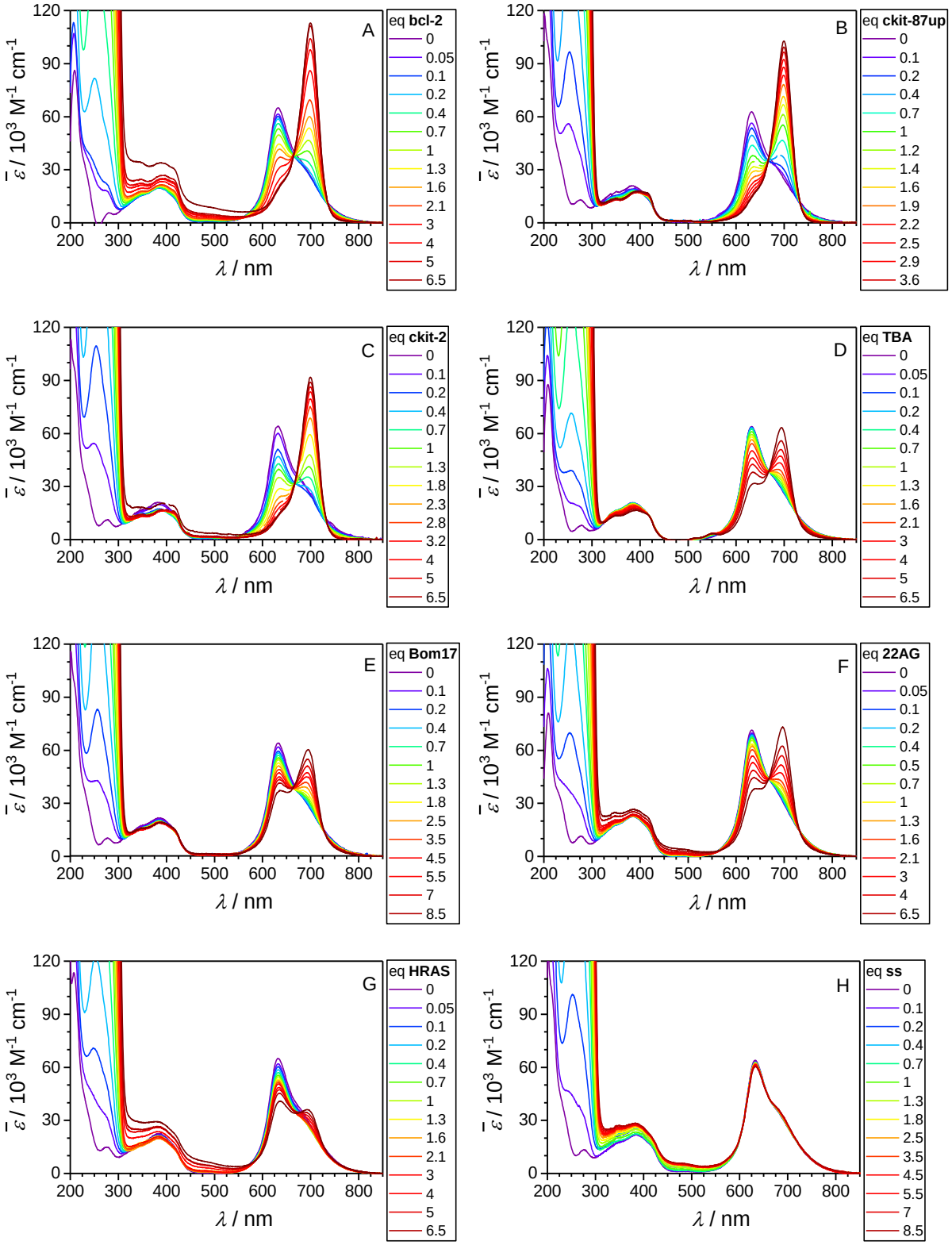

Figure S81. UV/Vis spectra of **CAS-C1** in buffered water solution (1.66×10^{-6} M, TRIS buffer c = 10 mM, pH = 7.2, KCl c = 100 mM) upon addition of various G4s (500 µM, buffered solution) at 25 °C: (A) bcl-2, (B) ckit-87up, (C) ckit-2, (D) TBA, (E) Bom17, (F) 22AG, (G) HRAS and (H) ss.

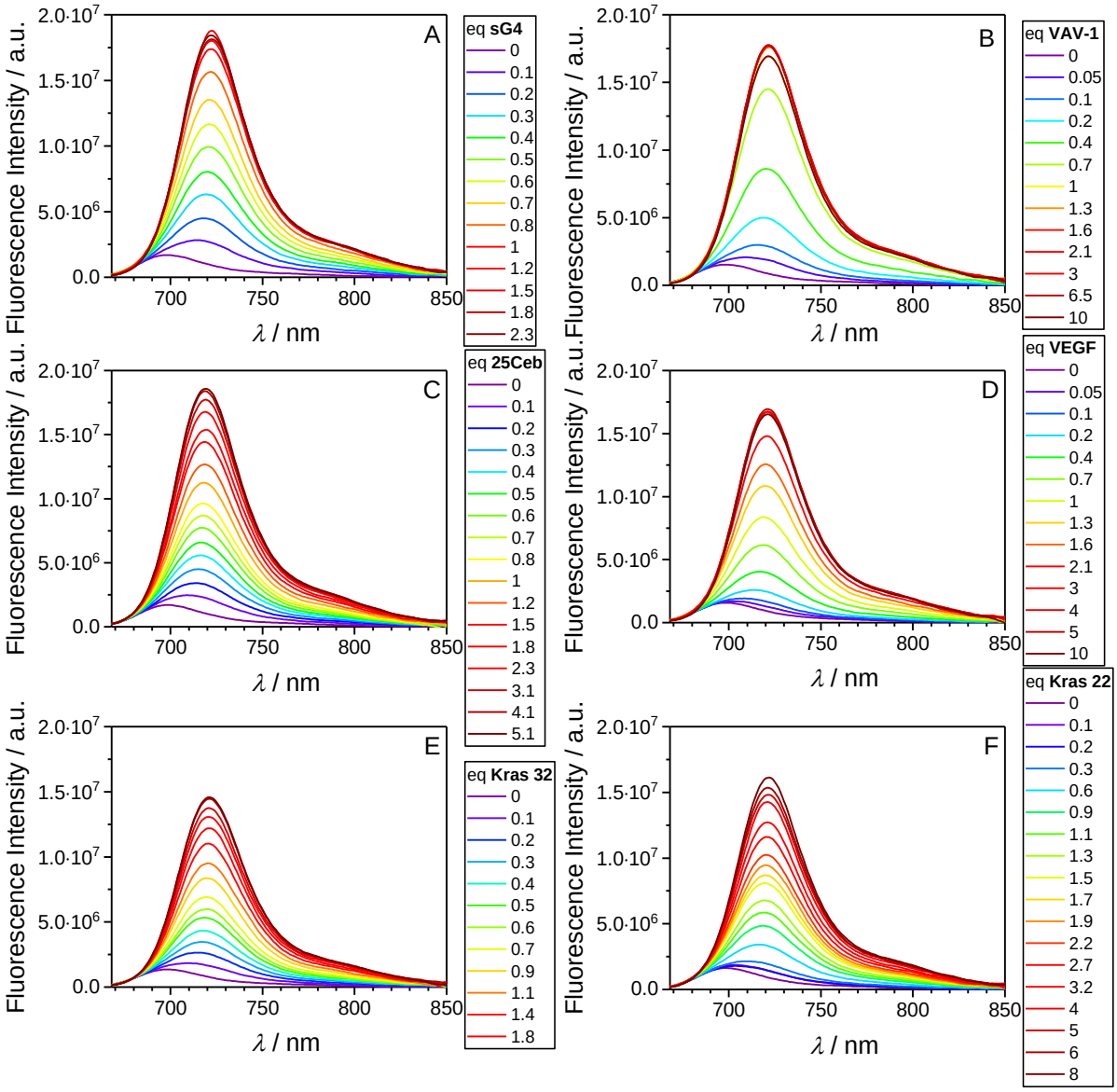

Figure S82. Fluorescence spectra (excitation at 660 nm) of **CAS-C1** in buffered water solution (1.66×10^{-6} M, TRIS buffer c = 10 mM, pH = 7.2, KCl c = 100 mM) upon addition of various G4s (500 µM, buffered solution) at 25 °C: (A) sG4, (B) VAV-1, (C) 25Ceb, (D) VEGF, (E) Kras 22 and (F) Kras 32.

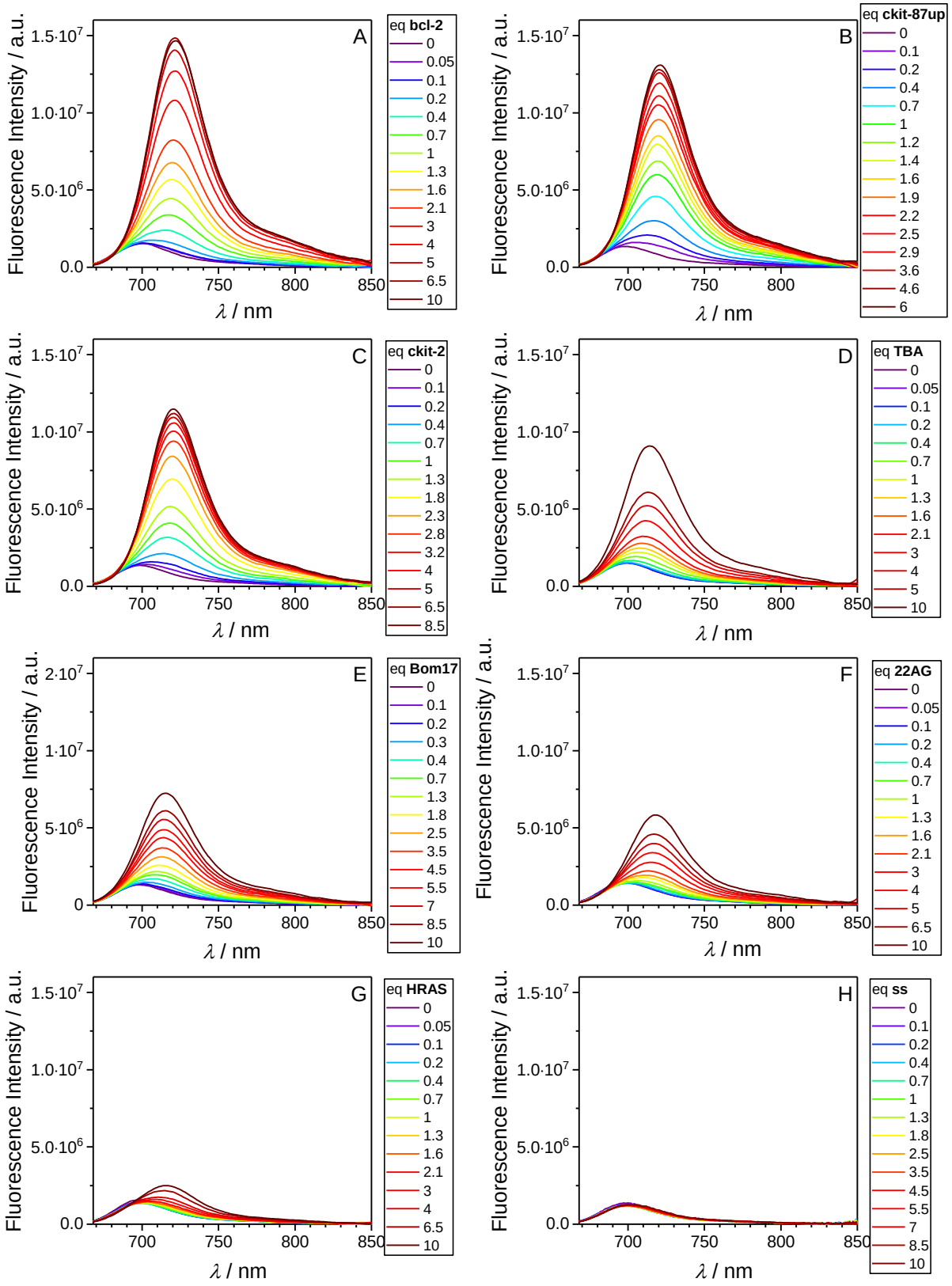

Figure S83. Fluorescence spectra (excitation at 660 nm) of **CAS-C1** in buffered water solution (1.66×10^{-6} M, TRIS buffer c = 10 mM, pH = 7.2, KCl c = 100 mM) upon addition of various G4s (500 µM, buffered solution) at 25 °C: (A) bcl-2, (B) ckit-87up, (C) ckit-2, (D) TBA, (E) Bom17, (F) 22AG, (G) HRAS and (H) ss.

Photophysical Characterization

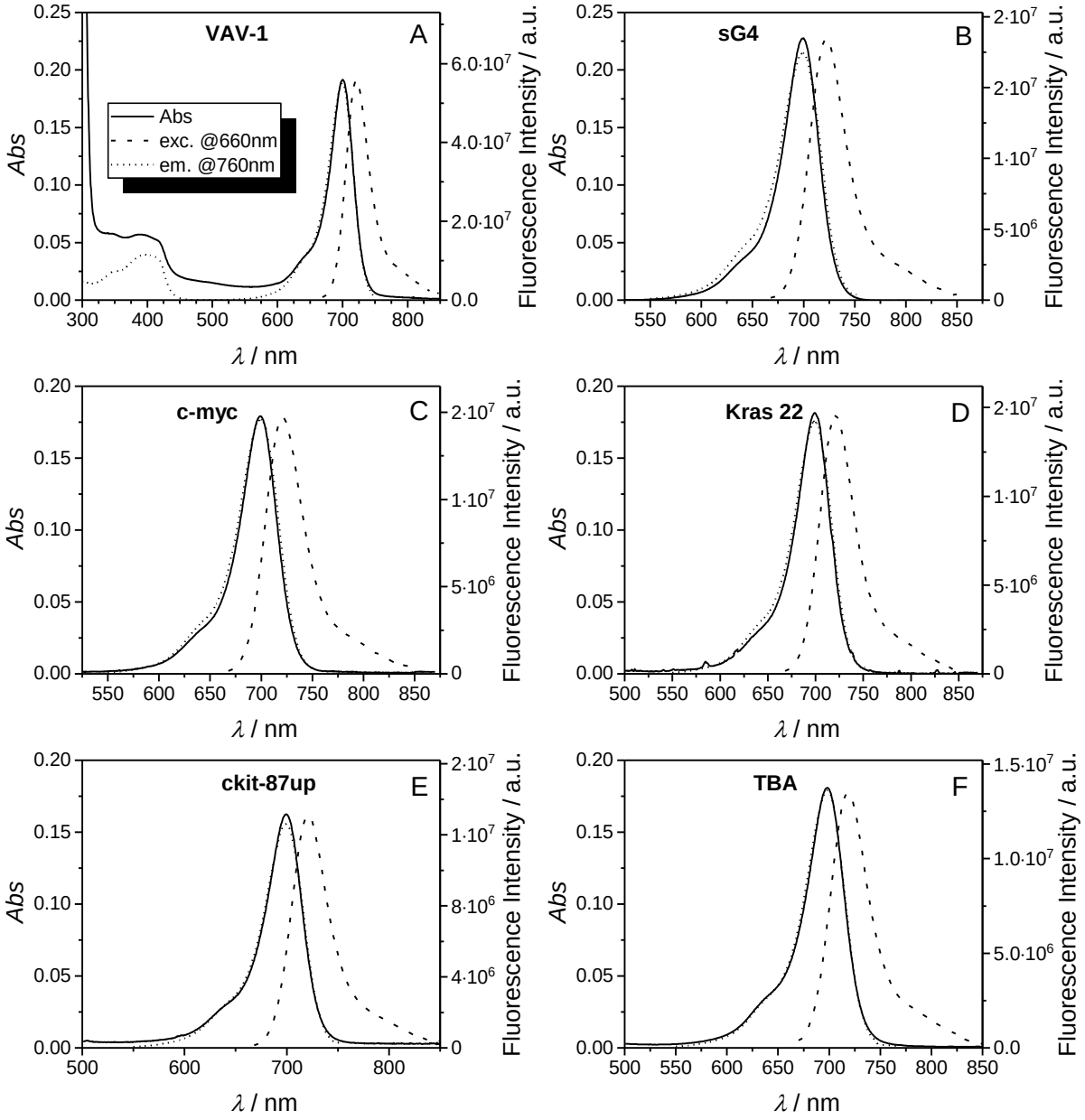

Figure S84. Absorption (filled line), emission (excitation at 660 nm, dashed) and excitation spectra (emission at 760 nm, dotted) of **CAS-C1** complex with: (A) 14 eq VAV-1, (B) 2.9 eq sG4, (C) 5.1 eq c-myc, (D) 10.8 eq Kras 22, (E) 9.3 eq ckit-87up and (F) 25 eq TBA.

Fluorescence Lifetimes

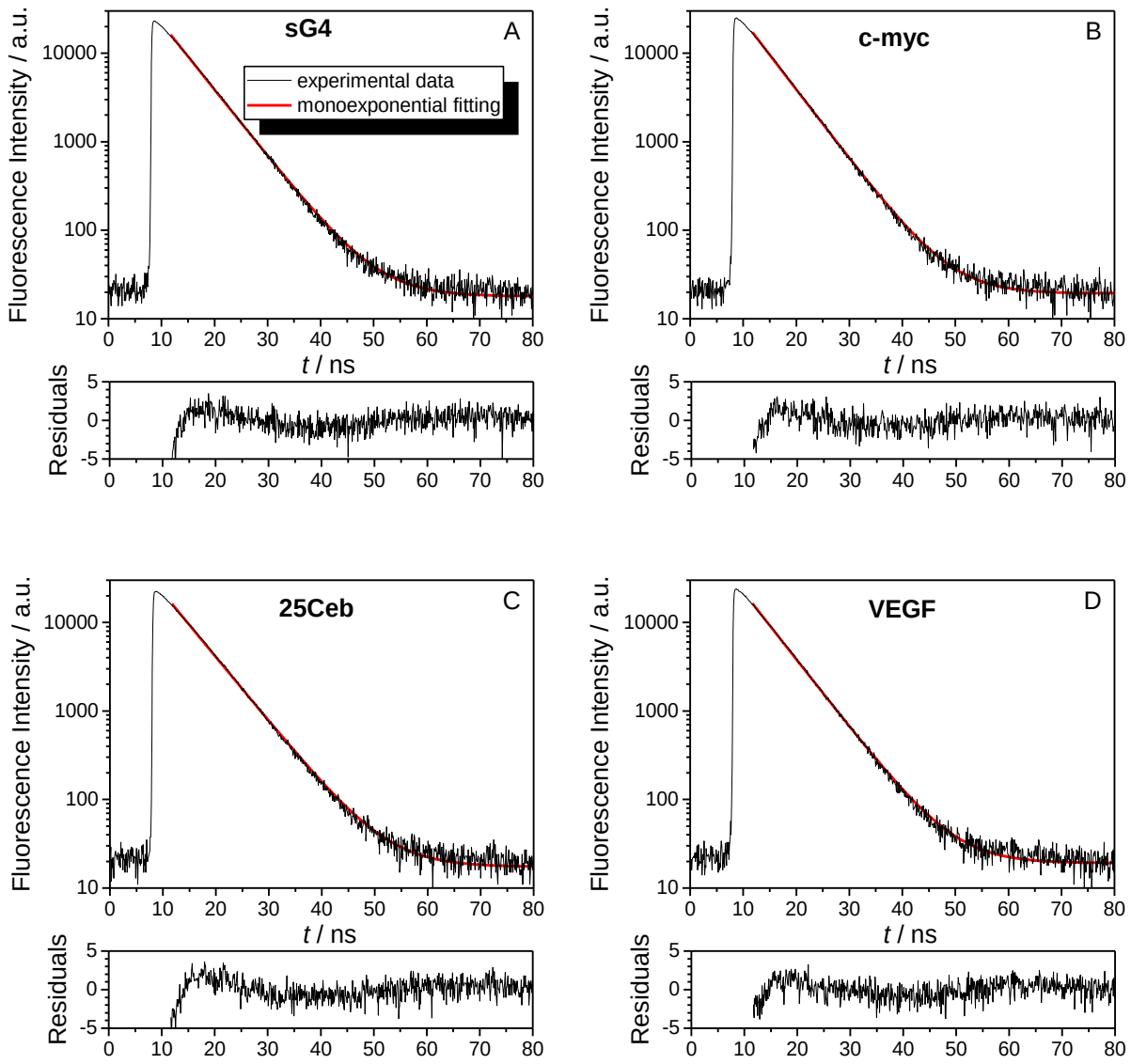

Figure S85. Time-correlated single photon counting decay (excitation at 670 nm) for **CAS-C1** with addition of (A) 2.9 eq sG4, (B) 5.1 eq c-myc, (C) 6.1 eq 25Ceb, (D) 14.5 eq VEGF (TRIS buffer *c* = 10 mM, pH = 7.2, KCl *c* = 100 mM, 25 °C). In red is shown the monoexponential fitting. The lifetime is shown in Table 6 (*Chapter 6*).

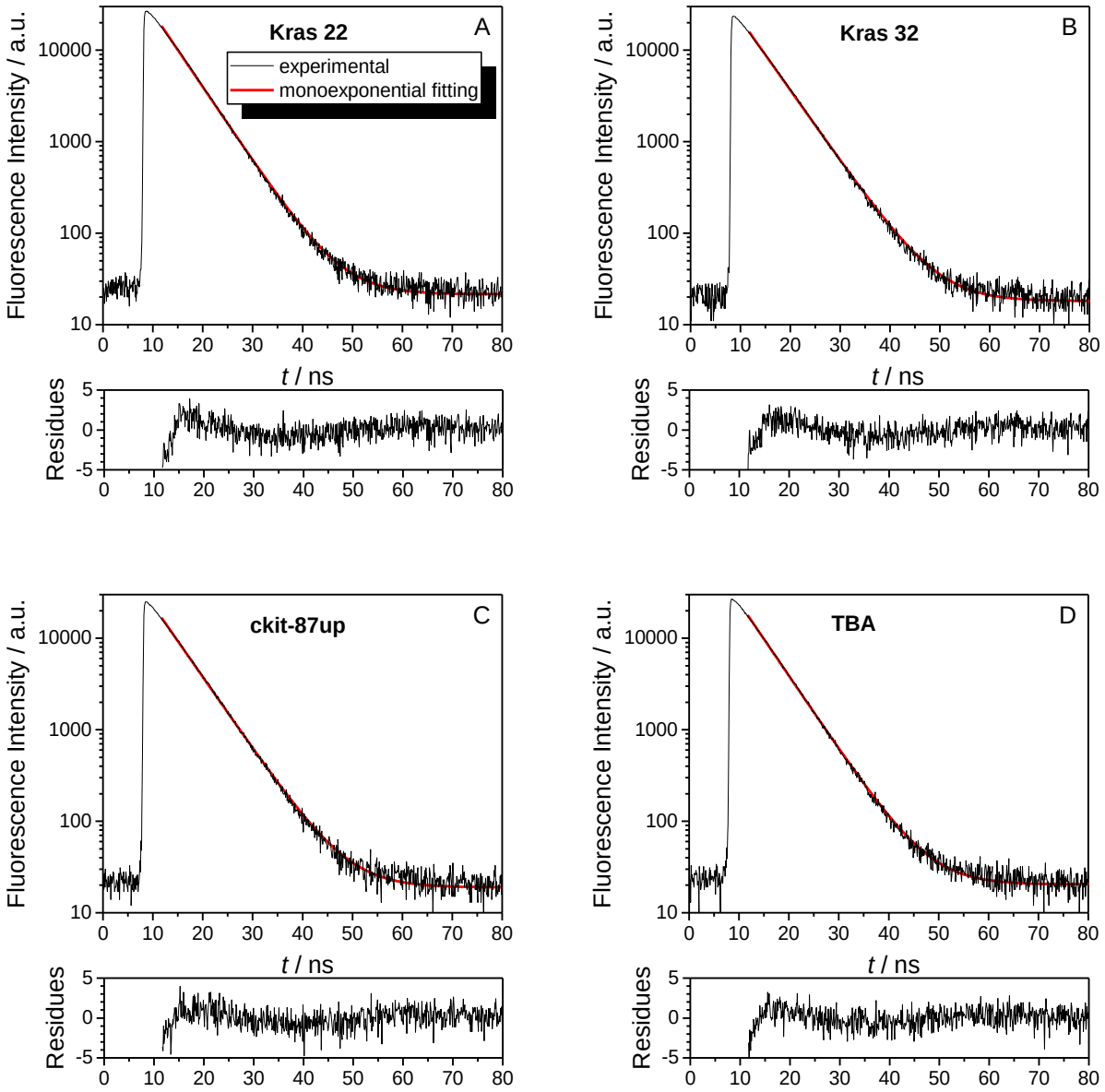

Figure S86. Time-correlated single photon counting decay (excitation at 670 nm) for **CAS-C1** with addition of (A) 10.8 eq Kras 22, (B) 9.2 eq Kras 32, (C) 9.4 eq ckit-87up, (D) 25 eq TBA (TRIS buffer *c* = 10 mM, pH = 7.2, KCl *c* = 100 mM, 25 °C). In red is shown the monoexponential fitting. The lifetime is shown in Table 6 (*Chapter 6*).

Job´s Plot and Stoichiometry

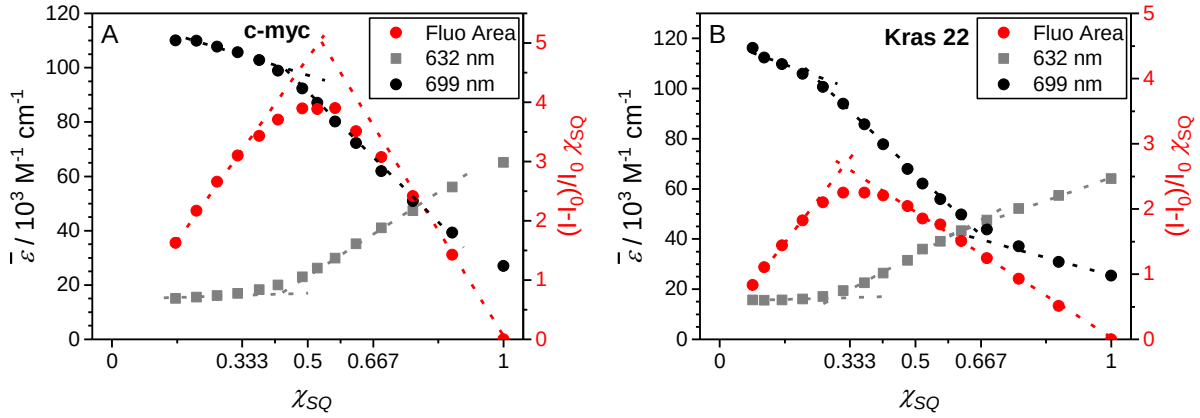

Figure 87. Job's plot for the titration of **CAS-C1** with (A) c-myc and (B) Kras 22 monitored in the absorption at the maximum wavelength of the aggregate (632 nm, grey) and the complex (699 nm, black) and the fluorescence total area (red).

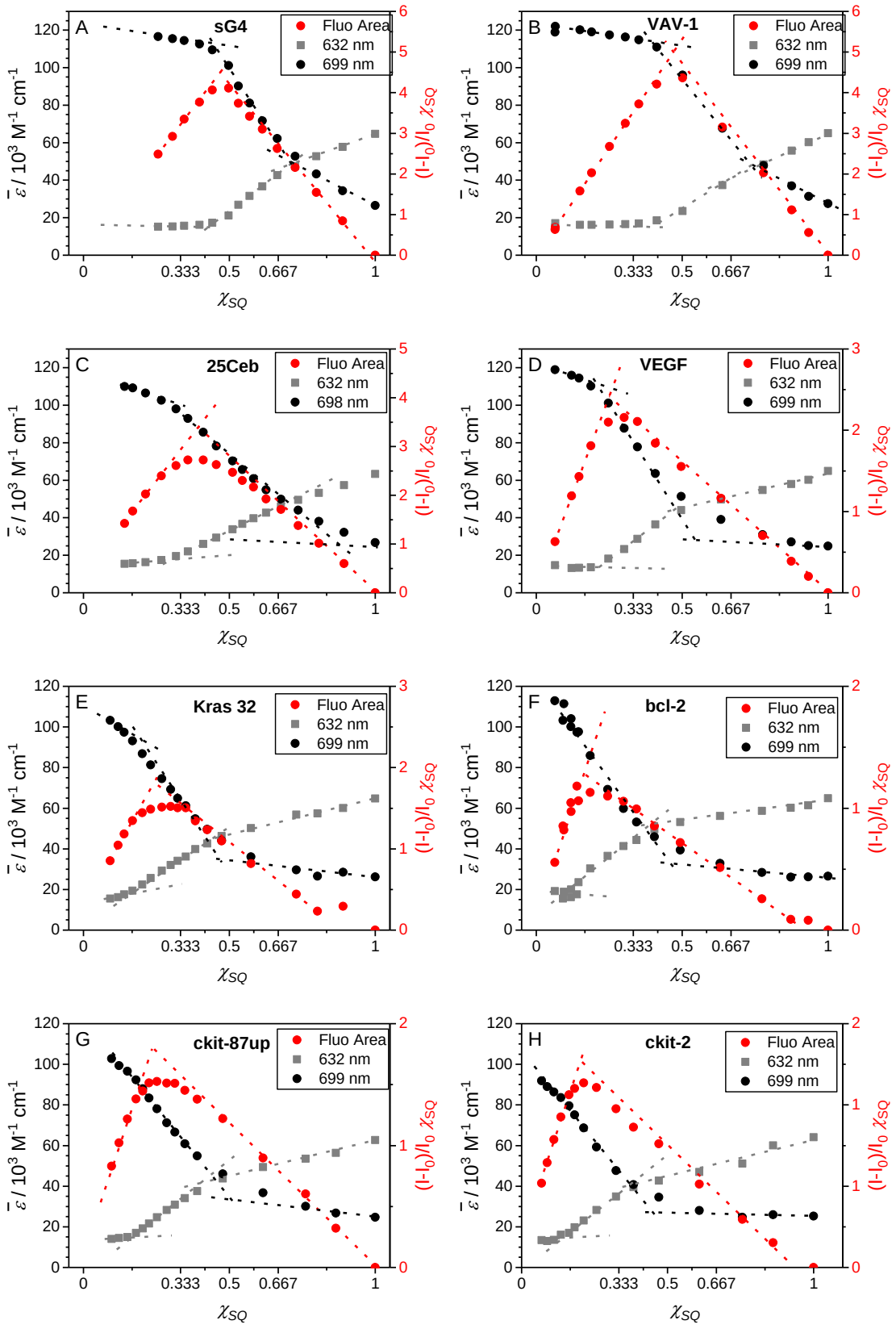

Figure S88. Job's plot for the titration of **CAS-C1** with various G4s (A−H) monitored in the absorption at the maximum wavelength of the aggregate (632 nm, grey) and the complex (699 nm, black) and the fluorescence total area (red).

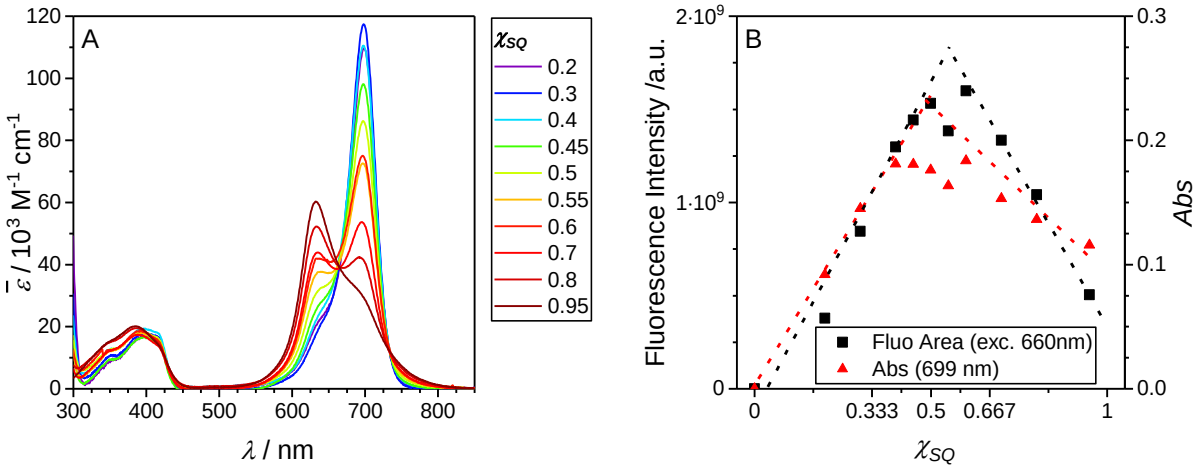

Figure S89. Job's plot by independent experiments obtained by mixing **CAS-C1** and VAV-1 at different ratios with a total concentration ([**CAS-C1**]+[VAV-1] = 4.0 × 10^{-6} M): A) absorption spectra and B) Job´s plot obtained by monitoring the absorption at 699 nm and the fluorescence total area (excitation at 660 nm). (TRIS buffer *c* = 10 mM, pH = 7.2, KCl *c* = 100 mM, 25 °C)

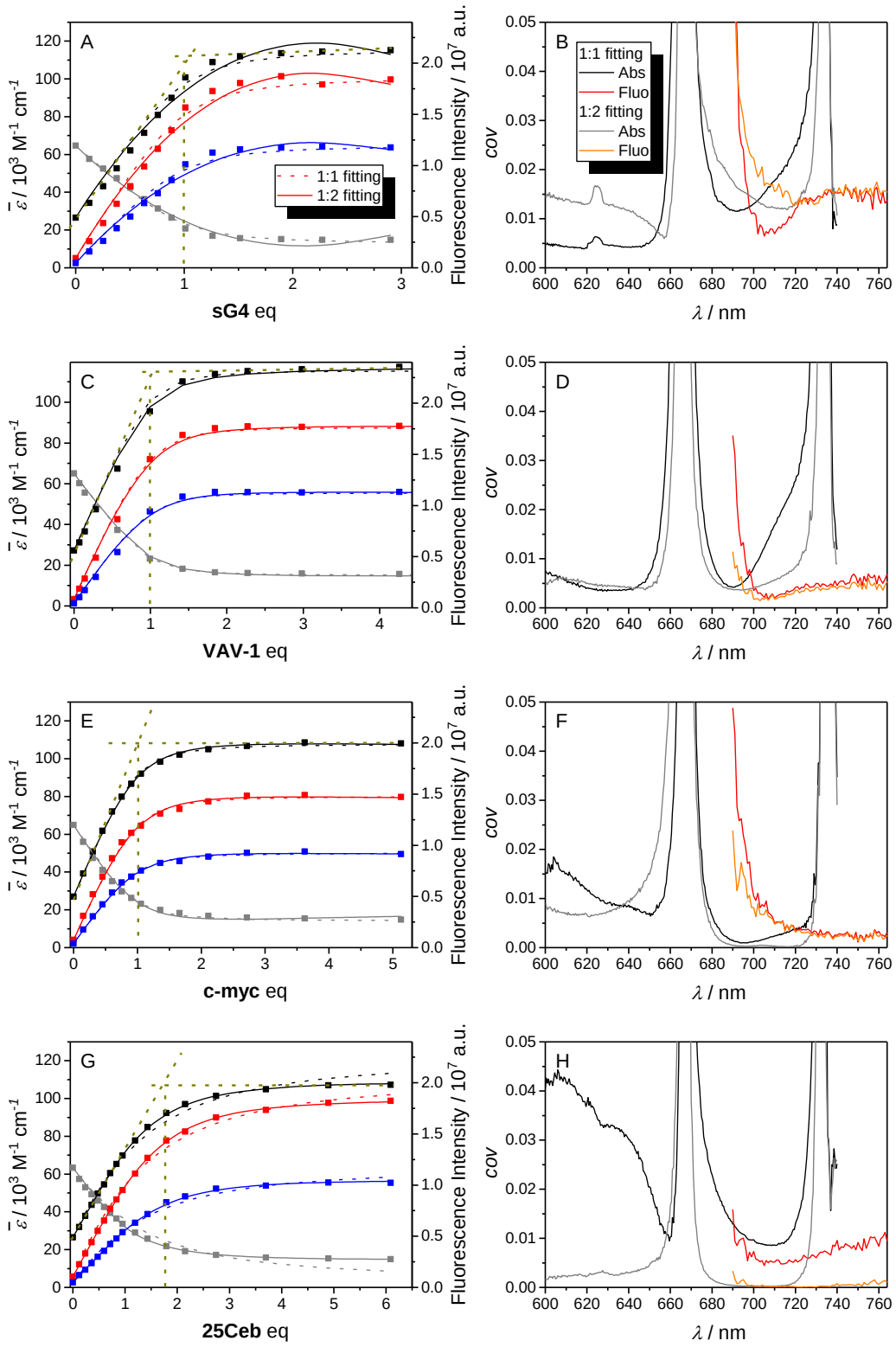

Figure S90 Global fitting of **CAS-C1** titration with (A) sG4, (C) VAV-1, (E) c-myc, (G) 25Ceb monitored in the absorption spectra at 632 nm (aggregate maximum wavelength, grey), 699 nm (complex maximum, black) and in the fluorescence spectra at the maximum emission wavelength (red) and at 740 nm (blue). The fitting is shown for 1:1 (dotted) and 1:2 (filled) binding model. The covariance is shown on the right (B, D, F, H for the respective G4s) for the 1:1 fitting of the absorption (black) and fluorescence (red) data, and the 1:2 fitting (grey for the absorption and orange for the fluorescence).

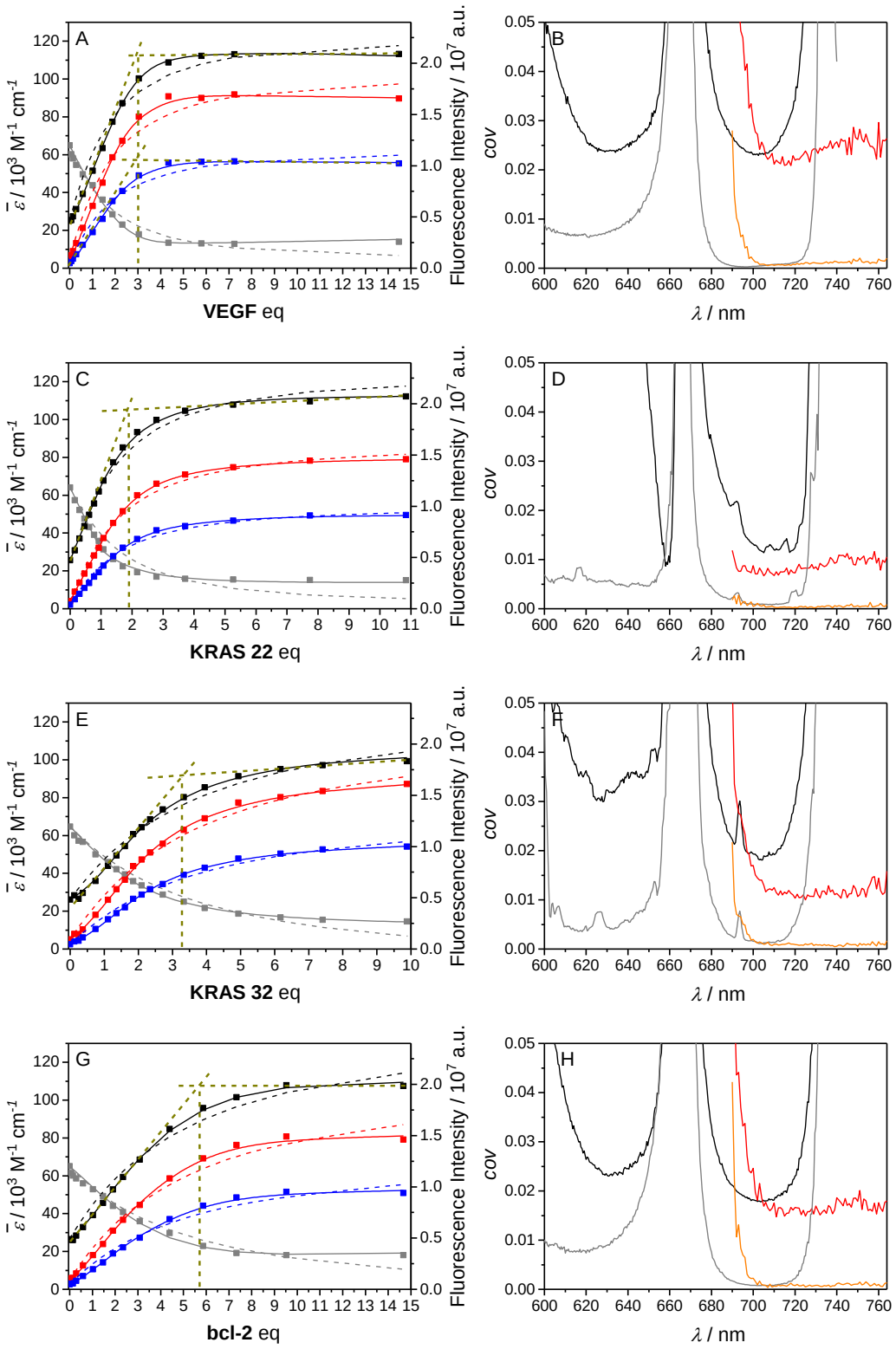

Figure S91. Global fitting of **CAS-C1** titration with (A) VEGF, (C) Kras 22, (E) Kras 32, (G) bcl-2 monitored in the absorption spectra at 632 nm (aggregate maximum wavelength, grey), 699 nm (complex maximum, black) and in the fluorescence spectra at the maximum emission wavelength (red) and at 740 nm (blue). The fitting is shown for 1:1 (dotted) and 1:2 (filled) binding model. The covariance is shown on the right (B, D, F, H for the respective G4s) for the 1:1 fitting of the absorption (black) and fluorescence (red) data, and the 1:2 fitting (grey for the absorption and orange for the fluorescence).

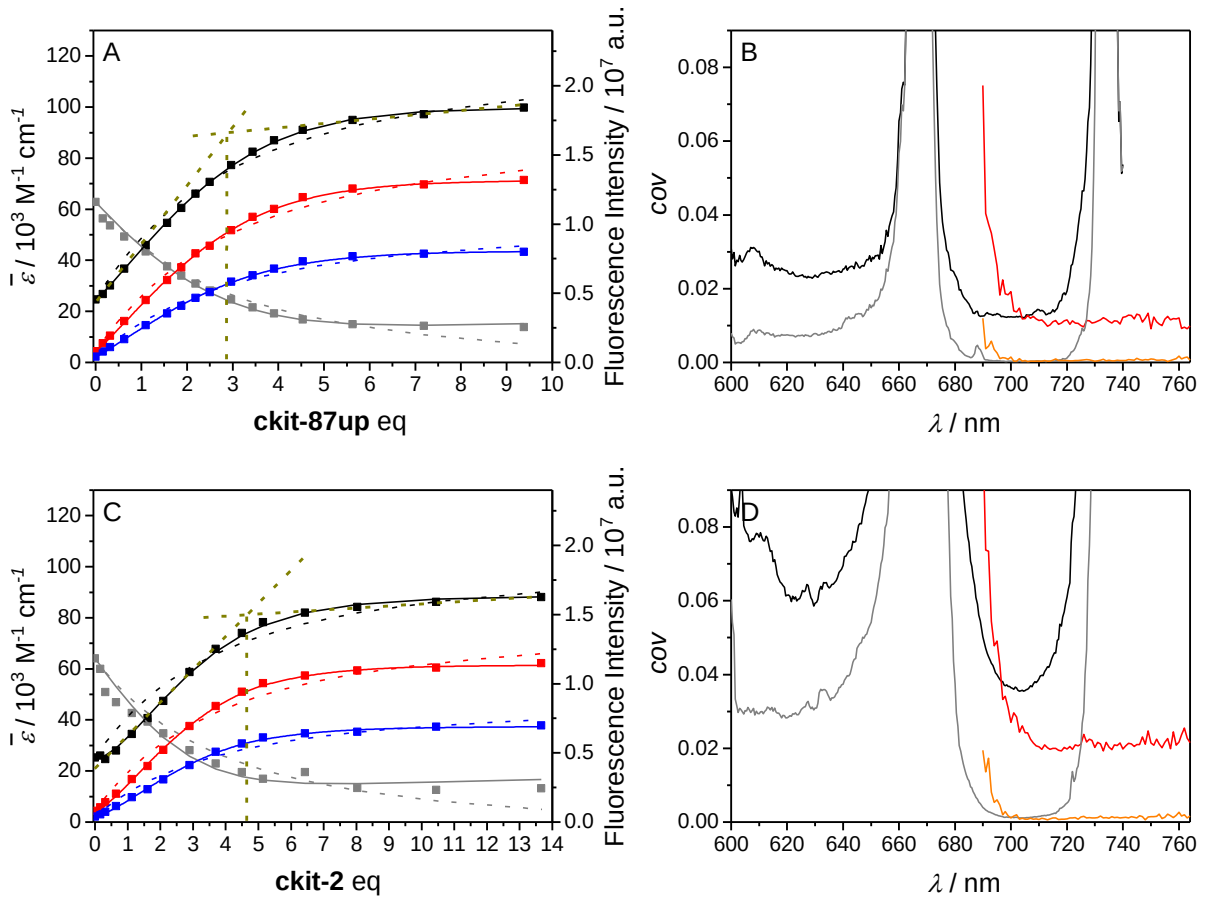

Figure S92. Global fitting of **CAS-C1** titration with (A) ckit-87up, (C) ckit-2 monitored in the absorption spectra at 632 nm (aggregate maximum wavelength, grey), 699 nm (complex maximum, black) and in the fluorescence spectra at the maximum emission wavelength (red) and at 740 nm (blue). The fitting is shown for 1:1 (dotted) and 1:2 (filled) binding model. The covariance is shown on the right (B, D for the respective G4s) for the 1:1 fitting of the absorption (black) and fluorescence (red) data, and the 1:2 fitting (grey for the absorption and orange for the fluorescence).

Competition Titrations

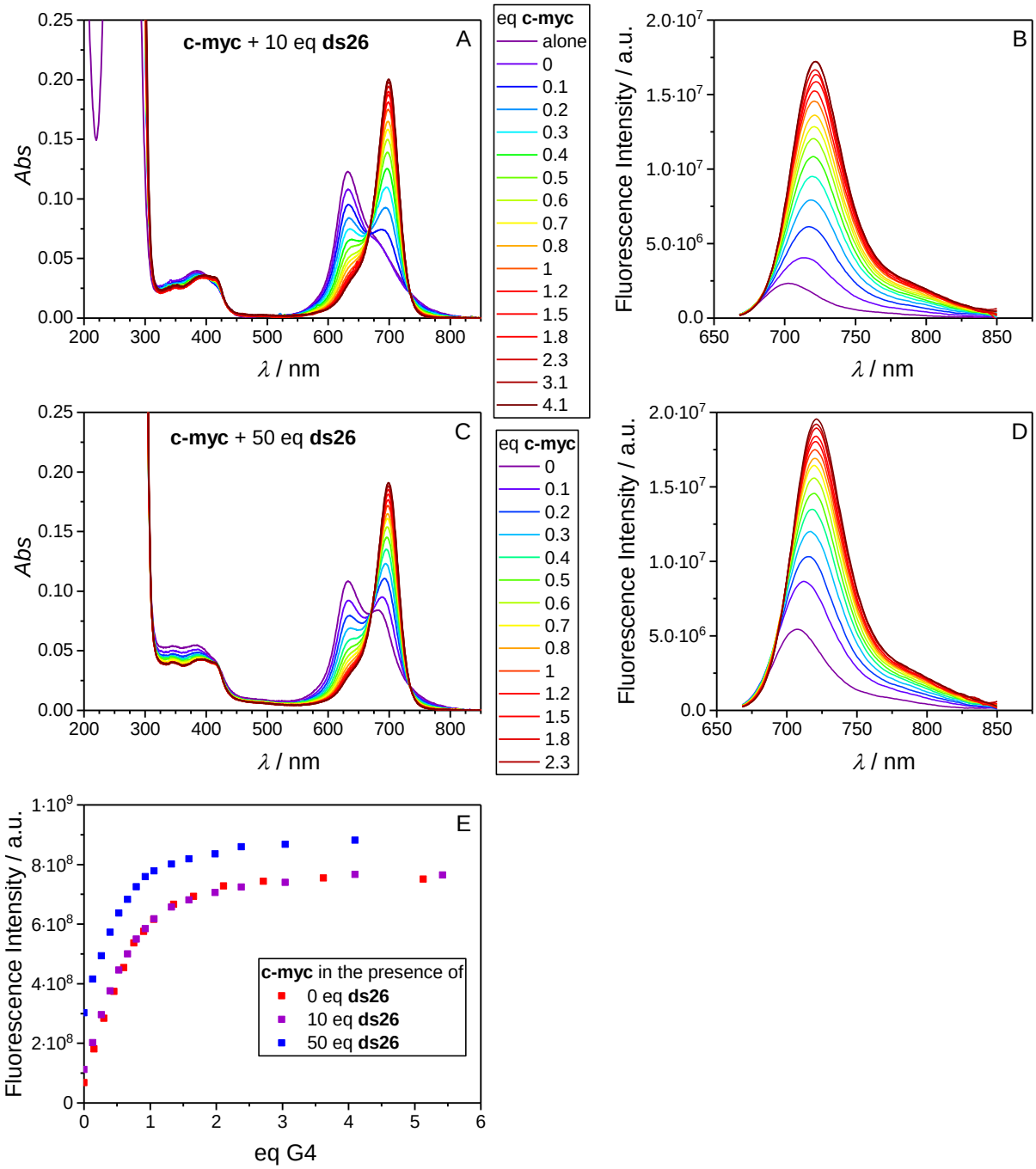

Figure S93. Spectrophotometric (A and C) and fluorimetric (B and D) titration of **CAS-C1** in buffered water solution (1.66×10^{-6} M, TRIS buffer c = 10 mM, pH = 7.2, KCl c = 100 mM) with c-myc (500 μM, buffered solution) at 25 °C in the presence of ds26 DNA: A-B) 10 eq, C-D) 50 eq. E) Comparison of the fluorescence total area (excitation at 660 nm) of the two experiments and the one in the absence of ds26 DNA. (b = 1.00 cm).

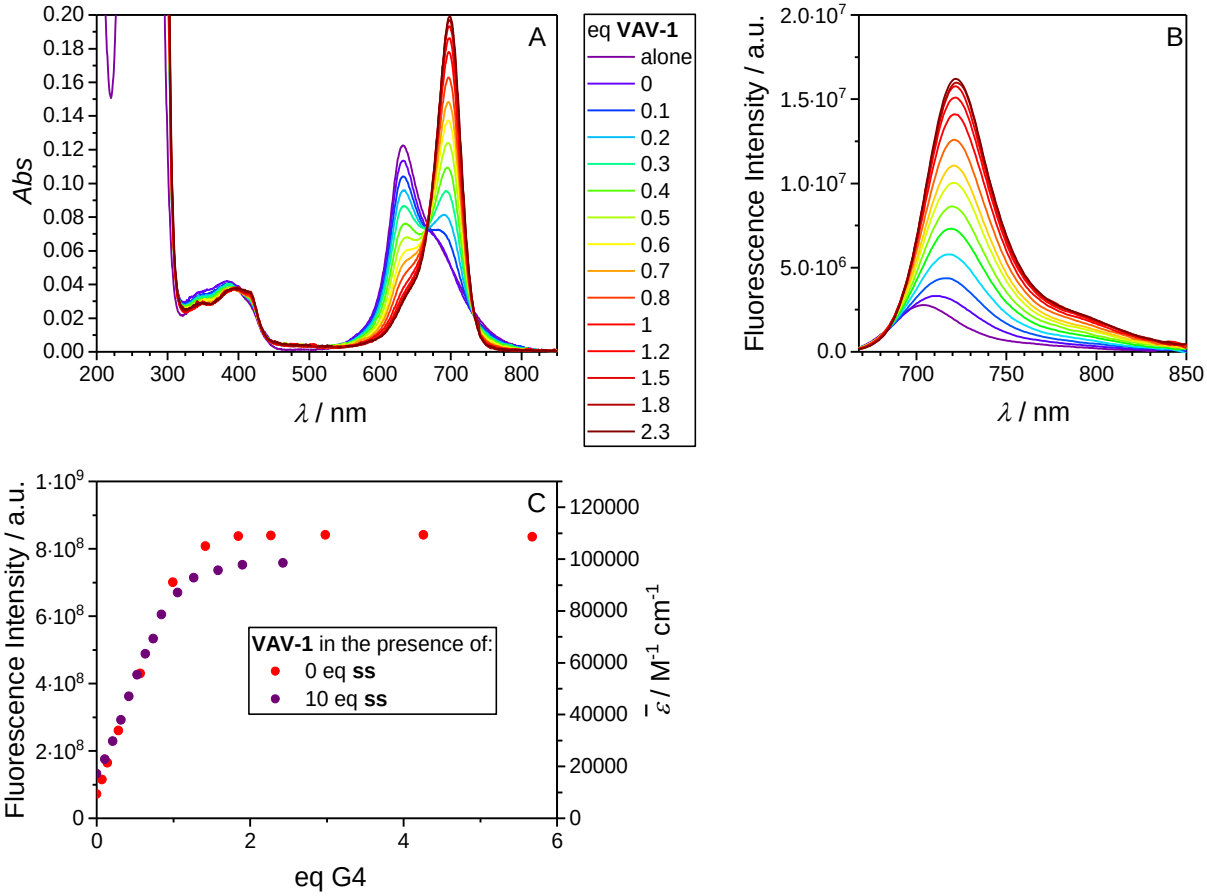

Figure S94. Spectrophotometric (A) and fluorimetric (B) titration of **CAS-C1** in buffered water solution (1.66×10^{-6} M, TRIS buffer c = 10 mM, pH = 7.2, KCl c = 100 mM) with VAV-1 (500 µM, buffered solution) at 25 °C in the presence of 10 eq ds26 DNA. C) Comparison of the fluorescence total area (excitation at 660 nm) of the two experiments and the one in the absence of ds26 DNA. (b = 1.00 cm).

Speciation Analysis

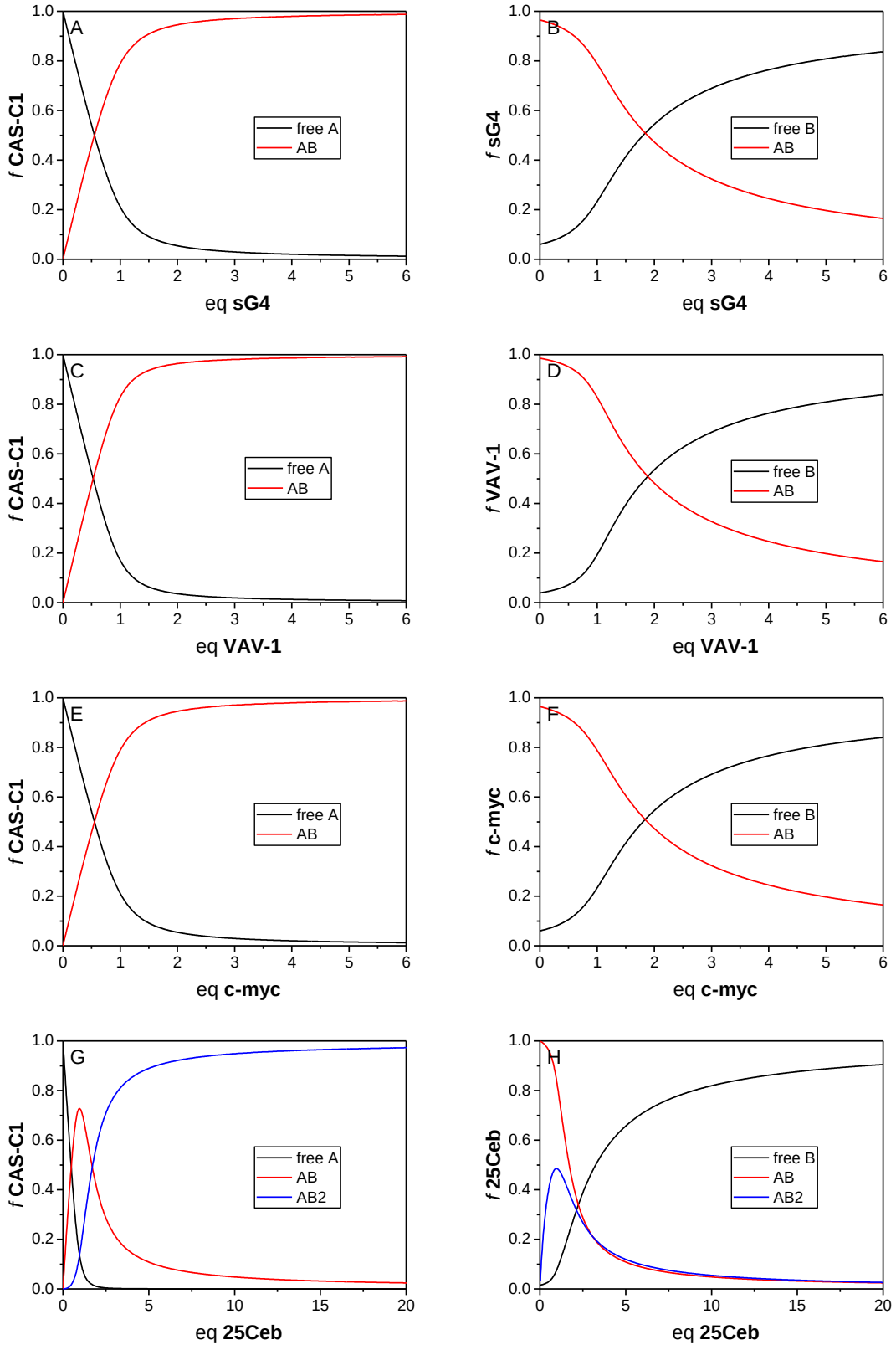

Figure S95. Speciation analysis for the titrations of **CAS-C1** with G4s utilizing the values of K_{11} (and K_{12}, when suitable) obtained by fitting as described in the references.[186,187]

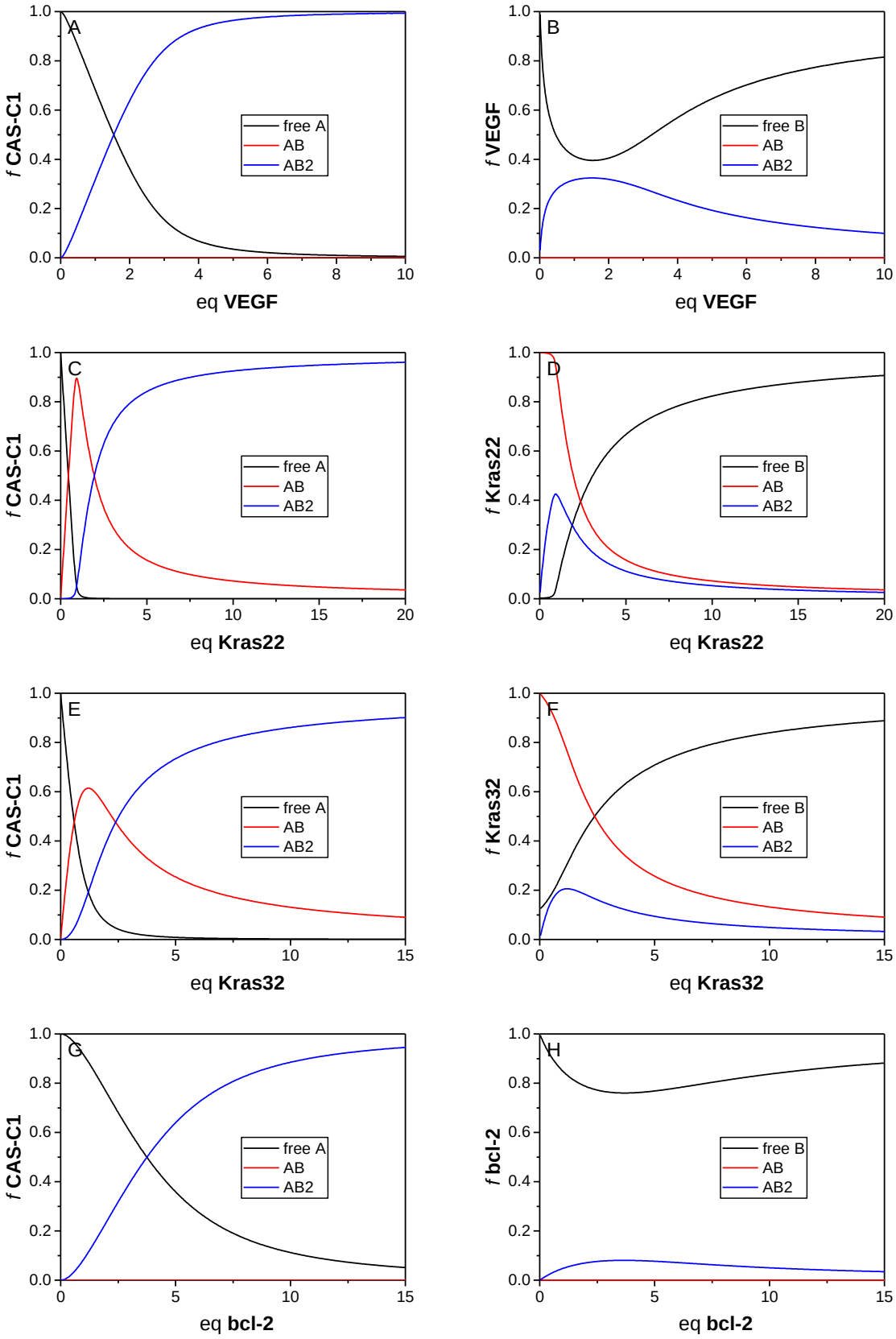

Figure S96. Speciation analysis for the titrations of **CAS-C1** with G4s utilizing the values of K_{11} (and K_{12}, when suitable) obtained by fitting as described in the references.[186,187]

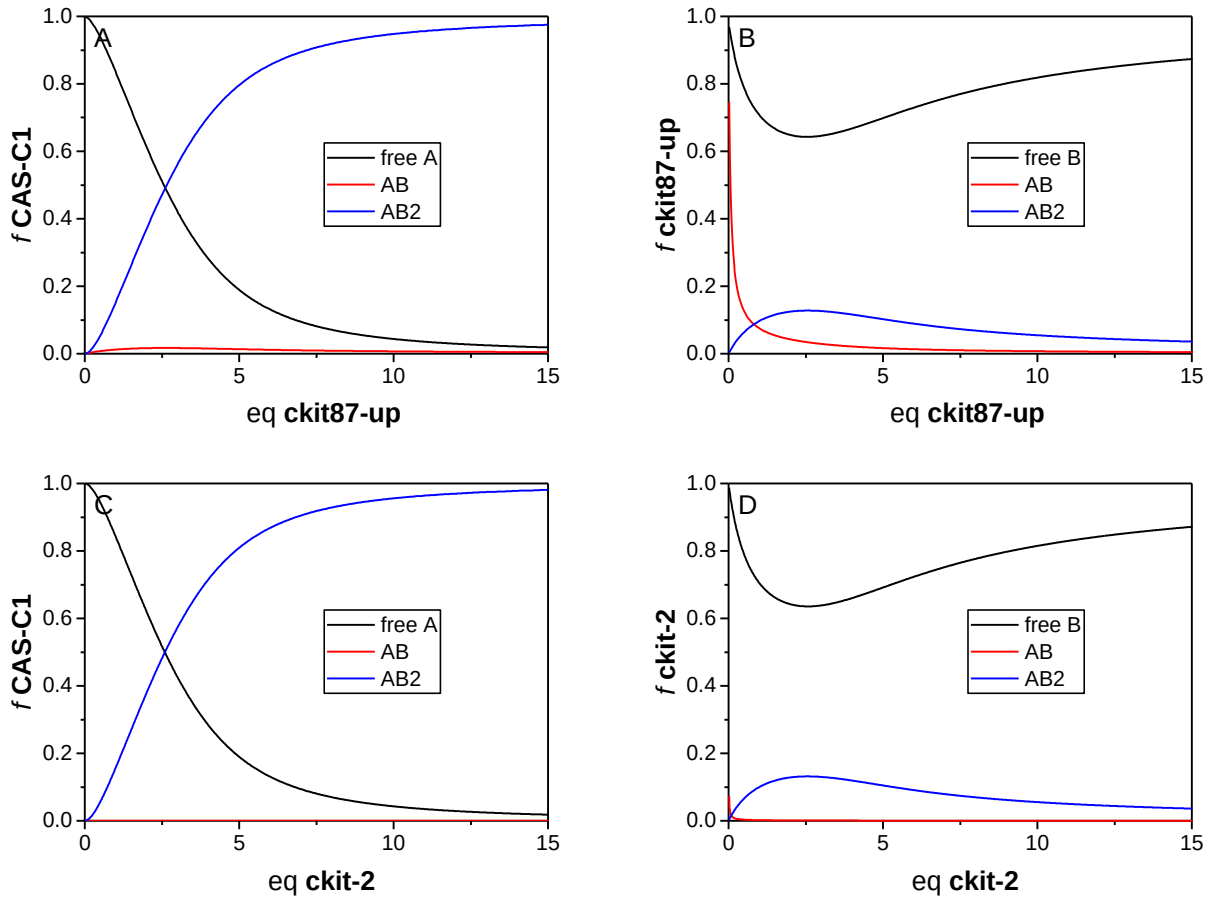

Figure S97. Speciation analysis for the titrations of **CAS-C1** with G4s utilizing the values of K_{11} (and K_{12}, when suitable) obtained by fitting as described in the references.[186,187]

Table S6. Comparison of the structure sequence of structurally related G4 and the binding constant associated to the formation of the 1:1 **CAS-C1**/G4 complexes.

Name	Sequence									K_{11} / 10^6 M^{-1}
KRAS 22	A	**GGG**	C	**GGTG**	T	**GGG**	AATA	**GGG**	AA	270
VAV1		**GGG**	CA	**GGG**	A	**GGG**	AACT	**GGG**		12
c-kit87up	A	**GGG**	A	**GGG**	CGCT	**GGG**	AGGA	**GGG**		10
c-myc	TGA	**GGG**	T	**GGG**	TA	**GGG**	T	**GGG**	TAA	9.7
sG4		**GGG**	T	**GGG**	TA	**GGG**	T	**GGG**		8.1
22AG	A	**GGG**	TTA	**GGG**	TTA	**GGG**	TTA	**GGG**		

9.4.6 Two-Photon Absorption

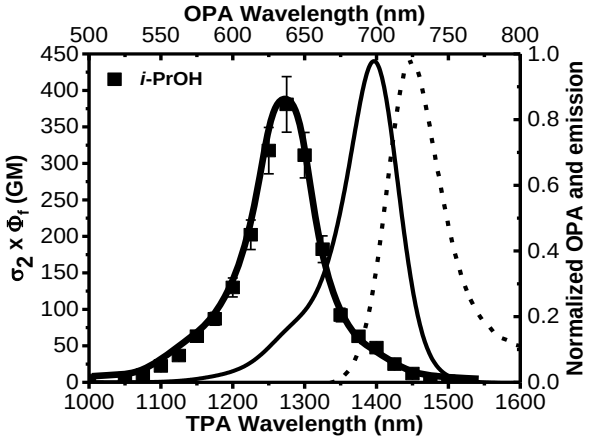

Figure S98. Molecular brightness ($\sigma_2 \times \Phi_{FL}$) plot of **CAS-C1** in *i*-PrOH.

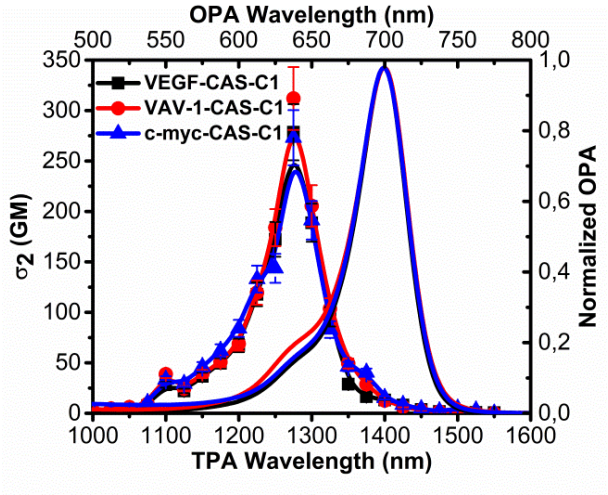

Figure S99. Two-photon absorption cross-section (σ_2) of **CAS-C1** in the presence of VEGF, VAV-1 and c-myc (10 mM Tris, 100 mM K^+, pH 7.2) at molar ratio (r) = 7.

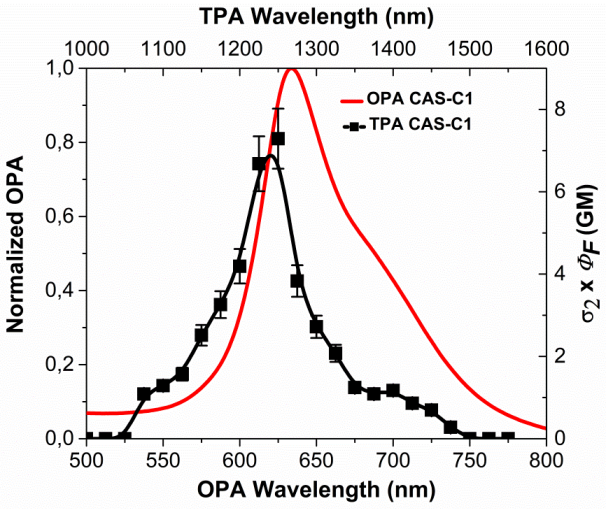

Figure S100. Molecular brightness ($\sigma_2 \times \Phi_{FL}$) plot of **CAS-C1** aggregate (10 mM Tris, 100 mM K^+, pH 7.2).

9.4.7 ECD Spectra

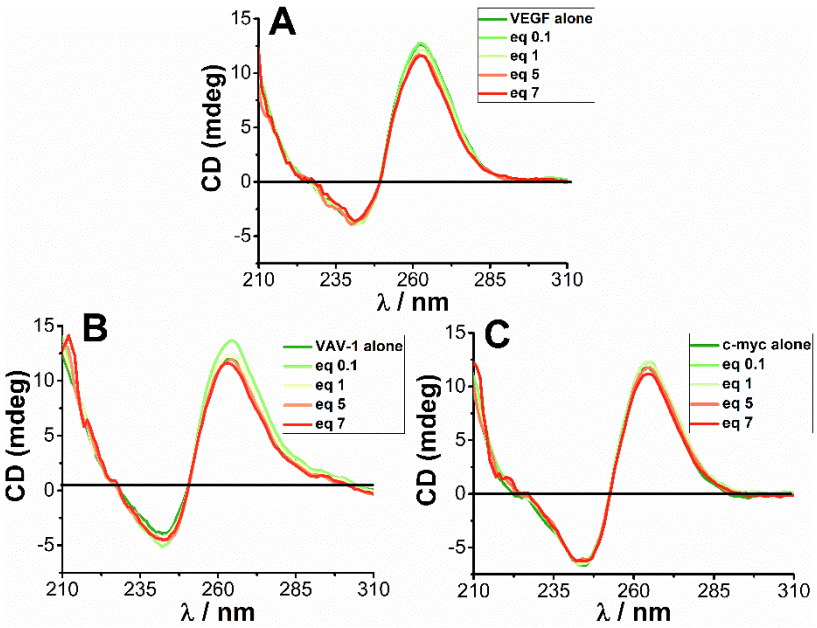

Figure S101. Electronic circular dichroism (ECD) spectra of (A) VEGF, (B) VAV-1 and (C) c-myc in buffered water solution (3×10^{-6} M, TRIS buffer c = 10 mM, pH = 7.2, KCl c = 100 mM) at 25 °C in the absence and presence of **CAS-C1** at different ratios.

9.4.8 NMR and HRMS Spectra of CAS-C1

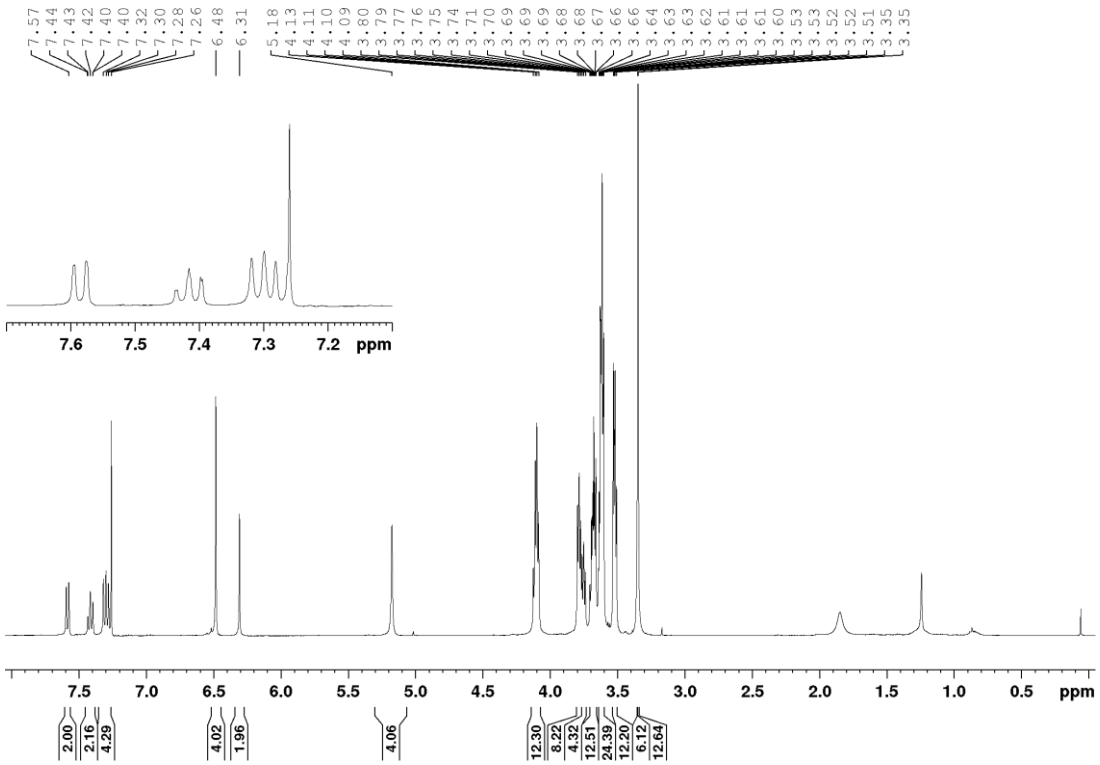

Figure S102. ^{1}H NMR (400 MHz, 298 K) spectrum of **CAS-C1** in $CDCl_3$ (inset: Signals of aromatic protons).

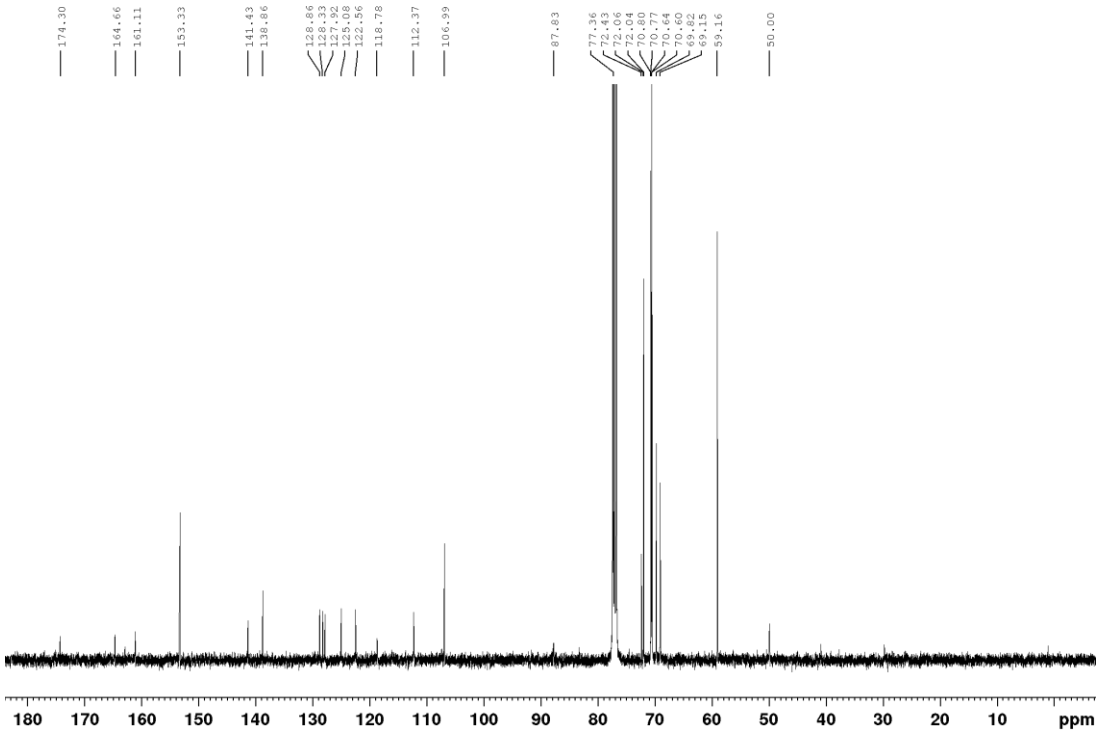

Figure S103. ^{13}C NMR (101 MHz, 298 K) spectrum of **CAS-C1** in $CDCl_3$.

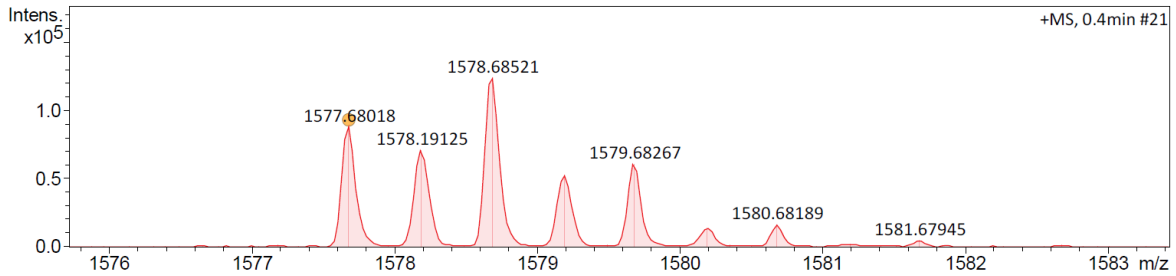

Figure S104. HRMS-ESI spectrum of **CAS-C1** (positive mode, acetonitrile/chloroform).

List of Publications

1. C.-A. Shen, D. Bialas, M. Hecht, V. Stepanenko, K. Sugiyasu, F. Würthner, *Angew. Chem. Int. Ed.* **2021**, DOI: 10.1002/anie.202102183.
2. C.-A. Shen, F. Würthner, *Chem. Commun.* **2020**, *56*, 9878−9881.
3. V. Grande, C.-A. Shen, M. Deiana, M. Dudek, J. Olesiak-Banska, K. Matczyszyn and F. Würthner, *Chem. Sci.* **2018**, *9*, 8375–8381.

Individual Contribution

The co-authors of the publications presented in this cumulative thesis are informed and agree with the reprint as well as with the individual contributions stated below.

Publication: NIR-Emitting Squaraine J-Aggregate Nanosheets, *Chem. Commun.* **2020**, *56*, 9878−9881.

Authors: Chia-An Shen (main author, CAS) and Frank Würthner (corresponding author, FW).

Detailed percentage of contributions from each author to the publication.

Author	**CAS**	**FW**	**∑ in Percent**
Research design	50%	50%	100%
Syntheses	100%	-	100%
Characterization of the compounds	100%	-	100%
Optical investigations	100%	-	100%
Morphology investigations	100%	-	100%
Manuscript writing	80%	20%	100%
Manuscript correction	20%	80%	100%
Coordination of the publication	20%	80%	100%

Publication: Polymorphism in Squaraine Dye Aggregates by Self-Assembly Pathway Differentiation: Panchromatic Tubular Dye Nanorods versus J-Aggregate Nanosheets, *Angew. Chem. Int. Ed.* **2021**, DOI: 10.1002/anie.202102183.

Authors: Chia-An Shen (main author, CAS), David Bialas (corresponding author, DB), Markus Hecht (co-author, MH), Vladimir Stepanenko (co-author, VS), Kazunori Sugiyasu (corresponding author, KS) and Frank Würthner (corresponding author, FW).

Detailed percentage of contributions from each author to the publication.

Author	**CAS**	**DB**	**MH**	**VS**	**KS**	**FW**	**∑ in Percent**
Research design	20%	20%	-	-	20%	40%	100%
Syntheses and characterization of compounds	100%	-	-	-	-	-	100%
Optical investigations	100%	-	-	-	-	-	100%
Morphology investigations (AFM)	-	-	-	100%	-	-	100%
Morphology investigations (WAXS & modeling)	-	-	100%	-	-	-	100%
Elucidation of self-assembly process	30%	10%	10%	-	30%	20%	100%
Theoretical Calculations	-	100%	-	-	-	-	100%
Manuscript writing	50%	30%	-	-	10%	10%	100%
Manuscript correction	20%	50%	-	-	10%	20%	100%
Coordination of the publication	10%	30%	-	-	-	60%	100%

Publication: Selective Parallel G-Quadruplex Recognition by a NIR-to-NIR Two-Photon Squaraine, *Chem. Sci.* **2018**, *9*, 8375–8381.

Authors: Vincenzo Grande (main author, VG), Chia-An Shen (main author, CAS), Marco Deiana (co-author, MDe), Marta Dudek (co-author, MDu), Joanna Olesiak-Banska (co-author, JOB), Katarzyna Matczyszyn (corresponding author, KM) and Frank Würthner (corresponding author, FW).

Detailed percentage of contributions from each author to the publication.

Author	**CAS**	**VG**	**MDe**	**MDu**	**JOB**	**KM**	**FW**	**∑ in Percent**
Research design	15%	15%	10%			20%	40%	100%
Syntheses	100%	-	-	-	-	-	-	100%
Characterization of the compounds	100%	-	-	-	-	-	-	100%
Optical investigations	30%	70%	-	-	-	-	-	100%
G-quadruplex binding studies	-	100%	-	-	-	-	-	100%
Two-photon studies	-	-	40%	30%	30%	-	-	100%
Manuscript writing	10%	50%	15%	5%	5%	5%	10%	100%
Manuscript correction	10%	40%	15%	-	-	10%	25%	100%
Coordination of the publication	-	40%	15%	-	-	15%	30%	100%

Acknowledgements

First and foremost, I would like to express my sincere gratitude to Prof. Dr. **Frank Würthner** for providing me the chance to pursue my PhD degree in his group and the constant guidance, inspirational ideas and valuable inputs throughout my studies. I am also grateful for the opportunities to conduct scientific work with advanced instruments under professional supervision in a mature and outstanding research environment.

Next I would like to thank Prof. Dr. **Kazunori Sugiyasu** for his great patience and guidance not only throughout his stay in Würzburg, but also during the manuscript preparation. I appreciate very much the countless discussions and the always constructive suggestions. The collaboration was a priceless experience.

My special thanks are sent to Dr. **Vincenzo Grande**, my greatest mentor when I first joined the group. I am grateful for his guidance and valuable knowledge for the topic of squaraines and G-quadruplexes. I also appreciate the time he spent to answer my questions, correct my reports/slides, and discuss with me about my projects.

I thank Dr. **David Bialas** for critically reading and correcting the manuscripts and some parts of my thesis, enabling me to improve my writing skills, and I thank him for his time and always being helpful. Moreover, I am very grateful for the theoretical calculations, which greatly assisted my research on squaraine aggregates.

Next, I would like to express my gratitude to Dr. **Matthias Stolte**, who has always been supportive not only for spectroscopic topics, but also for lab organizations. I thank him for reading through the last chapter of this thesis and I am grateful for the fruitful discussions and pleasant cooperation.

I thank Dr. **Chantu R. Saha-Möller** for carefully correcting the supporting information for one of my manuscripts, which allowed me to pay more attention to details during my studies afterwards. Moreover, I would like to thank him for taking care of the lab organizations.

I thank Dr. **Vladimir Stepanenko** for the countless AFM measurements and the constructive advice. It is always pleasant to work with him. Furthermore, I thank Dr. **Michael Büchner** and **Juliane Adelmann** for keeping the operation of mass spectrometry. I would like to show my special thanks to Dr. **Matthias Grüne**, Jun.-Prof. Dr. **Ann-Christin Pöppler**, Ms. **Patricia**

Altenberger, Ms. **Stefanie Schmitt** and all the co-workers at the NMR department for providing technical support, constructive advice, and precious assistances regarding NMR measurements.

I would like to express by deep gratitude toward Ms. **Christiana Toussaint** and Ms. **Eleonore Klaus** for assisting me with documents and contract stuff especially in the beginning of my stay in Germany. I thank Ms. **Sarah Bullnheimer** and the other administrative personnel of the institute for taking care of all the administrative tasks.

I appreciate the technical support including synthesis, general maintenance of lab facilities, chemical ordering…and so on, provided by Ms. **Anja Rausch**, Mr. **Maximilian Roth** and Ms. **Petra Seufert-Baumbach** in the IOC, and Mr. **Joachim Bialas**, Mr. **Julius Albert**, Ms. **Astrid Kudzus**, Ms. **Jennifer Begall**, Ms. **Ana-Maria Krause** and Ms. **Olga Anhalt** in the CNC. The research could not have been successful without them. Additionally, I would like to thank Ms. **Olga Anhalt** for the nice cooperation with GPC maintenance.

I am grateful for my mentors and co-workers: Dr. **Bartolome Soberats**, Dr. **Pradeep Peethambaran Nair Syamala**, Dr. **Meike Sapotta**, who guided and supported me greatly in every aspect with their knowledge and experience throughout my studies. Moreover, I appreciate the precious help from Dr. **Markus Hecht** for the modeling and X-ray experiments.

Additionally, I thank Mr. **Alexander Schulz**, Mr. **Tim Schlossarek**, Ms. **Jessica Rühe** and Ms. **Carina Mützel** for correcting various parts of this thesis.

Special thanks to my practical students: Mr. **Jonas Wolf**, Ms. **Isabelle Böswald**, Mr. **Haopeng Gao**, Ms. **Lena Breitschwerdt** and Ms. **Alexandra Phillipps**. It was my pleasure to work with them and I appreciate their support regarding syntheses.

I would like to express my hearty gratitude to Dr. **Vincenzo Grande**, Dr. **Pradeep Peethambaran Nair Syamala** and Mr. **Roberto Sánchez Naya** for the genuine friendship and the time we spent together during breaks and outside the lab. I thank Ms. **Natalie Schäfer**, who was my first lab "neighbor", Mr. **Alexander Schulz** and Dr. **Meike Sapotta**, who were my IOC neighbors, for sharing my ups and downs and providing pleasant working atmosphere. I thank Ms. **Carina Mützel**, Ms. **Anja Rausch** and Dr. **Rodger Rausch**, for the delightful lunch breaks and great assistance inside/outside the lab. I thank all the members of the Würthner group, the Beuerle group as well as the Nowak-Król group for the nice atmosphere and support over the past years.

Finally, I thank my friends who have been extremely understanding and encouraging. I especially would like to thank **Austin** wholeheartedly for his companion and always being ready to help. He made my PhD life a lot easier and I could not have made it without his support. Last but not least, I thank my family, especially my **parents**, for their unconditional support during my studies, which has always been my motivation and energy to move on.

References

1. U. Girreser, D. Giuffrida, F. H. Kohnke, J. P. Mathias, D. Philp, J. F. Stoddart, *Pure Appl. Chem.* **1993**, *65*, 119–125.
2. J. Wu, L. Gherghel, M. D. Watson, J. Li, Z. Wang, C. D. Simpson, U. Kolb, K. Müllen, *Macromolecules* **2003**, *36*, 7082–7089.
3. F. Mercuri, M. Baldoni, A. Sgamellotti, *Nanoscale*, **2012**, *4*, 369–379.
4. J. W. Steed, J. L. Atwood, *Supramolecular Chemistry, 2nd Ed.*; Wiley & Sons: Chichester, **2009**.
5. H.-D. Yu, M. D. Regulacio, E. Ye, M.-Y. Han, *Chem. Soc. Rev.* **2013**, 42, 6006–6018.
6. T. Ito, S. Okazaki, *Nature* **2000**, *406*, 1027–1031.
7. A. Biswas, I. S. Bayer, A. S. Biris, T. Wang, E. Dervishi, F. Faupel, *Adv. Colloid Interface Sci.* **2012**, *170*, 2–27.
8. J Saghaei, A. Fallahzadeh, T. Saghaei, *Sens. Actuators, A* **2016**, *247*, 150–155.
9. T. M. Swager, *ACS Macro Lett.* **2012**, *1*, 3–5.
10. V. Balzani, A. Credi, M. Venturi, *Chem. Eur. J.* **2002**, *8*, 5524–5532.
11. (a) R. P. Feynman, *Eng. Sci.* **1960**, *23*, 22; (b) R. P. Feynman, *Saturday Rev.* **1960**, *43*, 45.
12. G. M. Whitesides, B. Grzybowski, *Science* **2002**, *295*, 2418–2421.
13. J. M. Lehn, *Angw. Chem. Int. Ed. Engl.* **1988**, *27*, 89–112.
14. J. M. Lehn, *Pure Appl. Chem.* **1978**, *50*, 871–892.
15. (a) R. G. Saer, R. E. Blankenship, *Biochem. J.* **2017**, *474*, 2107–2131; (b) S. Bahatyrova, R. N. Frese, C. A. Siebert, J. D. Olsen, K. O. van der Werf, R. van Grondelle, R. A. Niederman, P. A. Bullough, C. Otto, C. N. Hunter, *Nature* **2004**, *430*, 1058–1062.
16. (a) T. Nozawa, K. Ohtomo, M. Suzuki, Y. Morishita, M. T. Madigan, *Bull. Chem. Soc. Jpn.* **1993**, *66*, 231–237; (b) Y. Saga, H. Tamiaki, *J. Biosci. Bioeng.* **2006**, *102*, 118–123.
17. (a) R. Khurana, A. S. Kakatkar, S. Chatterjee, N. Barooah, A. Kunwar, A. C. Bhasikuttan, J. Mohanty, *Front. Chem.* **2019**, *7*, 452; (b) E. A. Koposova, A. Offenhäusser, Y. E. Ermolenko, Y. G. Mourzina, *Front. Chem.* **2019**, *7*, 351; (c) T. Fukui, S. Kawai, S. Fujinuma, Y. Matsushita, T. Yasuda, T. Sakurai, S. Seki, M. Takeuchi, K. Sugiyasu, *Nat. Chem.* **2017**, *9*, 493–499.

18. (a) V. Huber, M. Lysetska, F. Würthner, *Small* **2007**, *3*, 1007–1014; (b) S. Sengupta, D. Ebeling, S. Patwardhan, X. Zhang, H. von Berlepsch, C. Böttcher, V. Stepanenko, S. Uemura, C. Hentschel, H. Fuchs, F. C. Grozema, L. D. A. Siebbeles, A. R. Holzwarth, L. Chi, F. Würthner, *Angew. Chem. Int. Ed.* **2012**, *51*, 6378–6382; *Angew. Chem.* **2012**, *124*, 6484–6488.

19. H. Kar, D. W. Gehrig, N. K. Allampally, G. Fernández, F. Laquai, S. Ghosh, *Chem. Sci.* **2016**, *7*, 1115–1120.

20. (a) H. Wang, T. E. Kaiser, S. Uemura, F. Würthner, *Chem. Commun.* **2008**, 1181–1183; (b) F. Würthner, T. E. Kaiser, C. R. Saha-Möller, *Angew. Chem. Int. Ed.* **2011**, *50*, 3376–3410; *Angew. Chem.* **2011**, *123*, 3436–3473; (c) F. Würthner, C. R. Saha-Möller, B. Fimmel, S. Ogi, P. Leowanawat, D. Schmidt, *Chem. Rev.* **2016**, *116*, 962–1052.

21. L. Brunsveld, B. J. B. Folmer, E. W. Meijer, R. P. Sijbesma, *Chem. Rev.* **2001**, *101*, 4071–4098.

22. S. Sreejith, P. Carol, P. Chithra, A. Ajayaghosh, *J. Mater. Chem.* **2008**, *18*, 264–274.

23. (a) L. Beverina, P. Salice, *Eur. J. Org. Chem.* **2010**, *7*, 1207–1225; (b) K. Ilina, W. M. MacCuaig, M. Laramie, J. N. Jeouty, L. R. McNally, M. Henary, *Bioconjugate Chem.* **2020**, *31*, 194–213.

24. J. J. Gassensmith, J. M. Baumes, B. D. Smith, *Chem. Commun.* **2009**, *42*, 6329–6338.

25. M. Gsänger, E. Kirchner, M. Stolte, C. Burschka, V. Stepanenko, J. Pflaum, F. Würthner, *J. Am. Chem. Soc.* **2014**, *136*, 2351–2362.

26. (a) U. Mayerhöffer, K. Deing, K. Gruss, H. Braunschweig, K. Meerholz, F. Würthner, *Angew. Chem. Int. Ed.* **2009**, *48*, 8776–8779; *Angew. Chem.* **2009**, *121*, 8934–8937; (b) K. C. Deing, U. Mayerhöffer, F. Würthner, K. Meerholz, *Phys. Chem. Chem. Phys.* **2012**, *14*, 8328–8334; (c) X. Xiao, G. D. Wei, S. Y. Wang, J. D. Zimmerman, C. K. Renshaw, M. E. Thompson, S. R. Forrest, *Adv. Mater.* **2012**, *24*, 1956–1960; (d) T. Maeda, T. Tsukamoto, A. Seto, S. Yagi, H. Nakazumi, *Macromol. Chem. Phys.* **2012**, *213*, 2590–2597; (e) G. Chen, H. Sasabe, W. Lu, X.-F. Wang, J. Kido, Z. Hong, Y. Yang, *J. Mater. Chem. C* **2013**, *1*, 6547−6552.

27. U. Mayerhöffer, M. Gsänger, M. Stolte, B. Fimmel, F. Würthner, *Chem. Eur. J.* **2013**, *19*, 218–232.

28. U. Mayerhöffer, F. Würthner, *Angew. Chem. Int. Ed.* **2012**, *51*, 5615–5619; *Angew. Chem.* **2012**, *124*, 5713–5717.

29. (a) F. Würthner, S. Yao, U. Beginn, *Angew. Chem. Int. Ed.* **2003**, *42*, 3247−3250; *Angew. Chem.* **2003**, *115*, 3368–3371; (b) S. Yao, U. Beginn, T. Gress, M. Lysetska, F. Würthner, *J. Am. Chem. Soc.* **2004**, *126*, 8336−8348.

30. F. Würthner, *Acc. Chem. Res.* **2016**, *49*, 868−876.

31. U. Mayerhöffer, B. Fimmel, F. Würthner, *Angew. Chem. Int. Ed.* **2012**, *51*, 164–167; *Angew. Chem.* **2012**, *124*, 168–171.

32. B. Jin, X. Zhang, W. Zheng, X. Liu, J. Zhou, N. Zhang, F. Wang, D. Shangguan, *Anal. Chem.* **2014**, *86*, 7063–7070.

33. V. Grande, F. Doria, M. Freccero, F. Würthner, *Angew. Chem. Int. Ed.* **2017**, *56*, 7520–7524; *Angew. Chem.* **2017**, *129*, 7628–7632.

34. S. Burge, G. N. Parkinson, P. Hazel, A. K. Todd, S. Neidle, *Nucleic. Acids. Res.* **2006**, *34*, 5402–6415.

35. A. Treibs, K. Jacob, *Angew. Chem. Int. Ed.* **1965**, *4*, 694; *Angew. Chem.* **1965**, *77*, 680–681.

36. J. Griffiths, S. Park, *Tetrahedron Lett.* **2002**, *43*, 7669–7671.

37. A. L. Tatarets, I. A. Fedyunyaeva, E. Terpetschnig, L.D. Patsenker, *Dyes Pigm.* **2005**, *64*, 125−134.

38. L. Beverina, R. Ruffo, C. M. Mari, G. A. Pagani, M. Sassi, F. De Angelis, S. Fantacci, J.-H. Yum, M. Grätzel, M. K. Nazeeruddin, *ChemSusChem* **2009**, *2*, 621–624.

39. C. Zhong, D. Bialas, C. J. Collison, F. C. Spano, *J. Phys. Chem. C* **2019**, *123*, 18734–18745.

40. G. Bachteler, K.-H. Drexhage, J. Arden-Jacob, K.-T. Han, M. Köllner, R. Müller, M. Sauer, S. Seeger, J. Wolfrum, *J. Lumin.* **1994**, *62*, 101–108.

41. X. Peng, F. Song, E. Lu, Y. Wang, W. Zhou, J. Fan, Y. Gao, *J. Am. Chem. Soc.* **2005**, *127*, 4170–4171.

42. D. Yao, Y. Wang, R. Zou, K. Bian, P. Liu, S. Shen, W. Yang, B. Zhang, D. Wang, *ACS Appl. Mater. Interfaces* **2020**, *12*, 4276–4284.

43. (a) E. G. McRae, M. Kasha, *J. Chem. Phys.* **1958**, *28*, 721–722; (b) M. Kasha, H. R. Rawls, M. A. El-Bayoumi, *Pure Appl. Chem.* **1965**, *11*, 371–392.

44. S. F. Völker, S. Uemura, M. Limpinsel, M. Mingebach, C. Deibel, V. Dyakonov, C. Lambert, *Macromol. Chem. Phys.* **2010**, *211*, 1098−1108.

45. S. F. Völker, C. Lambert, *Chem. Mater.* **2012**, *24*, 2541−2553.

46. C. Brüning, E. Welz, A. Heilos, V. Stehr, C. Walter, B. Engels, S. F. Völker, C. Lambert, V. Engel, *J. Phys. Chem. C* **2015**, *119*, 6174–6180.

47. S. F. Völker, A. Schmiedel, M. Holzapfel, K. Renziehausen, V. Engel, C. Lambert, *J. Phys. Chem. C* **2014**, *118*, 17467–17482.
48. C. A. Hunter, J. K. M. Sanders, *J. Am. Chem. Soc.* **1990**, *112*, 5525–5534.
49. C. A. Hunter, K. R. Lawson, J. Perkins, C. J. Urch, *J. Chem. Soc. Perkin Trans. 2* **2001**, 651–669.
50. Z. Chen, A. Lohr, C. R. Saha-Möller, F. Würthner, *Chem. Soc. Rev.* **2009**, *38*, 564–584.
51. K.-Y. Law, C. C. Chen, *J. Phys. Chem.* **1989**, *93*, 2533–2538.
52. K. Liang, K.-Y. Law, D. G. Whitten, *J. Phys. Chem.* **1994**, *98*, 13379–13384.
53. H. Chen, K.-Y. Law, D. G. Whitten, *J. Phys. Chem.* **1996**, *100*, 5949–5955.
54. A. J. McKerrow, E. Buncel, P. M. Kazmaier, *Can. J. Chem.* **1995**, *73*, 1605–1615.
55. K. Jyothish, M. Hariharan, D. Ramaiah, *Chem. Eur. J.* **2007**, *13*, 5944–5951.
56. U. Mayerhöffer, F. Würthner, *Chem. Sci.* **2012**, *3*, 1215–1220.
57. J. Li, B. Li, X. Li, J. Tang, L. Jiang, *Thin Solid Films* **1996**, *287*, 247–251.
58. M. Stanescu, H. Samha, J. Perlstein, D. G. Whitten, *Langmuir* **2000**, *16*, 275–281.
59. C. Geiger, M. Stanescu, L. Chen, D. G. Whitten, *Langmuir* **1999**, *15*, 2241–2245.
60. J. Wojtyk, A. McKerrow, P. Kazmaier, E. Buncel, *Can. J. Chem.* **1999**, *77*, 903–912.
61. H. Chen, M. S. Farahat, K-Y. Law, D. G. Whitten, *J. Am. Chem. Soc.* **1996**, *118*, 2584–2594.
62. S. Das, K. G. Thomas, K. J. Thomas, V. Madhavan, D. Liu, P. V. Kamat, M. V. George, *J. Phys. Chem.* **1996**, *100*, 17310–17315.
63. R. S. Stoll, N. Severin, J. P. Rabe, S. Hecht, *Adv. Mater.* **2006**, *18*, 1271–1275.
64. Y. Xu, Z. Li, A. Malkovskiy, S. Sun, Y. Pang, *J. Phys. Chem. B* **2010**, *114*, 8574–8580.
65. Y. Xu, A. Malkovskiy, Q. Wang, Y. Pang, *Org. Biomol. Chem.* **2011**, *9*, 2878–2884.
66. X. Fan, Q. He, S. Sun, H. Li, Y. Pei, Y. Xu, *Chem. Commun.* **2016**, *52*, 1178–1181.
67. Z. Yan, S. Guang, H. Xu, X. Su, X. Ji, X. Liu, *RSC Adv.* **2013**, *3*, 8021–8027.
68. S. Yefimova, A. Lebed, A. Sorokin, G. Guralchuk, I. Borovoy, Y. Malyukin, *J. Mol. Liq.* **2012**, *165*, 113–118.
69. Y. Zhang, B. Kim, S. Yao, M. V. Bondar, K. D. Belfield, *Langmuir* **2013**, *29*, 11005–11012.
70. T. Liu, X. Liu, Y. Zhang, M. V. Bondar, Y. Fang, K. D. Belfield, *Eur. J. Org. Chem.* **2018**, 4095–4102.
71. E. Arunkumar, P. Chithra, A. Ajayaghosh, *J. Am. Chem. Soc.* **2004**, *126*, 6590–6598.
72. S. Yagi, Y. Hyodo, M. Hirose, H. Nakazumi, Y. Sakurai, A. Ajayaghosh, *Org. Lett.* **2007**, *9*, 1999–2002.

73. A. Ajayaghosh, P. Chithra, R. Varghese, *Angew. Chem. Int. Ed.* **2007**, *46*, 230–233; *Angew. Chem.* **2007**, *119*, 234–237.

74. A. Ajayaghosh, P. Chithra, R. Varghese, K. P. Divya, *Chem. Commun.* **2008**, 969–971.

75. G. Hong, A. L. Antaris, H. Dai, *Nat. Biomed. Eng.* **2017**, *1*, 0010.

76. F.-P. Gao, Y.-X. Lin, L.-L. Li, Y. Liu, U. Mayerhöffer, P. Spenst, J.-G. Su, J.-Z. Li, F. Würthner, H. Wang, *Biomaterials* **2014**, *35*, 1004–1014.

77. S. Sreejith, J. Joseph, M. Lin, N. V. Menon, P. Borah, H. J. Ng, Y. X. Loong, Y. Kang, S. W.-K. Yu, Y. Zhao, *ACS Nano* **2015**, *9*, 5695–5704.

78. K. Sou, L. Y. Chan, S. Arai, C.-L. K. Lee, *Sci. Rep.* **2019**, *9*, 17991.

79. F.-F. An, Z.-J. Deng, J. Ye, J.-F. Zhang, Y.-L. Yang, C.-H. Li, C.-J. Zheng, X.-H. Zhang, *ACS Appl. Mater. Interfaces* **2014**, *6*, 17985–17992.

80. D. Zhang, Y.-X. Zhao, Z.-Y. Qiao, U. Mayerhöffer, P. Spenst, X.-J. Li, F. Würthner, H. Wang, *Bioconjugate Chem.* **2014**, *25*, 2021–2029.

81. P. Sun, Q. Wu, X. Sun, H. Maio, W. Deng, W. Zhang, Q. Fan, W. Huang, *Chem. Commun.* **2018**, *54*, 13395–13398.

82. L. V. Wang, S. Hu, *Science* **2012**, *335*, 1458–1462.

83. J. F. Lovell, C. S. Jin, E. Huynh, H. Jin, C. Kim, J. L. Rubinstein, W. C. W. Chan, W. Cao, L. V. Wang, G. Zheng, *Nat. Mater.* **2011**, *10*, 324–332.

84. T. E. Kaiser, H. Wang, V. Stepanenko, F. Würthner, *Angew. Chem. Int. Ed.* **2007**, *23*, 4310–4319; *Angew. Chem.* **2007**, *119*, 5637–5640.

85. H. Nakazumi, T. Ohta, H. Etoh, T. Uno, C. L. Colyer, Y. Hyodo, S. Yagi, *Synth. Met.* **2005**, *153*, 33–36.

86. K. D. Volkova, V. B. Kovalska, A. L. Tatarets, L. D. Patsenker, D. V. Kryvorotenko, S. M. Yarmoluk, *Dyes Pigm.* **2007**, *72*, 285–292.

87. Y. Xu, B. Li, L. Xiao, W. Li, C. Zhang, S. Sun, Y. Pang, *Chem. Commun.* **2013**, *49*, 7732–7734.

88. X. Zhang, Y. Wei, T. Bing, X. Liu, N. Zhang, J. Wang, J. He, B. Jin, D. Shangguan, *Sci. Rep.* **2017**, *7*, 4766.

89. V. S. Jisha, K. T. Arun, M. Hariharan, D. Ramaiah, *J. Am. Chem. Soc.* **2006**, *128*, 6024–6025.

90. K. Iida, S. Majima, T. Nakamura, H. Seimiya, K. Nagasawa, *Molecules* **2013**, *18*, 4328–4341.

91. S. Das, T. L. Thanulingam, K. G. Thomas, P. V. Kamat, M.V. George, *J. Phys. Chem.* **1993**, *97*, 13620–13624.

92. S. Alex, M. C. Basheer, K. T. Arun, D. Ramaiah, S. Das, *J. Phys. Chem. A* **2007**, *111*, 3226–3230.

93. T. E. Kaiser, V. Stepanenko, F. Würthner, *J. Am. Chem. Soc.* **2009**, *131*, 6719–6732.

94. G. Chen, H. Sasabe, T. Igarashi, Z. Hong, J. Kido, *J. Mater. Chem. A* **2015**, *3*, 14517–14534.

95. F. Silvestri, M. D. Irwin, L. Beverina, A. Facchetti, G. A. Pagani, T. J. Marks, *J. Am. Chem. Soc.* **2008**, *130*, 17640–17641.

96. S. Spencer, H. Hu, Q. Li, H. Y. Ahn, M. Qaddoura, A. Yao, A. Ioannidis, K. Belfield, C. J. Collison, *Prog. Photovolt.: Res. Appl.* **2014**, *22*, 488–493.

97. S. D. Spencer, C. Bougher, P. J. Heaphy, V. M. Murcia, C. P. Gallivan, A. Monfette, J. D. Anderson, J. A. Cody, B. R. Conrad, C. J. Collison, *Sol. Energy Mater. Sol. Cells* **2013**, *112*, 202–208.

98. G. Chen, H. Sasabe, Y. Sasaki, H. Katagiri, X.-F. Wang, T. Sano, Z. Hong, Y. Yang, J. Kido, *Chem. Mater.* **2014**, *26*, 1356–1364.

99. S. Brück, C. Krause, R. Turrisi, L. Beverina, S. Wilken, W. Saak, A. Lützen, H. Borchert, M. Schiek, J. Parisi, *Phys. Chem. Chem. Phys.* **2014**, *16*, 1067–1077.

100. G. de Miguel, M. Ziółek, M. Zitnan, J. A. Organero, S. S. Pandey, S. Hayase, A. Douhal, *J. Phys. Chem. C* **2012**, *116*, 9379–9389.

101. M. Schulz, J. Zablocki, O. S. Abdullaeva, S. Brück, F. Balzer, A. Lützen, O. Arteaga, M. Schiek, *Nat. Commun.* **2018**, *9*, 2413.

102. J. Gilot, R. Abbel, G. Lakhwani, E. W. Meijer, A. P. H. J. Schenning, S. C. J. Meskers, *Adv. Mater.* **2010**, *22*, 131–134.

103. D. Di Nuzzo, C. Kulkarni, B. Zhao, E. Smolinsky, F. Tassinari, S. C. J. Meskers, R. Naaman, E. W. Meijer, R. H. Friend, *ACS Nano* **2017**, *11*, 12713–12722.

104. H. Chen, K.-Y. Law, J. Perlstein, D. G. Whitten, *J. Am. Chem. Soc.* **1995**, *117*, 7257–7258.

105. M. Schulz, M. Mack, O. Kolloge, A. Lützen, M. Schiek, *Phys. Chem. Chem. Phys.* **2017**, *19*, 6996–7008.

106. A. T. Rösch, Q. Zhu, J. Robben, F. Tassinari, S. C. J. Meskers, R. Naaman, A. R. A. Palmans, E.W. Meijer, *Chem. Eur. J.* **2021**, *27*, 298–306.

107. G. Scheibe, *Angew. Chem.* **1937**, *50*, 212−219.

108. E. E. Jelley, *Nature* **1936**, *138*, 1009−1010.

109. N. J. Hestand, F. C. Spano, *Chem. Rev.* **2018**, *118*, 7069–7163.

110. C. Zheng, C. Zhong, C. J. Collison, F. C. Spano, *J. Phys. Chem. C* **2019**, *123*, 3203–3215.

111. V. Czikkely, H. D. Försterling, H. Kuhn, *Chem. Phys. Lett.* **1970**, *6*, 207–210.

112. (a) J. C. Chang, *J. Chem. Phys.* **1977**, *67*, 3901−3909; (b) C. Weiss, *J. Mol. Spectrosc.* **1972**, *44*, 37−80.

113. N. J. Hestand, C. Zheng, A. R. Penmetcha, B. Cona, J. A. Cody, F. C. Spano, C. J. Collison, *J. Phys. Chem. C* **2015**, *119*, 18964–18974.

114. (a) F. C. Spano, *J. Am. Chem. Soc.* **2009**, *131*, 4267–4278; (b) F. C. Spano, J. Clark, C. Silva, R. H. Friend, *J. Chem. Phys.* **2009**, *130*, 074904; (c) S. Sanyal, A. Painelli, S. K. Pati, F. Terenziani, C. Sissa, *Phys. Chem. Chem. Phys.* **2016**, *18*, 28198–28208.

115. (a) A. Painelli, F. Terenziani, *J. Phys. Chem. A* **2000**, *104*, 11041–11048; (b) F. Terenziani, A. Painelli, *Phys. Rev. B: Condens. Matter Mater. Phys.* **2003**, *68*, 165405.

116. B. Bardi, C. Dall'Agnese, K. I. Moineau-Chane Ching, A. Painelli, F. Terenziani, *J. Phys. Chem. C* **2017**, *121*, 17466–17478.

117. M. Tristani-Kendra, C. J. Eckhardt, *J. Chem. Phys.* **1984**, *81*, 1160−1173.

118. C.-A. Shen, F. Würthner, *Chem. Commun.* **2020**, *56*, 9878−9881.

119. N. R. Ávila-Rovelo, A. Ruiz-Carretero, *Organic Materials* **2020**, *02*, 047–063.

120. C. Sun, B. Li, M. Zhao, S. Wang, Z. Lei, L. Lu, H. Zhang, L. Feng, C. Dou, D. Yin, H. Xu, Y. Cheng, F. Zhang, *J. Am. Chem. Soc.* **2019**, *141*, 19221−19225.

121. A. Löhner, T. Kunsel, M. I. S. Röhr, T. L. C. Jansen, S. Sengupta, F. Würthner, J. Knoester, J. Köhler, *J. Phys. Chem. Lett.* **2019**, *10*, 2715−2724.

122. Z. Chen, Y. Liu, W. Wagner, V. Stepanenko, X. Ren, S. Ogi, F. Würthner, *Angew. Chem. Int. Ed.* **2017**, *56*, 5729−5733; *Angew. Chem.* **2017**, *129*, 5823−5827.

123. S. Herbst, B. Soberats, P. Leowanawat, M. Stolte, M. Lehmann, F. Würthner, *Nat. Commun*. **2018**, *9*, 2646.

124. F. C. Spano, *Acc. Chem. Res*. **2010**, *43*, 429−439.

125. U. Rösch, S. Yao, R. Wortmann, F. Würthner, *Angew. Chem. Int. Ed*. **2006**, *45*, 7026–7030; *Angew. Chem.* **2006**, *118*, 7184–7188.

126. H. Ceymann, A. Rosspeintner, M. H. Schreck, C. Mützel, A. Stoy, E. Vauthey, C. Lambert, *Phys. Chem. Chem. Phys.* **2016**, *18*, 16404−16413.

127. M. I. S. Röhr, H. Marciniak, J. Hoche, M. H. Schreck, H. Ceymann, R. Mitric, C. Lambert, *J. Phys. Chem. C* **2018**, *122*, 8082–8093.

128. M. M. J. Smulders, M. M. L. Nieuwenhuizen, T. F. A. de Greef, P. van der Schoot, A. P. H. J. Schenning, E. W. Meijer, *Chem. Eur. J.* **2010**, *16*, 362−367.

129. C. Rest, R. Kandanelli, G. Fernández, *Chem. Soc. Rev.* **2015**, *44*, 2543–2572.

130. T. Brixner, R. Hildner, J. Köhler, C. Lambert, F. Würthner, *Adv. Energy Mater*. **2017**, *7*, 1700236.

131. C.-A. Shen, D. Bialas, M. Hecht, V. Stepanenko, K. Sugiyasu, F. Würthner, *Angew. Chem. Int. Ed.* **2021**, DOI: 10.1002/anie.202102183.

132 . W. Herbst, K. Hunger, *Industrial Organic Pigments: Production, Properties, Applications, 3rd, Completely Revised Edition*, Wiley-VCH, Weinheim, **2004**.

133. J. Bernstein, *Polymorphism in Molecular Crystals*, Oxford University Press, Oxford, **2010**.

134. P. Erk, H. Hengelsberg, M. F. Haddow, R. van Gelder, *CrystEngComm* **2004**, *6*, 474–483.

135. M. Gsänger, D. Bialas, L. Huang, M. Stolte, F. Würthner, *Adv. Mater.* **2016**, *28*, 3615–3645.

136. (a) N. M. Matsumoto, R. P. M. Lafleur, X. Lou, K.-C. Shih, S. P. W. Wijnands, C. Guibert, J. W. A. M. van Rosendaal, I. K. Voets, A. R. A. Palmans, Y. Lin, E. W. Meijer, *J. Am. Chem. Soc.* **2018**, *140*, 13308−13316; (b) A. Langenstroer, K. K. Kartha, Y. Dorca, J. Droste, V. Stepanenko, R. Q. Albuquerque, M. R. Hansen, L. Sánchez, G. Fernández, *J. Am. Chem. Soc.* **2019**, *141*, 5192–5200; (c) M. Wehner, M. I. S. Röhr, M. Bühler, V. Stepanenko, W. Wagner, F. Würthner, *J. Am. Chem. Soc.* **2019**, *141*, 6092–6107; (d) N. Sasaki, M. F. J. Mabesoone, J. Kikkawa, T. Fukui, N. Shioya, T. Shimoaka, T. Hasegawa, H. Takagi, R. Haruki, N. Shimizu, S. Adachi, E. W. Meijer, M. Takeuchi, K. Sugiyasu, *Nat. Commun.* **2020**, *11*, 3578; (e) E. E. Greciano, J. Calbo, E. Ortí, L. Sánchez, *Angew. Chem. Int. Ed.* **2020**, *59*, 17517–17524; *Angew. Chem.* **2020**, *132*, 17670–17677; (f) M. Hecht, P. Leowanawat, T. Gerlach, V. Stepanenko, M. Stolte, M. Lehmann, F. Würthner, *Angew. Chem. Int. Ed.* **2020**, *59*, 17084–17090; *Angew. Chem.* **2020**, *132*, 17232 –17238; (g) J. Matern, K. K. Kartha, L. Sánchez, G. Fernández, *Chem. Sci.* **2020**, *11*, 6780–6788; (h) I. Helmers, B. Shen, K. K. Kartha, R. Q. Albuquerque, M. Lee, G. Fernández, *Angew. Chem. Int. Ed.* **2020**, *59*, 5675–5682; *Angew. Chem.* **2020**, *132*, 5724–5731; (i) T. Aizawa, K. Aratsu, S. Datta, T. Mashimo, T. Seki, T. Kajitani, F. Silly, S. Yagai, *Chem. Commun.* **2020**, *56*, 4280–4283.

137. For polymorphism studies in the field of squaraine thin films and crystals, see ref. 117 and (a) A. Viterisi, N. F. Montcada, C. V. Kumar, F. Gispert-Guirado, E. Martin, E. Escudero, E. Palomares, *J. Mater. Chem. A* **2014**, *2*, 3536–3542; (b) F. Balzer, H. Kollmann, M. Schulz, G. Schnakenburg, A. Lützen, M. Schmidtmann, C. Lienau, M. Silies, M. Schiek, *Cryst. Growth Des.* **2017**, *17*, 6455–6466; (c) J. Zablocki, O. Arteaga, F. Balzer, D. Hertel, J. J. Holstein, G. Clever, J. Anhäuser, R. Puttreddy, K. Rissanen, K. Meerholz, A. Lützen, M. Schiek, *Chirality* **2020**, *32*, 619–631.

138. (a) L. Gisslén, R. Scholz, *Phys. Rev. B* **2009**, *80*, 115309; (b) N. J. Hestand, F. C. Spano, *J. Chem. Phys.* **2015**, *143*, 244707; (c) B. Engels, V. Engel, *Phys. Chem. Chem. Phys.* **2017**, *19*, 12604–12619; (d) C. Kaufmann, D. Bialas, M. Stolte, F. Würthner, *J. Am. Chem. Soc.* **2018**, *140*, 9986–9995; (e) A. Oleson, T. Zhu, I. S. Dunn, D. Bialas, Y. Bai, W. Zhang, M. Dai, D. R. Reichman, R. Tempelaar, L. Huang, F. C. Spano, *J. Phys. Chem. C* **2019**, *123*, 20567–20578. (f) M. Hecht, F. Würthner, *Acc. Chem. Res.* **2020**, *54*, 642–653.

139. P. Chithra, R. Varghese, K. P. Divya, A. Ajayaghosh, *Chem. Eur J.* **2008**, *3*, 1365–1373.

140. (a) S. Ito, P. T. Herwig, T. Böhme, J. P. Rabe, W. Rettig, K. Müllen, *J. Am. Chem. Soc.* **2000**, *122*, 7698–7706; (b) S. Yagai, S. Kubota, T. Iwashima, K. Kishikawa, T. Nakanishi, T. Karatsu, A. Kitamura, *Chem. Eur. J.* **2008**, *14*, 5246–5257; (c) M. Yamauchi, Y. Chiba, T. Karatsu, A. Kitamura, S. Yagai, *Chem. Lett.* **2013**, *42*, 799–800; (d) X. Lin, Y. Okazawa, Y. Tani, H. Ouchi, K. Nakayama, S. Yagai, *Asian J. Org. Chem.* **2020**, *9*, 222–225.

141. S. Yagai, *Bull. Chem. Soc. Jpn.* **2015**, *88*, 28–58.

142. M. Wehner, M. I. S. Röhr, V. Stepanenko, F. Würthner, *Nat. Commun.* **2020**, *11*, 5460.

143. It is noteworthy that the appearance of helical structures for such supramolecular polymers is quite common. Accordingly, the situation for one-dimensional structures is different from three-dimensional crystals where conglomerates are the exceptions and racemic crystals the more general case, see: A. Palmans, *Mol. Syst. Des. Eng.* **2017**, *2*, 34–46.

144. S. Herbst, B. Soberats, P. Leowanawat, M. Lehmann, F. Würthner, *Angew. Chem. Int. Ed.* **2017**, *56*, 2162–2165; *Angew. Chem.* **2017**, *129*, 2194–2197.

145. W. Zhang, W. Jin, T. Fukushima, N. Ishii, T. Aida, *Angew. Chem. Int. Ed.* **2009**, *48*, 4747–4750; *Angew. Chem.* **2009**, *121*, 4841–4844.

146. F. Fennel, S. Wolter, Z. Xie, P.-A. Plötz, O. Kühn, F. Würthner, S. Lochbrunner, *J. Am. Chem. Soc.* **2013**, *135*, 18722–18725.

147. S. Ogi, T. Fukui, M. L. Jue, M. Takeuchi, K. Sugiyasu, *Angew. Chem. Int. Ed.* **2014**, *53*, 14363–14367; *Angew. Chem.* **2014**, *126*, 14591–14595.

148. L. Yang, G. Fan, X. Ren, L. Zhao, J. Wang, Z. Chen, *Phys. Chem. Chem. Phys.* **2015**, *17*, 9167–9172.

149. C. M. A. Leenders, L. Albertazzi, T. Mes, M. M. E. Koenigs, A. R. A. Palmans, E. W. Meijer, *Chem. Commun.* **2013**, *49*, 1963–1965.

150. A. Austin, N. J. Hestand, I. G. McKendry, C. Zhong, X. Zhu, M. J. Zdilla, F. C. Spano, J. M. Szarko, *J. Phys. Chem. Lett.* **2017**, *8*, 1118–1123.

151. C. Yan, S. Barlow, Z. Wang, H. Yan, A. K.-Y. Jen, S. R. Marder, X. Zhan, *Nat. Rev. Mater.* **2018**, *3*, 18003.

152. E. D. Cosco, A. L. Spearman, S. Ramakrishnan, J. G. P. Lingg, M. Saccomano, M. Pengshung, K. B. A. Arús, C. Y. Wong, S. Glasl, V. Ntziachristos, M. Warmer, R. R. McLaughlin, O. T. Bruns, E. M. Sletten, *Nat. Chem.* **2020**, *12*, 1123–1130.

153. A. Zampetti, A. Minotto, F. Cacialli, *Adv. Funct. Mater.* **2019**, *29*, 1807623.

154. F. C. Spano, C. Silva, *Ann. Rev. Phys. Chem.* **2014**, *65*, 477–500.

155. S. Xu, H.-W. Liu, S.-Y. Huan, L. Yuan, X.-B. Zhang, *Mater. Chem. Front.* **2021**, *5*, 1076–1089.

156. W. Zhao, E. M. Carreira, *Chem. Eur. J.* **2006**, *12*, 7254–7263.

157. J. R. Sommer, A. H. Shelton, A. Parthasarathy, I. Ghiviriga, J. R. Reynolds, K. S. Schanze, *Chem. Mater.* **2011**, *23*, 5296–5304.

158. H. Lu, J. Mack, Y. Yanga, Z. Shen, *Chem. Soc. Rev.* **2014**, *43*, 4778–4823.

159. A. Loudet, K. Burgess, *Chem. Rev.* **2007**, *107*, 4891–4932.

160. I. Lim, A. Vian, H. L. Wouw, R. A. Day, C. Gomez, Y. Liu, A. L. Rheingold, O. Campàs, E. M. Sletten, *J. Am. Chem. Soc.* **2020**, *142*, 16072−16081.

161. T. Weil, T. Vosch, J. Hofkens, K. Peneva, K. Müllen, *Angew. Chem. Int. Ed.* **2010**, *22*, 9068–9093; *Angew. Chem.* **2010**, *122*, 9252–9278.

162. H. Marciniak, N. Auerhammer, S. Ricker, A. Schmiedel, M. Holzapfel, C. Lambert, *J. Phys. Chem. C* **2019**, *123*, 3426−3432.

163. T.-S. Ahn, R. O. Al-Kaysi, A. M. Müller, K. M. Wentz, C. J. Bardeen, *Rev. Sci. Instrum.* **2007**, *78*, 086105.

164. A. L. Antaris, H. Chen, K. Cheng, Y. Sun, G. Hong, C. Qu, S. Diao, Z. Deng, X. Hu, B. Zhang, X. Zhang, O. K. Yaghi, Z. R. Alamparambil, X. Hong, Z. Cheng, H. Dai, *Nat. Mater.* **2016**, *15*, 235–243.

165. B. Li, L. Lu, M. Zhao, Z. Lei, F. Zhang, *Angew. Chem. Int. Ed.* **2018**, *57*, 7483–7487; *Angew. Chem.* **2018**, *130*, 7605–7609.

166. M. Pengshung, J. Li, F. Mukafum, S. A. Lopez, E. M. Sletten, *Org. Lett.* **2020**, *22*, 6150−6154.

167. Q. Yang, Z. Hu, S. Zhu, R. Ma, H. Ma, Z. Ma, H. Wan, T. Zhu, Z. Jiang, W. Liu, L. Jiao, H. Sun, Y. Liang, H. Dai, *J. Am. Chem. Soc.* **2018**, *140*, 1715–1724.

168. L. Bai, P. Sun, Y. Liu, H. Zhang, W. Hu, W. Zhang, Z. Liu, Q. Fan, L. Li, W. Huang, *Chem. Commun.* **2019**, *55*, 10920–10923.

169. Q. Yang, H. Ma, Y. Liang, H. Dai, *Acc. Mater. Res.* **2021**, *2*, 170–183.

170. J. H. Kim, A. Liess, M. Stolte, A.-M. Krause, V. Stepanenko, C. Zhong, D. Bialas, F. Spano, F. Würthner, *Adv. Mater.* **2021**, in press.

171. J. J. Stewart, *J. Mol. Model.* **2007**, *13*, 1173–1213.

172. E. Michail, M. H. Schreck, L. Wittmann, M. Holzapfel, C. Lambert, *Chem. Mater.* **2021**, DOI: 10.1021/acs.chemmater.0c04780.

173. V. Grande, C.-A. Shen, M. Deiana, M. Dudek, J. Olesiak-Banska, K.Matczyszyn, F. Würthner, *Chem. Sci.* **2018**, *9*, 8375–8381.

174. P. Murat, S. Balasubramanian, *Curr. Opin. Genet. Dev.* **2014**, *25*, 22−29.

175. R. Hänsel-Hertsch, M. Di Antonio, S. Balasubramanian, *Nat. Rev. Mol. Cell. Biol.* **2017**, *18*, 279−284.

176. A. M. Fleming, J. Zhu, Y. Ding, J. A. Visser, J. Zhu, C. J. Burrows, *Biochemistry* **2018**, *57*, 991−1002.

177. A. Bedrat, L. Lacroix, J.-L. Mergny, *Nucleic Acids Res.* **2016**, *44*, 1746−1759.

178. (a) P. Williams, L. Li, X. Dong, Y. Wang, *J. Am. Chem. Soc.* **2017**, *139*, 12426−12429; (b) S. Zhang, Y. Wu, W. Zhang, *ChemMedChem* **2014**, *9*, 899−911; (c) T. M. Ou, Y. J. Lu, J. H. Tan, Z. S. Huang, K. Y. Wong, L. Q. Gu, *ChemMedChem* **2008**, *3*, 690−713; (d) S. Balasubramanian, L. H. Hurley, S. Neidle, *Nat. Rev. Drug Discovery* **2011**, *10*, 261−275; (e) Q. Cao, Y. Li, E. Freisinger, P. Z. Qin, R. K. O. Sigel, Z.-W. Mao, *Inorg. Chem. Front.* **2017**, *4*, 10−32; (f) L. Tuong Vy Thi, H. Sujin, C. Junghyun, P. Hyun-Ju, *Curr. Pharm. Des.* **2012**, *18*, 1948−1972.

179. (a) A. Garci, K. J. Castor, J. Fakhoury, J.-L. Do, J. Di Trani, P. Chidchob, R. S. Stein, A. K. Mittermaier, T. Friščić, H. Sleiman, *J. Am. Chem. Soc.* **2017**, *139*, 16913−1692; (b) M. Wang, Z. Mao, T.-S. Kang, C.-Y. Wong, J.-L. Mergny, C.-H. Leung, D.-L. Ma, *Chem. Sci.* **2016**, *7*, 2516−2523; (c) K.-H. Leung, H.-Z. He, B. He, H.-J. Zhong, S. Lin, Y.-T. Wang, D.-L. Ma, C.-H. Leung, *Chem. Sci.* **2015**, *6*, 2166−2171.

180. A. C. Bhasikuttan, J. Mohanty, *Chem. Commun.* **2015**, *51*, 7581−7597.

181. B. R. Vummidi, J. Alzeer, N. W. Luedtke, *ChemBioChem* **2013**, *14*, 540−558.

182. Z. Li, K. B. Grant, *RSC Adv.* **2016**, *6*, 24617−24634.

183. J. Zhao, D. Zhong, S. Zhou, *J. Mater. Chem. B* **2018**, *6*, 349−365.

184. (a) M. Zuffo, A. Guédin, E.-D. Leriche, F. Doria, V. Pirota, V. Gabelica, J.-L. Mergny, M. Freccero, *Nucleic Acids Res.* **2018**, *46*, e115; (b) A. Laguerre, Y. Chang, M. Pirrotta, N. Desbois, C. P. Gros, E. Lesniewska, D. Monchaud, *Org. Biomol. Chem.* **2015**, *13*, 7034−7039; (c) F. Cuenca, O. Greciano, M. Gunaratnam, S. Haider, D. Munnur, R. Nanjunda, W. D. Wilson, S. Neidle, *Bioorg. Med. Chem. Lett.* **2008**, *18*, 1668−1673.

185. L. K. S. von Krbek, C. A. Schalley, P. Thordarson, *Chem. Soc. Rev.* **2017**, *46*, 2622−2637.

186. D. B. Hibbert, P. Thordarson, *Chem. Commun.* **2016**, *52*, 12792−12805.

187. P. Thordarson, *Chem. Soc. Rev.* **2011**, *40*, 1305−1323.

188. W. Xu, K. M. Chan, E. T. Kool, *Nat. Chem.* **2017**, *9*, 1043−1055.

189. Y. V. Suseela, N. Narayanaswamy, S. Pratihar, T. Govindaraju, *Chem. Soc. Rev.* **2018**, *47*, 1098−1131.

190. D. Miyoshi, H. Karimata, N. Sugimoto, *J. Am. Chem. Soc.* **2006**, *128*, 7957−7963.

191. J. Moreno, M. Gerecke, L. Grubert, S. A. Kovalenko, S. Hecht, *Angew. Chem. Int. Ed.* **2016**, *55*, 1544−1547; *Angew. Chem.* **2016**, *128*, 1569–1573.

192. B. Dumat, G. Bordeau, E. Faurel-Paul, F. Mahuteau-Betzer, N. Saettel, G. Metge, C. Fiorini-Debuisschert, F. Charra, M.-P. Teulade-Fichou, *J. Am. Chem. Soc.* **2013**, *135*, 12697−12706.

193. (a) N. S. Makarov, S. Mukhopadhyay, K. Yesudas, J. L. Brédas, J. W. Perry, A. Pron, M. Kivala, K. Müllen, *J. Phys. Chem. A* **2012**, *116*, 3781−3793; (b) Q. Zou, Y. Zhao, N. S. Makarov, J. Campo, H. Yuan, D. C. Fang, J. W. Perry, F. Wu, *Phys. Chem. Chem. Phys.* **2012**, *14*, 11743−11752; (c) S. Pascal, S. Denis-Quanquin, F. Appaix, A. Duperray, A. Grichine, B. L. Guennic, D. Jacquemin, J. Cuny, S. H. Chi, J. W. Perry, B. v. d. Sanden, C. Monnereau, C. Andraud, O. Maury, *Chem. Sci.* **2017**, *8*, 381−394; (d) B. Mettra, F. Appaix, J. Olesiak-Banska, T. Le Bahers, A. Leung, K. Matczyszyn, M. Samoc, B. van der Sanden, C. Monnereau, C. Andraud, *ACS Appl. Mater. Interfaces* **2016**, *8*, 17047−17059.

194. P. H. Doan, D. R. G. Pitter, A. Kocher, J. N. Wilson, T. Goodson, *J. Am. Chem. Soc.* **2015**, *137*, 9198−9201.

195. M. Deiana, B. Mettra, K. Matczyszyn, D. Pitrat, J. Olesiak-Banska, C. Monnereau, C. Andraud, M. Samoc, *Biomacromolecules* **2016**, *17*, 3609−3618.

196. M. Deiana, B. Mettra, L. Martinez-Fernandez, L. M. Mazur, K. Pawlik, C. Andraud, M. Samoc, R. Improta, C. Monnereau, K. Matczyszyn, *J. Phys. Chem. Lett.* **2017**, *8*, 5915−5920.

197. R. del Villar-Guerra, J. O. Trent, J. Chaires, *Angew. Chem. Int. Ed.* **2018**, *57*, 7171−7175; *Angew. Chem.* **2018**, *130*, 7289–7293.

198. A. Ajayaghosh, *Acc. Chem. Res.* **2005**, *38*, 449−459.

199. C. Lambert, F. Koch, S. F. Völker, A. Schmiedel, M. Holzapfel, A. Humeniuk, M. I. S. Röhr, R. Mitric, T. Brixner, *J. Am. Chem. Soc.* **2015**, *137*, 7851−7861.

200. A. D. Becke, *J. Chem. Phys.* **1993**, *98*, 5648−5652.

201. C. Lee, W. Yang, R. G. Parr, Phys. Rev. B **1988**, *37*, 785−789.

202. G. A. Petersson, A. Bennett, T. G. Tensfeldt, M. A. Al-Laham, W. A. Shirley, *J. Chem. Phys.* **1988**, *89*, 2193−2218.

203. Gaussian 09, Revision D.01, M. J. Frisch, G. W. Trucks, H. B. Schlegel, G. E. Scuseria, M. A. Robb, J. R. Cheeseman, G. Scalmani, V. Barone, G. A. Petersson, H. Nakatsuji, X. Li, M. Caricato, A. Marenich, J. Bloino, B. G. Janesko, R. Gomperts, B. Mennucci, H. P. Hratchian, J. V. Ortiz, A. F. Izmaylov, J. L. Sonnenberg, D. Williams-Young, F. Ding, F. Lipparini, F. Egidi, J. Goings, B. Peng, A. Petrone, T. Henderson, D. Ranasinghe, V. G. Zakrzewski, J. Gao, N. Rega, G. Zheng, W. Liang, M. Hada, M. Ehara, K. Toyota, R. Fukuda, J. Hasegawa, M. Ishida, T. Nakajima, Y. Honda, O. Kitao, H. Nakai, T. Vreven, K. Throssell, J. A. Montgomery, Jr., J. E. Peralta, F. Ogliaro, M. Bearpark, J. J. Heyd, E. Brothers, K. N. Kudin, V. N. Staroverov, T. Keith, R. Kobayashi, J. Normand, K. Raghavachari, A. Rendell, J. C. Burant, S. S. Iyengar, J. Tomasi, M. Cossi, J. M. Millam, M. Klene, C. Adamo, R. Cammi, J. W. Ochterski, R. L. Martin, K. Morokuma, O. Farkas, J. B. Foresman, D. J. Fox, Gaussian, Inc., Wallingford CT, **2016**.

204. M. M. J. Smulders, A. P. H. J. Schenning, E. W. Meijer, *J. Am. Chem. Soc.* **2008**, *130*, 606−611.

205. F. Würthner, S. Yao, T. Debaerdemaeker, R. Wortmann, *J. Am. Chem. Soc.* **2002**, *124*, 9431−9447.

206. R. B. Martin, *Chem. Rev.* **1996**, *96*, 3043−3064.

207. T. Yanai, D. P. Tew, N. C. Handy, *Chem. Phys. Lett.* **2004**, *393*, 51–57.

208. F. Weigend, R. Ahlrichs, *Phys. Chem. Chem. Phys.* **2005**, *7*, 3297–3305.

209. E. F. Pettersen, T. D. Goddard, C. C. Huang, G. S. Couch, D. M. Greenblatt, E. C. Meng, T. E. Ferrin, *J. Comput. Chem.* **2004**, *25*, 1605–1612.

210. D. Bialas, C. Zhong, F. Würthner and F. C. Spano, *J. Phys. Chem. C* **2019**, *123*, 18654–18664.

211. (a) J. E. Lewis, M. Maroncelli, *Chem. Phys. Lett.* **1998**, *282*, 197−203; (b) N. Q. Chako, *J. Chem. Phys.* **1934**, *2*, 644−653.

212. C. Würth, M. Grabolle, J. Pauli, M. Spieles, U. Resch-Genger, *Nat. Protoc.* **2013**, *8*, 1535–1550.

213. Gaussian 09, Revision D.01, Frisch, M. J.; Trucks, G. W.; Schlegel, H. B.; Scuseria, G. E.; Robb, M. A.; Cheeseman, J. R.; Scalmani, G.; Barone, V. G.; Petersson, A.; Nakatsuji, H.; Li, X.; Caricato, M.; Marenich, A.; Bloino, J.; Janesko, B. G.; Gomperts, R.; Mennucci, B. H.; Hratchian, P.; Ortiz, J. V.; Izmaylov, A. F.; Sonnenberg, J. L.; Williams-Young, D.; Ding, F.; Lipparini, F.; Egidi, F.; Goings, J.; Peng, B.; Petrone, A.; Henderson, T.;

Ranasinghe, D.; Zakrzewski, V. G.; Gao, J.; Rega, N.; Zheng, G.; Liang, W.; Hada, M.; Ehara, M.; Toyota, K.; Fukuda, R.; Hasegawa, J.; Ishida, M.; Nakajima, T.; Honda, Y.; Kitao, O.; Nakai, H.; Vreven, T.; Throssell, K.; Montgomery, Jr., J. A.; Peralta, J. E.; Ogliaro, F.; Bearpark, M.; Heyd, J. J.; Brothers, E.; Kudin, K. N.; Staroverov, V. N.; Keith, T.; Kobayashi, R.; Normand, J.; Raghavachari, K.; Rendell, A.; Burant, J. C.; Iyengar, S. S.; Tomasi, J.; Cossi, M.; Millam, J. M.; Klene, M.; Adamo, C.; Cammi, R.; Ochterski, J. W.; Martin, R. L.; Morokuma, K.; Farkas, O.; Foresman, J. B.; Fox, D. J., Gaussian, Inc., Wallingford CT, **2013**.

214. A. Alessi, M. Salvalaggio, G. Ruzzon, *J. Lumin.* **2013**, *134*, 385−389.

215. J. R. Lakowicz, *Principles of Fluorescence Spectroscopy*, Kluwer Academic / Plenum Publishers, **1999**.

216. E. Largy, J.-L. Mergny, *Nucleic Acids Res.* **2014**, *42*, e149.

217. A. Kerkour, J. Marquevielle, S. Ivashchenko, L. A. Yatsunyk, J.-L. Mergny, G. F. Salgado, *J. Biol. Chem.* **2017**, *292*, 8082−8091.

218. J. M. Nicoludis, S. P. Barrett, J.-L. Mergny, L. A. Yatsunyk, *Nucleic Acids Res.* **2012**, *40*, 5432−5447.

219. A. De Rache, J.-L. Mergny, *Biochimie* **2015**, *115*, 194−202.

220. N. Kumar, S. Maiti, *Nucleic Acids Res.* **2008**, *36*, 5610−5622.

221. A. T. Phan, *FEBS J.* **2010**, *277*, 1107−1117.

222. A. T. Phan, V. Kuryavyi, S. Burge, S. Neidle, D. J. Patel, *J. Am. Chem. Soc.* **2007**, *129*, 4386−4392.

223. Z. Zhang, J. Dai, E. Veliath, R. A. Jones, D. Yang, *Nucleic Acids Res.* **2010**, *38*, 1009−1021.

224. N. S. Makarov, M. Drobizhev, A. Rebane, *Opt. Express* **2008**, *16*, 4029−4047.

225. M. Y. Berezin, C. Zhan, H. Lee, C. Joo, W. J. Akers, S. Yazdanfar, S. Achilefu, *J. Phys. Chem. B* **2011**, *115*, 11530−11535.

226. Gaussian 09, M. J. Frisch, G. W. Trucks, H. B. Schlegel, G. E. Scuseria, M. A. Robb, J. R. Cheeseman, G. Scalmani, V. Barone, B. Mennucci, G. A. Petersson, H. Nakatsuji, M. Caricato, X. Li, H. P. Hratchian, A. F. Izmaylov, J. Bloino, G. Zheng, J. L. Sonnenberg, M. Hada, M. Ehara, K. Toyota, R. Fukuda, J. Hasegawa, M. Ishida, T. Nakajima, Y. Honda, O. Kitao, H. Nakai, T. Vreven, J. A. Montgomery, J. E. Peralta, F. Ogliaro, M. Bearpark, J. J. Heyd, E. Brothers, K. N. Kudin, V. N. Staroverov, R. Kobayashi, J. Normand, K. Raghavachari, A. Rendell, J. C. Burant, S. S. Iyengar, J. Tomasi, M. Cossi, N. Rega, J. M. Millam, M. Klene, J. E. Knox, J. B. Cross, V. Bakken, C. Adamo, J. Jaramillo, R.

Gomperts, R. E. Stratmann, O. Yazyev, A. J. Austin, R. Cammi, C. Pomelli, J. W. Ochterski, R. L. Martin, K. Morokuma, V. G. Zakrzewski, G. A. Voth, P. Salvador, J. J. Dannenberg, S. Dapprich, A. D. Daniels, O. Farkas, J. B. Foresman, J. V. Ortiz, J. Cioslowski, D. J. Fox, Gaussian, Inc., **2009**.

227. RCSB Protein Data Bank, https://www.rcsb.org/, (accessed in April 2018).
228. O. Trott, A. J. Olson, *J. Comput. Chem.* **2010**, *31*, 455−461.
229. M. Su, S.-Y. Shi, Q. Wang, N. Liu, J. Yin, C. Liu, Y. Ding, Z.-Q. Wu, *Polym. Chem.* **2015**, *6*, 6519−6528.